Method and Instrumentation for the Measurement and Characterization of MEMS Fabricated Electrical Contacts

by

Melissa B. Read

S.B., Massachusetts Institute of Technology (2004)
S.M., Massachusetts Institute of Technology (2006)

Submitted to the Department of Mechanical Engineering
in partial fulfillment of the requirements for the degree of

Doctor of Philosophy

at the

MASSACHUSETTS INSTITUTE OF TECHNOLOGY

February 2010

Author .....
Department of Mechanical Engineering
January 19, 2010

Certified by .....
Alexander H. Slocum
Pappalardo Professor of Mechanical Engineering
Chairman of the Committee
Thesis Supervisor

Accepted by .....
David E. Hardt
Chairman, Department Committee on Graduate Students

Method and Instrumentation for the Measurement and Characterization of MEMS Fabricated Electrical Contacts

by

Melissa B. Read

Submitted to the Department of Mechanical Engineering
on January 19, 2010, in partial fulfillment of the
requirements for the degree of
Doctor of Philosophy

Abstract

MEMS fabricated electrical contacts consist of two MEMS fabricated surfaces which are physically separated and brought together for the purpose of carrying current. MEMS fabricated electrical contacts are used in a wide variety of applications including MEMS relays, wafer probing applications, and the packaging and assembly of MEMS devices. In all of these devices, low, stable contact resistance is desired. Modeling these contacts is difficult because much of traditional contact resistance theory was derived for macro scale contacts and relies on assumptions not valid at the MEMS scale. A large variety of factors affect contact resistance including contact force, contact scrub, contact material, and contact geometry. Additionally, electrical characteristics of these contacts can change over many cycles. The result of this is that the MEMS fabricated electrical contacts used in a variety of devices are often designed using a trial and error approach to determine which contact materials and geometries work best. Since these devices are often expensive and timely to manufacture, this method of design is far from ideal.

The objective of my research is to develop a system for measuring and characterizing a wide variety of MEMS fabricated electrical contacts. The system consists of two silicon coupons which can be assembled and disassembled with a positional repeatability of less than one micron. This system allows any combination of contact force and contact scrub to be imparted on a pair of MEMS fabricated electrical contacts. The contacts themselves can consist of a wide variety of materials fabricated in a wide variety of ways including sputtering contact material, plating contact material, unconventional contact materials, plated tips, and three-dimensional tips. The repeatable assembly and disassembly of the coupons allows the contacts to be tested, observed using metrology such as an SEM or AFM, and then reassembled for further testing. This allows the changes in the contact surface to be observed as the contact is cycled. The instrumentation to impart force, scrub and measure contact resistance has also been developed.

This system is used to measure the contact resistance between flat-on-flat contacts, plated tip contacts, and spherical contacts. The results of these tests offer fundamen-

tal insights into the contact resistance between two thin films as well as compile a variety of data regarding multiple contact materials and contact geometries. The results of these tests are used to create guidelines for designers of MEMS fabricated electrical contacts. Additionally, this platform can be used as a method of measurement and characterization for designers of MEMS fabricated electrical contacts to test any new contact geometries and materials in a quick cost effective manner. This method can also be used by research scientists investigating the fundamental physics of MEMS scale electrical contacts.

Thesis Supervisor: Alexander H. Slocum
Title: Pappalardo Professor of Mechanical Engineering
Chairman of the Committee

Acknowledgments

Many individuals contributed not only to this thesis, but also to my remarkable graduate school experience. I would like to thank a few of them specifically.

- Professor Alex Slocum for being a fantastic research advisor who encouraged all of his graduate students to be great snowboarders as well as great scientists.
- Professor Jeff Lang for participating on my committee as well and working with me on many papers.
- Professor Carl Thompson for participating on my committee.
- Dr. Rod Martens for working with me on all of the contact resistance aspects of this thesis, participating on my committee, and his infinite patience.
- Professor Alexandra Techet for advising my master's thesis.
- The staffs of the Microsystems Technology Lab, the Papparaldo Machine Shop, and the Edgerton Student Shop.
- Aaron Gawlik and Adam Wahab for their work on the original instrumentation.
- My colleagues in the Precision Engineering Research Group.
- My friends and roommates for their continued support.
- My parents Wayne and Ceil Read, my brother Justin Read, and the rest of my extended family for always encouraging and supporting me.

Contents

List of Figures

List of Tables

Chapter 1

Objectives, Motivation, and Chapter Preview

1.1 Objectives

This thesis undertakes an experimental investigation of MEMS fabricated electrical contacts. Correspondingly, the objectives of this thesis are: to develop a system for measuring and characterizing MEMS fabricated electrical contacts, to create guidelines for designing these contacts, and to suggest a method for testing other contacts.

A pair of MEMS fabricated electrical contacts is essentially two conductive surfaces which are brought into and out of physical contact. Their dimensions are typically on the order of microns and the force across them is on the order of micro to milli Newtons. They are fabricated using MEMS processes such as sputtering of thin metal layers or chemical vapor deposition of carbon nanotubes. When these surfaces are in physical contact, they carry a current. The resistance across a pair of contacts is higher than it would be if these contacts were made of a solid piece of material. This higher resistance is the result of several factors such as oxide films and contamination. Another large factor is that the actual physical contact area between the surfaces is very small compared to the apparent contact area. The surfaces only truly meet at small asperities, or local high points. The current must constrict into these small asperities, which causes an increase in contact resistance. Contact resistance

is in addition to any bulk resistance. The value of contact resistance is dependent on many factors including the contact force, the contact material, and any lateral motion between the two sides of the contact. The effect of each of these factors on contact resistance is difficult to model and must be observed experimentally.

This thesis presents a two-coupon system capable of measuring the contact resistance of a wide array of contact materials and geometries while varying the force on the contact and the lateral motion between the two contact halves. This system can be assembled and reassembled with a positional repeatability of less than one micron. This enables contact resistance to be measured, the contacts to be disassembled and observed under an SEM, and then reassembled for further testing. The positional repeatability is crucial because contact resistance is dominated by asperity level contacts and if the two contact halves shifted relative to each other, contact resistance would be affected. The electrical properties of these contacts are measured using instrumentation specifically designed for the two-coupon system. Tests were performed on a variety of contact materials to generate guidelines as to which types of contacts are appropriate for certain applications. The results of these tests are used to suggest a testing methodology to be used on future contacts so that the results can be accurately compared with those from other contacts.

1.2 Motivation

The initial motivation for this thesis was the result of a collaboration with Dr. Alexis Weber on his Ph.D. thesis 'MEMS Relays for Make-Break Power Switching Applications: 111 Silicon Etched Planar Electrical Contacts' [65]. Weber worked on a MEMS relay, which is essentially a small switch fabricated using MEMS processes. The most common switch is a solid state transistor, which always has a small amount of current leakage. Certain applications require a hard-off or hard-on state with no current leakage. This is achieved by physically separating two halves of an electrical contact. Weber created a MEMS relay which separated and brought together two flat, parallel electrical contacts as shown in Figure 1-1. The performance of the device was depen-

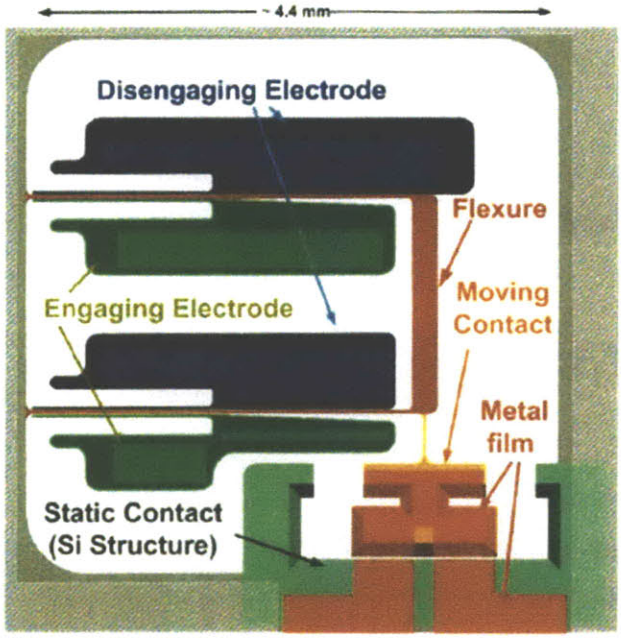

Figure 1-1: The MEMS relay created by Weber which contained two flat-on-flat gold contacts.

dent on a low contact resistance across the contacts since the primary purpose of the relay was to switch high power, low frequency applications. Therefore, Weber wanted to choose a material that would have a low and stable contact resistance. However, the material would also have to maintain this low contact resistance for the lifetime of the device. Since each MEMS relay took several months to fabricate and was quite costly, testing different contact materials using actual devices did not make financial sense. Therefore, a two-coupon system was created which could be fabricated much faster than Weber's device and at a fraction of the cost. This device could mimic the mechanical and electrical conditions seen in Weber's relay and allowed multiple contact materials to be tested without having to build multiple relays. It also allowed for the assembly and disassembly of the coupons with excellent positional repeatability so that physical changes in the contact could be viewed throughout life cycle testing.

The designers of other types of MEMS relays could also benefit from a device which enables the rapid and simple characterization of MEMS fabricated electrical contacts. In 1993, Hosaka reported on the potential impact of MEMS relays say-

ing "Microrelays have the same advantage of mechanical relays over semiconductor switches, in that they have lower on-resistance, higher off-resistance, higher dielectric strength, lower power consumption, and lower cost. Furthermore, by introducing MEMS technology to mechanical relays, size, cost, and switching time are greatly improved, and combined production with other electronic components becomes possible." He went on to say that the very first step in the development of this technology was to characterize the electrical properties of the contacts employed in MEMS relays. Hosaka, like Weber, was interested in the effect of changing the contact metal in his relays and how that would affect the actuator force which was needed to obtain a low, stable contact resistance [20].

The design of MEMS probe cards also requires a precise knowledge of what affects contact resistance. Eleven years after Hosaka declared characterization of electrical contacts to be the first step in improving MEMS relays, Kataoka noted that some of the microsprings he had fabricated for use in a probe card could not produce enough force to obtain a stable value for contact resistance [26]. These two papers were written over a decade apart, but both dealt with the same fundamental problem: one cannot design a device which relies on the relationship between contact force and contact resistance without having prior knowledge of this relationship. Probing applications also look at the effects of cycling on contact resistance. Chung was interested in the relationship between force and contact resistance for MEMS probes touching down on an aluminum substrate and the wear that would be incurred after 10,000 touchdowns [6]. The probes and probe cards Chung was investigating are shown in Figure 1-2.

Yet another application which could benefit from the characterization of MEMS fabricated electrical contacts is the packaging and assembly of MEMS devices. One type of assembly is known as a flip chip, which allows MEMS devices to be assembled by preloading two electrical contacts together. Krueger proposed using flip chip technology to temporarily assemble MEMS devices for testing. This is shown in Figure 1-3. Three elliptical shaped contact bumps were tested to determine which would have the lowest contact resistance in a flip chip [28]. These, like in MEMS relays,

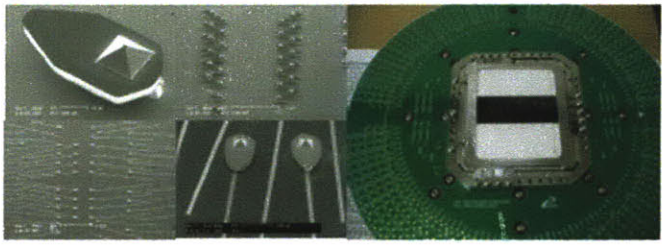

Figure 1-2: Left: A single MEMS probe. Right: a full probe card containing many MEMS probes. [6].

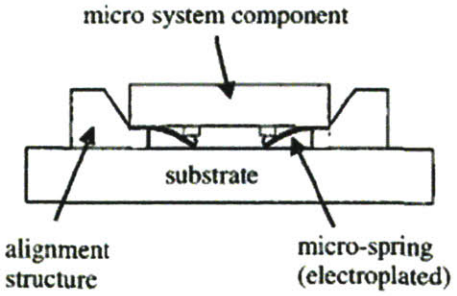

Figure 1-3: A flip chip for MEMS assembly [28].

were tested on full devices requiring full fabrication runs. Additionally, the forces that could be tested were limited to the forces that could be created using the current flip chip design even though optimizing contact resistance might require a higher force requiring a new flip chip design.

A fourth area which could benefit from a standardized platform for testing MEMS fabricated electrical contacts is academic research. There are currently many academic questions regarding MEMS fabricated electrical contacts, such as the effect of very thin films [3] or certain contaminants [10]. Often these studies are done on platforms designed specifically for the study. This means each study must not only evaluate its results, but also the accuracy to which the platform can provide measurements. A standard, characterized platform for these experiments could save the scientists the time it takes to develop a test setup as well as ensure confidence in their results by using a thoroughly characterized system.

The development of a system to characterize MEMS fabricated electrical contacts would benefit the designers of applications such as MEMS relays, probe cards, and

flip chips. It would be useful to those conducting academic research on the properties of these types of contacts. Lastly, by creating a platform which could test all types of MEMS fabricated electrical contacts, it would enable the rapid characterization of future contacts which would allow for the direct comparison of different types of contacts. Therefore, there is ample motivation for creating a system capable of characterizing a wide variety of MEMS fabricated electrical contacts. This thesis presents such a system which is able to test numerous contact materials and geometries while subjecting them to a user defined contact force and lateral scrubbing motion. It also allows for the monitoring of physical changes to the contacts between tests. This system has significantly more functionality than the one initially designed to assist Weber in choosing a contact material for his relay. This thesis presents the characterization system system, the results obtained from contacts tested using this system, and suggests a test methodology for evaluating MEMS fabricated electrical contacts.

1.3 Chapter Preview

Chapter 2 of this thesis is entitled Review of Theory and Literature. In the first part of this chapter, contact resistance is defined; and contact resistance theory is reviewed. The particular aspects of contact resistance theory discussed are contact between clean, flat surfaces; the effect of conductive thin films on contact resistance; the effect of oxides and other non-conductive thin films on contact resistance which includes the effects of scrubbing and fritting; and, finally, the effect of decreasing film thickness on contact resistance. Next, previous work pertaining to contact resistance is discussed, specifically with regard to the following five areas: contact material, contact geometry, nature of the contact, adhesion, and the effects of wear and cycling.

Chapter 3 details the design and fabrication of the first generation two-coupon system used to measure and characterize contact resistance. This system uses a kinematic coupling configuration for alignment. Chapter 4 details the second generation two-coupon system which utilizes an elastic averaging mechanism for alignment. This mechanism consists of 32 KOH-etched pyramids on 32 flexible arms that mate with

32 pits. Chapter 5 covers the final-two coupon system, which includes scrubbing capability and the ability to test tips of multiple heights.

Chapter 6 discusses the instrumentation used to measure contact resistance in the two-coupon system while imparting a user defined force, scrub, and source current.

Chapter 7 discusses the results of contact resistance experiments of flat, thin films. It examines two models for the behavior of the contact resistance in flat thin films and determines that each of the models and dominate in different ranges. Chapter 8 discusses the contact resistance between spheres and flat surfaces and between plated tips and flat surfaces. It determines that the radius of the sphere in sphere-on-flat contact can affect contact resistance, that a force and scrub applied together results in a more stable contact resistance than force and scrub applied in series, that material selection is very important in scrubbing contact, and that contact pressure is very important when making contact to surfaces which have an non-conductive oxide film.

Chapter 9 summarizes this thesis, discusses general design recommendations for MEMS fabricated electrical contact, and discusses future work.

Chapter 2

Review of Theory and Literature

List of Symbols	
a	Asperity radius
A	Apparent contact area
A_c	Actual contact area
α	Holm contact radius
d	Film thickness
e	Electric charge
E	Young's modulus
E_e	Equivalent Young's modulus
F	Force
h	Plank's constant
H	Vicker's hardness
I	Current
j	Current density
L	Lorenz constant $2.45\text{x}10^{-8}$ V^2/K^2
m	Mass of electron
μ	Parameter representing equipotential surfaces
ϕ	Work function of metal conductors
r	Radial direction

continued from previous page

List of Symbols	
R	Cylinder radius
R_c	Contact resistance
R_e	Equivalent radius
R_t	Contact resistance with tunneling effects
ρ	Resistivity
T_m	Melting Temperature
T_o	Bulk Temperature
V_m	Melting voltage
z	Axial direction

This chapter discusses an overview of contact resistance, the derivation and empirical conformation of classic contact resistance theory, and the literature pertaining to five specific aspects of MEMS fabricated electrical contacts which affect contact resistance. These aspects are contact material, contact geometry, nature of the contact, adhesion, and the effects of wear and cycling. Previous approaches to characterizing MEMS fabricated electrical contacts are also discussed.

2.1 Contact Resistance

Contact resistance is a resistance in addition to bulk resistance. Figure 2-1a shows two cylinders coming into contact end to end. If these cylinders were to have contact at every point along the joint between them, then the total resistance would simply be that of the bulk resistance of the first cylinder plus that of the bulk resistance of the second cylinder. In that case, the current lines would be straight and run axially along the cylinder. In actuality, contact is made only at asperities, local high spots on the contacting surfaces of each cylinder. Therefore, the actual contact area is much less than the apparent contact area. In Figure 2-1a, the current lines suggest that the two cylinders are only meeting at a single asperity. Therefore, the actual

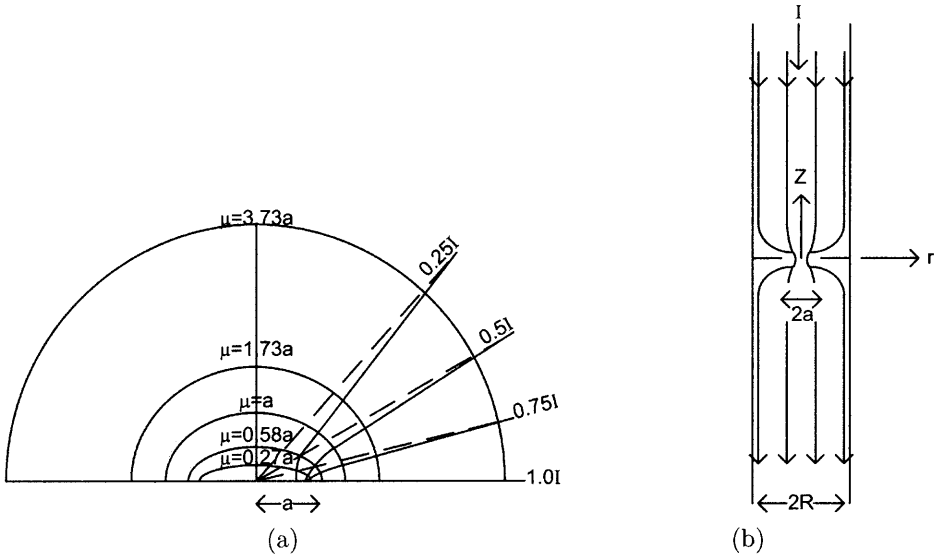

Figure 2-1: (a) The equipotential and current lines a single contact point where μ is defined in Equation 2.1. (b) Two cylindrical bodies of radius R making contact at a flat spot of radius a. This figure was take from [54]

resistance across this section is the bulk resistance of the top cylinder plus the bulk resistance of the bottom cylinder, plus an additional resistance which comes from the current lines constricting into the asperity from the first cylinder and then spreading from the asperity into the second cylinder. This additional resistance is called *contact resistance.*

2.2 Classic Contact Resistance Theory

Much of the classic contact resistance theory referenced in this thesis comes from Ragnar Holm's 'Electrical Contacts: Theory and Applications' [19]. The simplicity and universalism of this theory is remarkable. It has been proven empirically in numerous materials and configurations. However, the theory presented by Holm relates mostly to macro scale electrical contacts, and some of the assumptions do not hold true at the MEMS scale. Much of this macro scale theory is eloquently described in Paul Slade's 'Electrical Contacts: Principles and Applications' [54]. The following section summarizes the portions of this classic contact theory which are

most applicable to the challenges addressed by this thesis.

2.2.1 Electrical Contact Between Clean, Nominally Flat Surfaces

The simplest representation of a pair of electrical contacts is two cylindrical bodies of radius R meeting at a single flat point of radius a, as shown in Figure 2-1a. This area of contact is known as an asperity, a-spot, or constriction. A two-dimensional cross section of one-half of this contact is shown in Figure 2-1b, which also shows the equipotential surfaces and current lines radiating from the contact. The equipotential surfaces are defined by the equation [54]

$$\frac{r^2}{a^2+\mu^2}+\frac{z^2}{\mu^2}=1 \tag{2.1}$$

where μ is a parameter representing the equipotential surfaces, a is the asperity radius, and r and z are the cylindrical coordinates, as defined in Figure 2-1b. The resistance caused by this curving of the current lines (as opposed to the straight current lines that would exist if the two cylinders were completely connected), is referred to as the contact resistance, spreading resistance, or constriction resistance, and is given by [19, 54]

$$R_c=\rho/2\pi\int_0^{\mu}d\mu/(a^2+u^2)=(\rho/2\pi a)tan^{-1}(\mu/a) \tag{2.2}$$

where ρ is the resistivity of the material. Far away from the constriction, as $\mu\rightarrow\infty$, this reduces

$$R_c=\rho/4a \tag{2.3}$$

and since this is the resistance on one-half the contact, the entire contact resistance is, therefore,

$$R_c=\rho_1/4a+\rho_2/4a \tag{2.4}$$

where ρ_1 is the resistivity of the top surface material and ρ_2 is the resistivity of the bottom surface material. If both contact surfaces have the same resistivity, then this

equation reduces to

$$R_c = \rho/2a \tag{2.5}$$

For values of $a/R_c < 0.5$, the current density in this contact spot is given by [54]

$$j(r) = I/2\pi a^2(1 - r^2/a^2)^{1/2} \tag{2.6}$$

having a maximum current density in the center of the contact of

$$j(r) = I/2\pi a^2 \tag{2.7}$$

The relationship between the size of a constriction and the contact resistance is relatively straight forward. However, to understand the relationship between contact force and contact resistance, one must understand how contact force affects contact area. Physical contact between two surfaces occurs only at the asperities. The size and position of these asperities is a function of surface roughness. In MEMS fabricated electrical contacts, a typical asperity might be on the order of 1 μm [22]. If two such asperities come into contact, the initial deformation will be perfectly elastic and dominated by Hertzian contact force [54]. The radius of contact as a function of the Hertz contact force is given by [56]

$$a = \left(\frac{3FR_e}{2E_e}\right)^{1/3} \tag{2.8}$$

where F is the contact force, R_e is the equivalent radius, and E_e is the equivalent modulus of elasticity of the system. For two spherical contacts, R_e is given by

$$R_e = \frac{1}{\frac{2}{R_1} + \frac{2}{R_2}} \tag{2.9}$$

where R_1 is the radius of one spherical asperity and R_2 is the radius of the other spherical asperity. The equivalent modulus of elasticity is given by

$$E_e = \frac{1}{\frac{1-\nu_1^2}{E_1} + \frac{1-\nu_2^2}{E_2}} \tag{2.10}$$

where E_1 and E_2 are the Young's Moduli of the the two surfaces and ν_1 and ν_2 are the Poisson's ratios of the two surfaces. This behavior continues until the the contact enters the plastic region. For asperities on the order of 1 μm, plasticity can set in at a very low force. For two gold spherical contacts with radii of 1 μm, plasticity would begin at a force of approximately 100 μN. If the contact pressure on the asperity causes it to yield, then the area will continue to increase to accommodate this yield. This flowing is generally accepted to begin when the pressure is equal to the material hardness. Therefore, in plasticity, the relationship between force and contact radius is given by

$$F = A_c H \tag{2.11}$$

$$A_c = \pi a^2 \tag{2.12}$$

$$a = \left(\frac{F}{\pi H}\right)^{1/2} \tag{2.13}$$

where A_c is the actual contact area, and H is the hardness of the softer material between the two contacts. In reality, however, contacts do not meet at one single growing asperity. They first meet at one asperity, then as that asperity deforms, more asperities come into contact. Each asperity only experiences elastic deformation during its initial deformation and then experiences plastic deformation. Therefore, as more and more asperities come into contact, the vast majority of asperities experience plastic deformation. A more detailed look at the elastic plastic transition can be found in Greenwood and Williamson's 'Contact of Nominally Flat Surfaces,' which takes into account the distribution of asperity heights [15]. It is generally assumed that in the region outside of that for which Hertz contact forces dominate, that all asperities are effectively experiencing plastic deformation. This means that all of the

asperities experience a pressure equal to the hardness of the material. Therefore, just as was true for a single asperity in Equation 2.12, the total contact area A_c is still related to contact force by the equation

$$F = A_c H \tag{2.14}$$

where the total contact area is now

$$A_c = \sum_{i=1}^{n} \pi a_i^2 \tag{2.15}$$

$$A_c = n\pi\bar{a} \tag{2.16}$$

where $\bar{a}$ is the average size of each of the n asperities each having an individual radius of a_i. An equivalent radius of contact α is therefore defined as

$$\pi\alpha^2 = n\pi\bar{a}^2 \tag{2.17}$$

$$\alpha = n^{1/2}\bar{a} \tag{2.18}$$

This equivalent radius of contact α is referred to as the *Holm radius*, and is written in terms of force and material hardness as

$$\alpha = \left(\frac{F}{\pi H}\right)^{1/2} \tag{2.19}$$

Although the Holm radius is relatively simple to derive, the contact resistance of these multiple spots is less straight forward. If these spots simply acted as resistors in parallel, as determined from Equation 2.5, then the net contact resistance would be approximately

$$R_c = \frac{\rho}{2n\bar{a}} \tag{2.20}$$

Substituting for the Holm radius using Equation 2.18

$$R_c = \frac{\rho}{2n^{1/2}\alpha} \tag{2.21}$$

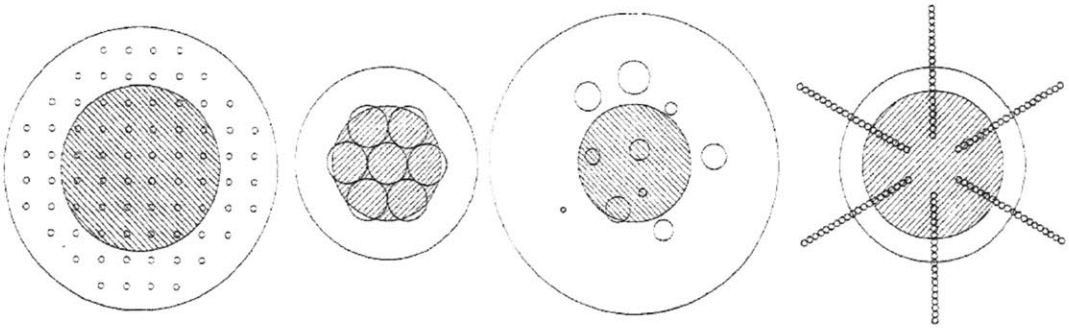

Figure 2-2: Several of the asperity configurations examined in [14].

However, this ignores all interactions between the asperities. The predominate work dealing with these interactions is Greenwood's 'Contact Resistance and the Real Area of Contact.' This paper looked at a large array of contact spot sizes, some of which are shown in Figure 2-2, and distributions. For these parameters, it found a remarkably robust result. Regardless of the number of contact spots or their distribution, the overall contact resistance was always approximately given by

$$R_c = \rho\left(\frac{1}{2n\bar{a}} + \frac{1}{2\alpha}\right) \tag{2.22}$$

where $\bar{a}$ is the average asperity size, and α is the Holm radius as defined by Equation 2.19. Combining this with Equation 2.18 yields

$$R_c = \frac{1 + n^{-1/2}}{1}\frac{\rho}{2\alpha} \tag{2.23}$$

Therefore, as n becomes large, this equation reduces to

$$R_c = \frac{\rho}{2\alpha} \tag{2.24}$$

When combined with Equation 2.19 this yields

$$R_c = \frac{\rho}{2}\left(\frac{\pi H}{F}\right)^{1/2} \tag{2.25}$$

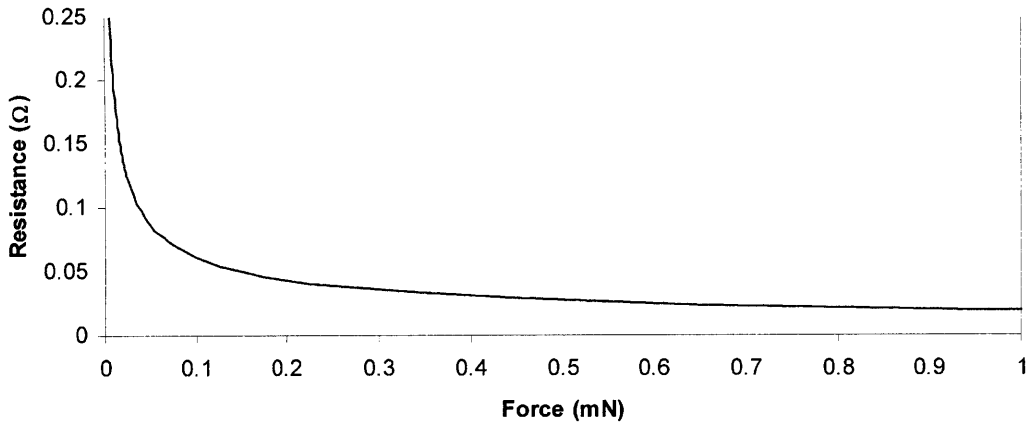

Figure 2-3: A typical force vs. contact resistance curve. The values were calculated using the properties of plated gold.

which gives contact resistance as a function of contact force and material hardness. Therefore, for any smooth clean conducting contacts, the relationship between force and contact resistance will have the same shape as that shown in Figure 2-3. This particular curve was calculated using a hardness of 1 GPa and a resistivity of $2.18\text{x}10^{-8}$ Ωm, which are the approximate properties for plated gold. This result can vary for non-circular contact spots or irregular distributions and for very thin films. Additionally, contact resistance can decrease after several loadings as asperities become permanently flattened or the contact surface work hardens, increasing the amount of force needed to bring new asperities into contact [54]. However, numerous experiments have empirically shown that this result holds for large numbers of contact materials and contact geometries [37, 36]. It is the fundamental equation in contact theory.

2.2.2 The Effect of Conductive Surface Coatings on Contact Resistance

Often, an electrical contact is made up of layers of different materials. A primary contact material may be chosen for hardness, while a surface coating chosen for resistance to oxidation or corrosion. In this case, additional constriction resistance occurs

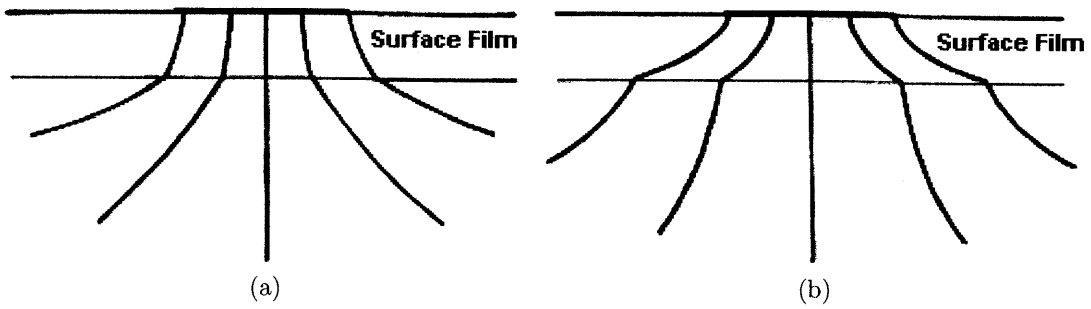

Figure 2-4: The effect of a conductive surface film on contact resistance. (a) shows the current flow lines when the resistivity of the surface film is larger than the resistivity of the bulk material. (b) shows the current flow lines when the resistivity of the surface film is less than the resistivity of the bulk material. This figure is taken from [54]

as the current lines transition from one layer to the next. If the resistivity of the surface film is larger than the resistivity of the bulk material, the current lines look like those shown in Figure 2-4a whereas if the resistivity of the surface film is larger, the current lines look like those shown in Figure 2-4b. The overall contact resistance for one side of a contact, is then given by [54]

$$R_c = \frac{1}{4a}\left(1 + \frac{4}{\pi}\frac{\rho_f}{\rho}\frac{d}{a}\right) \tag{2.26}$$

where ρ_f is the resistivity of the surface film, ρ is the resistivity of the bulk of the contact, and d is the film thickness. Equation 2.26 is for one side of a contact. If both sides of the contact are identical, the total contact resistance will be twice this. It should be noted that this is the simplest case. Often, the materials will form intermetallic layers with different resistivities than either of the pure materials. Additionally, this analysis is not valid for nonconducting films, which are addressed in the next subsection.

2.2.3 The Effect of Non-Conductive Films on Contact Resistance

Often times, electrical contacts will be made of materials such as copper or aluminum. Both of these materials will grow non-conductive oxides in ambient conditions and substantially thick non-conductive oxides when exposed to elevated temperatures. In fact, these oxides are essentially perfect insulators. There is a finite resistance at very thin film thicknesses only because of quantum tunneling effects. These effects are governed by the following equation, which is valid for two identical metals sandwiching a layer of non-conductive oxide:

$$R_t = \frac{d}{A}\left(\frac{h}{e}\right)^2 \frac{2}{3\sqrt{2m\phi}} exp\left(\frac{4\pi d}{h}\sqrt{2m\phi}\right) \tag{2.27}$$

where R_t is the contact resistance in Ohms accounting for tunneling effects, d is the thickness of the oxide film, A is the surface area of the oxide film, h is Plank's constance, e is the electronic charge, and m is the mass of an electron, and ϕ is the work function of the metal conductors. This equation comes from [54] which calculated that a 2 nm aluminum oxide layer between two aluminum layers each 1 cm by 1 cm in area would have a contact resistance of 11.6 Ω. Acceptable contact resistances are in the mΩ range. Therefore, this oxide must be removed to make good contact.

To make reliable electrical contact, these brittle layers must be fractured to allow the underlying conductive bulk material to make physical contact. This fracture is caused by mechanical means or electrically, through a processes known as *fritting* [54].

Scrub/Wipe

The first method of mechanical fracture to create electrical contact would be akin to hammering through a sheet of ice with an ice pick in order to get the mud beneath the ice to seep through to the surface. Essentially, this method would attempt to penetrate through the oxide with a relatively sharp point in order to create stress

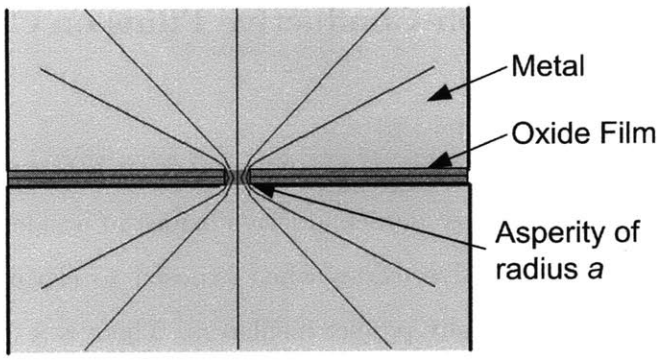

Figure 2-5: In order to make contact through an oxide film, breaks in that film must exist such that the underlying conductive material can make contact.

induced cracking and expose the conductive underlying material. This type of contact would likely damage the softer conductive material beneath the oxide. However, it has been shown that at the forces seen in most electrical contacts, this type of hammering is not effective. Rather, the mechanical fracture of insulating oxides is usually done through a process called wiping or scrubbing [33]. In order to wipe contacts, they are first brought together in a normal fashion by applying a contact force. Next, the contacts are moved parallel to each other while the contact force remains constant or continues to increase. This has the effect of breaking up surface oxides and then pushing them out of the way. Surface contaminants are also pushed out of the way. This allows the underlying conductive materials to make contact. The exact physics of this process are not completely understood but involve oxide fracture, which is not something that can be deterministically calculated. It must be analyzed stochastically. The force and scrub which will cause the film to fracture depend on the exact thickness of the film, its crystalline structure, its adhesion to the substrate material, the hardness of the substrate, the geometry of the tip causing the fracture, and the kinematics between the film and the tip. All of this can be very difficult to model, which is why a simple experimental setup is very advantageous to studying this problem.

Fritting

Compared to wiping, electrical fritting is a much better understood method of fracturing a non-conductive oxide, though not necessarily more effective. Electrical fritting essentially increases the voltage across a film until that oxide film breaks down and contact can be made through individual asperities which break through the oxide, as shown in Figure 2-5. There are two types of fritting: A-fritting and B-fritting. In A-fritting, the oxide film breaks down leading to the instant melting of metallic bridges. This occurs when the voltage is higher than the melting voltage. The melting voltage is the voltage at which the contact material temperature becomes higher than its melting temperature. This occurs at

$$V_m = (4L(T_m^2 - T_0^2))\cdot 5 \tag{2.28}$$

where L is the Lorenz constant $2.45\text{x}10^{-8}\text{V}^2/\text{K}^2$, T_m is the melting Temperature in Kelvin, T_0 is the bulk temperature in Kelvin, and V_m is the melting voltage in volts.

In B-fritting, the voltage drop across the contact is less than the melting voltage, so it causes a breakdown of the film without melting the underlying contact material. This type of fritting is generally assisted by a mechanical fracture of the oxide, such as an increased normal force between the contacts.

2.2.4 Thin Film Effects

The last section of the theory deals with thin film contacts. For contacts in which the film thickness is on the order of the Holm equivalent radius, traditional contact theory no longer applies. This is because in a typical contact, the current lines spread in all directions upon exiting the asperities. However, in a thin film, the current lines must immediately curve due to the restrictive geometry. These two current line scenarios are shown in Figure 2-6. The exact effect of this is not immediately obvious. Various models have come up with different answers. In Chapter 7 of this thesis, experiments are performed to characterize this effect.

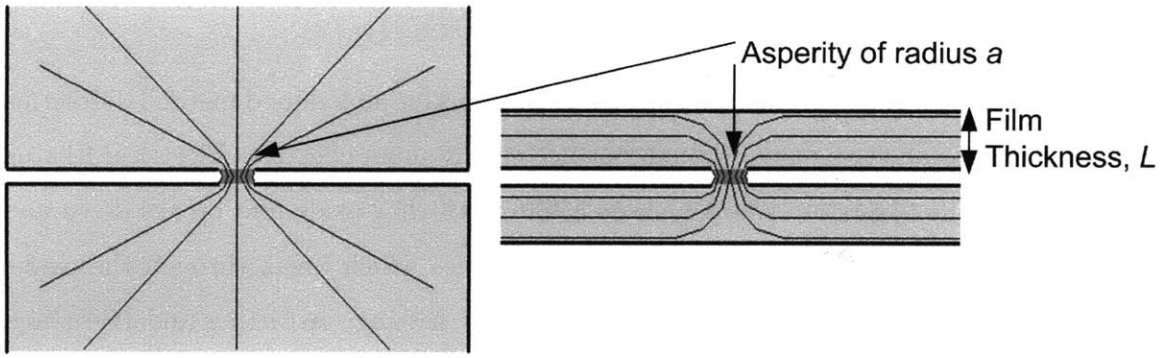

Figure 2-6: Right:A typical contact and current lines as modeled by Holm. Left: A thin film contact and current lines, which have to curve more rapidly than those seen in the Holm model.

2.3 Literature Review of Experiments Pertaining to MEMS Fabricated Electrical Contacts

This section reviews the literature pertaining to five broad factors which affect the performance of MEMS fabricated electrical contacts. These factors are: contact material, contact geometry, nature of the contact, adhesion, and the effects of wear and cycling.

2.3.1 Contact Material

The contact material itself is one of the most important aspects of a contact. Certain materials are more appropriate for MEMS fabricated electrical contacts. Good contact materials can be those that will not oxidize, have an easily removable oxide, or have a conductive oxide. Some materials will stay intact for many cycles, while others will quickly break down. Common contact materials include gold [22], gold alloys, rhodium [51], palladium [4], silver [20], nickel-tungsten [28], aluminum [6], copper [29, 26], platinum [12], and various other alloys [7]. New materials, such as carbon nanotubes, are also being investigated as electrical contacts [66]. The deposition of the material can also affect its properties. Additionally, exposing materials to high temperatures or different atmospheres can alter how a material behaves as

an electrical contact. Metal deposition methods include sputtering, [41], evaporation [64], electroplating [5], or even prefabricated rivets [50]. Sputtered metals tend to be harder than plated or evaporated metals, which can mean a higher contact resistance according to Equation 2.25.

2.3.2 Contact Geometry

Contact geometry is also very important to a contact. This includes the shape of the contacts as well as the thickness. Some contacts consist of a sphere on a sphere or a sphere on a flat [12, 44]. Holm theory says sphere-on-sphere contact is the best but that sphere on flat contact is easier to implement [19]. Many MEMS-scale electrical contacts use flat-on-flat geometry because it is simple to produce while other contacts use a unique configurations such as point contact [5]. The term tip geometry is used when referring to a probe on flat configuration. Tip geometry can be spherical, conical, or other various shapes. Two-dimensional tips consist of any tip which is flat on the bottom, but has some sort of shape (square, circle, triangle) and will typically touchdown on a flat.

The effects of film thickness on contact resistance are somewhat disputed. Timsit found that for very low levels of a/L, where a is asperity radius and L is film thickness, as shown in Figure 2-6, contact resistance decreases as film thickness decreases, for the same applied force [60] and is typically lower than the contact resistant predicted by Holm theory, specifically Equation 2.25. However, these results were limited to the cases where $a/L < 0.5$. In an FEM study, Norberg found the opposite was true: that contact resistance increased as film thickness decreased for thin films 1 μm to 1 mm and that contact resistance was actually higher than that predicted by Holm theory [38]. However, these results were for much higher values of a/L. Bilhaut shows that for very very thin films, $L < 300nm$, the actual resistivity of the film changes [3]. Coutu also looks at the effects of ballistic electron transport, quasi-ballistic electron transport, and diffusive electron transport [8]. He finds that in general after accounting for these factors contact resistance is higher in thin films than in thick films. The consensus is that contact resistance in thin films behaves

differently than contact resistance in bulk materials, but there is no consensus on the exact mechanism for this difference or the exact effect this produces.

2.3.3 Nature of the Contact

The nature of the contact is defined as the way the two sides of the contact come together. The simplest way is in a normal force fashion. The two contacts are pressed together, but not slid in anyway. The next type of contact is a wiping or scrubbing contact, in which the contacts are brought together and slid across each other while some normal force is applied. A variation on this type of contact would be a rotary scrub, where the contacts are brought together and then rotated about the center of the contact. These scrubbing or wiping motions can improve contact resistance by wiping away oxides or contaminates but cause the contact to degrade, which can ultimately raise contact resistance.

The simplest type of contact is flat-on-flat contact with no scrub. This is often used in sealed environments with no contaminates on contact materials that do not form a non conductive oxide. One such device is a MEMS relay which uses flat on flat parallel gold coated contacts [64]. For non thin film cases, this type of contact is thought to be well approximated by Holm theory; however, some work is being done to improve on this: specifically looking at the exact way the asperities deform [23].

Many contacts use some sort of lateral, in-plane scrub. Brockman investigated the effects of wipe on gold and palladium hemispherical contacts. The contacts were loaded to 50 g of normal force and then wiped. For clean contacts, the wipe had no effect. However, for very dusty contacts, contact resistance was greatly improved by the wiping action [4]. Gray attempted to model the effect of wiping or scrubbing for a specific device using dynamic behavior of the device, as well as discrete changes in position due to frictional effects [13]. Hotschkiss looks at the non-probe side of the contact during scrubbing contact. In that specific case, a metal bump is probed using a scrubbing motion and then later must be wire bonded. During the scrubbing touchdown, the metal bump can be damaged. Too much damage can make later attachment to these contacts impossible. Not enough damage may mean that ade-

quate contact is not being made. An optimal point between pad damage and contact resistance is desired [21].

For some contacts, out of plane rotation also plays a roll in contact resistance. Broz describes a probing application in which probe tips rock from heel to toe (front to back) during touchdown which seems to lower contact resistance [58]. Another device described by Marcus has a rolled coil tip which rotates upon touchdown creating out of plane and in plane scrub [34].

2.3.4 Adhesion

An additional factor in the force-contact resistance relationship is adhesion. Adhesion is caused by a variety of factors, including capillary forces, electrostatic forces, van der Waals attractive forces, and hydrogen bonding [27]. Adhesion causes apparent hysteresis in the force-contact resistance relationship because the applied force is no longer the net force [31]. Adhesion is correlated with micro-structural changes to the contact surfaces and increases with cycling [16]. These micro-structural changes cause changes to the contact resistance. Various methods have been used to study adhesion in MEMS fabricated electrical contacts.

Gregori used an RF-MEMS switch to measure adhesive forces in gold contacts. The switches were cycles up to 10^7 cycles. The total applied force for each cycle was on the order of 50 μN. Between cycles, the contact surfaces were examined using an AFM. The findings were that adhesion force increased with the number of cycles. The contact surface also changed during this time. There were relatively large changes, such as a depression in the area of contact, as well as relatively small changes, such as a flattening of the individual grains in the contact area [16].

Kogut discussed an analytic approach to determining adhesion force. It found that the relationship between adhesion force and contact resistance does not depend on the surface topography of the contacts in the plastic deformation regime [27]. Typically, MEMS contacts move from the elastic regime to the plastic regime at force ranges of 10-100 nN [32].

Majumander measures the adhesion force and contact resistance between a sput-

tered gold contact bump of 2 μm in diameter on a sputtered gold drain. This adhesion causes hysteresis as seen in the applied force contact resistance curve shown in Figure 2-7. It notes that in some MEMS devices, adhesion forces can be higher than restoring forces of springs causing stiction failures. [31].

Pashley showed that adhesion force increases with the total touch down force for tungsten and nickel contacts. At a total touchdown force of 1 μN, adhesion forces were on the order of 10 μN. At a total touchdown force of 1000 μN, adhesion forces were on the order of 100 μN. It also discussed how values of hardness and resistivity can vary at the scale of MEMS fabricated electrical contacts [40].

Sharma looked at the adhesion forces of various contact materials. The touchdown forces were on the order of 40 mN, and the adhesion forces were on the order of 10-20 mN. The contacts made of soft diffused gold, plated ruthenium, and plated rhodium had relatively low adhesion forces. The contacts made of cobalt hardened gold, silver-gold alloy, and pure gold had relatively high adhesion forces [52].

In short, adhesion can be a destructive force in MEMS fabricated electrical contacts by causing stiction failure. The magnitude of adhesive forces is typically about an order of magnitude less than the touchdown force but can be even greater than the touchdown force in certain circumstances. Adhesive forces increase with cycling. The material of the contact plays a very important role in adhesion, with softer materials typically exhibiting greater adhesion forces than harder materials. The effects of adhesion are inseparable from the contact material properties and cycling.

2.3.5 Effects of Wear and Cycling

Contacts may behave differently over many cycles than they do after the first cycle, often because of contact wear. This is an important area for high cycling devices such as MEMS relays. Latent contamination has been shown to have a critical role in the performance of these contacts [61]. Silicone oil can cause degradation of the contacts [10]. Factors such as humidity also affect the contacts [1]. Hot switching can increase these wear effects [11]. Wear is also linked to cycling. The properties of these contacts can change drastically with cycling, as many of these devices must

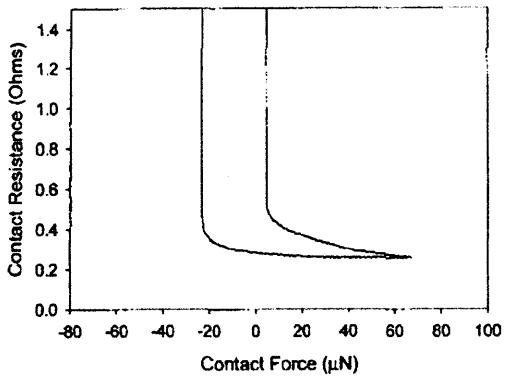

Figure 2-7: The hysteresis seen in a contact experiencing adhesion as force is loaded and unloaded. Taken from [31].

withstand millions of cycles [32]. Wear on probe tips has been measured as a function of touchdowns [6].

2.3.6 Combination Effects

As important as each of these factors are, it is equally important to realize that they are not independent. DeNatale notes that "The small contact area and low-force nature of the switch construction makes it inherently susceptible to resistance degradation. Modifications to the contact resistance...may be affected by design, material, processing, environment, or operational cycling [9]." Scrubbing can often remove contaminants [53]. Adhesive forces can increase with cycling [16]. Probe shape can cause stresses and wear in contacts [30]. To truly characterize a contact, one must know and understand the roles each of these factors play individually and in combination

2.4 Previous Approaches

A variety of approaches have been taken in an attempt to solve this characterization problem. These approaches all cover some of the design considerations covered in the previous section, but none cover all of them. The following is a brief summary of the different characterization systems as well as the advantages and disadvantages of

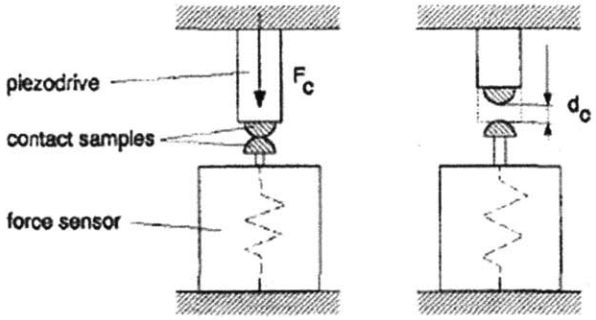

Figure 2-8: A device used to test the contact resistance of contact rivets [50].

each.

Schimkat recognized that contact material choice was crucial in the performance of a microrelay. He looked at three types of materials commonly used in relay contacts: Au, $AuNi_5$ and Rh. His setup involved pressing two contacts together while measuring force and contact resistance. The forces measured went as high as 10 mN. For $AuNi_5$, the lowest contact resistance seen was about 15 mΩ [51]. His results garnered insights into the relationships between contact force, resistance, adhesion, and the cleaning method used on the sample. However, Schimkat used contact rivets as opposed to microfabricated contacts [50]. This test setup is shown in Figure 2-8. The properties of rivets will most certainly vary from those of microfabricated contacts. Additionally, microfabricated contacts of the same material fabricated using different methods or different conditions will have different properties. This method also does not allow for the testing of scrub contacts or the variation of contact geometry, thickness, or tip geometry. Additionally, MEMS contacts change over multiple cycles. Ideally a test setup would allow contacts to be tested, disassembled and observed with an SEM, and then reassembled in precisely the same position for further testing. This method does not allow for that.

Hyman looked at flat on sphere contact for gold contacts. A contact dimple on a spring was brought into contact with a flat contact as shown in Figure 2-9. The contact areas are on the order of several μ m^2, because Hyman looked at individual asperities. This system varied electrical current which affected the asperities by melt-

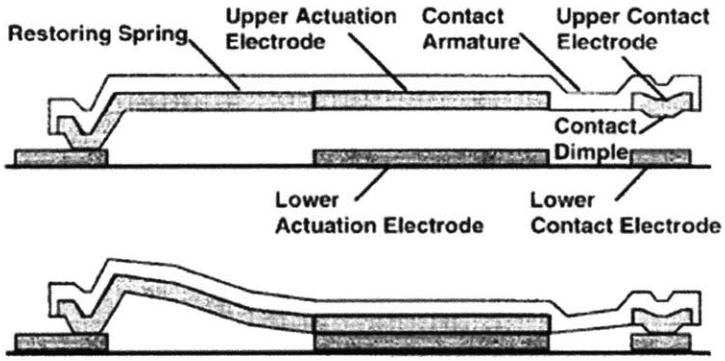

Figure 2-9: A device used to measure the contact resistance of gold sphere on flat contacts at very low force values [22].

ing them which changed the force vs. resistance curve. Hyman looked at forces up to 500 μN and observed contact resistances on the order of 100 mΩ [22]. This system allows the contacts to be observed after testing, but they can not be reassembled afterwards, therefore, this setup could not be used to observed changes in the contact between multiple rounds of testing. Additionally, the forces looked at were very low; so the data obtained is of limited value to higher force relays and probes.

Bromley created a system which allowed microfabricated contacts to come together in a somewhat parallel fashion or in point contact. The system allowed contact material and geometry to be varied but only tested gold on gold. It looked at contact forces up to 100 mN and measured contact resistances as low as 20 mΩ. The system attempted parallel contact by attaching the top sample to a suction cup and lowering it onto the bottom sample, but the parallelism was limited to what could be obtained visually as shown in Figure 2-10 [5]. While this system is promising in that multiple metals, geometries, and force types could be tested, the suction cup aspect limits the repeatability of the alignment of the samples, which is crucial when dealing with high cycle tests.

Peroulis stated that "A thorough understanding of the metal-to-metal contact in microrelays and RF MEMS switches is therefore essential in improving the performance and reliability of these components, as well as in designing actuators suitable for providing sufficiently high contact forces." Peroulis characterized contacts by

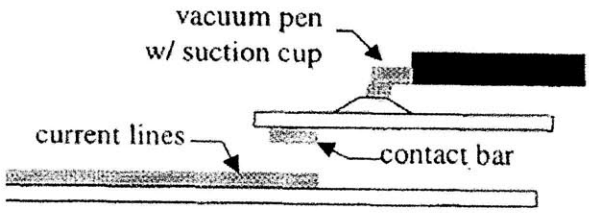

Figure 2-10: A device which attempts to measure contact resistance in parallel flat-on-flat contact [5].

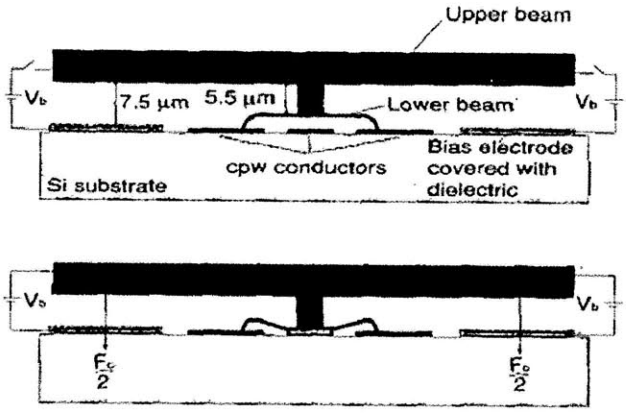

Figure 2-11: A device which measures contact resistance between non scrubbing beams [41].

bringing two beams together using electrostatic actuator as shown in Figure 2-11. The maximum contact force was about 75 μN, and a gold on gold contact resistance on the order of a few hundred mΩ was observed. [41] Unfortunately, this kind of characterization is limited to switches almost identical to that of Peroulis. Multiple tip geometries can not be tried, nor can scrubbing contacts nor can forces above 75 μN be measured. Peroulis also designed MEMS switches using the information obtained from that characterization [42].

The title of Beth Pruitt's Ph.D. research at Standford was 'Piezoresistive Cantilevers for Characterizing Thin-Film Gold Electrical Contacts' [43]. It was motivated by the desire to replace processes like soldering and wiring bonding with MEMS contacts on flexures. The research focused on gold contacts using various types of spherical probe tips, different gold thicknesses, and even scrubbing contact. The probe tip

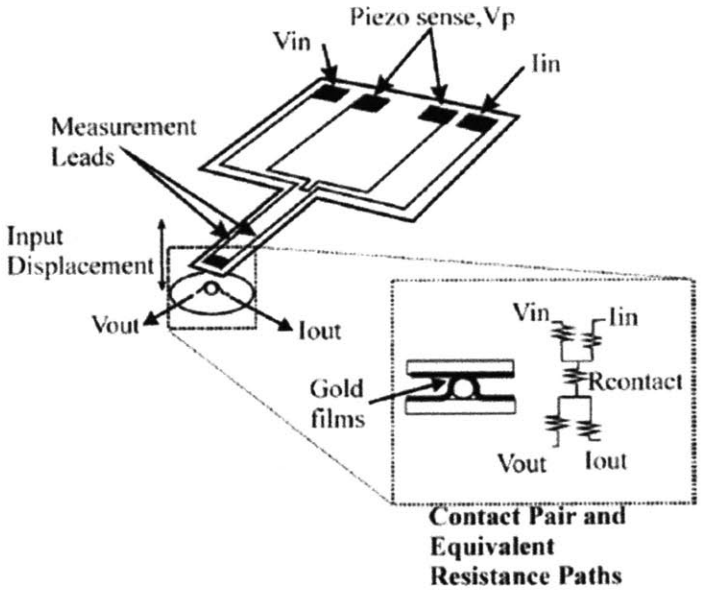

Figure 2-12: A device which measures contact resistance of gold coated microspheres [43].

radii were varied as was the manner in which they were fabricated. The maximum force examined was 10 mN, and the lowest contact resistance seen was on the order of 100 mΩ. The measurement device itself was a piezoresistive cantilever as shown in Figure 2-12 [43]. The piezoresistive cantilever could accurately record forces in the nN-mN range. The system also tested both evaporated and sputtered gold [44]. Data from these tests showed that the behavior of the contacts was dominated by the asperities which caused deviation from Hertzian theory [45]. This approach allows for a large number of variables to be tested, but because one of the contacts is on an integrated cantilever, the contacts can only be observed by destroying the device.

Jang created a two-chip system to characterize the relationship between contact resistance and contact force which is shown in Figure 2-13. The two chips are soldered together. The height of the solder leaves a gap in between the coupons. The top chip consists of a probe attached to springs and can be pushed into the bottom chip. Contact force and resistance can be measured. Additionally, after testing, the chips can be separated; and the roughness of the contact can be measured. The two-chips can be resoldered for further testing. Jang investigated the relationship between

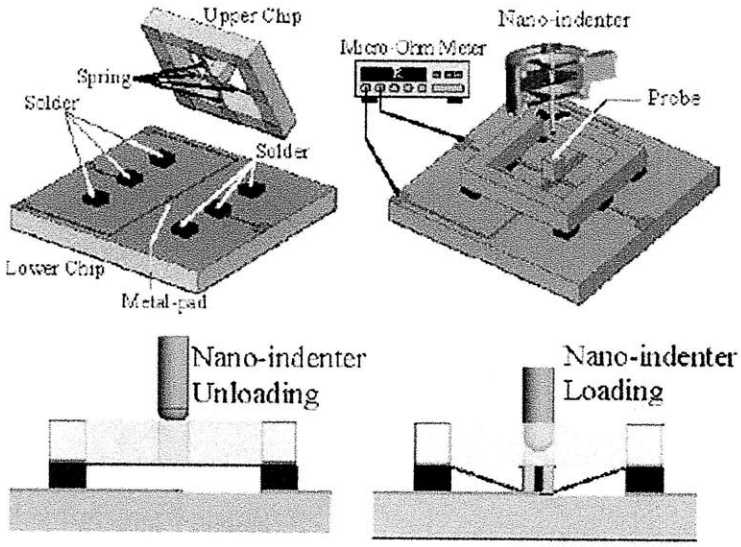

Figure 2-13: A device which allows top and bottom coupons to be observed between testing cycles but requires soldering and desoldering [24].

contact resistance, roughness, and contact cycles [24]. The two-chip concept has the big advantage of being able to observe the contact in between testing cycles. Jang looked at forces up to 120 mN and saw resistances on the order of 3 Ω for aluminum. However, connecting the two chips using solder presents a few problems. Although solder reflow is relatively predictable, it is unlikely that this test setup would allow the contacts to be reassembled within one micron of their original position. This is necessary to ensure the asperities that were aligned during the original testing are still aligned during subsequent testing. This setup is far from ideal in terms of ease of use. Additionally, the heat from the solder may change the properties of certain types of contacts. Additionally this setup is not equipped to observe scrubbing contacts.

Vincent created a device for testing MEMS contacts using a reed switch [62]. It allows for multiple materials and atmospheres to be tested, but is limited to the force profile dictated by the reed switch. It cannot impart any force or scrub motion independently, and the geometry of the contacts that can be tested is also quite limited. However, it is excellent for performing high cycle testing. This test setup is shown in Figure 2-14.

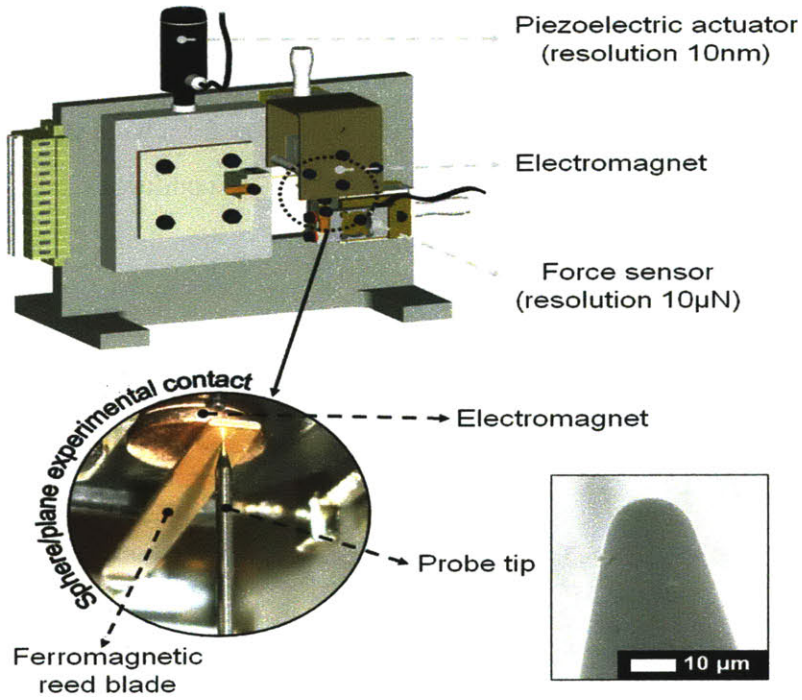

Figure 2-14: A device used to test high cycle MEMS fabricated electrical contacts [62].

2.5 Conclusions

After a thorough review of the current contact theory and literature, several conclusions can be made. The first is that although contact theory is very well understood at the macro scale, there are many aspects of this theory that might not be valid in MEMS scale devices. Therefore an empirical method of characterizing MEMS fabricated electrical contacts is needed. Second, there are multiple factors which affect contact resistance that any test setup must be able to vary. These include contact material, contact geometry, the normal force applied to the contact, and the scrubbing motion of the contact. The contact properties are also very dependent on how the contact was fabricated. A sputtered gold contact fabricated under certain conditions might behave very differently than a sputtered gold contact fabricated under slightly different conditions. Additionally, the properties of a contact will change over many cycles. Therefore, any test setup must to be able to test a contact, disassemble it, observe it using metrolgy such as an SEM or AFM, and reassemble the contact so

that it is in its exact original position. This ensures that any asperities lined up in the initial testing will still be lined up in subsequent testing. Several attempts have been made to create such a test setup, but none of them allow for a wide variety of contacts to be characterized accurately under a wide variety of conditions. Addressing this issue is a major contribution of this thesis.

Chapter 3

Kinematic Coupling Two-Coupon System Design

List of Symbols	
a	Square membrane width
b	Equivalent membrane width
D	Ball diameter
D_{b-max}	Maximum distance between balls
D_{b-min}	Minimum distance between balls
D_{c-max}	Maximum distance between a ball and the center of the coupon
D_{c-min}	Minimum distance between a ball and the center of the coupon
D_c	Distance between a ball and the center of the coupon
D_{max}	Maximum possible ball diameter
D_{min}	Minimum possible ball diameter
δ	Probe displacement
$\delta_{SF=3}$	Membrane displacement when actual stress is one-third of the yield stress
Δbdv	Allowable ball diameter variation
Δdsf	Deviation from spherical form for balls
$\Delta sraa$	Surface roughness arithmetical average for balls
Δbdt	Basic diameter tolerance for balls

continued from previous page

List of Symbols	
$\Delta aldv$	Allowable lot diameter variation for balls
Δmax	Total possible difference in diameter of largest ball and smallest ball
e_g	Difference between measured gap and design gap
$e_{litho-max}$	Error caused by lithography
$e_{membrane}$	Membrane tilt error from off center or off axis force application
e_ϕ	Parallelism error
e_{theta}	Rotational error
e_x	Translational error in the x-direction
e_y	Translational error in the y-direction
e_XY	Generalized Translational error
E	Young's Modulus
F	Force
$F_{contact}$	Force seen by the contact surfaces
$F_{measured}$	Force applied by the probe
g_x	Distance between target and x-capacitance probe
g_y	Distance between target and y-capacitance probe
G	Actual Gap
G_i	Design Gap
$\bar{G}$	Average of the gaps at each of the ball/pit interfaces. Taken to be the actual gap
G_{max}	Maximum gap at each of the three ball/pit interfaces
G_{min}	Minimum gap at each of the three ball/pit interfaces
k	Stiffness of the membrane
σ_{max}	Maximum stress seen by the membrane
σ_y	Yield stress
W	Nominal pit width
W_{max}	The longer of the two sides of a single pit
$W_{max-min}$	The difference in lengths of the two sides of a single pit

continued from previous page

List of Symbols	
W_{min}	The shorter of the two sides of a single pit

A two-coupon system was designed, fabricated, and tested for the purpose of characterizing a wide array of MEMS-fabricated electrical contacts. This chapter discusses the original concept of this system. This initial design came from from Dr. Alexis Weber's Ph.D. thesis 'MEMS Relays for Make-Break Power Switching Applications: 111 Silicon Etched Planar Electrical Contacts' [65]. This first pass concentrated only on flat-on-flat electrical contacts and is referred to as the kinematic coupling two-coupon system, named for its alignment mechanism. This chapter covers the design, fabrication, error analysis, characterization, and testing of the kinematic coupling two-coupon system. An alternative two-coupon system is presented in Chapter 4 and the final two-coupon system with scrubbing capabilities is presented in Chapter 5.

3.1 Design

The functional requirements used to design the first version of the two-coupon system stem from the desire to measure contact resistance for flat-on-flat contacts and observe how the contact evolves over multiple touchdowns, since MEMS-relays can be put through more than 100,000 cycles [65]. In order to observe these changes, the contacts need to be separable, so that they can be observed using metrology tools such as an SEM or AFM, and then reassembled for further testing. Contact resistance is dominated by asperity level contact, which is often on the order of 1 μm, so, the position repeatability of this assembly/disassembly should also be on the order of 1 μm or better [22]. This initial research was conducted in partnership with Oklahoma State University which had agreed to perform the electrical testing of the devices. This meant that the original design had to be compatible with the test equipment at OSU. Force and resistance measurement accuracy requirements were based on the force and resistance measured in prior work. The functional requirements for this

original design were as follows.

1. Measure contact resistance in the mΩ range.
2. Measure contact force in the 100 μN range.
3. Bring contacts together in a parallel manner.
4. Measure multiple cycles.
5. Assembly/disassembly repeatability better than 1 μm.
6. Allow for the observation of the physical changes to the contact between cycles using metrology including, but not limited to, the SEM and AFM.
7. Use no more than 50 mN of force (to comply with OSU test setup).
8. No more than 10 μm of displacement (to comply with OSU test setup).

These functional requirements were achieved with a two-coupon system. The bottom coupon is a 12.5 mm x 40 mm silicon rectangle. Its thickness is approximately 670 μm, the thickness of the wafer. A 2 mm wide trace of the contact material is deposited longways across the rectangle. Three KOH-etched pits are arranged around the center of the coupon. The top coupon is an 18 mm x 18 mm silicon square. The thickness is also 670 μm, also the thickness of the wafer. The front side of the coupon contains a 2 mm wide trace of the contact material and three KOH-etched pits. A square membrane is etched on the backside of the coupon. In the center of this square membrane is a stiff pyramid boss. The membrane is 20 μm thick.

The coupons are assembled by placing three Grade 3 stainless steel balls in the KOH-etched pits of the bottom coupon. The specifications regarding Grade 3 balls are listed in Table 3.4. The KOH-etched pits of the top coupon are then placed over the stainless steel balls. This type of assembly is known as a kinematic coupling configuration [55]. It is used extensively in macro-scale alignment mechanisms and has been shown to have excellent positional repeatability for the assembly and disassembly of modules. When assembled, the balls provide a gap between the top and

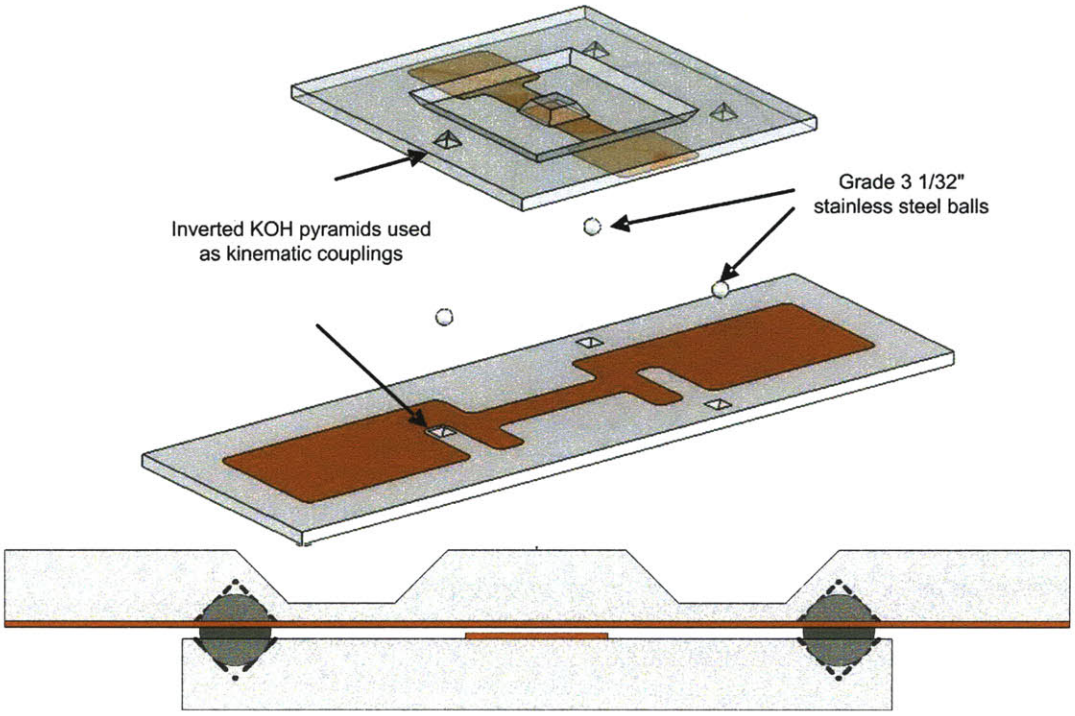

Figure 3-1: Top: Exploded view of the kinematic coupling two-coupon assembly. Bottom: A not-to-scale representative cross section of the assembly.

bottom coupons. When the membrane is displaced, the metal trace of the top coupon comes into contact with the metal trace of the bottom coupon. An integrated Kelvin structure allows for the measurement of this contact resistance. External instrumentation allows for the measurement of contact force and membrane displacement. This assembly is shown in Figure 3-1.

The three main modules of this design are: the KOH-etched pits and balls; the membrane which allows for the bottom and top metal traces to come together; and the integrated Kelvin structure.

3.1.1 KOH-etched Pits and Balls

The KOH-etched pits and the balls which sit in them have two functions. The first is to allow for repeatable assembly and disassembly and the second is to maintain a gap between the top and bottom coupons. The original experimental plan called for

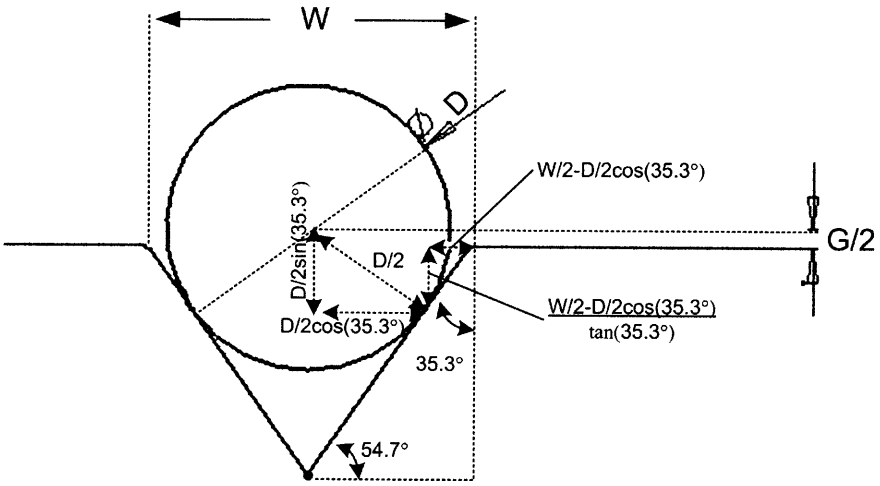

Figure 3-2: The geometry relating the pit width W and the ball diameter D to the gap height G. In this image, G/2 is shown because the top half of the coupon would be symmetrical, resulting in a total gap height of G.

these coupons to be tested using equipment whose force probe had a maximum of 10 μm of travel. Half of this travel was reserved for the deflection of the membrane. Therefore, the KOH-etched pits and ball module was designed to create a 5 μm gap between the two coupons. Grade 3 1/32" (793.75 μm) stainless steel balls were chosen because they were the smallest standard size precision ball available. The size of the pits needed to maintain the desired gap was then calculated from the geometry. A diagram of this geometry is shown in Figure 3-2.

From Figure 3-2, it can be determined that the relationship between pit width, ball diameter, and gap is

$$G = Dsin(35.3) - \frac{W - Dcos(35.3)}{tan(35.3)} \tag{3.1}$$

where G is gap, D is ball diameter, and W is pit width. Therefore, for a target gap of 5 μm, the width of the pits should be 967.6 μm across. An error analysis as to whether this is feasible is included later in this chapter.

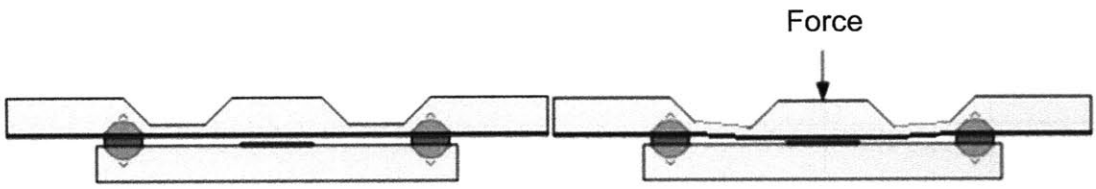

Figure 3-3: Left: The kinematic coupling two-coupon assembly with a not-to-scale gap. Right: An applied force bringing the membrane into contact with the bottom coupon.

3.1.2 Membrane

The purpose of the membrane is to bridge the gap created by the KOH-etched pits and balls in order to allow the top and bottom metal traces to make contact in a controlled manner, as shown in Figure 3-3.

In order to make contact, the membrane is displaced by external means. The geometry of the membrane determines how stiff the membrane is, or how much force will lead to a certain deflection. Once the top and bottom coupons make contact, the membrane stops deflecting. Since deflection is the only means of carrying additional force through the membrane, this means all additional applied force will be taken by the contact.

Since the OSU test equipment could only provide 50 mN of force, it was important that not all of this force be used deflecting the membrane. Allowing 10 mN of force for the deflection of the membrane leaves 40 mN of force to be applied to the contact. Therefore the geometry of the membrane was chosen to ensure that it took no more than 10 mN of force to close the 5 μm gap, or a stiffness of 2 mN/μm.

The thickness of the membrane was chosen to be 20 μm because anything thinner would be extremely fragile. The geometry chosen was a square with a pyramid boss on the center because that could be created from a KOH-etch. KOH-etches provide relatively flat bottom surfaces and tend to be fairly uniform across the wafer. The base of the pyramid boss was chosen to be 2.5 mm across because a 2 mm contact metal trace needed to span it.

A finite element model and simple membrane model were used to determine the

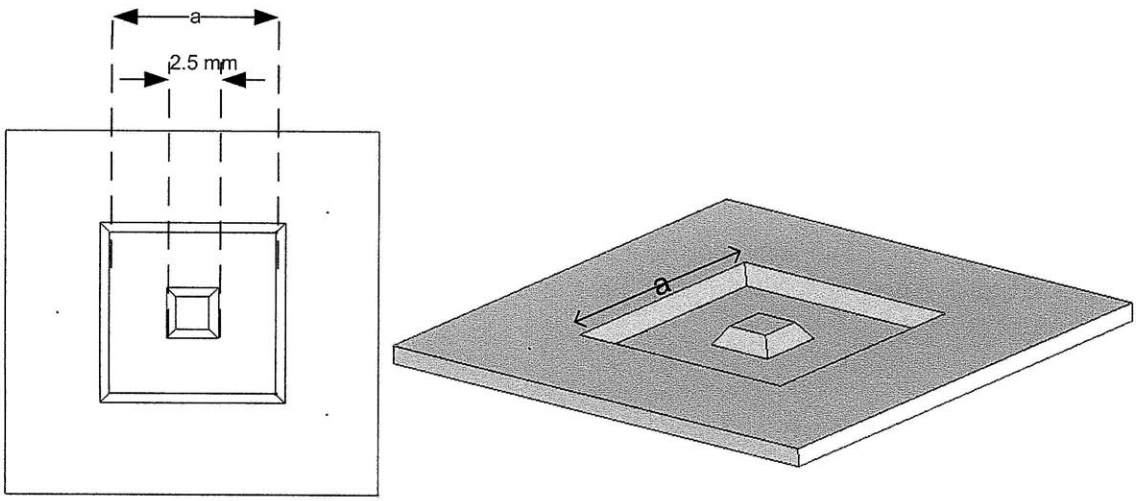

Figure 3-4: Geometry of the membrane. The parameter a was varied in the FEM model

size of the membrane which would have the designed stiffness of 2 mN/μm. The geometry of this membrane is shown in Figure 3-4. The outer membrane dimension a was varied until the results lined up with the desired properties. The deflection at which the membrane would reach 1/3 of its yield stress was also calculated. The yield stress of silicon was assumed to be 120 MPa.

When the parameter a equals 8 mm, stiffness and deflection results were on target. The stiffness at this point was 1.8 mN/μm. The FEM was also used to look at the effect of a positional offset of force (if the force was applied off-center), and the effect of the force angle (if the force applied off-axis). Positional offset and force angle are shown in Figure 3-6. The results of this FEM analysis are shown in Figure 3-5. The stiffness and tilt seen in of each of these cases is shown in Table 3.2.

A numerical model was also used to predict the stiffness of the membrane. This model is for a square membrane with a force applied at the center. The geometry of this model is shown in Figure 3-7.

Since the numerical model geometry does not have a stiff center pyramid, the model width dimension b was taken to be 5.5 mm. This number was arrived at by subtracting the 2.5 mm wide pyramid from the 8 mm wide membrane. This model has the following relationship between force and displacement [47]:

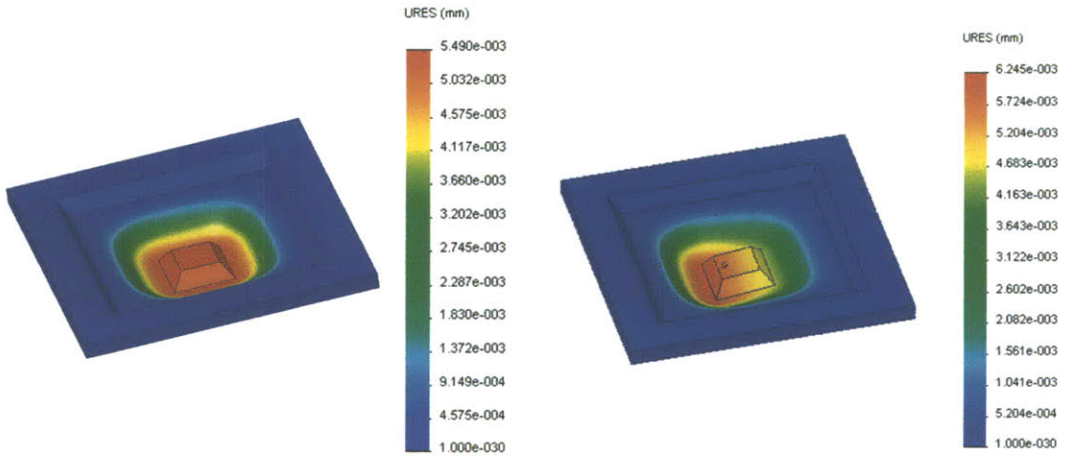

(a) 0 mm center offset; 0° force angle

(b) 0.5 mm center offset; 0° force angle

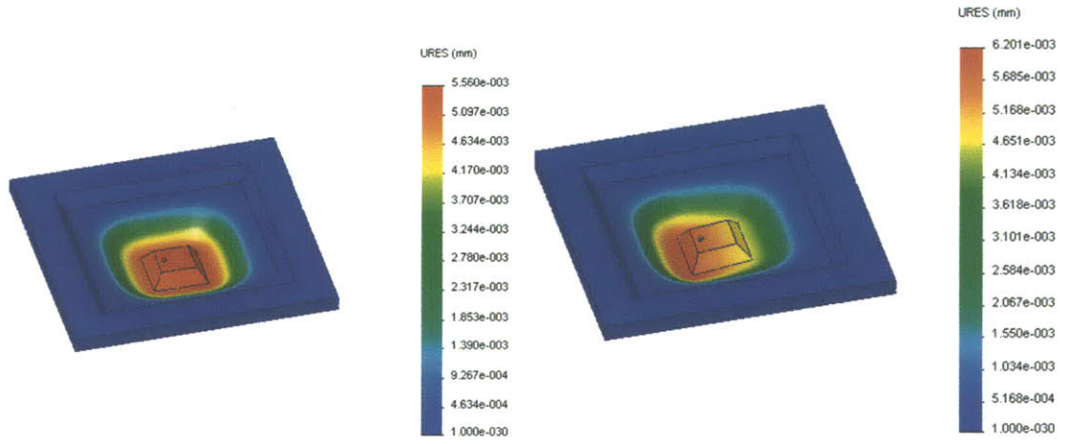

(c) 0 mm center offset; 5° force angle

(d) 0.5 mm center offset; 5° force angle

Figure 3-5: The FEM model results for the KOH-etched membrane when a force of 10 mN was applied.

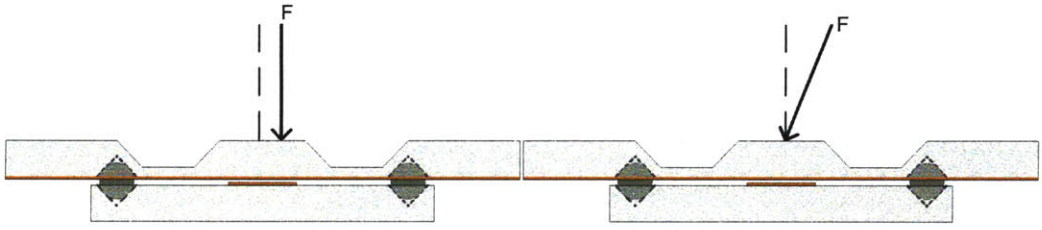

Figure 3-6: Left: A force applied with a positional offset. Right: A force applied with a non zero force angle

Analysis Method	Positional Offset mm	Force Angle degrees	Stiffness @ 10 mN mN/μm	Tilt @ 10 mN mrad	Displacement when Safety Factor=3 μm
FEM	0	0	1.82	0	21
FEM	0.5	0	1.60	0.6	21
FEM	0	5	1.61	0	21
FEM	0.5	5	1.80	0.6	21
Numerical	0	0	0.67	0	33

Table 3.2: The calculated displacements and tilts of the KOH-etched membrane when 10 mN of force is applied.

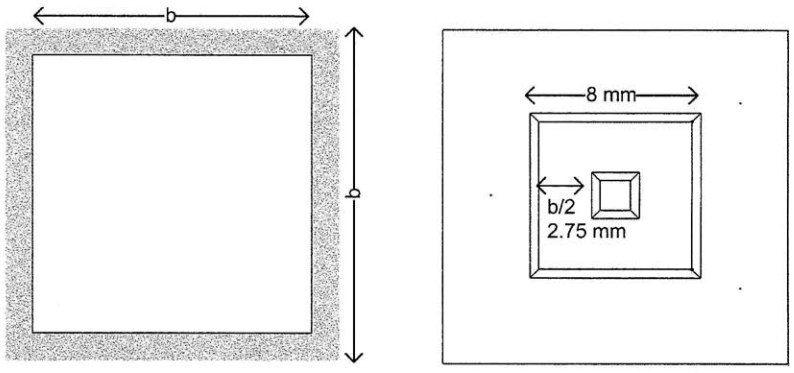

Figure 3-7: Numerical model geometry.

$$\delta = \frac{0.0611Fb^2}{Et^3} \tag{3.2}$$

where F is force, a is the length of the square membrane, E is the Young's modulus of the membrane, which for silicon is 150 GPa, and t is the thickness of the membrane. This is equation comes from Table 26, case 8b. of Roark's Formulas for Stress and Strain [47]. For a membrane having a width b of 5.5 mm and a thickness of 20 μm, a force of 10 mN will result in a displacement of 15 μm. Stiffness k is

$$k = \frac{Et^3}{0.0611b^2}. \tag{3.3}$$

For this model, stiffness is 0.67 mN/μm, which is only about 37 percent of the stiffness seen in the FEM model. Force goes with the cube of the thickness of the membrane. This means that a 16 μm thick membrane would be approximately half as stiff as a 20 μm thick membrane which would in turn be approximately half as stiff as a 25 μm thick membrane. So in order to have good control over stiffness, the thickness of the membrane needs to be very well controlled which is very difficult. In chapter 6, the instrumentation which performs the measurements on these devices is described. This instrumentation can measure the stiffness of the membrane while the sample is being tested. This allows for some looseness in the tolerances regarding membrane stiffness.

The maximum stress seen in this model is

$$\sigma_{max} = \frac{0.7542F}{t^2}. \tag{3.4}$$

This can be combined with Equation 3.2 to find the displacement seen at 1/3 of the the yield stress to get

$$\delta_{SF=3} = \frac{0.0611\left(\frac{\sigma_y t^2}{(3)(0.7542)}\right)a^2}{Et^3} \tag{3.5}$$

where $\delta_{SF=3}$ is the displacement at 1/3 of the yield stress, σ_y, which is 120 MPa in silicon. In this case, $\delta_{SF=3}$ is 33 μm. Since the membrane only needs to travel 5 μm,

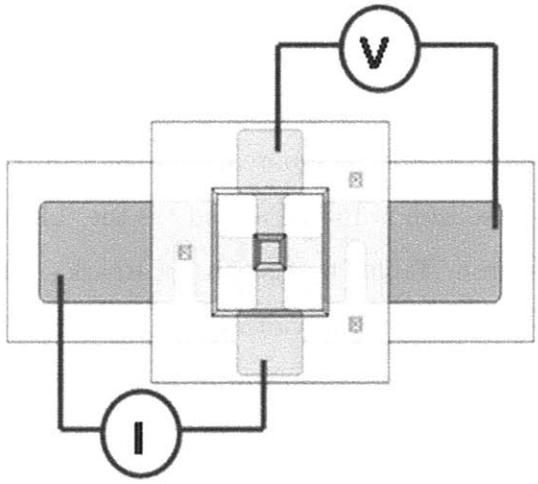

Figure 3-8: The integrated Kelvin structure of the kinematic coupling two-coupon system. By sourcing current in one loop and measuring voltage in the other, contact resistance can be measured independent of lead resistance.

all stresses will be acceptable.

The results of this numerical model are also seen in Table 3.2. This model would only need about 3 mN of force to close the gap between the top and bottom coupons. Therefore the FEM model is the worst case and is still good enough, so the geometry determined from the FEM model should be adequate for achieving the functional requirements of this coupon.

Kelvin Structure

After the membrane is deflected, an integrated Kelvin structure capable of measuring the contact resistance is formed between the two traces which is shown in Figure 3-8. This type of system was previously used to measure the resistance in carbon nanotubes [66]. In a Kelvin structure, current is sourced in one loop, and voltage is measured in the other. Since there is no current in the leads of the voltage loop, there is only a voltage drop across the contact. Therefore the resistance measured, R=V/I, is only the resistance across the contact and is independent of lead resistance.

3.2 Fabrication

A flow chart showing the fabrication steps for the kinematic coupling two-coupon system is shown in Figure 3-9. The top and bottom coupons are fabricated on different wafers using different masks. Both the top and bottom coupon wafers begin as plain 150 mm silicon wafers with a thickness of about 670 μm. This flow chart shows the eight steps of fabrication. Each step is detailed in this section.

Step 1: DRIE Alignment Marks

The first step in fabrication is placing alignment marks on the wafers. This step is identical for both top and bottom coupon wafers. The wafers are coated with HMDS to improve the adhesion of photo resist. The wafers are coated with 2 μm of thin positive resist which is then patterned using standard lithography methods. The wafers are then etched in the STS deep reactive ion etcher (DRIE) using SF_6 plasma for thirty seconds. This etches the alignment mark pattern about one micron into the surface of the wafer. Afterwards, the wafers are placed in an oxide asher to remove any residual Teflon from the DRIE process. The wafers are then stripped of photo resist. The result is two alignment marks whose structure and location on the wafer are shown in Figure 3-10.

All subsequent masks contain an alignment feature in the same location as the alignment marks. This alignment feature, as well as how the alignment mark appears when viewed through the alignment feature, is shown in Figure 3-11.

Step 2: Nitride growth and patterning

For both the top and bottom coupon wafers, nitride is used as a mask for the KOH-etching of the pits. Both the top and bottom coupons are placed in a furnace for the low pressure chemical vapor deposition of 4000 Å of nitride, Si_3N_4, on the wafer. This nitride is used as a mask in the KOH-etching of the pits. The nitride is deposited through a chemical reaction between DichlorSilan, $SiCl_2H_2$, and ammonia, NH_3, at a temperature of 775° C and a pressure of 220 mTorr. The deposition rate is about 23

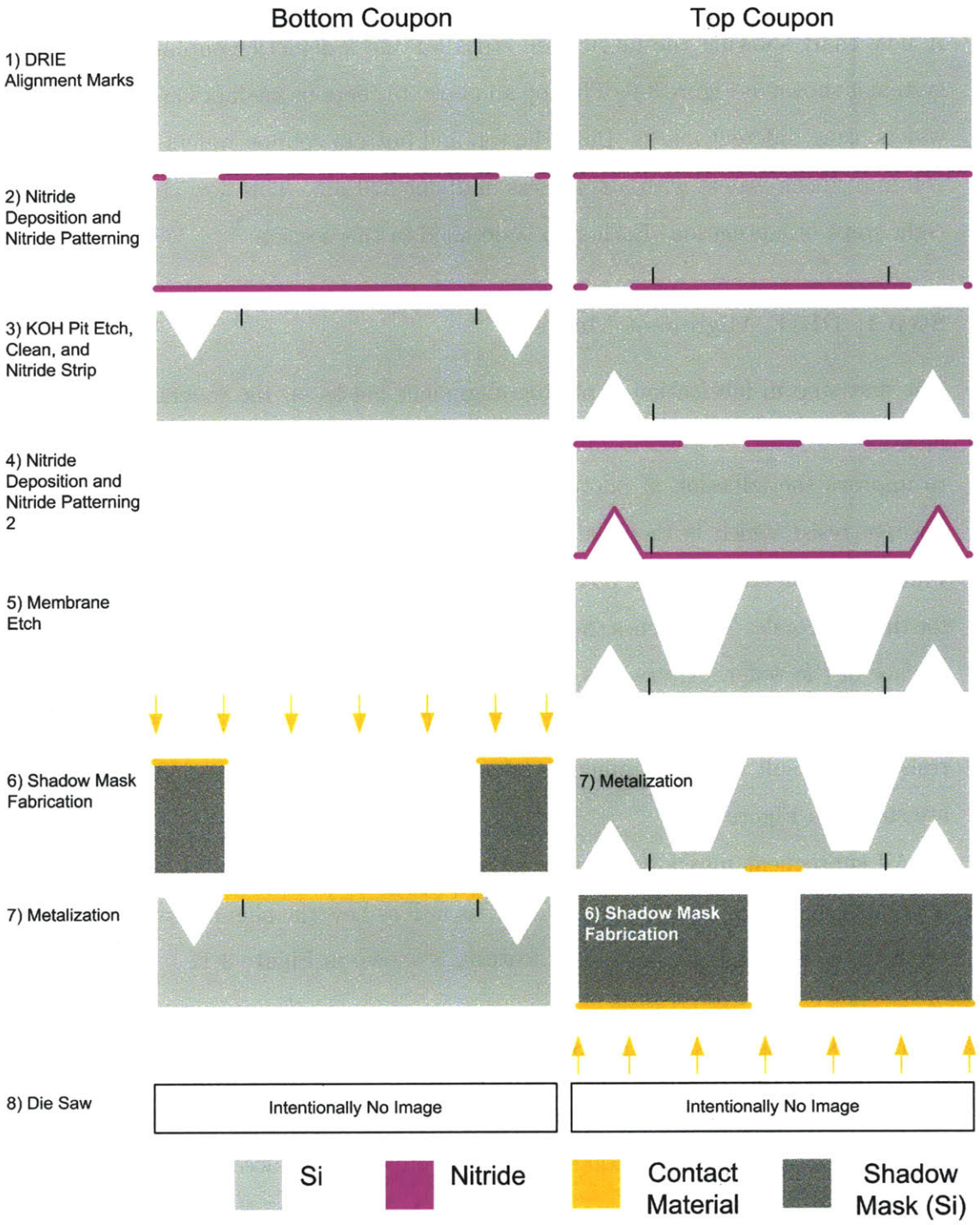

Figure 3-9: The fabrication process for the kinematic coupling two-coupon system.

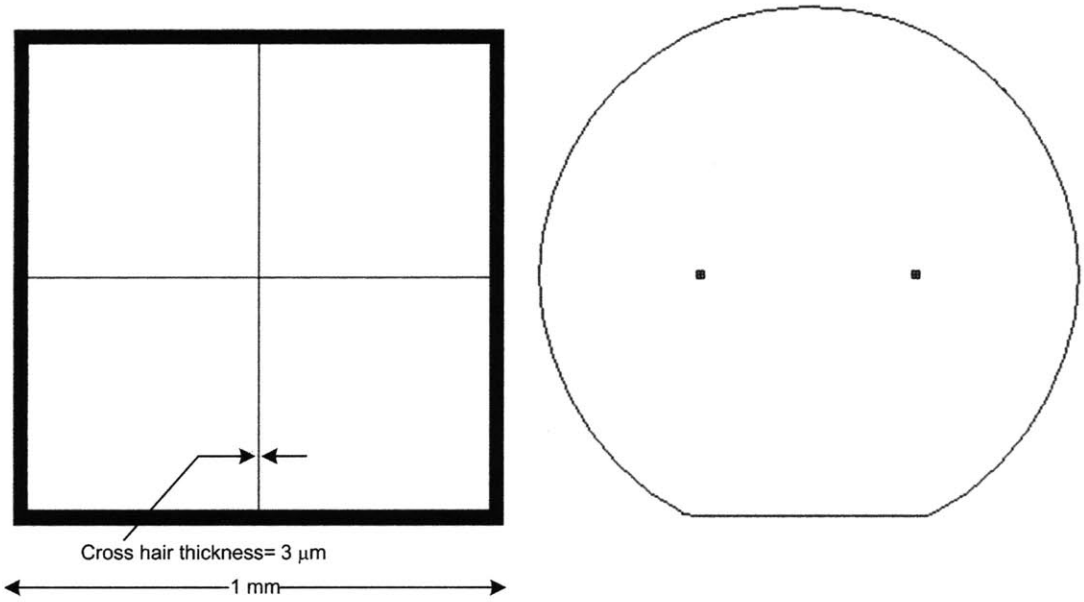

Figure 3-10: Left: The geometry of a single alignment mark. Right: The placement of the two alignment marks on a wafer.

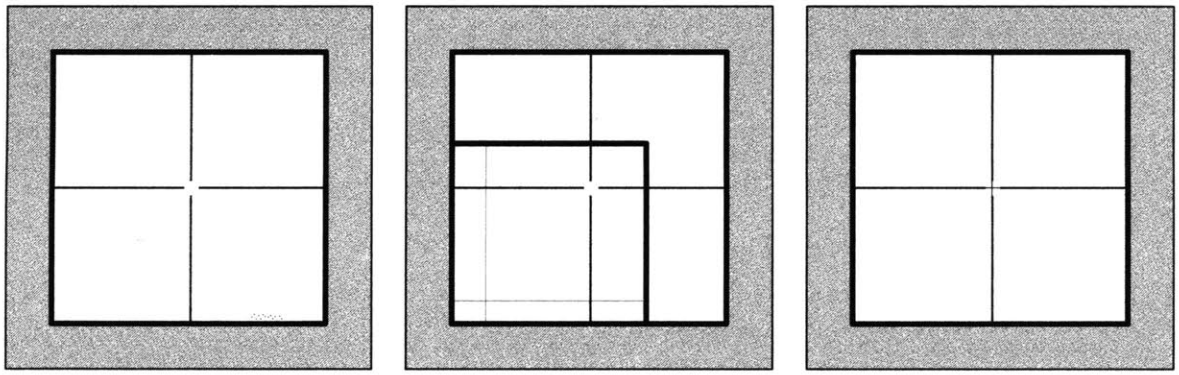

Figure 3-11: Left: an alignment feature on a mask. The cross hatched area is chrome, the non cross hatched area is transparent soda lime glass. Center: a misaligned mask and wafer alignment mark. Right: a correctly aligned mask and wafer alignment mark.

Å/min for a total deposition time of about 174 minutes. This time does not include the temperature ramp up and cool down times. For this thickness of nitride, the variability of thickness across the wafer can be up to 100 Å.

The nitride is then patterned to create the mask for the KOH-etch. The top coupon wafers and bottom coupon wafers each use different masks. Each mask consists of small circles which will ultimately become the KOH-etched pits. Each mask also contains an alignment feature as shown in Figure 3-11. Two microns of thin positive photo resist are spun onto the wafer and patterned using standard lithography tools. The alignment marks are then painted over using red resist to prevent them from being etched away. The nitride is then patterned using an AME 5000, a radio frequency etcher which uses Halocarbon 14, CH_4, to etch nitride . The etch rate is dependent on the area being etched, which for both the top and bottom masks is about 37 Å/s. Therefore, this etch takes about 108 seconds. The wafers are then measured optically and using a profilometer to ensure that the nitride has completely cleared. The photoresist is then stripped.

Step 3: KOH Etch, Clean and Nitride Etch

KOH solution is used to etch the pits which will later contain the stainless steel balls. The top and bottom wafers are both placed in 80°C 30% KOH solution. In this solution, silicon etches on the (100) plane rapidly but on the (111) plane slowly. This results in inverted pyramid shaped pit with a circular nitride film over it. In order for the balls to fit completely, the depth of these pits must be at least 392 μm, so, the target depth is 420 μm. The etch rate in these conditions is about 1.08 μm/min. Therefore, the minimum etch time was 389 minutes. The target width of the KOH pits is 968 μm; however, the circles defined by the mask are only 900 μm. That is because not only is there a very slow etch rate of the 111 surface, about 0.009 μm/min [49], but also, the interface between the nitride mask and the silicon can be attacked causing the feature to increase in size. During the initial fabrication of these wafers, this attack rate was found to be slower than what was predicted. Therefore, the coupons were allowed to etch longer to acheive the target lateral pit dimension of 968

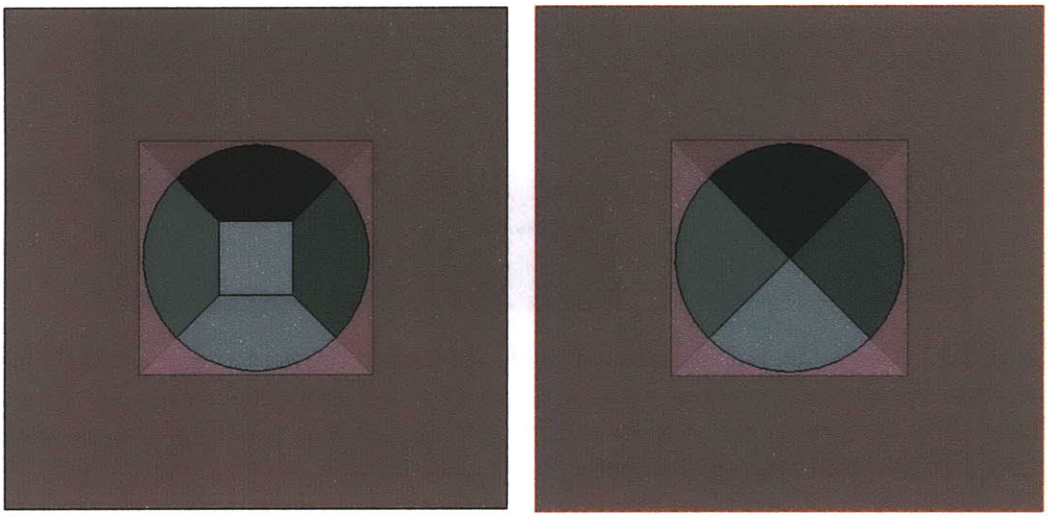

Figure 3-12: Left: A pit which has been etched 420 μm deep and has not terminated at a point. The purple area is the area covered by the nitride mask, which appears somewhat transparent over the corners of the pit. Left: A pit which is 670 μm deep and has terminated at a point. The lateral dimensions of the pit are slightly larger than the circular nitride mask because the nitride silicon interface is slowly attacked.

μm. The total etch time was 637 minutes. By this time the pits had reached their terminal size, meaning there was no flat bottom and the pits were perfect inverted pyramids. The total depth of these pits was roughly the thickness of the wafer. The etch rate of nitride in KOH is basizally zero, so this extended etch time had no effect on the mask thickness. These pit dimensions are shown in Figure 3-12.

After the KOH-etch, the wafers are cleaned by performing two ten-minute piranha cleans and one thirty-second 50:1 HF dip. A piranha clean is 3 parts hydrogen peroxide and one part sulfuric acid. The nitride is then stripped by placing the wafers in 165° C phosphoric acid. The etch rate is about 65 Å/min, meaning this nitride strip took 62 minutes. This process is very harsh and has a yield of only 50 percent. The nitride must be stripped so that the circular overhangs do not later break off and land in the pits, which would cause misalignment or land near the contact surfaces, which would affect the resistance measurement.

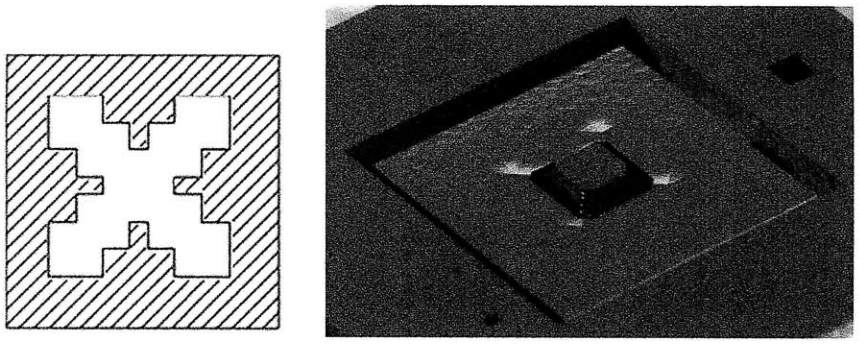

Figure 3-13: Left: The pattern of the nitride mask used during the second KOH-etch. The white areas are protected with nitride and the crosshatched areas are exposed silicon. This pattern creates convex corners [67]. Right: The resulting thin membrane with a stiff pyramid boss in the center.

Step 4: Nitride Deposition and Nitride Patterning 2

In order to mask the KOH-etch of the flexible membrane, the top coupon wafers go through a second nitride deposition identical to the first nitride deposition described in Step 2. Then, the nitride is patterned using the AME 5000 with a CH_4 chemistry. The mask for the membrane is somewhat complicated because it has to create convex corners with a KOH-etch. The mask pattern for a single membrane and the resulting silicon structure are shown in Figure 3-13. This pattern was designed by Dr. Alexis Weber and relies on previous work done to calculate the etch rates of convex corners [67].

Step 5: Membrane Etch, Clean, and Nitride Strip

In order to etch the thin membrane, the patterned nitride structure is immersed in 80°C 30% KOH solution. The silicon etch rate is 1.08 μm/min. In this case, the lateral dimension is not nearly as important as the depth. The aim is to leave a 20 μm thick membrane. In order to do this, the original thickness of the wafer is measured. Then the time to etch all but 20 μm is calculated. The wafer is taken out of the solution at set intervals to optically measure the depth of the pit to ensure the etch rate has not changed. It is very important to ensure the optical measurement is correctly callibrated. An error of only three percent could result in etching through

the entire wafer, leaving no membrane at all. The resulting structure is shown in Figure 3-13.

After the etch, the wafers are cleaned with two ten-minute piranha cleans and one thirty-second 50:1 HF dip. The first nitride strip used hot phosphoric acid which caused 50 percent of the wafers to break. In order to avoid losing another 50 percent of the wafers in a second hot phosphoric acid process, an alternative process is used. The wafers are soaked in 49% HF for several hours. While this process is easier on the wafers, it is extremely dangerous as it requires the use of large quantities of 49% HF which is extremely toxic as well as costly. Ideally the fabrication would require neither a hot phosporic or HF process. This was achieved in the final version of the two-coupon system by switching to an oxide mask.

Step 6: Shadow Mask Fabrication

The metal traces on these coupons are evaporated through shadow masks, which are wafers that have been through-etched using a DRIE (deep reactive ion etch) process. There are different masks for the top and bottom coupons. In order to make these masks, two plain silicon wafers are coated with HMDS. Immediately afterwards, 15 μm of thick positive resist are spun onto the wafer which is patterned using standard lithography techniques. The wafers are mounted to a quartz wafer because as the membrane gets very thin, there is the possibility that it could break and fall into the DRIE chamber. The quartz backing wafer prevents this. Additionally, the KOH-etch often leaves the edge of the wafer ragged; so it can be difficult to obtain a proper seal when the wafer is loaded into the DRIE. The quartz wafer has a very smooth edge enabling a proper seal to be formed. These wafers are then etched in the DRIE. Due to the large area of silicon being removed, the etch rate is very slow, around 1 μm/min. Therefore, the total etch time was about 670 minutes. At the end of this, a wafer with cutouts of the metal patterns for each of the top and bottom coupon wafers was created. These patterns are shown in Figure 3-14.

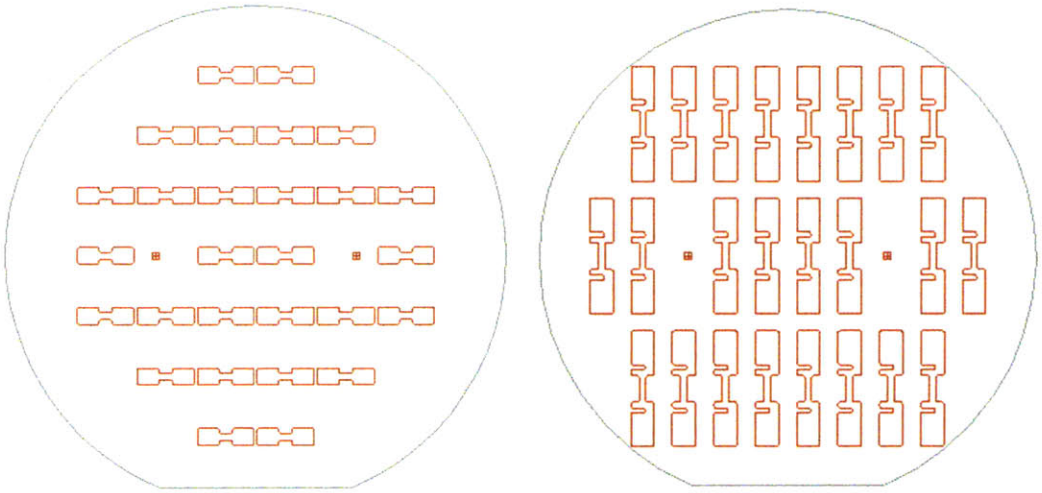

Figure 3-14: Left: The shadow mask for the top coupon. Right: The shadow mask for the bottom coupon.

Step 7: Metalization

Evaporation of metal through a shadow wafer is used to create the metal traces on the top and bottom coupons. The trace material is gold (Au). The shadow wafers are aligned to the top and bottom coupon wafers by aligning each of the wafer flats together. Small dabs of photo resist around the edges of the wafers are used to temporarily glue the device wafers to the shadow wafers. The wafers are then placed in an evaporative deposition system. 300 Å of titanium (Ti) is evaporated through the shadow mask to act as an adhesion layer between the silicon and the gold. 7000 Å of gold is then evaporated through the shadow mask. The device wafers, along with the shadow masks, are then briefly soaked in acetone to dissolve the photo resist holding them together. Any other evaporated material can be used in place of gold and additional metals can be plated onto individual coupons once the wafers have been diced.

Step 8: Die Saw

Finally, the individual coupons are diced. The bottom coupon wafers are simply attached to die saw tape and diced using conventional means. Since the top coupon wafers contained a thin membrane, they can not be placed under a vacuum. Therefore,

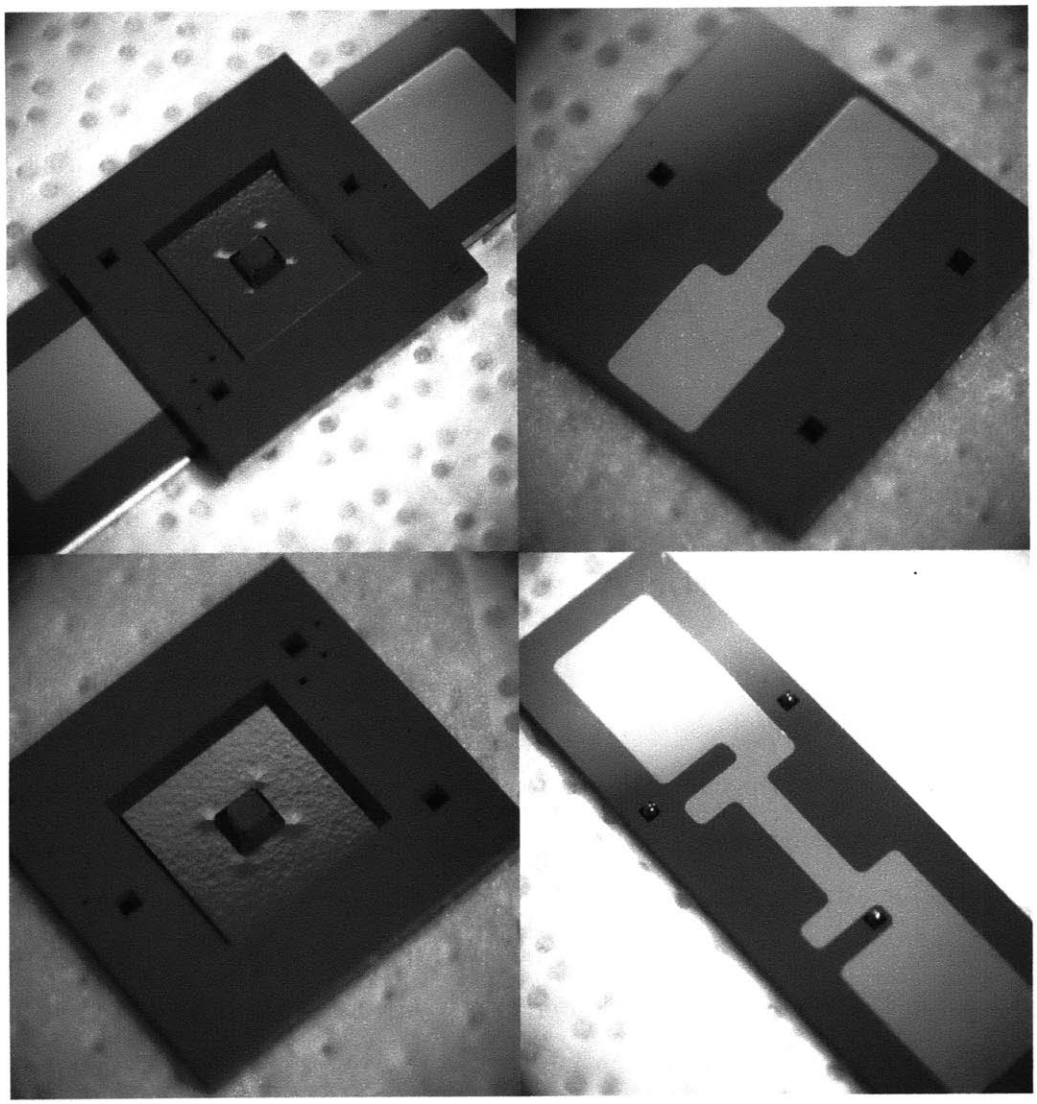

Figure 3-15: The assembled and disassembled kinematic coupling two-coupon system.

they are attached to a dummy wafer, membrane side up, using Crystal Bond. They are then diced and soaked in acetone overnight to remove the crystal bond. Water at 80°C can also be used to instantaneously dissolve Crystal Bond. The completed dies are shown in Figure 3-15. Each top coupon wafer contains 28 dies while each bottom coupon wafer contains 24 dies.

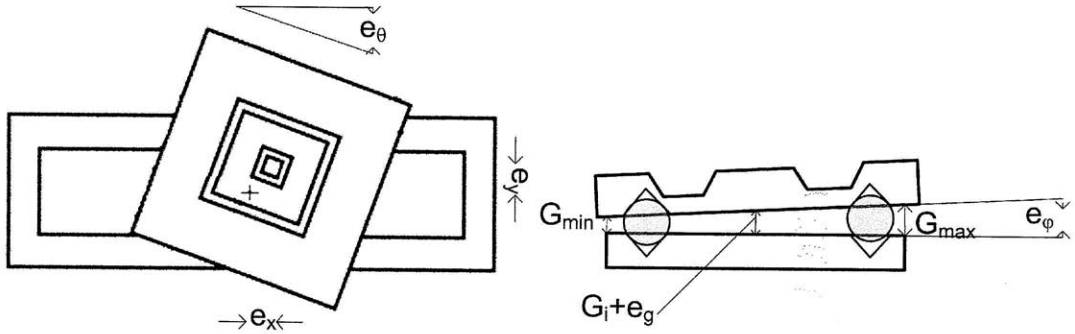

Figure 3-16: The four types of alignment errors: e_x and e_y are translational errors, e_θ is rotational error, e_g is gap error, and e_ϕ is the parallelism error. The maximum and minimum gap at each ball/pit interface are G_{max} and G_{min} respectively.

3.3 Position Error Analysis and Measurement

One of the important functional requirements of this coupon is that it be able to be taken apart and put back together in a repeatable manner. This repeatability is limited by certain aspects of the system which are not entirely repeatable such as lithography misalignment, ball geometry variation, and pit geometry variation. These variable aspects then contribute to the measurable errors of the system such as gap error, parallelism error, translational error, and rotational error. These errors are shown in Figure 3-16. Translation error is e_x in the x-direction and e_y in the y direction. Sometimes general translation error is referred to as e_{xy}. Rotational error is e_θ, gap error is e_g, and parallelism error is e_ϕ. This section first looks at lithography misalignment and finds that it is a negligible contributor to all measured errors. Next error budgets for the gap error, parallelism error, translational error, and rotational error are detailed. Finally, these errors are compared to the measured errors of the kinematic coupling two-coupon system.

3.3.1 Lithography Misalignment Error

When the mask which patterns the KOH-etched pits is aligned with the device wafer, it is possible that the mask and wafer are not completely parallel. This can be because of non-planarities in each of the mask and wafer, which can be up to 20 μm

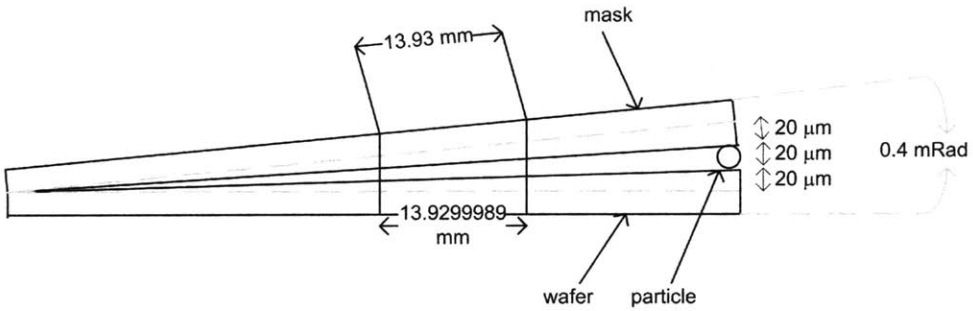

Figure 3-17: Shows the stack up of the wafer planarity error, the mask planarity error, and particle errors on the total lithography error.

Dimension	Target Dimension mm	Minimum Dimension mm	Maximum Error $e_{litho-max}$ nm
D_{b-max}	13.93	13.929999	1
D_{b-min}	10	9.9999992	0.8
D_{c-max}	8.2	8.1999993	0.7
D_{c-min}	6.5	6.4999995	0.5

Table 3.3: The effect of lithography misalignment error on the geometry of the kinematic coupling two-coupon system.

each and also particles, which can be up to 20 μm in size. This can result in one side of the wafer being 60 μm higher than the other side of the wafer, which is 150 mm away. Therefore the maximum angle between the mask and the wafer is 0.4 mrad. This means that for any given dimension being pattered on the wafer, the maximum dimension will be the target dimension while the minimum dimension is defined as

$$\text{Minimum Dimension} = (\text{Target Dimension}) \cos 0.0004 \tag{3.6}$$

and maximum error is

$$e_{litho-max} = \text{Target Dimension} - \text{Minimum Dimension} \tag{3.7}$$

Figure 3-17 displays this lithography misalignment error and Table 3.3 shows the effects of this error on each of the important dimensions of the coupons. These dimensions are shown in Figure 3-18.

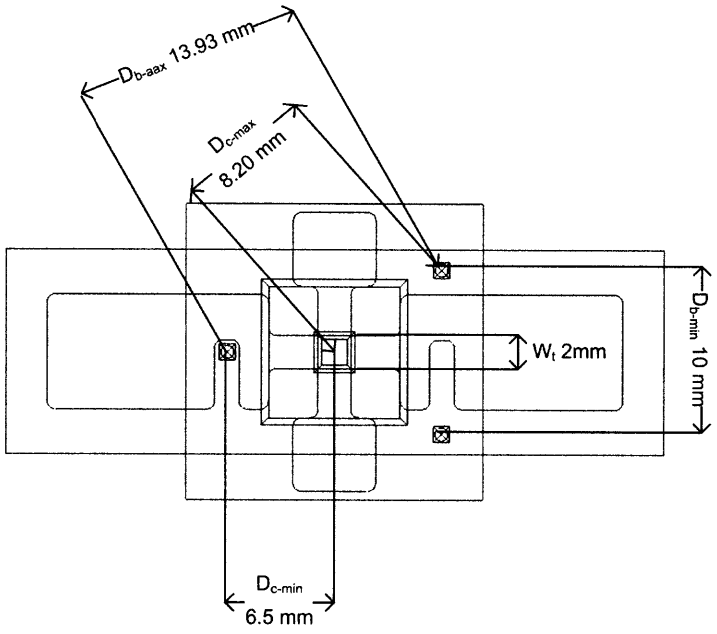

Figure 3-18: Geometry of the assembly. The distances between balls, D_{b-max} and D_{b-min}; the distances between the balls and the center, D_{c-max} and D_{c-min}, and the width of the contact metal trace w_t.

The maximum effect lithography misalignment error will have on the relative positions of the pits is 1 nm. This does not affect translation error because the center of the top coupon would still be over the center of the bottom coupon. It does not affect rotational error for the same reason. The effect of this lithography misalignment error on the gap height would be to increase the gap slightly because the balls would be pushed to the outside of the pits as shown in Figure 3-19. Assuming that half of this lateral error was taken up by each ball, then the net upward position would be 0.71 nm, or roughly three times the diameter of a single silicon atom, so it is safe so say the effect of lithography error on gap height error is negligible. For the same reason, lithography misalignment error has no measurable affect on parallelism error.

Gap Height Error

The gap height is designed to be 5 μm. From Figure 3-16, gap error can be defined as

$$e_g = \bar{G} - G_i \tag{3.8}$$

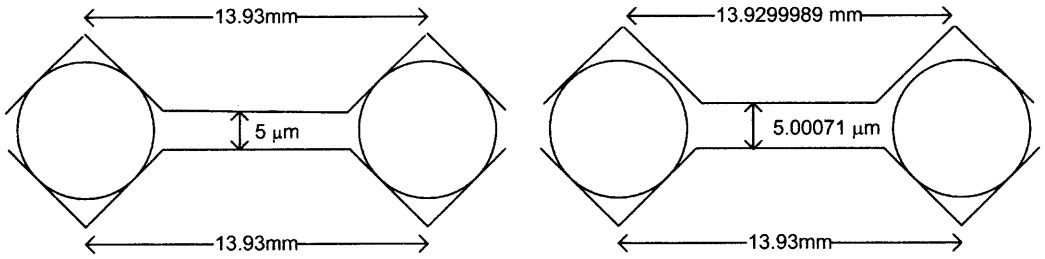

Figure 3-19: The effect of lithography error on gap. Figure not to scale.

	μ"	μm
Allowable Ball Diameter Variation Δ_{bdv}	3	0.0762
Deviation from Spherical Form Δ_{dsf}	3	0.0762
Surface Roughness Arithmetical Average Δ_{sraa}	0.5	0.0127
Basic Diameter Tolerance Δ_{bdt}	+/- 30	+/- 0.762
Allowable Lot Diameter Variation Δ_{aldv}	5	0.127

Table 3.4: Tolerances of Grade 3 Balls

where $\bar{G}$ is the average of the gaps at each of the three ball/pit interfaces and G_i is the designed gap. The dependence of the gap at each ball/pit interface is given in Equation 3.1. If the pit is not perfectly square and one side of the pit is longer than the other side of the pit, the height at which the ball sit in the pit will be a function of the small dimension, W_{min}. The ball will then be able to roll along the wider dimension, W_{max}. This is shown in Figure 3-20.

From Equation 3.1 and in Figure 3-20, gap height at each ball/pit interface is a function of the ball diameter, D, and the smallest pit dimension, W_{min}. In order to determine how variable gap height is, the variability of ball diameter and the smallest pit dimension must be established.

The balls used are precision stainless steel balls, but are still not perfect spheres. They are Grade 3 balls with a target diameter or 1/32", or 794 μm. The various tolerances of Grade 3 balls in both micro-inches and microns are listed in Table 3.4.

Within one lot of balls, the difference between the smallest diameter at any point on any ball and the largest diameter at any point on any ball is defined as

$$\Delta_{max} = \Delta_{bdv} + \Delta_{dsf} + \Delta_{sraa} + \Delta_{aldv} \tag{3.9}$$

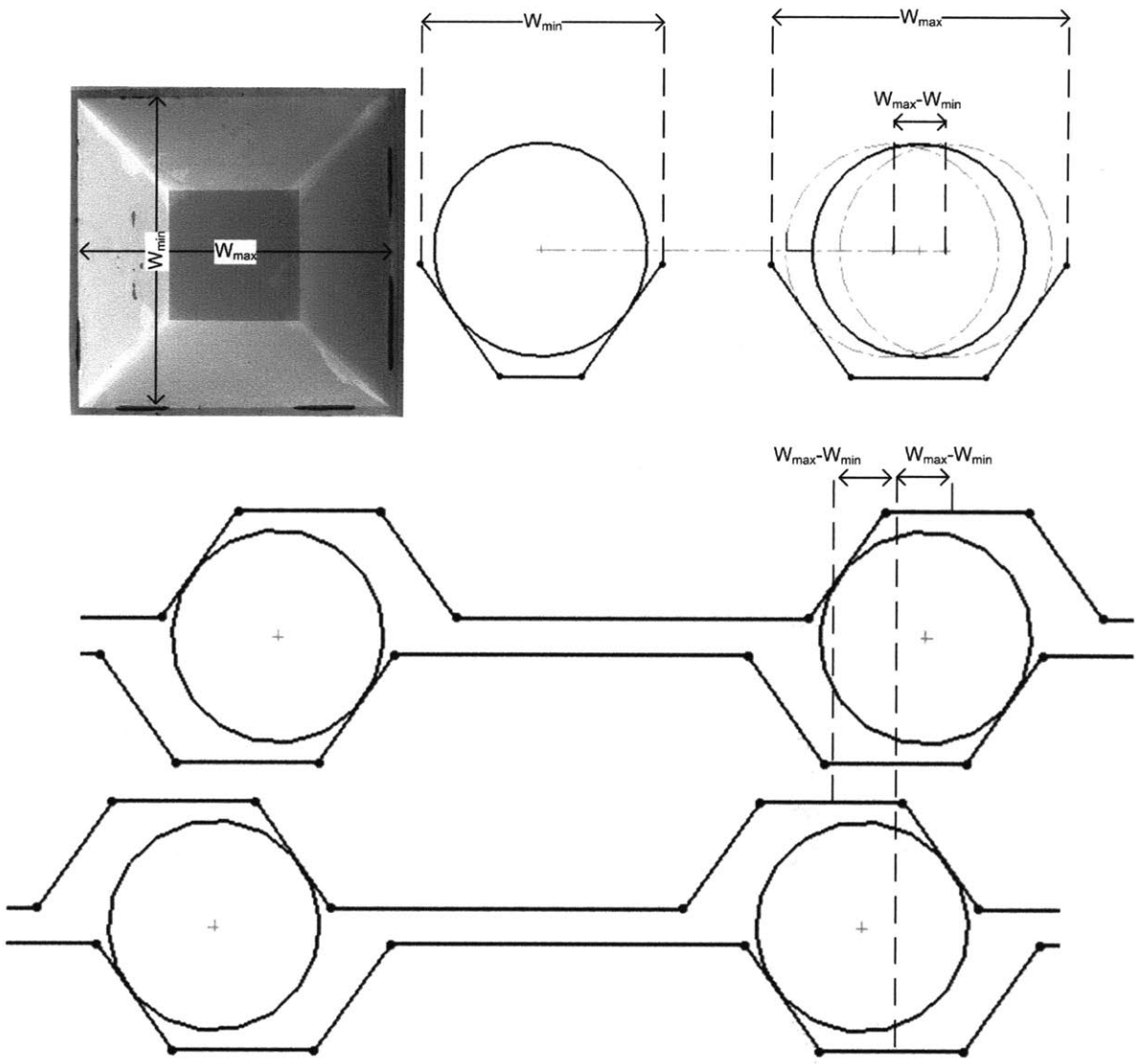

Figure 3-20: The effects of the pit geometry on translational error. Figure not to scale.

Minimum Average Lot Diameter D_{max}	792.988 μm
Maximum Average Lot Diameter D_{min}	794.512 μm
Maximum Diameter Variation Within a Lot Δ_{max}	0.291 μm

Table 3.5: Variations in Grade 3 Ball Geometry

	W_{min} μm	$W_{max} - W_{min}$ μm
Average Value	965.7	2.75
Standard Deviation	2.9	1.62
Maximum Value	971.1	6.1
Minimum Value	960	0.3

Table 3.6: Variability of Pit Geometry

where Δ_{bdv}, Δ_{dsf}, Δ_{sraa}, and Δ_{aldv} are various tolerances of the balls defined in Table 3.4. The minimum average ball diameter is

$$D_{min} = D_{target} - \Delta_{bdt} \tag{3.10}$$

where Δ_{bdt} is the basic diameter tolerance of each ball. This is defined in Table 3.4. The maximum average ball diameter is

$$D_{max} = D_{target} + \Delta_{bdt} \tag{3.11}$$

These values are summarized in Table 3.5

Minimum pit width was determined by measuring 28 different pits with an optical microscope. The minimum and maximum pit width for each were recorded. This raw data is shown in Figure 3-21. The average pit minimum width, W_{min}, was 965.7 μm with a standard deviation of 2.9 μm. The minimum pit size measured was 960 μm and the maximum was 971.1 μm. The average difference between these two dimensions, $W_{max} - Wmin$, was 2.75 μm, with a standard deviation of 1.62 μm, and a maximum value of 6.1 μm. This data is also presented in Table 3.6.

The overall gap height will be highest when all the ball/pit interfaces have the maximum possible gap. According to Equation 3.1, this occurs when the balls are as large as possible and the minimum pit width dimension is as small as possible. The

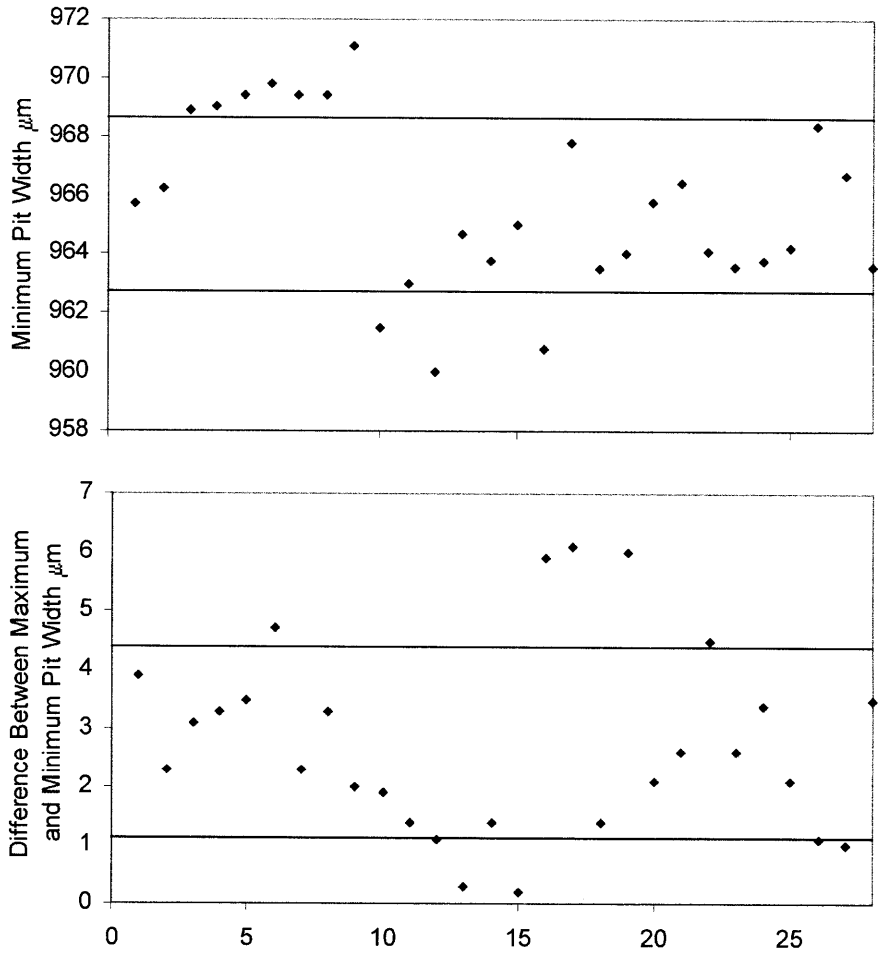

Figure 3-21: The measurements of the minimum pit width and difference between the maximum and minimum pit width of 28 pits.

	Minimum Case	Maximum Case	Average Case
Ball Diameter μm	792.8	794.7	793.8
Minimum Pit Dimension μm	971.1	960	965.7
Gap Height μm	0.4	19.4	9.7
Gap Error μm	-4.6	+14.4	4.7

Table 3.7: The maximum and minimum gap heights in the kinematic coupling two-coupon system.

overall gap height will be lowest when all the ball/pit interfaces have the minimum possible gap. This occurs when the balls are as small as possible and pit width is as large as possible. The ball geometries are given in Table 3.5 and the minimum pit width geometries are given in Table 3.6. The maximum ball diameter is the maximum average lot diameter plus one-half of the maximum deviation within a lot. The minimum ball diameter is the minimum average lot diameter minus one-half of the maximum diameter variation within a lot. The actual gap error is the difference between the gap height and the design gap height of 5 μm. Using Equation 3.1, the actual gap between any set of coupons will be between 0.25 μm and 19.6 μm. These conditions and the resulting gap heights and errors are shown in Table 3.7.

In the gap height error, no components can move in between assembly and disassembly. Therefore, while there is gap error variation between sets of coupons, there should be almost no variation in gap error between the assembly and disassembly of the same set of coupons. Small errors may occur from particles getting on the balls or the top coupon not settling correctly, but these can be hard to predict.

In order to test the predictions for gap height error as well as determine the assembly/disassembly error, gap height was experimentally measured. Gap error was tested by measuring the height difference between the bottom coupon and top coupon at four different places. The thickness of the top coupon, which was measured with micro-meters, was subtracted to get the true gap at each of these four places. This is shown in Figure 3-22.

The gap distance was taken as the average height difference at each of the four locations minus the thickness of the top coupon. This height was measured by focusing on the top coupon and then focusing on the bottom coupon and recording the dif-

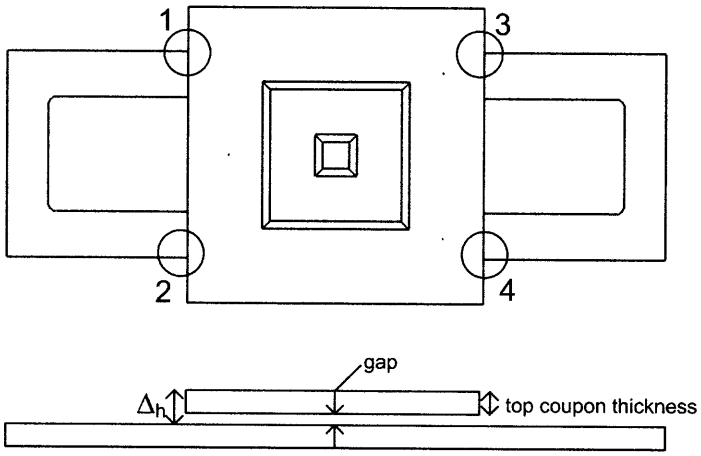

Figure 3-22: The four places gap height was measured for the kinematic coupling two-coupon system.

ference in focal heights. Three sets of coupons were assembled and disassembled five times and their gaps recorded. An additional seven sets of coupons were assembled and disassembled once and their gap recorded. The raw data for these experiments is shown in Figure 3-23.

Table 3.8 displays the measured minimum gap height, maximum gap height, and average gap height compared to those predicted in Table 3.7. It also displays the statistics relating to assembly and disassembly.

The measured gaps ranged from 0.6 μm to 18.6 μm, which is very close to what

		Predicted	Measured
Different Sets of Coupons	Average Gap Height/Error μm	9.7/4.7	13.5/8.5
	Minimum Gap Height/Error μm	0.4//-4.6	0.6/-4.2
	Maximum Gap Height/Error μm	19.4/14.4	18.6/13.6
	Standard Deviation Gap Error μm	N/A	5.9
Assembly/ Disassembly	Standard Deviation μm	N/A	1.2
	Maximum Deviation from Average μm	N/A	3.1

Table 3.8: The maximum and minimum gap heights in the kinematic coupling two-coupon system.

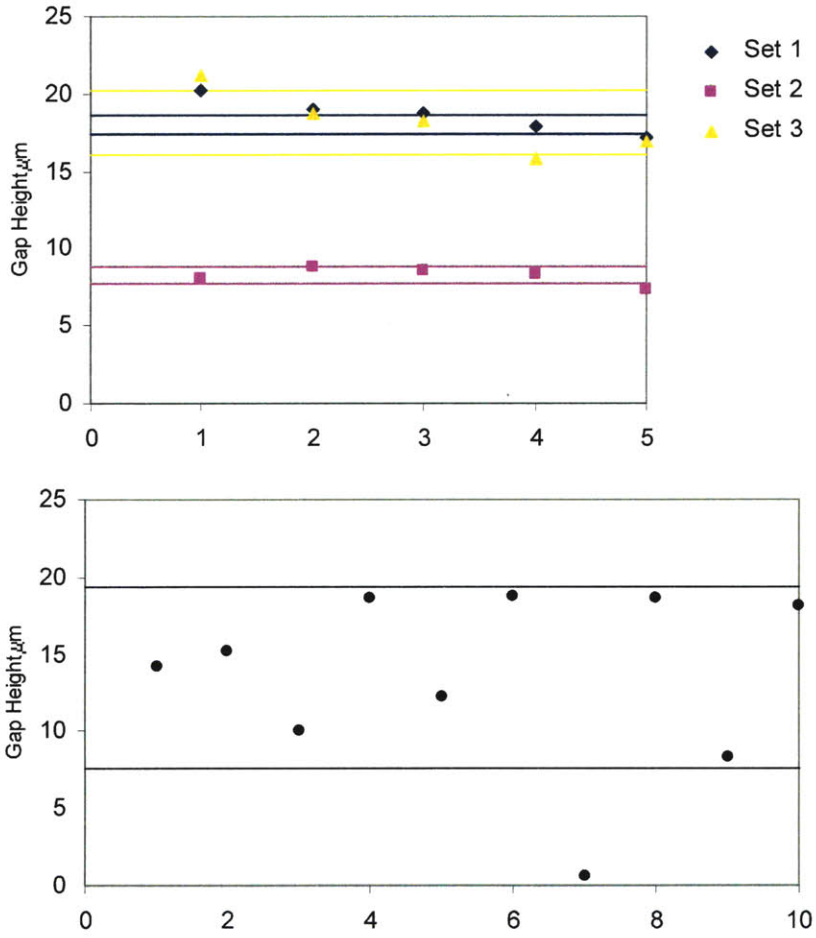

Figure 3-23: Top: The repeatability of the average gap for three coupons. Bottom: The average gap of ten coupons.

was predicted in the error budget. The standard deviations of gap height for the three sets of coupons that were assembled and disassembled five times were 1.2 μm, 0.6 μm, and 1.8 μm, which averaged to 1.2 μm. In the third set, the average gap height was 18.175; however there was one assembly of that same set of coupons that resulted in a gap height of 3.1 μm. This was the maximum deviation from average for any of the assembly/disassembly tests. It should be noted that these gap heights were measured with an optical microscope with a resolution of about 1 μm. The errors were found to be around the resolution of the microscope, so the actual repeatability may be even better.

Parallelism Error

From Figure 3-16 it can be determined that the parallelism error is

$$e_\theta = \arctan \frac{G_{max} - G_{min}}{D_{b-min}} \tag{3.12}$$

where G_{max} is the largest ball/pit interface gap, G_{min} is the smallest ball/pit interface gap, and D_{b-min} is the distance between these two ball/pit interfaces. This parallelism error would be largest when D_{b-min} and G_{min} are as small as possible and G_{max} is as large as possible. The smallest distance between two interfaces is 10 mm, as shown in Figure 3-18. The maximum G_{max} is 19.4 μm and the minimum G_{min} is 0.4 μm. These are given in Table 3.7. The leads to a maximum parallelism error of 1.9 mrad. The minimum parallelism error would be zero and would occur when all ball/pit interfaces had the same gap height.

Parallelism error was measured using the same data used to determine gap height error. This involved assembling and disassembling three sets of coupons five times and measuring the height in four places as shown in Figure 3-22. Seven additional sets of coupons were assembled once and their height measured at four different places. The parallelism angle used positions 1, 2, and 3 to create a plane. The angle of that plane relative to a flat plane was taken to be the parallelism angle error. A plane can be described as a normal vector and a point. That point can be any of the positions

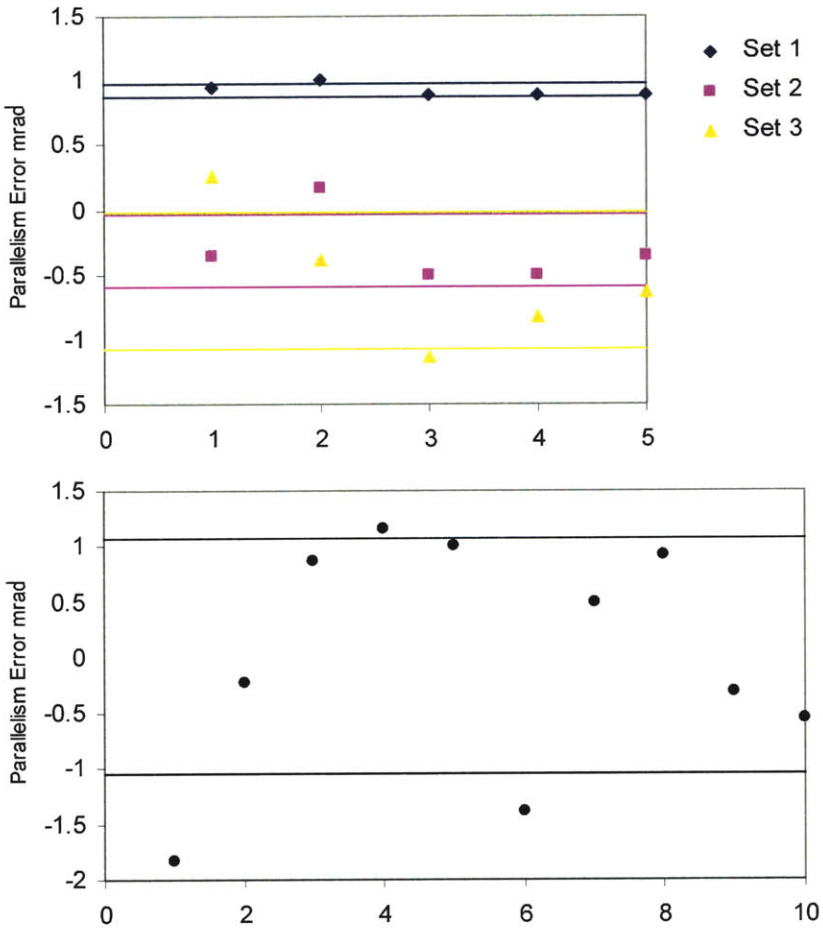

Figure 3-24: Top: The repeatability of parallelism of three samples. Bottom: The average parallelism error of ten samples.

1, 2, or 3. The normal vector is then

$$n = (p_2 - p_1) \times (p_3 - p_1) \tag{3.13}$$

This will result in a 1x3 vector $[n_1; n_2; n_3]$. The parallelism angle is then given by

$$e_a = \frac{\pi}{2} - \arctan \frac{n_3}{\sqrt{n_1^2 + n_2^2}}. \tag{3.14}$$

The raw data for these experiments is shown in Figure 3-24.

		Predicted	Measured
Different Sets of Coupons	Average Absolute Error mrad	N/A	0.88
	Minimum Absolute Error mrad	0	0.22
	Maximum Absolute Error mrad	1.9	1.83
	Standard Deviation Error mrad	N/A	1.1
Assembly/ Disassembly	Standard Deviation mrad	N/A	0.28
	Maximum Deviation from Average mrad	N/A	0.59

Table 3.9: The parallelism error e_ϕ in the kinematic coupling two-coupon system.

Table 3.9 displays the maximum parallelism error, and the standard deviation of the parallelism error and compares it to the predicted maximum parallelism error of 1.9 mrad. It also displays the statistics relating to assembly and disassembly.

The absolute parallelism error ranged from 0.22 mrad to 1.83 mrad, slightly less than the maximum predicted parallelism error of 1.9 mrad. The standard deviations of parallelism for the three sets of coupons that were assembled and disassembled five times were 0.05 mrad, 0.28 mrad, and 0.52 mrad, which averaged to 0.28 mrad. Although all of these standard deviations are very small, there is a wide variation between them. The first set of coupons had a repeatability ten times better than the third set of coupons. In the third set, the average parallelism error was -0.52 mrad; however there was one assembly of that same set of coupons that resulted in a parallelism error of -1.14 mrad. This was the maximum deviation from average for any of the assembly/disassembly tests.

Translational Error

The only error affecting the translational errors, e_x and e_y is the non-squareness of the pits.

From Figure 3-20, one can see that the total translational error is equal to the maximum difference between the long dimension of the pit, W_{max} and the short

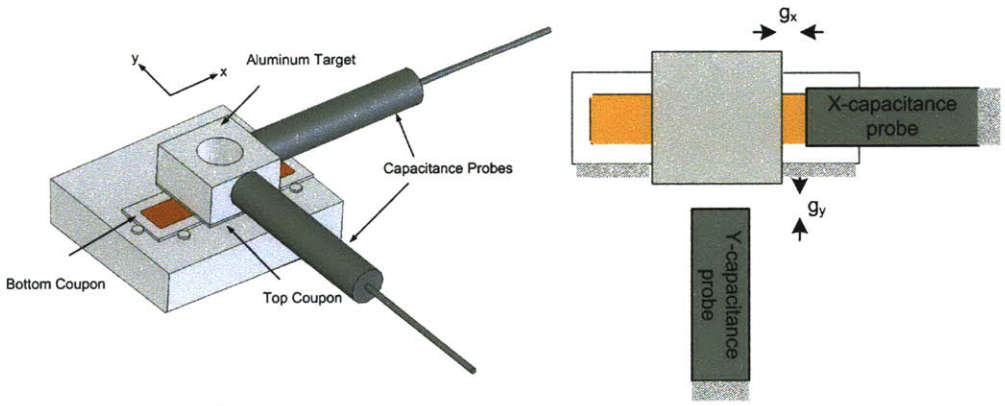

Figure 3-25: The test setup used to measure XY repeatability.

dimension of the pit W_{min}. Therefore

$$e_{XY} = +/- (W_{max} - W_{min}) \tag{3.15}$$

According to data for pit geometry variability in Table 3.6, the maximum value for this error is +/- 6.1 μm and the average value for this error is 2.75 μm.

The accuracy of this error estimation was then tested. Translational error was measured using the test setup shown in Figure 3-25.

In this test setup, an aluminum target was mounted on top of a top coupon using super glue. This aluminum target had a wire which grounded it. The bottom coupon was glued to a mount which contained two capacitance probes which could measure the gap distance between the end of the probe and the aluminum target on the top samples. The coupons were assembled, and the capacitance probes were positioned within range. The coupons were then disassembled, and reassembled twenty times. The gap at the X-capacitance probe, g_x, and the gap at the Y-capacitance probe, g_y, were recorded after each reassembly. Since this gap was a function of how close the capacitance probe was set up to the target initially, the average x-gap and the average y-gap were subtracted from the raw data to get the gap fluctuation around the average. The results of this data are shown in Figure 3-26.

In the x-direction, the standard deviation of the x-gap data was 1.54 μm. The maximum offset between the average gap and a single point in the "+" direction was

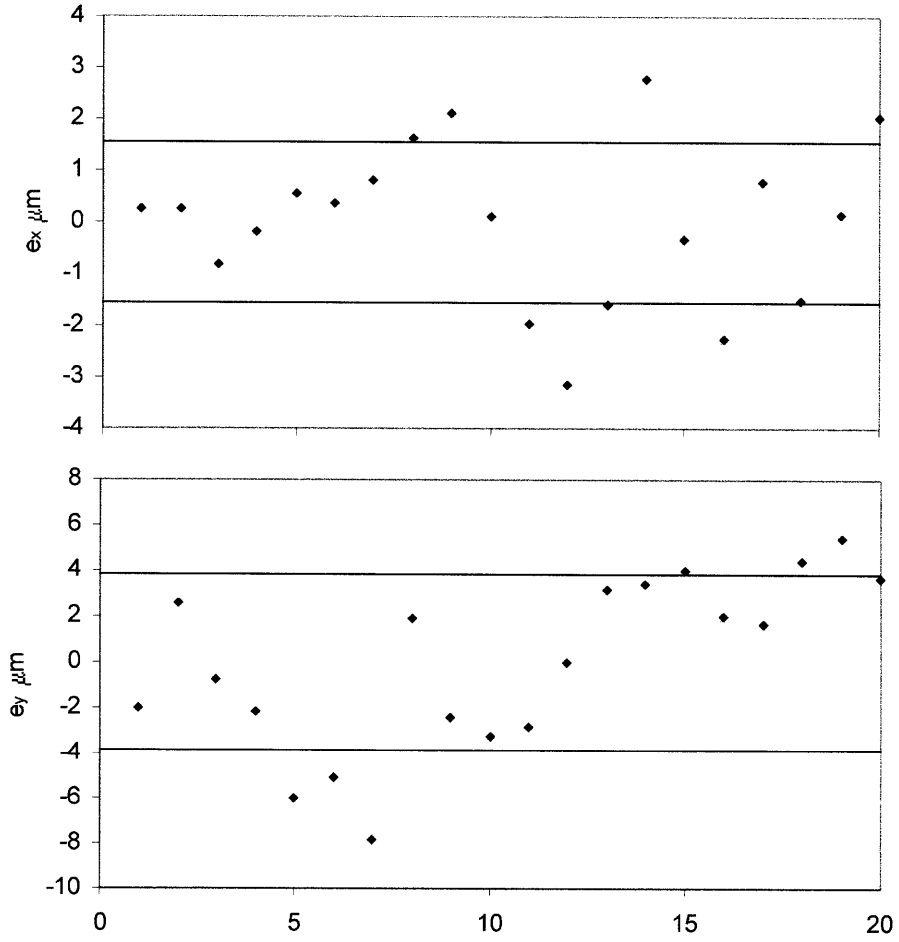

Figure 3-26: The translational repeatability of the kinematic coupling two-coupon system.

	Predicted e_{XY}	Measured e_X	Measured e_Y
Standard Deviation of Error (μm)	2.79	1.54	3.80
Maximum "+" Error (μm)	6.1	2.79	5.43
Maximum "-" Error (μm)	6.1	3.14	7.87

Table 3.10: The translational error in the kinematic coupling two-coupon system.

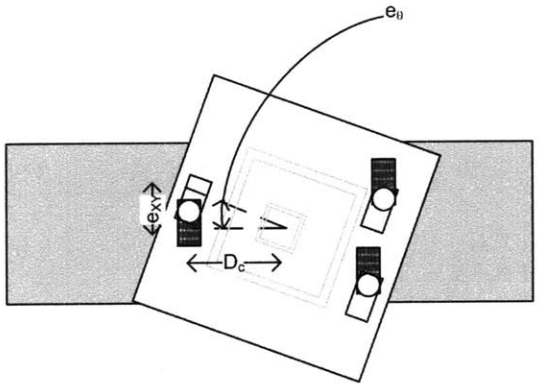

Figure 3-27: Rectangular pits leading to tip rotation.

2.79 μm while the maximum offset between the average gap and a single point in the "-" direction was 3.14 μm. In the y-direction, the standard deviation of the y-gap data was 3.80 μm. The maximum offset between the average gap and a single point in the "+" direction was 5.43 μm while the maximum offset between the average gap and a single point in the "-" direction was 7.87 μm. These results are summarized in Table 3.10.

Rotational Error

The rotational error comes from the coupon being able to rotate slightly as a result of non-square nature of the pits. This error is shown in Figure 3-27.

The rotational error can be described in terms of the translational error by the equation

$$e_\theta = \tan \frac{e_{XY}}{D_c} \tag{3.16}$$

where e_θ is the rotational error and e_{XY} is the translational error. The rotational error will be greatest when D_c is the smallest, or 6.5 mm, as is shown in Figure 3-18.

	Different Sets of Coupons			Assembly/Disassembly		
	Average	Standard Deviation	Maximum Absolute	Average	Standard Deviation	Maximum Absolute
G/e_g μm						
Predicted	9.7/4.7	N/A	19.4/14.4	N/A	N/A	N/A
Measured	13.5/8.5	5.9	18.6/13.6	N/A	1.2	3.1
e_ϕ mrad						
Predicted	0	N/A	1.9	N/A	N/A	1.9
Measured	0.88	1.1	1.83	N/A	0.28	0.59
e_{XY} μm						
Predicted	N/A	2.79	6.1	N/A	2.79	6.1
Measured	N/A	3.80	7.87	N/A	3.80	7.87
$e_\theta mrad$						
Predicted	0	0.6	1.2	0	0.6	1.2
Measured	N/A	N/A	N/A	N/A	N/A	N/A

Table 3.11: The predicted and measured errors of the kinematic-coupling two-coupon system

The maximum and standard deviation for rotational error can be calculated by using the maximum and standard deviation values for translational error in Equation 3.16. The translational error values come from Table 3.10. At the maximum measured translational error of 7.87 μm, the maximum rotational error is 1.2 mrad. The y-translational error had a standard deviation of 3.8 μm. Therefore the rotational error will have a standard deviation of 0.6 mrad. The minimum possible rotational error is zero.

All values for the rotational error are very, very small. Unfortunately the test setup shown in Figure 3-25 did not allow for the rotational error of this kinematic coupling two-coupon system to be tested, so there are no measured values to compare to the predicated values of rotational error. This was rectified and all later versions of the two-coupon system were tested for rotational error.

Error Summary

All of the predicted and measured values for each of the errors (translational, rotational, gap error, and parallelism error) are displayed in Table 3.11

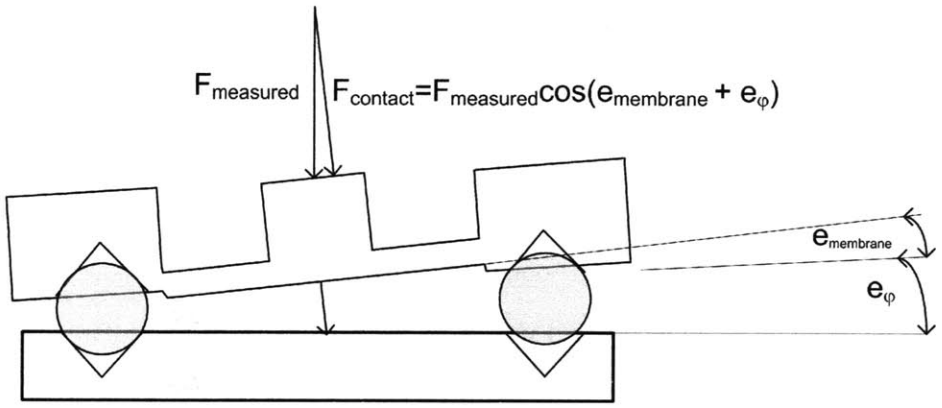

Figure 3-28: The membrane tilt error combining with the assembly parallelism error to create a force error.

3.3.2 Error Interpretation

This section briefly analyzes the effects of the repeatability errors in the final two-coupon system. There are two areas affected by errors. The translational errors affect the asperity level contact. The second area affected is that membrane tilt and parallelism error have an effect on the applied force.

In the kinematic coupling two-coupon design, the standard deviation of translational repeatability was 3.80 μm. The asperities in many MEMS fabricated contacts are on the order of 1 μm [22]. According to the measured data shown in Figure 3-26, 20% of the time, the position of the top coupon relative to the bottom coupon will be less than 0.5 μm from the average position, meaning at least half of the diameter of any two asperities will overlap. 32.5% of the time, the position of the top coupon relative to the bottom coupon will be less than 1 μm from the average position, meaning at least some small portion of the any two asperities will overlap. This means that 67.5% of the time, the asperities will completely miss each other. This is why the positional repeatability of the system needs to be improved.

In the kinematic coupling two-coupon design, the worst case membrane tilt error was 0.6 mrad. The worst parallelism error was 1.2 mrad. These errors can sum, leading to the actual force on the contact being slightly less than the measured force. This is shown in Figure 3-28. The relationship between the measured and force and

the actual force on the contact is

$$F_{contact} = F_{measured} \cos\left(e_{membrane-tilt} + e_{\phi}\right). \tag{3.17}$$

For the worst case scenario, where the sum of the two contributing errors is 1.8 mrad, the actual contact force will be 99.9998% of the measured contact force. This is less than the accuracy of the mechanism used to measure the force.

3.4 Proof of Concept Testing

The kinematic coupling two-coupon system was tested using a CETR Tribometer force and displacement measurement system. Lead wires were soldered to the bottom coupon which was then taped to a piece of silicon wafer. Lead wires were also soldered to the top coupon. This had to be done very carefully as the height of this solder and wire could not exceed 670 μm, or it would interfere with the assembly. Then the top coupon was assembled to the bottom coupon. This had to be taped onto the bottom coupon so that the wires which attach to the top coupon did not act as a spring and disassemble the coupons. This assembly is shown in Figure 3-29

This coupon assembly was then placed in the Tribometer, which had its own integrated 50 g load cell and piezo displacement system. A Keithly 2420 source-measure unit was used to record contact resistance. The Tribometer was used instead of the original Oklahoma State measurement tool because the two-coupon system could not operate within the strict displacement limits of the OSU tool. This test setup is shown in Figure 3-30.

Finally, contact resistance and membrane displacement were both measured as a function of force. The contact resistance was measured on both a clean set of coupons and a dirty set of coupons. Each set was measured twice. The results of this experiment are shown in Figure 3-31.

This demonstrates that the coupons can function as designed, to provide a relationship between force and contact resistance. However, the resolution of force taken

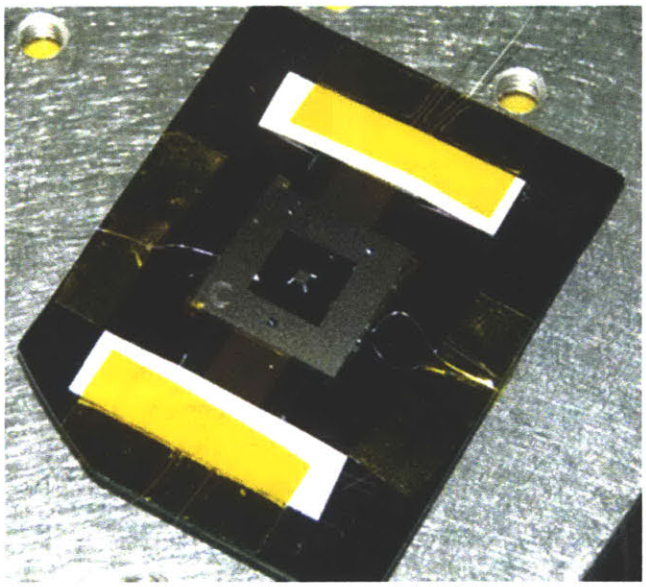

Figure 3-29: The two-coupon system ready for testing. The assembly had to be taped down to prevent the wires on the top coupon from springing upwards and disassembling the coupons.

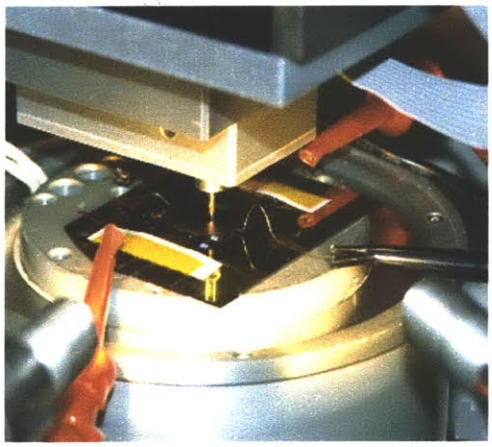

Figure 3-30: Left: The probe of the Tribometer over the two-coupon system. Right: The full Tribometer.

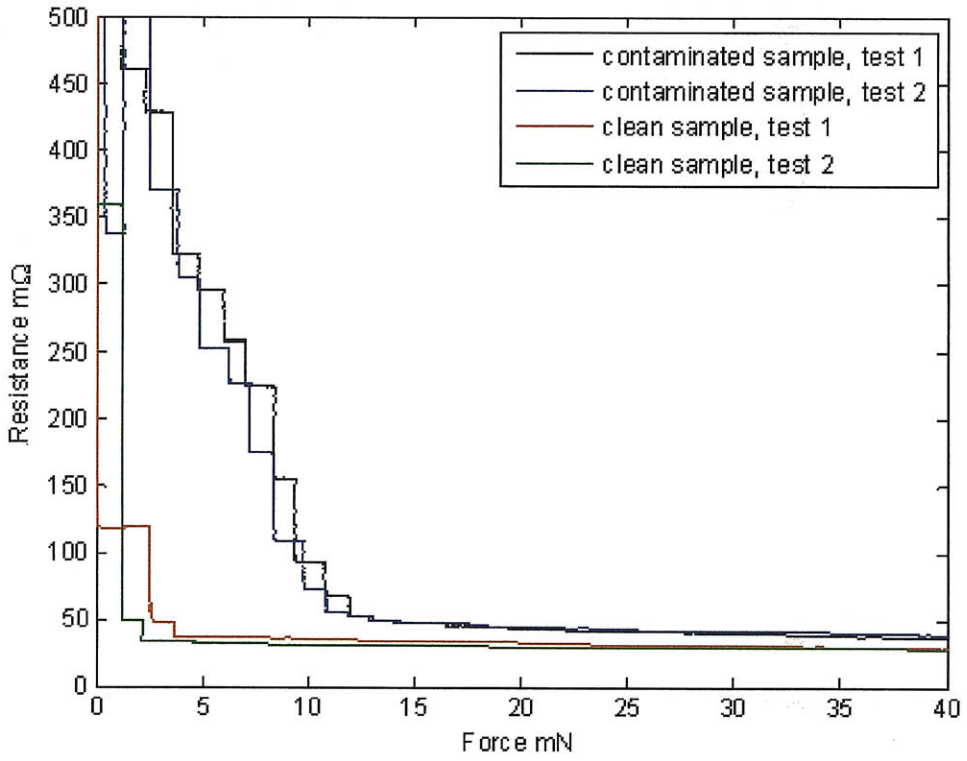

Figure 3-31: Contact resistance measurement results for the kinematic coupling two-coupon system. Results for both clean and contaminated samples are shown.

by the Tribometer is inadequate and creates stepped rather than continuous data.

The membrane displacement as a function of force compared to the contact resistance results is shown in Figure 3-32.

The force displacement curve has three regions. In Zone 1 the probe has not yet reached the top coupon, so the displacement of probe increases; but force is essentially zero. The force does drift a bit due to sensor drift. In Zone 2 the probe displacement increases linearly with the force. This is the area when the membrane is being deflected, but the top coupon has not made contact with the bottom coupon. At the beginning of Zone 3, the top coupon bottoms out on the bottom coupon. Force continues to increase, but the probe stops moving. Any probe movement seen is due to sensor drift or the deflection of the silicon which would be very, very insignificant (Å scale). During Zone 2, the probe is displaced 12.2 μm while force is increased by 5.98 mN. The resulting stiffness is, therefore, 0.49 mN/μm. This is less than the 0.67 mN/μm predicted by the numerical model and far less than the 1.8 mN/μm predicted by the FEM. According to Equation 3.3, the numerical model stiffness goes with membrane thickness cubed. If the membrane in the experimental case was 18 μm thick instead of 20 μm thick, then the numerical model would be correct. It is entirely plausible that this is the case since the depth etch is a timed etch with a rate of 1.08 μm/min, and the total etch depth was 650 μm.

3.4.1 Design performance compared to the functional requirements

Table 3.12 summarizes how the two-coupon system's performance compared to the performance dictated by the functional requirements.

3.4.2 Summary and Improvement Opportunities

This chapter presented a two-coupon system which was successfully used to measure the contact resistance in flat-on-flat contacts. The design of this system utilized a macro-scale alignment technique, the kinematic coupling, to achieve excellent posi-

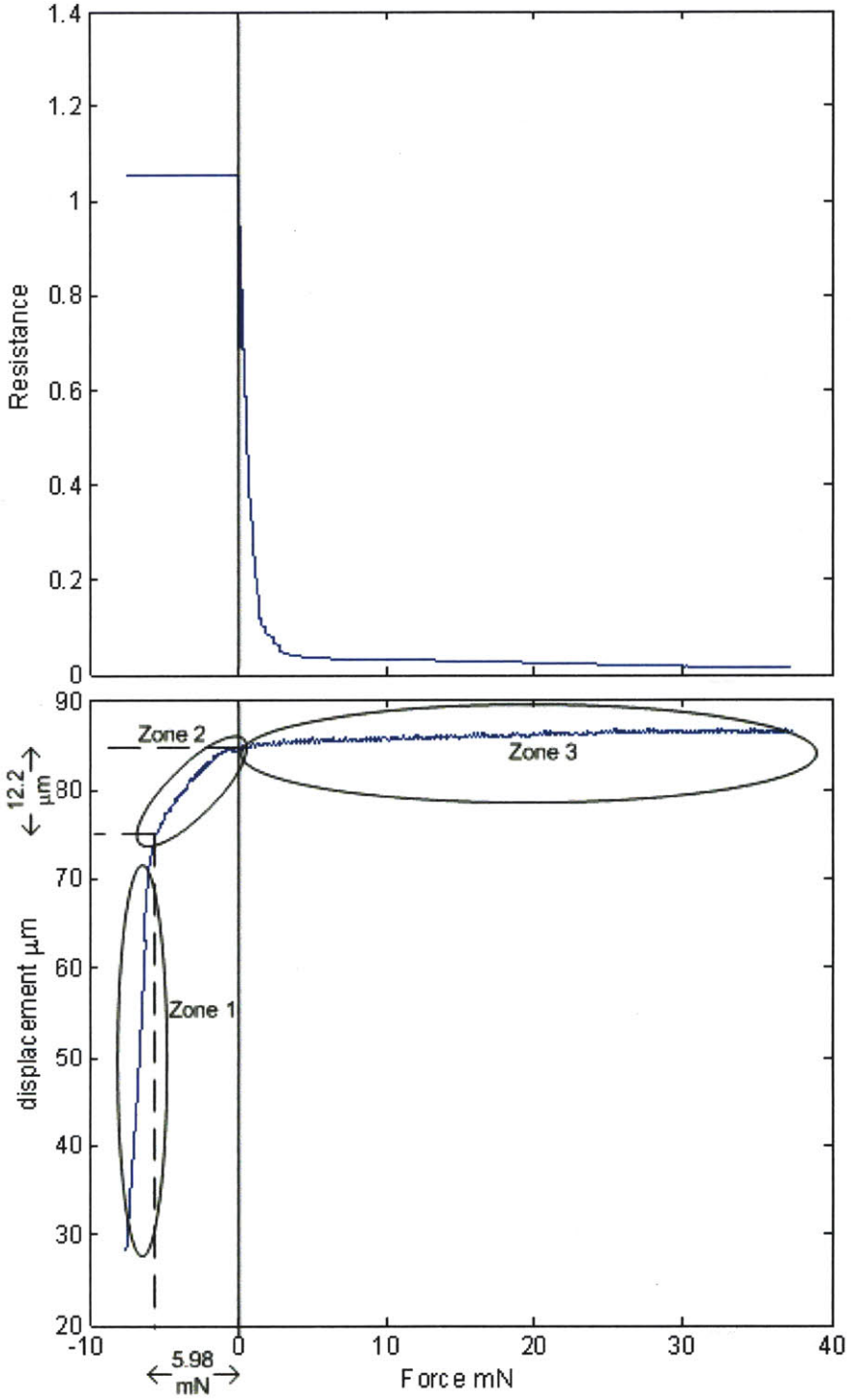

Figure 3-32: A representative relationship between force, contact resistance, and probe displacement.

Functional Requirement	**Performance of 1st generation two-coupon system**
Measure contact resistance in the mΩ range .	Achieved.
Measure contact force in the 100 μN.	Coupon achieved, instrumentation lacking.
Bring contacts together in a parallel manner.	Achieved parallelism standard deviation of 0.28 mrad and maximum of 0.59 mrad.
Measure multiple cycles.	Achieved.
Assembly/disassembly repeatability better than 1μm.	Not achieved. Repeatability was 3.08 μm in the worst direction
Allow for the observation of the physical changes to the contact between cycles using metrology including, but not limited to, the SEM and AFM.	Achieved.
Use no more than 50 mN of force (to comply with OSU test setup)	Achieved using 5.98 mN of force.
No more than 10μm of displacement (to comply with OSU test setup)	Not achieved. Contact gap could be up to 19.5 μm.

Table 3.12: The performance of the 1st generation two-coupon system compared to its original functional requirements..

tional repeatability after disassembly and reassembly. Multiple opportunities for improvement were found in this initial design. These are all issues which are addressed in the subsequent versions of the two-coupon system.

The first design opportunity is that using boiling phosphoric acid to remove the nitride from the wafers resulted in a very poor yield. The alternative process involved handling large quantities of 49% HF which can be quite dangerous and expensive. An improvement to the design would be using an oxide mask instead. Since silicon to thermally grown oxide interfaces are not attacked by KOH solution, as nitride to silicon interfaces are, this would also create more control over the pit etch. One downside to making this switch is that oxide does etch in KOH, albeit very slowly, so the mask would wear away during a long etch.

The second design opportunity is with the KOH-etched membrane. Patterning and etching a KOH membrane is a very laborious process. Unlike the pits, there is no reason to have sloped walls for the membrane. Another etch process, such as deep reactive ion etching, could be used instead. This uses photoresist as a mask, so it is

a much simpler process.

The third design opportunity is that the XY translational repeatability goal of 1 μm was not met.

The fourth design opportunity is the wiring. Wiring to the top coupon is very, very difficult. Subsequent versions of the two-coupon system have the metal traces run through the balls so that all wiring can be done to the bottom coupon.

The fifth design opportunity is the balls themselves. Having to put the balls in and out of the KOH-etched pits whenever the coupons are assembled and disassembled allows contaminants to get on the balls, which can negatively affect the alignment repeatability of the system. It is also very difficult for anyone using the system to handle the balls, which are only 794 μm in diameter.

There was an additional problem which did not have to do with the design. That was that the Tribometer used to do the testing was incapable of syncing resistance measurements with force and displacement measurements. Additionally, the force resolution on the Tribometer was far less than was desired. Therefore, specialized instrumentation was created which is described in Chapter 6.

Chapter 4

Pyramid/Pit Two-Coupon System

List of Symbols	
a	Membrane radius
b	Stiff cylindrical boss radius or width of a flexure
D_{cp-min}	Minimum distance between the center of the coupons and a pyramid/pit interface
D_{p-min}	Minimum distance between two pyramid/pit interfaces
δ	Probe displacement
$\delta_{SF=3}$	Membrane displacement when actual stress is one-third of the yield stress
e_g	Difference between measured gap and design gap
e_ϕ	Parallelism error
e_{theta}	Rotational error
e_x	Translational error in the x-direction
e_y	Translational error in the y-direction
$e_X Y$	Generalized Translational error
E	Young's Modulus
F	Force
$g_x 1$	Distance between target and x1-capacitance probe
$\bar{g_x} 1$	Average distance between target and x1-capacitance probe
$g_x 2$	Distance between target and x2-capacitance probe

continued from previous page

List of Symbols	
$\bar{g_x 2}$	Average distance between target and x2-capacitance probe
g_y	Distance between target and y-capacitance probe
$\bar{g_y}$	Average distance between target and y-capacitance probe
G	Actual Gap
G_i	Design Gap
$\bar{G}$	Average of the gaps at each of the ball/pit interfaces. Taken to be the actual gap
G_{max}	Maximum gap at each of the three ball/pit interfaces
G_{min}	Minimum gap at each of the three ball/pit interfaces
$H_{pyramid}$	Height of a KOH-etched pyramid
k	Stiffness of the membrane
$k_{lateral}$	Stiffness of the arms in-plane with the coupon
$k_{outofplane}$	Stiffness of the arms out-of-plane with the coupon
L	Length of the arms
σ_{max}	Maximum stress seen by the membrane
σ_y	Yield stress
t	Flexure thickness
t_{metal}	Metalization thickness
W	Nominal pit width
W_{max}	The longer of the two sides of a single pit
$W_{max-min}$	The difference in lengths of the two sides of a single pit
W_{min}	The shorter of the two sides of a single pit

This chapter presents the pyramid/pit two coupon system. This system improves upon the kinematic coupling two-coupon system presented in Chapter 3. It uses an elastic averaging alignment mechanism to improve repeatability. It also integrates the Kelvin structure with the assembly mechanism allowing for all wiring to be done to the bottom coupon. This chapter details the design, fabrication, error budget, and

testing of the pyramid/pit two-coupon system.

4.1 Design

The following functional requirements were used to design the next generation of the two-coupon system. These functional requirements were retained from the original design functional requirements:

1. Measure contact resistance in the mΩ range.
2. Measure contact force in the 100 μN range.
3. Bring contacts together in a parallel manner.
4. Measure multiple cycles.
5. Assembly/disassembly repeatability better than 1 μm.
6. Allow for the observation of the physical changes to the contact between cycles using metrology including, but not limited to, the SEM and AFM.

New instrumentation was used for the second generation coupons which allowed for a total of 100 mN of force and 50 μm of displacement. Therefore the following two functional requirements were adjusted in accordance with the capabilities of the new instrumentation:

7. Use no more than 50 mN of force to deflect membrane.
8. Use no more than 25 μm of displacement to deflect membrane.

The following new functional requirements were added to address design opportunities discovered in the first design:

9. Robust fabrication process which would not have the significant yield loss seen during the hot phosphoric acid step in the first process.
10. Membrane fabrication which would not use a KOH-etch.

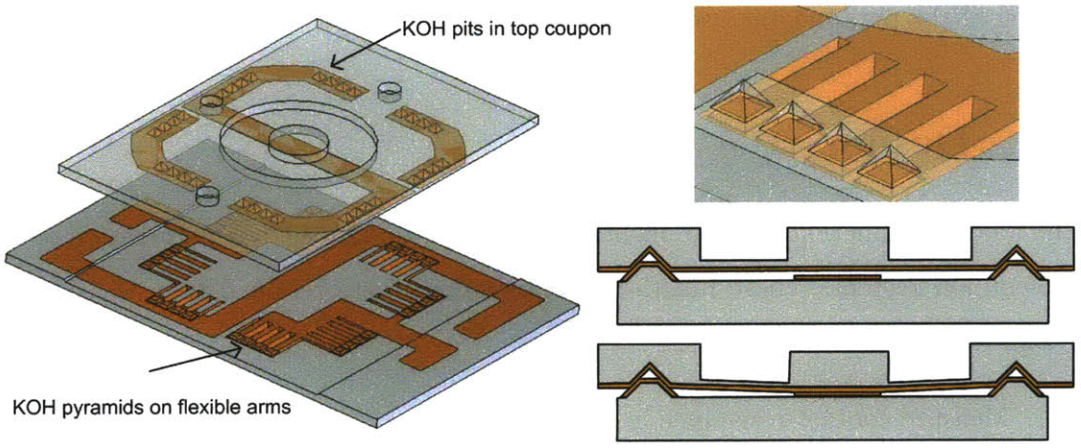

Figure 4-1: The elastic averaging two-coupon system.

11. No wiring to the top coupon.

12. No ball handling.

These functional requirements were achieved using an elastic averaging two-coupon system. This system is comprised of a bottom silicon coupon having 32 KOH-etched pyramids and a top silicon coupon having 32 KOH-etched pits on flexible arms. The bottom coupon is 21x32 mm and the top coupon is 19x27 mm. The pits and pyramids mate with each other,which also creates a gap between the top and bottom metal traces. The flexibility of the arms creates an elastic averaging positioning system, which has been shown to have very repeatable positioning in the macro scale [2]. This particular elastic averaging scheme is based on the one developed for wafer to wafer alignment [57]. A DRIE manufactured circular membrane with a stiff center cylindrical boss allows the two metal traces to come together. An SOI wafer is used for the top coupon with the device layer functioning as this membrane. The pits and pyramids are metalized allowing an integrated Kelvin structure to travel through the pit/pyramid interface, which allows all wiring to be done to the bottom coupon. The elastic averaging two-coupon system design is shown in Figure 4-1.

The elastic averaging system has three main modules: the pyramid/pit configuration, the membrane, and the integrated Kelvin structure. Each module will be discussed in the remainder of this section.

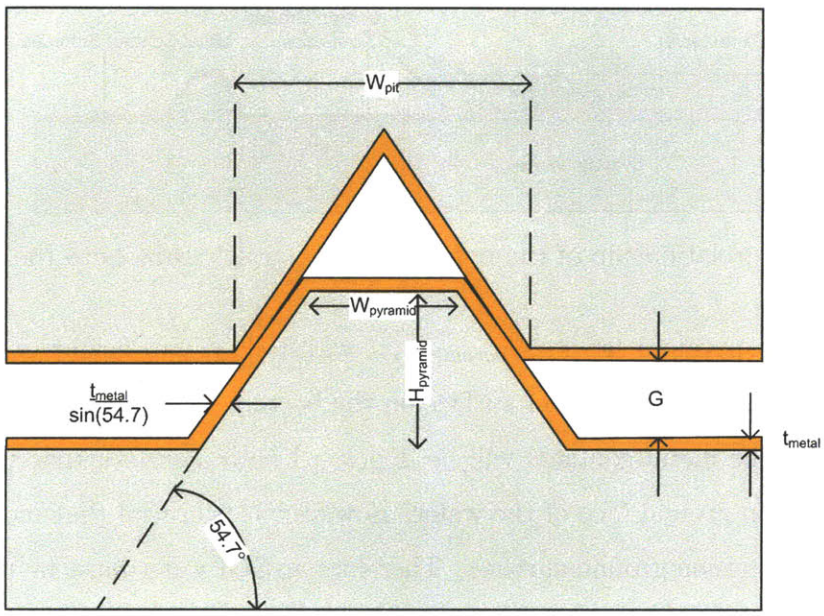

Figure 4-2: The geometry of the mating pyramids and pits.

4.1.1 Pyramid and Pit Configuration

The pyramid and pit configuration has three purposes purposes. The first is to align the top coupon to the bottom coupon, the second is to keep a gap between the top coupon and the bottom coupon, and the third is to provide an electrical path from the top coupon to the bottom coupon. The alignment mechanism works by having the pits cup the pyramids. The flexibility in the arms prevent the assembly from being over constrained. Since the new instrumentation allowed for a larger gap between the top and bottom metal traces, the target gap was set at 25 μm. The geometry for the pyramid was chosen to be a scaled down version of the pyramids used in a wafer to wafer alignment mechanism [63]. This particular geometry was chosen because it was proven to create convex cornered pyramids in a KOH-etch. The dimensions for the KOH-etched pits which would leave a 25 μm gap between the coupons was calculated from their geometry. This geometry also accounted for the micron of gold sputtered onto the pyramids and pits which created the electrical path between them. This geometry is shown in Figure 4-2.

Figure 4-2 displays the pyramid width, $W_{pyramid}$, defined as the width at the top

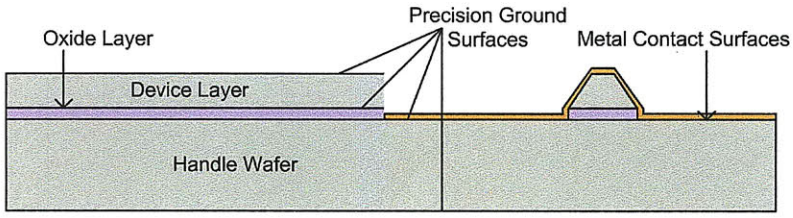

Figure 4-3: The relationship of the pyramids and contact surfaces to the SOI wafer.

of the pyramid; pyramid height $H_{pyramid}$; pit width W_{pit}, gap height G, and metal thickness t_{metal}. Since the contact surface on the bottom coupon is below the tops of the pyramids, the metal contacts will be deposited onto a surface that was not the original precision ground face of the wafer. However, it is crucial that metal only be deposited on precision ground surfaces. Therefore an SOI wafer must be used for the bottom coupon. An SOI wafer, or silicon on insulator wafer, consists of a thick silicon handle wafer, a thin layer of oxide, and a thin silicon device layer. By etching the pyramids in the device layer, and then removing the oxide, the contact material can be deposited onto the precision ground surface of the silicon handle wafer, as shown in Figure 4-3. This is discussed in more detail in Section 4.2

Using an SOI wafer limits the options one has for deciding the pyramid height. A large pyramid height is desirable because it offers the largest amount of contact area which improves alignment and also provides greater resistance to lateral forces or moments. The largest standard device layer available on an SOI wafer was 150 μm therefore this was chosen as the pyramid height. The pattern used for the KOH mask to create these pyramids required a 3.57 ratio between pyramid width and pyramid height. Therefore, the pyramid width was chosen as 536 μm. A typical metalization height is 1 μm. The desired gap between top and bottom coupons was 25 μm. Pit width as a function of the other geometries is define as:

$$W_{pit} = W_{pyramid} + \frac{2}{tan(54.7)}(H_{pyramid} - G - 2t_{metal}) + \frac{4t_{metal}}{sin(54.7)} \qquad (4.1)$$

which determines the pit width should be 679 μm to achieve a gap of 25 μm.

The elastic averaging concept requires compliance be built into the device to prevent over constraining. This particular design has 32 pits on 32 flexible arms

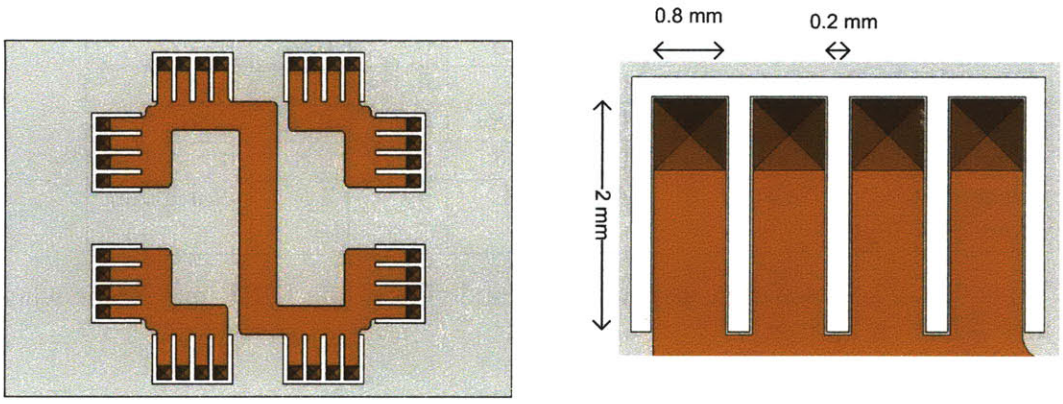

Figure 4-4: The geometry of the flexible arms on which the pits are located. The thickness of the arms is the thickness of the wafer, about 670 μm

which mate with 32 fixed pyramids. The compliance comes from the arms. They are compliant in both the lateral and out of plane directions. Figure 4-4 shows the geometry of these flexible members.

In order to determine how compliant the arms were, the stiffness of the arm in the lateral and out of plane directions are calculated based on simple beam theory.

$$k_{lateral} = \frac{Etb^3}{4L^3} \tag{4.2}$$

$$k_{outofplane} = \frac{Ebt^3}{4L^3} \tag{4.3}$$

The lateral stiffness, $k_{lateral}$, is 1.6 mN/nm and the out of plane stiffness, $k_{outofplane}$, is 1.1 mN/nm. Any misalignment would likely be do to lithography errors, which previously in this chapter were calculated to be on the order of 1 nm. Therefore only a few mN of force will be acting on the arms when compensating for lithography errors. This compliance could also cause deformations in the center of the coupon. The net vertical forces which will be acting on these coupons will be on the order of 50 mN which will be distributed amongst each of the 32 arms, for about 1.6 mN/arm. Therefore even at full load, the whole coupon will deform only 1-2 nm.

Analysis Method	FEM	FEM	FEM	FEM	Numerical
Center Offset (mm)	0	0.5	0	0.5	0
Force Angle (°)	0	0	5	5	0
Stiffness @ 10 mN (mN/μm)	0.90	0.80	0.90	0.80	0.88
Tilt @ 10 mN (mrad)	0	0.8	0	0.8	0
Displacement @ Safety Factor = 3 (μm)	48	44	49	44	Not given

Table 4.2: The calculated displacements and tilts of the DRIE membrane when 10 mN of force is applied.

4.1.2 DRIE Membrane

The membrane was changed to a pattern that could be fabricated using a DRIE-etch and photo resist mask as opposed to a KOH-etch and nitride mask. It is a circular membrane 10.5 mm in diameter with a stiff cylindrical boss in the center. The stiff cylindrical boss is 4 mm in diameter and is as thick as the wafer. The membrane itself is 20 μm thick, the same as the first generation membrane. The size of the membrane was based on geometrical considerations and efforts to have the stiffness close to the 0.5-1 mN/μm stiffness of the first generation membrane. The stiffness of the membrane was modeled two ways: using FEM and using a numerical model.

The FEM model was used to test the deflection of the membrane under 10 mN of force. The effects of having a non zero force angle of 5° as well as the effects of a 0.5 mm positional offset were also considered. Force angle and positional offset are shown in Figure 3-6. The membrane deflections in each of these cases are shown in Figure 4-5.

In all cases, the modeled stiffness of the membrane was 0.8-0.9 mN/μm. The maximum rotational error seen in any case was 0.8 mrad. The deflection at 10 mN was 11-13 μm which is slightly larger than the actual gap size. The resulting stiffness, deflection at which point 1/3 of the yield stress is reached, and tilt seen by the membrane are recorded in Table 4.2.

The actual stiffness of the first generation membrane was much closer to the numerical model of that membrane than the FEM analysis. Therefore, the second generation membrane was also modeled using a numerical membrane model. The

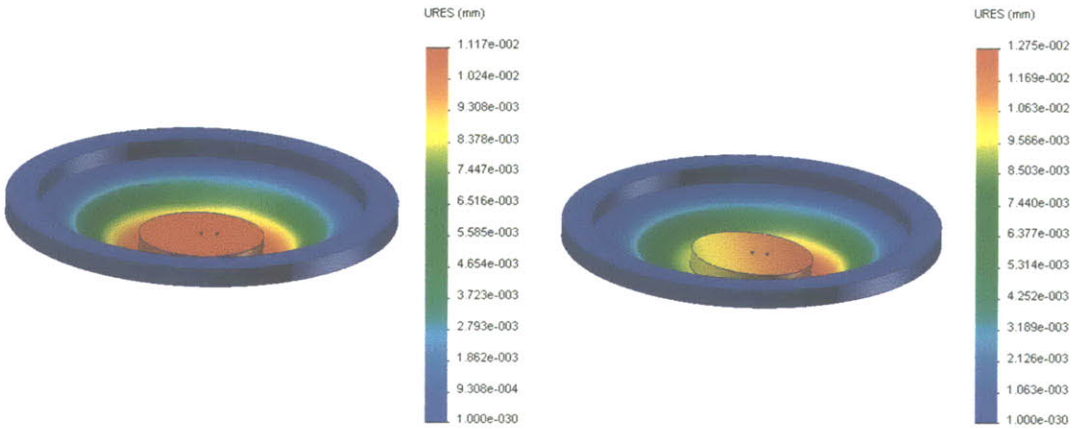

(a) 0 mm center offset; 0° force angle

(b) 0.5 mm center offset; 0° force angle

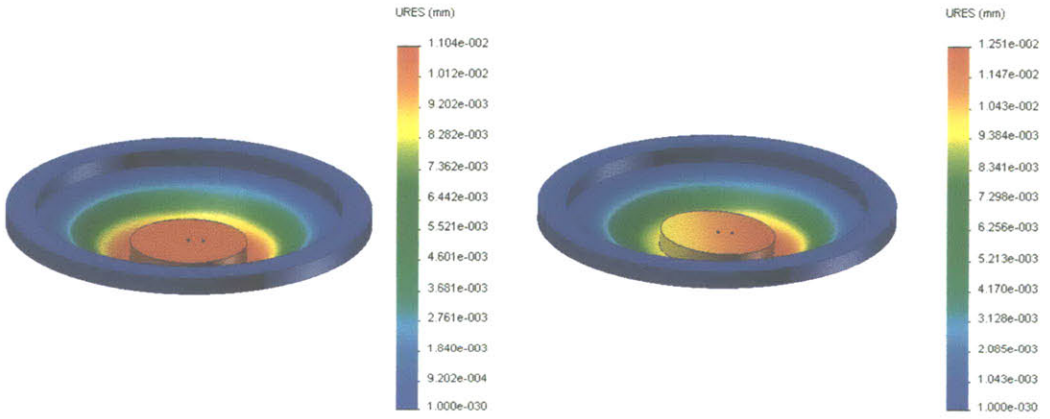

(c) 0 mm center offset; 5° force angle

(d) 0.5 mm center offset; 5° force angle

Figure 4-5: The FEM results for the DRIE-etched membrane when a force of 10 mN was applied. See Table 4.2.

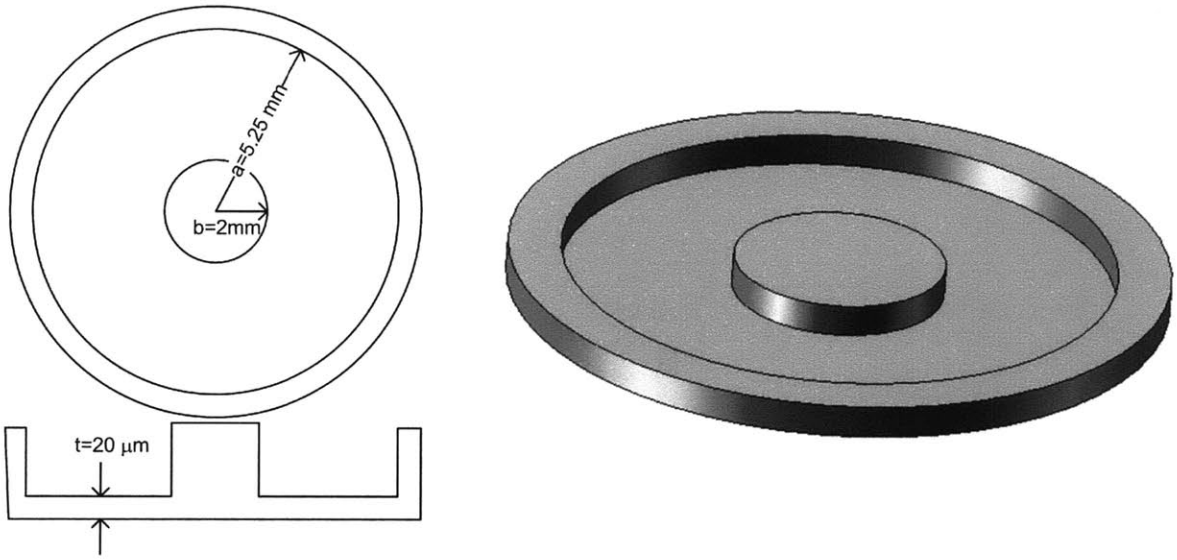

Figure 4-6: The membrane geometry used in the numerical model which is identical to the actual membrane geometry.

geometry for the numerical model is exactly that of the membrane design and is shown in Figure 4-6.

The displacement for the numerical model is given by Table 24, case 1f. of Roark's Formulas for Stress and Strain [47] as

$$
\begin{aligned}
\delta &= \frac{6Fa^3(1-\nu^2)}{\pi E t^3 b}\left(\frac{C_2 L_6}{C_5} - L_3\right) \qquad (4.4)\\
C_2 &= \frac{1}{4}[1-(b/a)^2(1+2\ln(a/b))]\\
L_6 &= \frac{b}{4a}[(b/a)^2 - 1 + 2\ln(a/b)]\\
C_5 &= \frac{1}{2}[1-(b/a)^2]\\
L_3 &= \frac{b}{4a}[((b/a)^2+1)\ln(a/b) + (b/a)^2 - 1]
\end{aligned}
$$

where δ is displacement of the membrane, F is the applied force, a is the outer radius of the membrane, b is the outer radius of the cylindrical boss, E is the Young's modulus of silicon, ν is the Poisson's ration of silicon, and t is the thickness of the

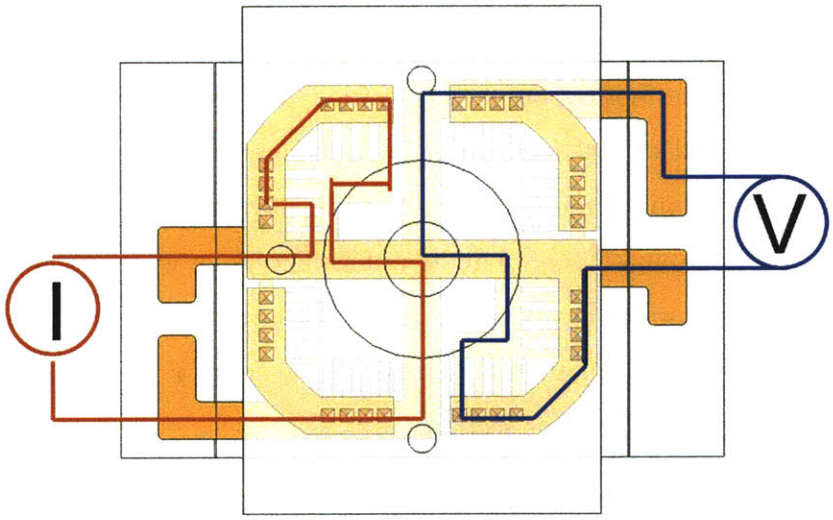

Figure 4-7: The integrated Kelvin structure in the pyramid/pit two-coupon system.

membrane.

This can be rearranged to solve for stiffness. The result is:

$$k = \frac{\pi E t^3 b}{6a^3(1-\nu^2)} \left(\frac{C_5}{C_2 L_6 - C_5 L_3} \right) \tag{4.5}$$

Substituting in all appropriate values, this numerical model gives a stiffness of 0.88 mN/μm. This is very close to the 0.90 mN/μm stiffness value found using the FEM. Remembering that the designed membrane deflection was 25 μm, it should take about 28 mN to deflect the membrane. The FEM model showed that the displacement at 1/3 of the yield stress was 44-49 μm. Therefore this membrane could accommodate a gap twice as large as the design gap and still have a maximum stress of only 1/3 its yield stress.

4.1.3 Kelvin Structure for the Pyramid/Pit Design

In order to avoid wiring to the top coupon, the integrated Kelvin structure was designed to make contact through the metalized pyramid/pit interfaces. This circuit is shown in Figure 4-7.

4.2 Fabrication

This section details the fabrication of the pyramid/pit design. The top and bottom coupons are fabricated on different wafers using different masks. The wafer which will comprise the bottom coupons is an SOI wafer having a 150 μm device layer, 2 μm BOX (oxide) later, and 520 μm handle wafer. The wafer which will comprise the top coupon is an SOI wafer having a 20 μm device layer, 2 μm BOX (oxide) later, and 650 μm handle wafer. Figure 4-8 displays a flow chart of the eleven fabrication steps. Each step is detailed in this section.

Step 1: DRIE Alignment Marks

This step is identical to the first step of the fabrication of the first generation ball/pit design. The first step in fabrication is placing alignment marks on the wafers. This step is identical for both top and bottom coupon wafers. The wafers are coated with HDMS to improve the adhesion of photo resist. The wafers are coated with 2 μm of thin positive resist which is then patterned using standard lithography methods. The wafers are then etched in the STS deep reactive ion etcher (DRIE) using SF_6 plasma for thirty seconds. This etches the alignment mark pattern about 1 micron into the surface of the wafer. Afterwards, the wafers are placed in an oxide asher to remove any residual Teflon from the DRIE process. The wafers are then stripped of photo resist. The result is two alignment marks whose structure and location on the wafer are shown in Figure 3-10.

Step 2: Nitride Deposition and Nitride Etch

This section describes the patterning of the nitride which acts as a mask for the subsequent KOH-etches in both the top and bottom coupons. Nitride is deposited on the both the top and bottom coupon wafers using low pressure chemical vapor deposition. 4000 Å of nitride, Si_3N_4, is grown on the wafer. This nitride is used as a mask in the KOH-etching of the pits. The nitride is deposited through a chemical reaction between DichlorSilan, $SiCl_2H_2$, and ammonia, NH_3, at a temperature of 775°

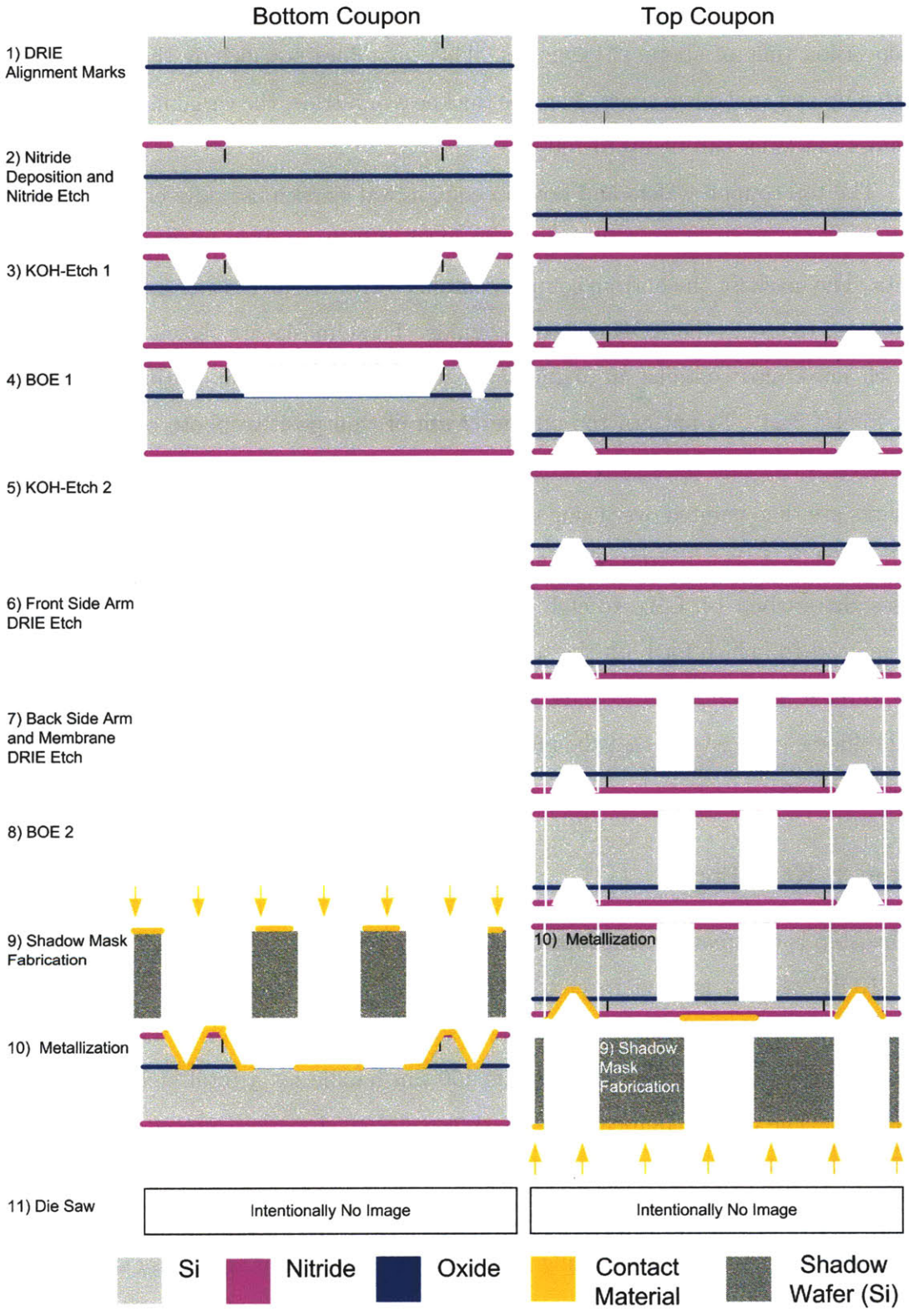

Figure 4-8: The fabrication process for the pyramid/pit two-coupon system.

C and a pressure of 220 mTorr. The deposition rate is about 23 Å/min for a total deposition time of about 174 minutes. This time does not include the temperature ramp up and cool down times. For this thickness of nitride, the variability of thickness across the wafer can be up to 100 Å.

The top coupon wafers and bottom coupon wafers each use different masks. The mask for the top coupon contains circles which will be used to etch the KOH-etched pits. The mask for the bottom coupon contains corner compensating structures which are used to create the KOH-etched pyramids. These masks are shown in Figure 4-9. Each mask also contains an alignment feature. The alignment features are shown in Figure 3-11. To pattern the nitride, 2 μm of thin positive photo resist are spun onto the wafer and patterned using standard lithography techniques. The alignment marks are then painted over using red resist to prevent them from being etched away. The nitride is then patterned using an AME 5000, a radio frequency etcher which uses Halocarbon 14, CH_4, to etch nitride . The etch rate is dependent on the area being etched, which for both the top and bottom masks is about 37 Å/s. Therefore, this etch takes about 108 seconds. The wafers are then measured optically and using a profilometer to ensure that the nitride has completely cleared. The photo resist was then stripped.

Step 3: KOH-Etch 1

This step is different for the bottom and top coupons.

KOH solution is used to etch pyramids on the bottom coupon. The bottom wafers are both placed in 80°C 30% KOH solution. The silicon etch rate is 1.08 μm/ min. The silicon is etched through the 150 μm handle for a total etch time of 139 minutes. The corner compensating mask was designed so that after etching for this period of time, the pyramids would be fully formed. Under etching the pyramids can leave structurers on the corners of the pyramids. These would interfere with the pyramid/pit mating. Over etching the pyramids reduces the amount of surface area on the pyramids and would eventually etch away the pyramids completely. Under etchedand properly etched pyramid structures are shown in Figure 4-10.

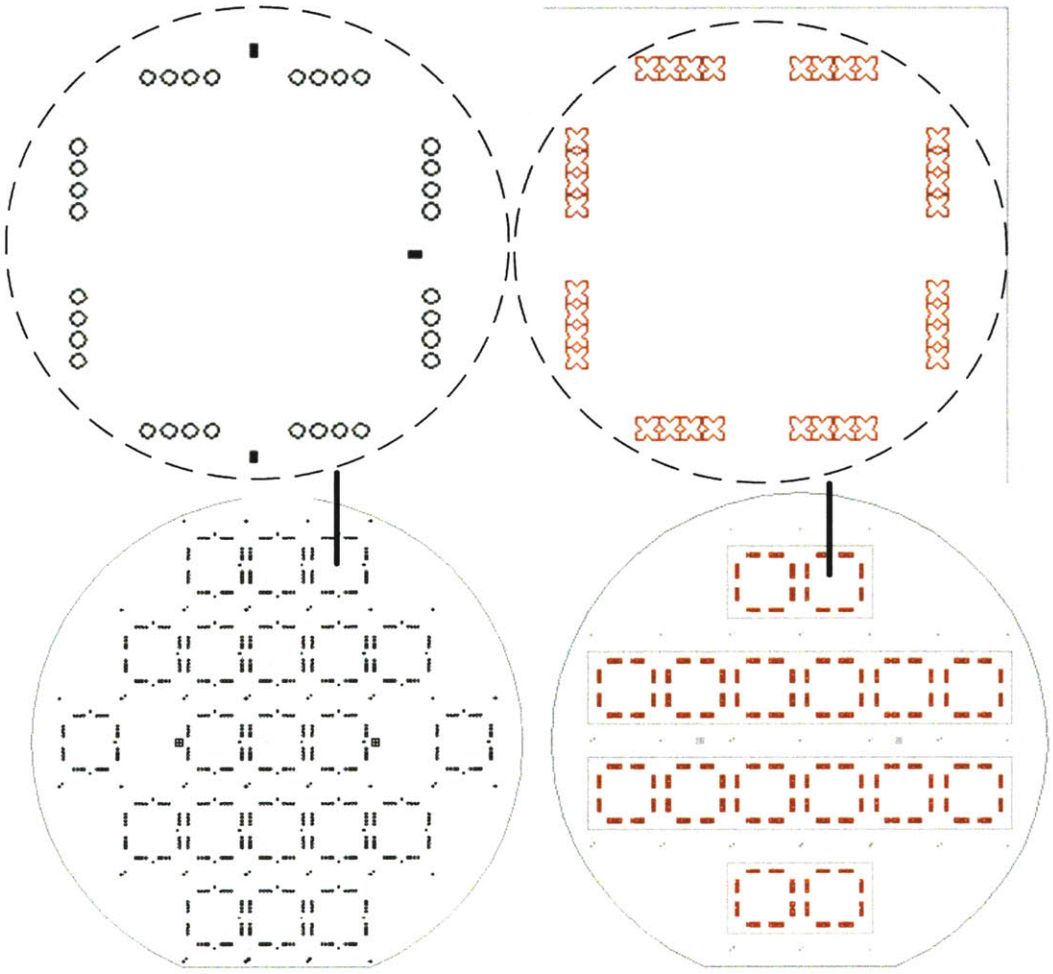

Figure 4-9: Left: The top coupon wafer mask which forms the KOH-etched pits. Right: The bottom coupon wafer mask which forms the KOH-etched pyramids.

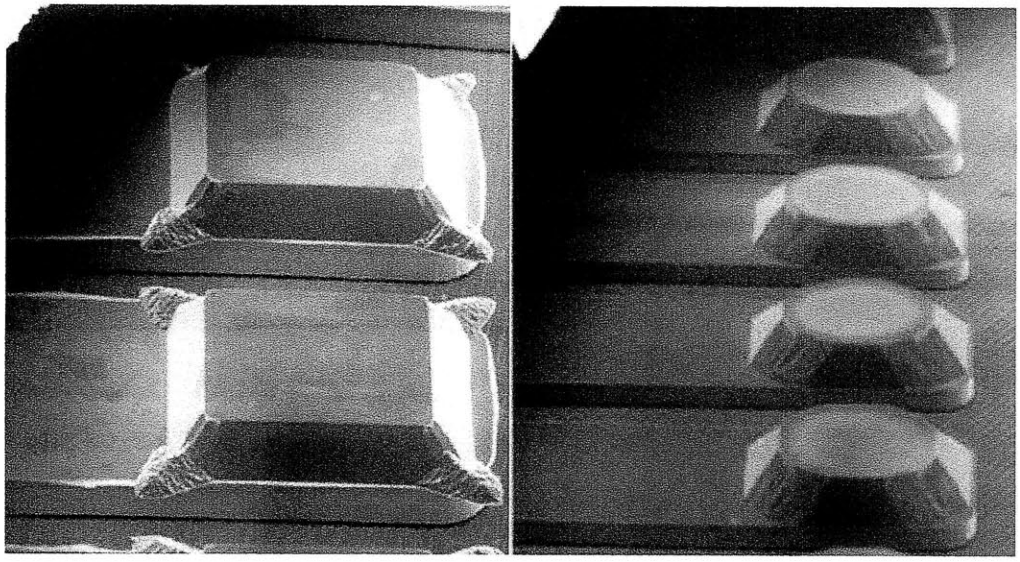

Figure 4-10: Left: Under etched pyramid features. Right: Properly etched pyramid features. Images from [63].

KOH solution is used to etch the pits on the top coupon. The top wafers were placed in 80°C 30% KOH solution. The silicon etch rate is 1.08 μm/min. The silicon was etched through the 20 μm handle for a total etch time of 18.5 minutes. At this point, the BOX (oxide) layer was reached, as shown in the flow chart in Figure 4-8. Since KOH etches oxide extremely slowly, the oxide had to be removed by other means so the wafers are removed from the KOH solution.

After the KOH etch, the both the top and bottom coupon wafers were cleaned by performing two ten-minute piranha cleans and one thirty-second 50:1 HF dip.

Step 4: BOE 1

After the first KOH etch, both the top and bottom coupon wafers need a buffered oxide etch (BOE), but for different reasons. In the bottom coupon wafers, this is done so that the contact material can be deposited directly onto the ground silicon surface of the handle wafer, as is shown in Figure 4-3. In the top coupon wafers, this is done to remove the oxide preventing the remainder of the KOH-etched pits from being etched.

Both the top and bottom coupon wafers are placed in 32°C 6:1 BOE. The etch

rate is approximately 0.1 μm/min, so the etch lasted 20 minutes.

Step 5: KOH-etch 2

This step is only performed on the top coupon wafers. After the BOE removes the oxide layer inside the partially KOH-etched pits, the top coupon wafers are returned to the KOH bath so the remainder of the pits can be etched. A total depth of at least 140 μm has to be achieved to allow the pyramids to fully mate. However, the pits were etched to 200 μm to allow any particles to be pushed into the bottoms of the pits and not interfere with mating. Therefore, after the BOE, an additional 180 μm of silicon had to be etched. This required an additional 167 minutes in the KOH solution. After the KOH etch, the wafers were cleaned by performing two ten-minute piranha cleans and one thirty-second 50:1 HF dip.

It was important to remove the nitride from the top coupons since the circular overhangs would interfere with the mating of the pyramids and pits. These circular nitride overhangs are shown in Figure 3-12. However, after the KOH/BOE/KOH cleaning processes, the wafers were observed under a microscope and it was noted that all of the overhangs had fallen off. Since using hot phosphoric acid to remove the rest of the nitride would probably have damaged the wafers, this step was skipped and the nitride was left on the surface of the wafer. Likewise, the nitride was not stripped from the top of the pyramids on the bottom coupon wafers. This is because the original process, hot phosphoric acid nitride etch, led to low wafer yield and the alternative process, 49% HF, would attack the oxide under the pyramids and cause them to dislodge from the wafer.

Step 6: Front Side Arm DRIE Etch

This step is performed only on the top coupon wafers. On the top coupon wafers, each of the KOH-etched pits is on the end of a flexible arm, as shown in Figure 4-4. This arm is released using a STS DRIE tool to etch the silicon surrounding it. This requires etching through both the device layer of silicon, the handle layer of silicon, and the oxide layer between them. This step etches through the device layer. The top

coupon wafers are coated with 2 μm of thin positive resist which is then patterned using standard lithography techniques. The mask used is shown in Figure 4-11. The alignment marks are painted over with red resist. The wafers are then placed in the DRIE tool. Two gases, SF_6 and CH_4 are alternated. The SF_6 flows for twelve seconds which etches the silicon, as well as the thin nitride layer which was never removed. The CH_4 is then used for eight seconds as a passivation gas to coat the sidewalls of the etch allowing the sidewalls to remain vertical. This cycle is repeated for approximately eight minutes at which point the entire device layer is etched through and the BOX layer has been reached. This chemistry etches oxide very slowly, so at this point the wafer is removed from the STS. Afterwards, the wafers are placed in an oxide asher to remove any residual Teflon from the DRIE process. Finally, the photo resist stripped.

Step 7: Back Side Arm and Membrane DRIE Etch

This step is performed only on the top coupon wafers. Since both the flexible arms and the membranes need to etch through the handle wafer using a DRIE, these etches are performed at the same time. First the backside of the wafer is coated with 15 μm of thick positive resist. The resist is exposed through the mask patterning the flexible arms, as shown in Figure 4-11. Prior to the resist being developed, the resist is exposed again through the mask patterning the flexible membranes, as shown in Figure 4-12. The wafers are then developed using normal lithography procedures. The wafers are then attached to a quartz backing wafer to prevent the wafer from breaking and falling into the DRIE chamber. Finally, the wafers are placed in the DRIE chamber, where again, SF_6 and CH_4 are used in 12 and 8 second increments to vertically etch through the silicon and the thin layer of nitride. At an etch rate of 2.5 μm/min, this took about 260 minutes. The etch stops when the handle wafer has been etched through and the oxide layer is reached. Afterwards, the wafers are placed in an oxide asher to remove any residual Teflon from the DRIE process. They are then soaked in acetone to remove the quartz backing wafer. The photo resist is stripped.

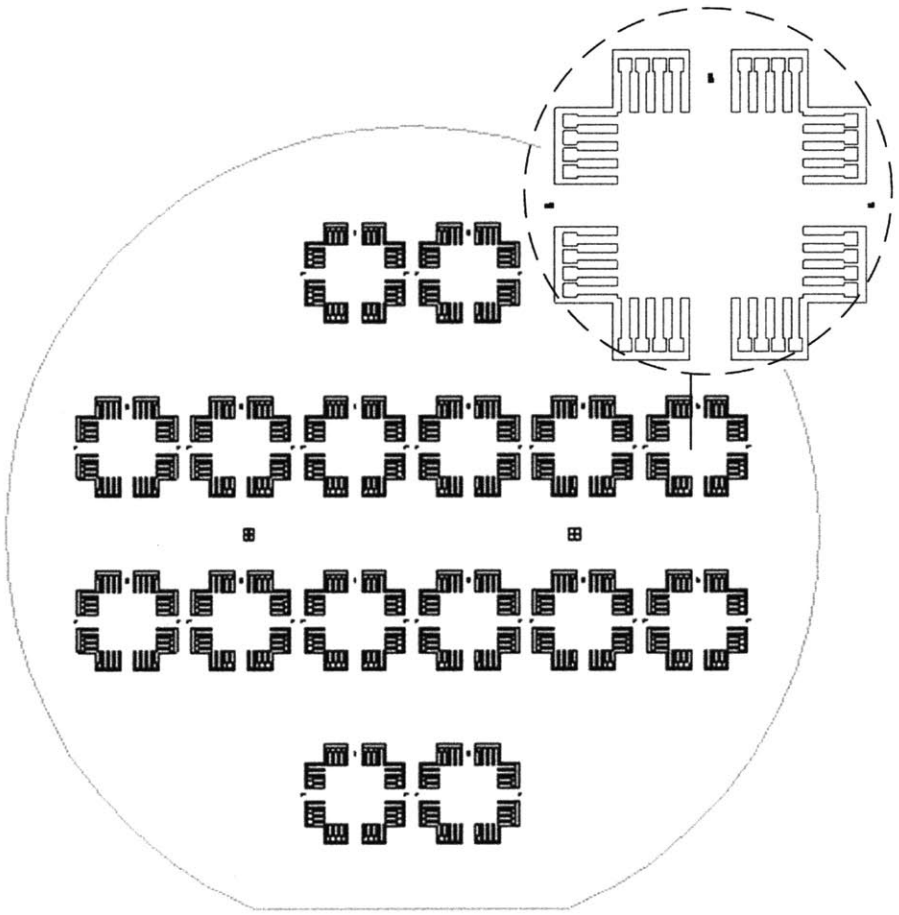

Figure 4-11: The mask used to release the flexible arms in the pyramid/pit design. The white areas are not etched and the black areas are etched. Each black line is actually 200 μm thick. The large areas around the flexible arms are released like dough cut with a cookie cutter after the thin lines have been etched through.

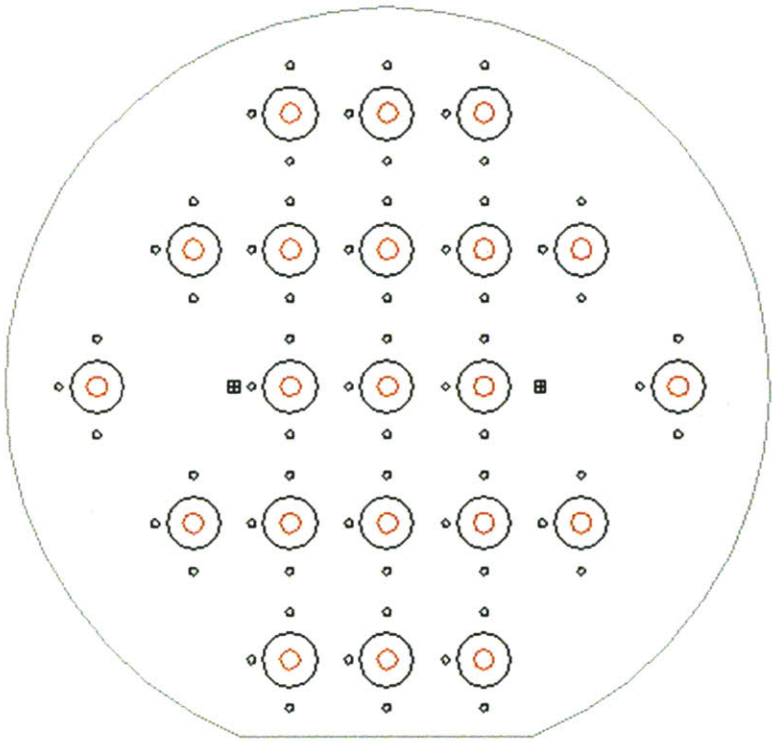

Figure 4-12: The mask which patterns the membranes in the pyramid/pit design as well as the final two-coupon design.

Step 8: BOE 2

This step is performed on only the top coupons. In order to remove the oxide layer from the top of the membrane as well as the oxide layer preventing the flexible arms from being released, the top coupon wafers are placed in 32° 6:1 BOE for 20 minutes which etches through the 2 μm BOX layer.

Step 9: Shadow Mask Fabrication

The metal traces on these coupons are evaporated through shadow masks, which are wafers that have been through-etched using a DRIE (deep reactive ion etcher). The particular shadow masks used in this design were haloed. This means instead of etching all of the area, only a 200 μm outline of each area is etched. The etched areas then fall out of the wafer like a sheet of dough cut with a cookie cutter. Since DRIE etch time is dependent on area, this also greatly reduced the amount of time it takes to etch through the shadow masks. There are different masks for the top and bottom coupons. In order to make these masks, two plain silicon wafers are coated with 15 μm of thick positive resist which is then patterned with the haloed shapes. The wafers are mounted to a quartz wafer using photo resist as a temporary glue. The quartz backing wafers prevent the cut out sections from falling into the DRIE chamber. These wafers are then etched in the DRIE. The etch rate is about 2.5 μm/min, which is fairly fast, because only the halos are being etched. Therefore, the total etch time was about 268 minutes. Afterwards, the device wafer and quartz wafer are soaked in acetone to remove the photo resist between them and allow the cut out shapes to float away. The result of this process is wafers with cutouts of the metal patterns for both the top and bottom coupon wafers. These patterns are shown in Figure 4-13.

Step 10: Metalization

Evaporation of metal through a shadow wafer is used to create the metal traces on the top and bottom coupons. The trace material is gold (Au). The shadow wafers

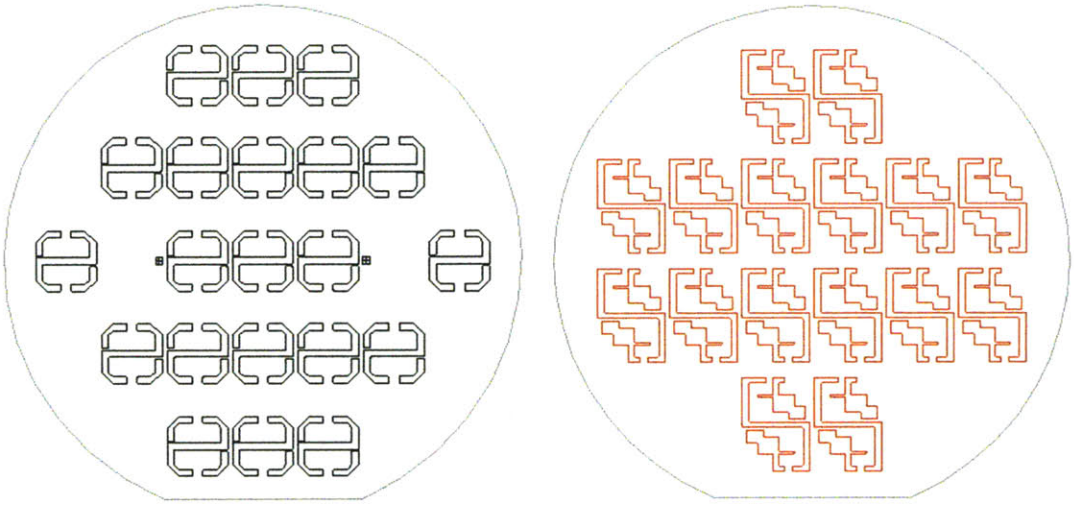

Figure 4-13: Left: The shadow mask used to deposit metal onto the top coupon wafers of the pyramid/pit design. Right: The shadow mask used to deposit metal onto the bottom coupon wafers of the pyramid/pit design.

are aligned to the top and bottom coupon wafers by aligning each of the wafer flats together. Small dabs of photo resist around the edges of the wafers are used to temporarily glue the device wafers to the shadow wafers. The wafers are then placed in an evaporative deposition system. 300 Å of Titanium (Ti) is evaporated through the shadow mask to act as an adhesion layer between the silicon and the gold. 7000 Å of gold is then evaporated through the shadow mask. The device wafers, along with the shadow masks, are then briefly soaked in acetone to dissolve the photo resist holding them together.

Step 11: Die Saw

Finally, the individual coupons are diced. The bottom coupons are simply attached to die saw tape and diced using conventional means. Since the top coupons contain a thin membrane, they cannot be placed under a vacuum. Therefore, they are attached to a dummy wafer, membrane side up, using Crystal Bond. They are then diced and soaked in acetone overnight to remove the crystal bond. Water at 80°C can also be used to instantaneously dissolve Crystal Bond. The completed dies are shown in

Figure 4-14. Each top coupon wafer contains 21 dies while each bottom coupon wafer contains 16 dies.

4.3 Position Error Analysis and Measurement

One of the important functional requirements of this two-coupon system is that it be able to be taken apart and put back together in a repeatable manner. This repeatability is limited by certain aspects of the system which are not entirely repeatable. There are four errors that can occur: gap height error, parallelism error, translational error, and rotational error. These errors are shown in Figure 4-15.

4.3.1 Gap Error

As shown in Figure 4-2, the height gap between the top and bottom coupons is dependent on the pyramid width and the pit width. This is true if these two are perfectly square. However, normally both the pit and pyramid are slightly rectangular. Therefore, at any pit/pyramid interface, the gap is determined by using the maximum pyramid width and the minimum pit width in Equation 4.1. Maximum pyramid width with the larger of the two widths of a single non-square pyramid. Minimum pit width is the smaller of the two widths of a single non-square pit.

The overall gap height will be maximum when all the pit/pyramid interfaces see the maximum possible gap. The overall gap height will be minimum when all of the pit/pyramid interfaces see the minimum possible gap. In order to determine these two extremes, the maximum width between the two sides of a single pyramid and the minimum width between two sides of single pyramid were measured. These lengths were measured on twenty different pyramids and twenty different pits. This raw data is shown in Figure 4-16. The statistics for this data are listed in Table 4.3.

The average, maximum, and minimum gap heights could then be determined by substituting the appropriate values for pyramid and pit width into Equation 4.1. These conditions and results are displayed in Table 4.4

The largest expected possible gap is 14.4 μm, the smallest expected possible gap

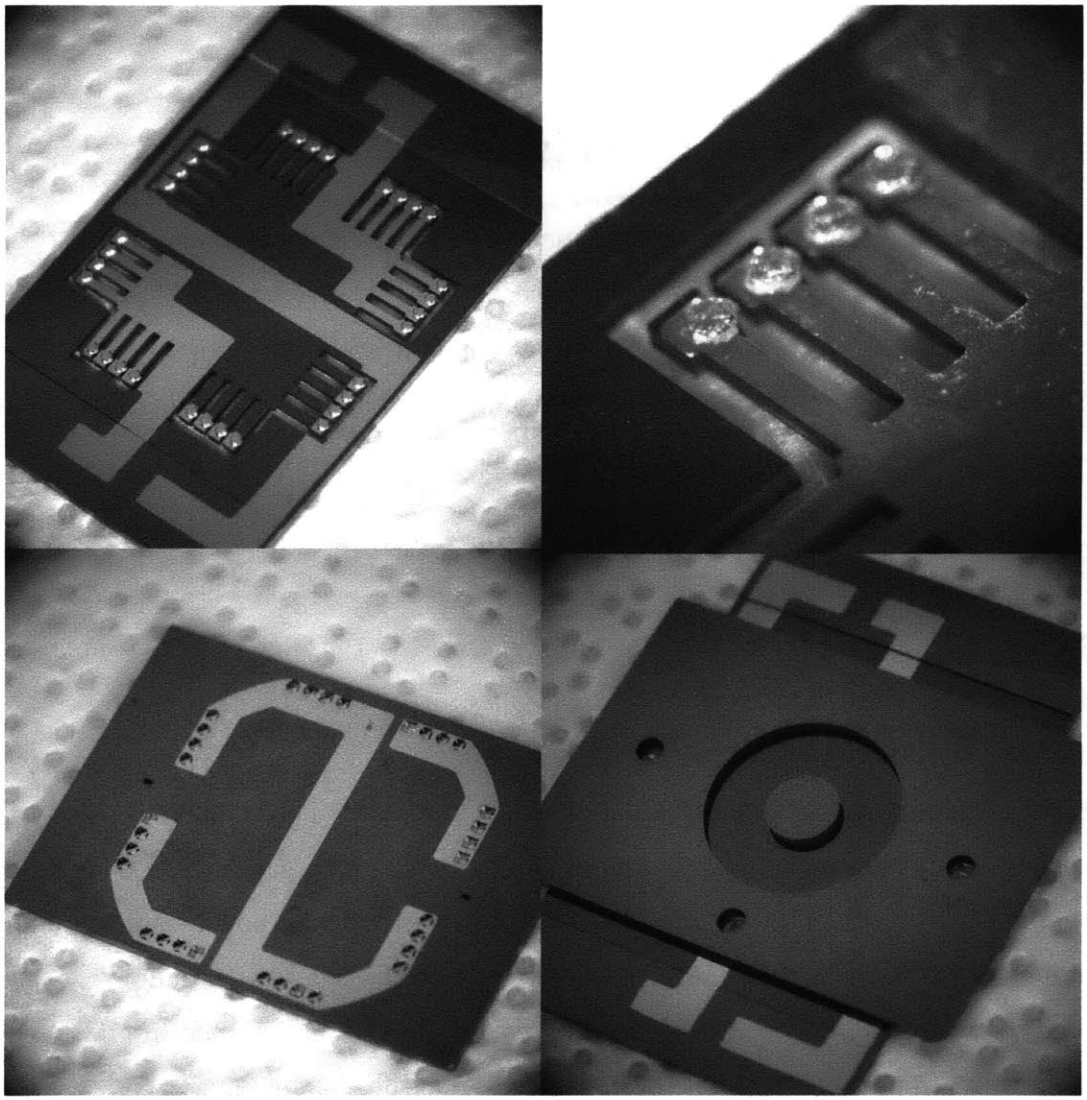

Figure 4-14: The assembled and disassembled pyramid/pit two-coupon system.

	Average μm	Standard Deviation μm	Maximum μm	Minimum μm
Maximum Pyramid Width	535.4	2.74	540.1	528.8
Minimum Pit Width	738.5	3.1	743.2	734.2

Table 4.3: The maximum pyramid widths and minimum pit widths

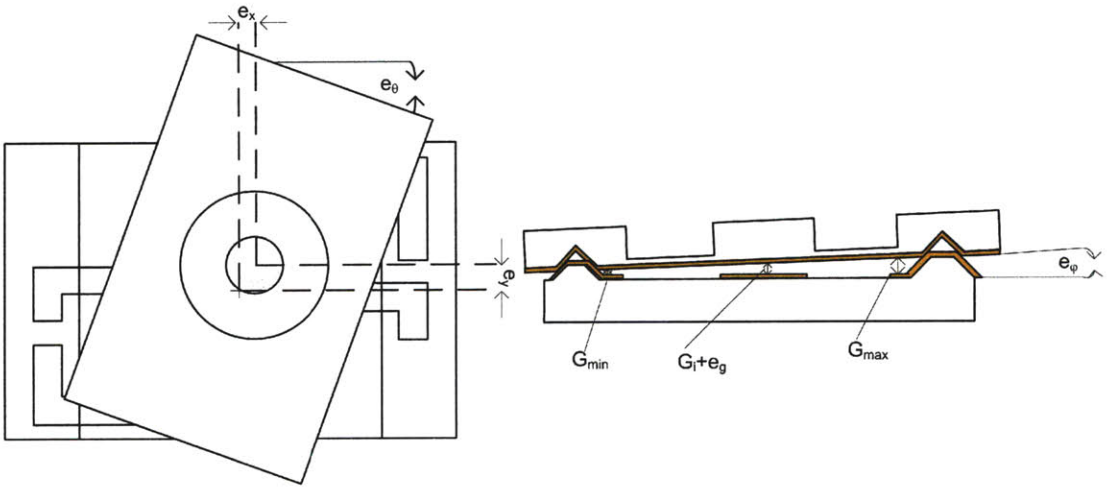

Figure 4-15: The four measurable errors of the pyramid/pit two-coupon system: translational, e_x and e_y
; rotational, e_θ; gap, e_g, and parallelism, e_ϕ.

	Average Gap	Maximum Gap	Minimum Gap
Maximum Pyramid Width μm	738.5	734.2	743.2
Minimum Pit Width μm	535.4	540.1	528.8
Gap Height G μm	8	14.4	0.1
Gap Error e_g μm	-17	-10.6	-24.1

Table 4.4: The conditions creating the average, maximum, and minimum gap.

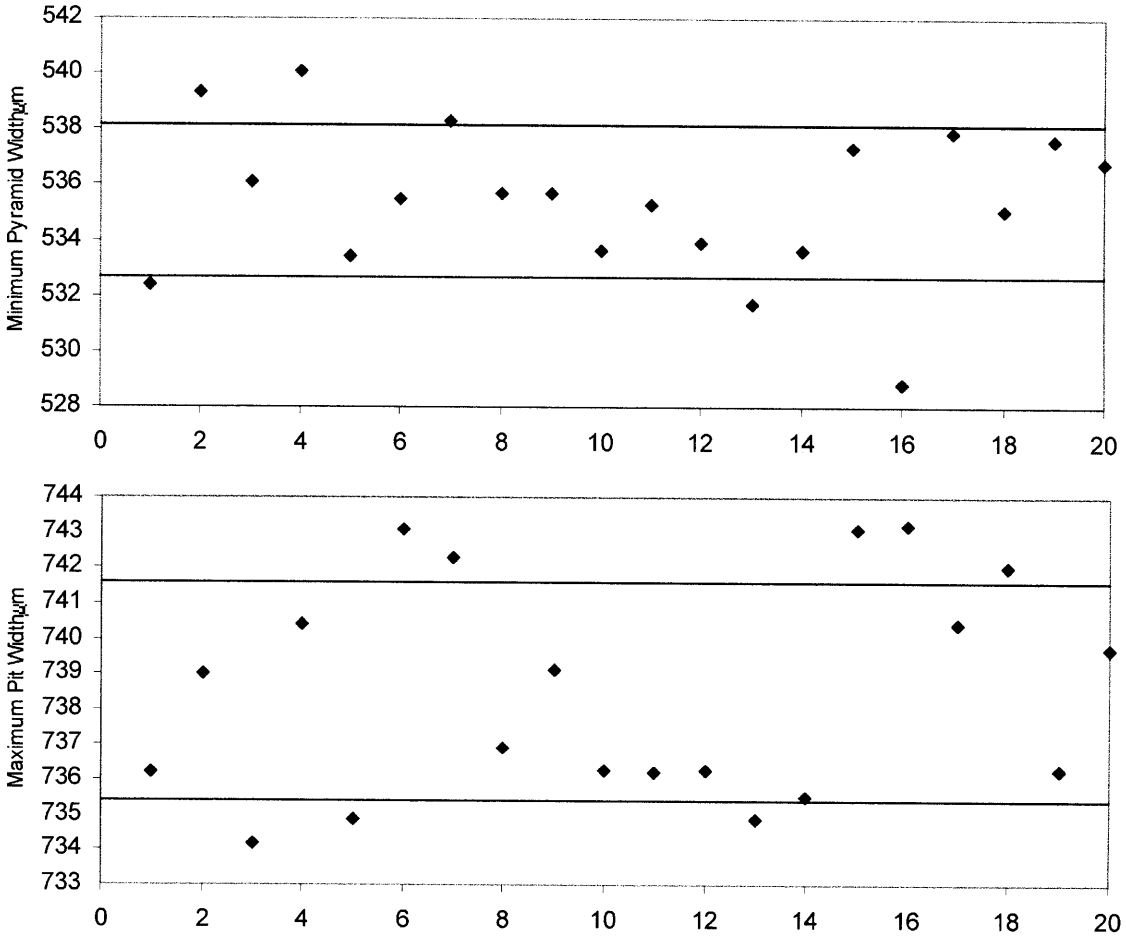

Figure 4-16: Maximum pyramid width and minimum pit width for twenty pyramids and pits.

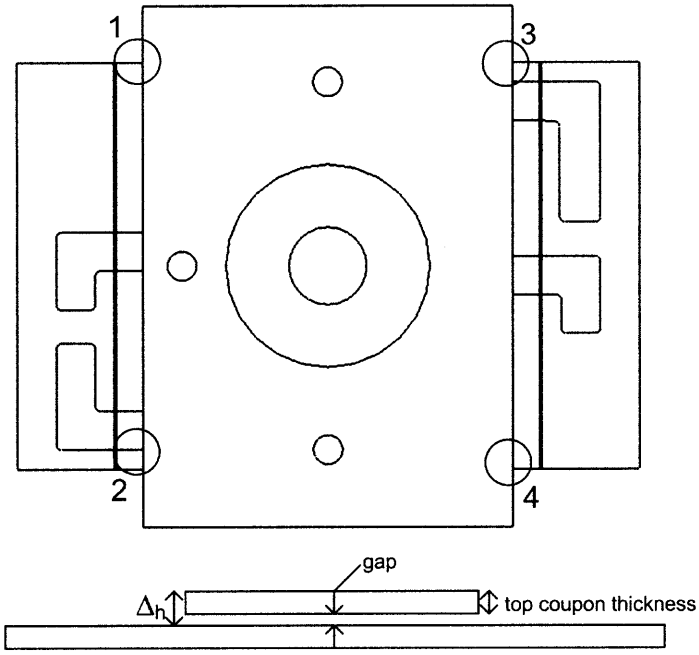

Figure 4-17: Gap height measurement locations.

is 0.1 μm, the average expected gap is 8 μm. This predicts how the gap will vary across different sets of coupons. It predicts that the same coupon can be assembled and disassembled with no change to gap height. It does not account for the coupons not settling all the way or particles interfering with the pyramid pit mating. An experiment was performed to see both how the gap height varied across different sets of coupons and also how gap height varied as a single set of coupons was assembled and disassembled. Gap height was measured at four areas on each assembled two-coupon system, as shown in Figure 4-17.

An optical microscope was focused on the top coupon, and then the bottom coupon, and the difference in focal lengths recorded. The thickness of the top coupon was then subtracted from the difference in focal lengths to arrive at the measured gap. The gap was taken to be the average gap measured at all four positions shown in Figure 4-17. The gap was measured for 10 different top and bottom coupon combinations. On three top and bottom coupon combinations, the coupons were assembled, measured, disassembled and remeasured five times each. The raw data for both the average gap of all ten coupon sets and the repeatability of the gap for the three

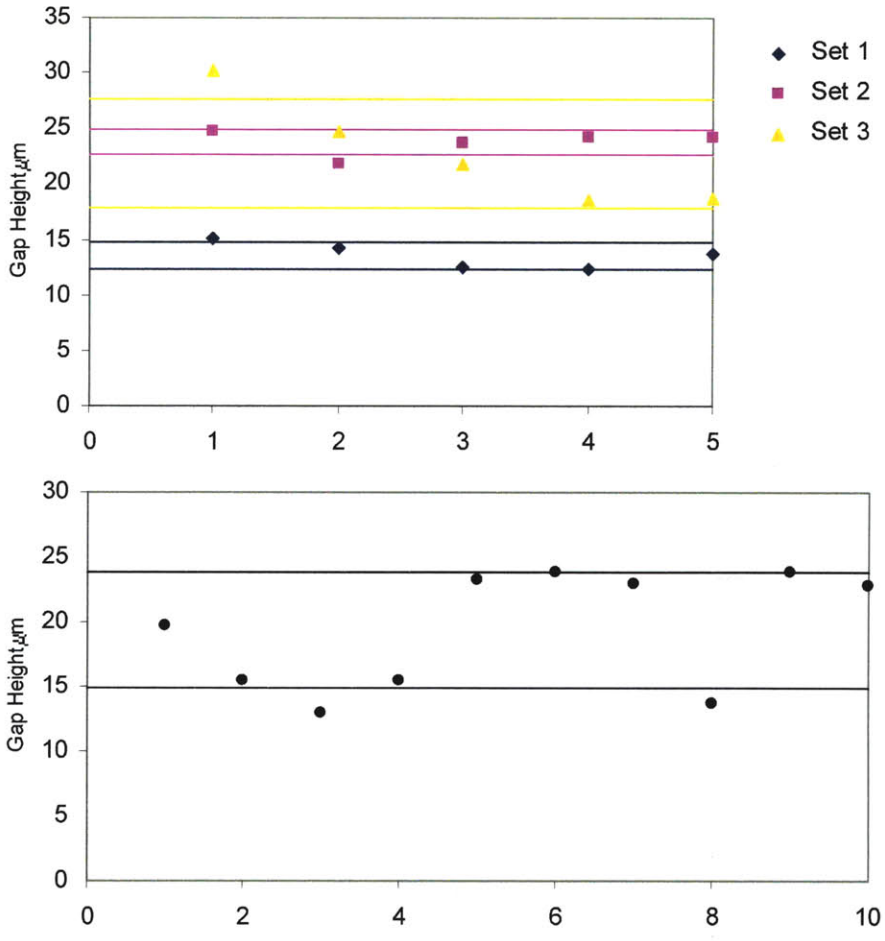

Figure 4-18: Gap heights raw data.

coupon sets is shown in Figure 4-18

These actual gap height measurements are compared to the predicted gap height in Table 4.5.

The predicted gaps were smaller than the measured gaps most likely because the predicted gaps did not take into account particles or settling errors. The standard deviation of average gap heights was 4.5 μm. For the three sets of coupons assembled and disassembled, the standard deviations or gap error of assembly and disassembly were 1.1 μm, 1.2 μm, and 4.9 μm which averaged to 2.4 μm. The first two sets of coupons had a very small assembly and disassembly standard deviation. The third set of coupons may have had a particle lodged in one of the pyramid pit interfaces.

		Predicted	Measured
Different Sets of Coupons	Average Gap Height/Error μm	8/-17	19.4/-5.6
	Minimum Gap Height/Error μm	0.1/-24.9	12.4/-12.6
	Maximum Gap Height/Error μm	14.4/-10.6	30.2/5.2
Assembly/ Disassembly	Standard Deviation μm	N/A	2.4
	Maximum Deviation from Average μm	N/A	7.4

Table 4.5: The maximum and minimum gap heights in the pyramid/pit two-coupon system.

4.3.2 Parallelism Error

Parallelism error occurs when one side of the coupon is higher than the other side, as shown in Figure 4-15. The parallelism error is defined as

$$e_\phi = \arctan \frac{G_{max} - G_{min}}{D_p} \tag{4.6}$$

where G_{max} is the maximum gap at a single pyramid/pit interface, G_{min} in the minimum gap at a single pyramid/pit interface, and D_p is the distance between the two pits. This parallelism error, e_ϕ, will be greatest when the distance between the pits is smallest. The shortest possible distance between two pits is 1 mm, as shown in Figure 4-19. Therefore the maximum parallelism error occurs when one pyramid/pit interface has the greatest possible gap of 14.4 μm, and a pyramid/pit interface 1 mm away has the smallest possible gap of 0.1 μm. Therefore the greatest possible parallelism error is 14.3 mrad. This again is the greatest possible angle error or any two coupons put together. What is not known is the repeatability of a single set of two coupons being assembled and disassembled. This is harder to model and is measured experimentally.

The parallelism gap was calculated using the same data used to measure gap error. The gap at positions 1, 2, and 3, shown in Figure 4-17, were used to determine the angle of the top coupon relative to the bottom coupon. The equations relating these three heights to parallelism error are Equation 3.13 and Equation 3.14. Ten sets of coupons had their parallelism error mentioned once, while 3 sets of coupons were each taken apart and put back together five times to determine parallelism error.

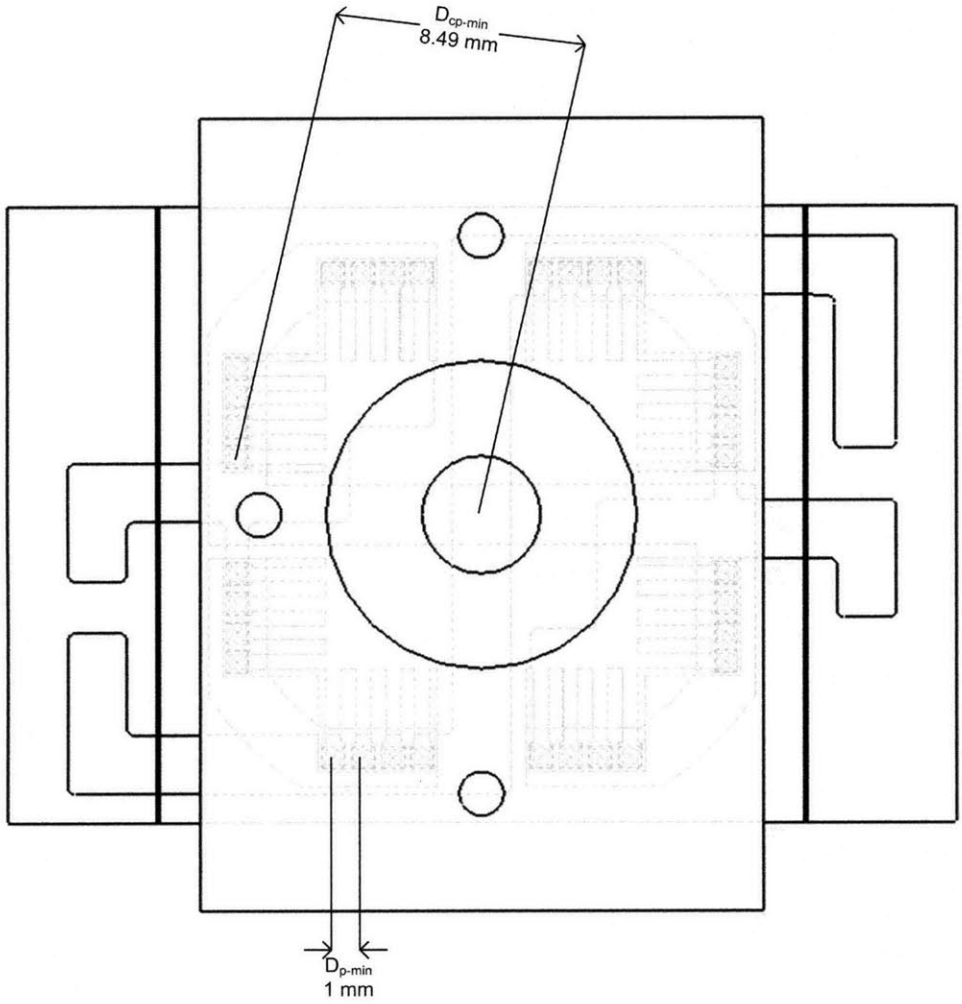

Figure 4-19: Geometry of the pyramid/pit two-coupon assembly.

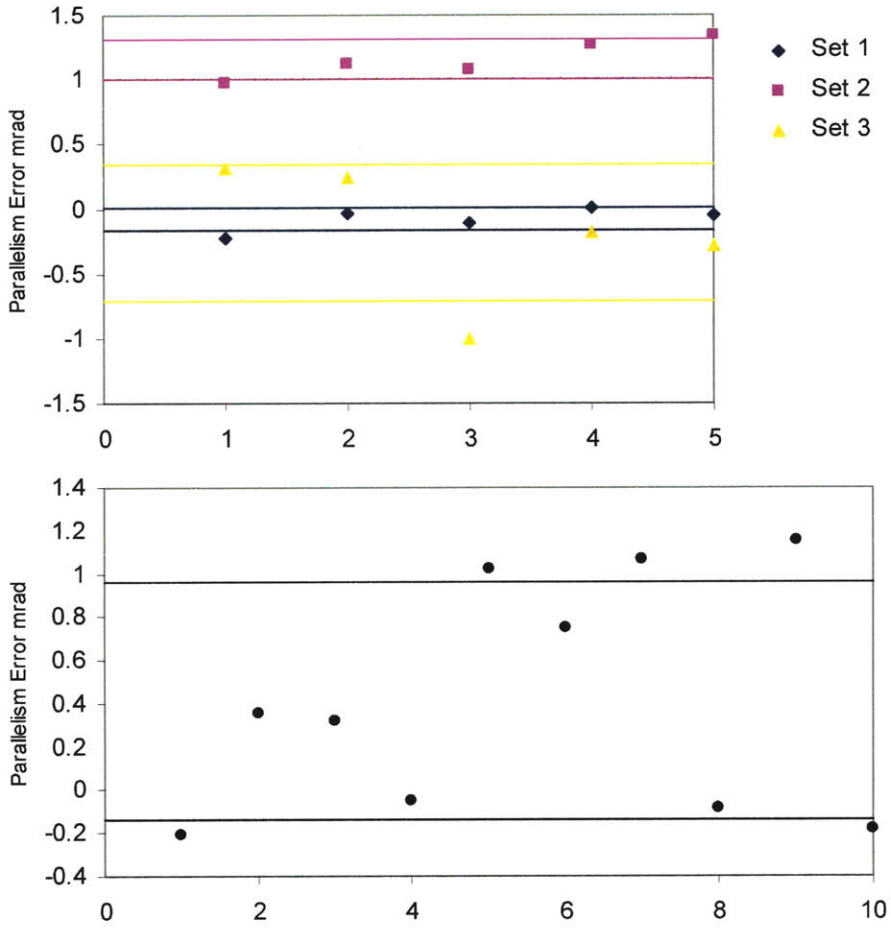

Figure 4-20: Parallelism error, e_ϕ, raw data.

This data is shown in Figure 4-20.

These actual parallelism error measurements are compared to the predicted parallelism error in Table 4.6.

The actual parallelism errors were much less than the maximum predicted parallelism error. This makes sense because in order for the maximum predicted parallelism error to occur the largest possible gap and the smallest possible gap would have to be right next to each other. Between the ten different sets of coupons, the standard deviation of parallelism error is 0.55 mrad. For the three sets of coupons which were assembled and disassembled, the assembly and disassembly standard deviations were 0.09 mrad, 0.15 mrad, and 0.52 mrad which average to 0.25 mrad. The third set of

		Predicted	Measured
Different Sets of Coupons	Average Absolute Error mrad	N/A	0.42 mrad
	Minimum Absolute Error mrad	0	0.21 mrad
	Maximum Absolute Error mrad	14.3	1.15 mrad
Assembly/ Disassembly	Standard Deviation mrad	N/A	0.25 mrad
	Maximum Deviation from Average mrad	N/A	0.81 mrad

Table 4.6: The parallelism error e_ϕ in the pyramid/pit two-coupon system.

coupons may have had a particle lodged somewhere.

Translation Error

Translation error is caused by the non-squareness of the pyramids and pits. The gap created by a single pyramid/pit interface is determined by the largest pyramid width and the smallest pit width. When the pyramids and pits are non-square, the difference between the long side and the short side of the pyramid or pit allows for slop. This is shown in Figure 4-21.

The translational error as a result of this non-squareness is

$$e_{XY} = +/- [(W_{pyramid-max} - W_{pyramid-min}) + (W_{pit-max} - W_{pit-min})]. \quad (4.7)$$

To estimate this translational error, twenty pyramids and twenty pits were measured. The maximum and minimum width of each individual pyramid or pit was recorded. This raw data is shown in Figure 4-22.

The average width difference for pyramids was 3 μm with a standard deviation of 2.9 μm, and a maximum difference of 12.5 μm. The average width difference for pits was 2.6 μm with a standard deviation of 1.9 μm, and a maximum difference of 6.9 μm. Substituting these numbers into Equation 4.7, the average translational error would be 4.9 μm and the maximum translational error would be 19.4 μm. However, for this to happen every pyramids would have to have the maximum width different and every pit would have to have the maximum width difference. Furthermore, these maximum width differences would all have to occur either in the x or y direction. In actuality, the pyramid/pit interface with the smallest width differences will constrain

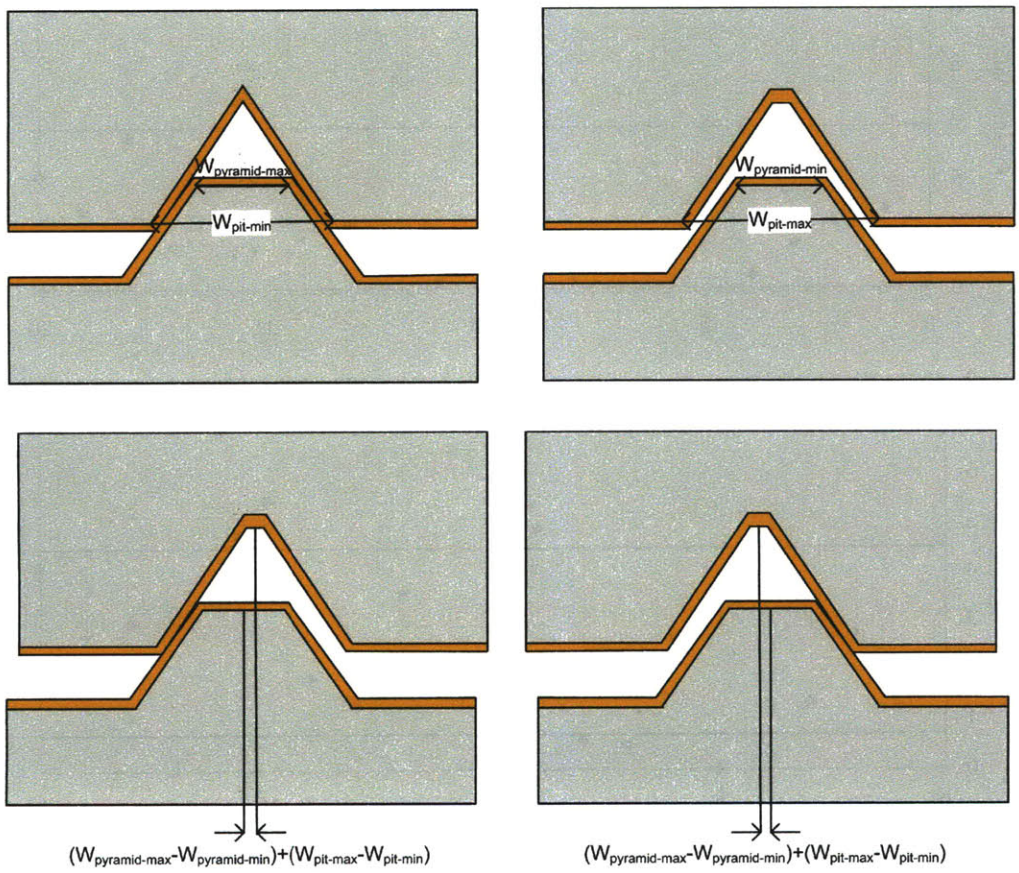

Figure 4-21: The effect of non-squareness on translational error.

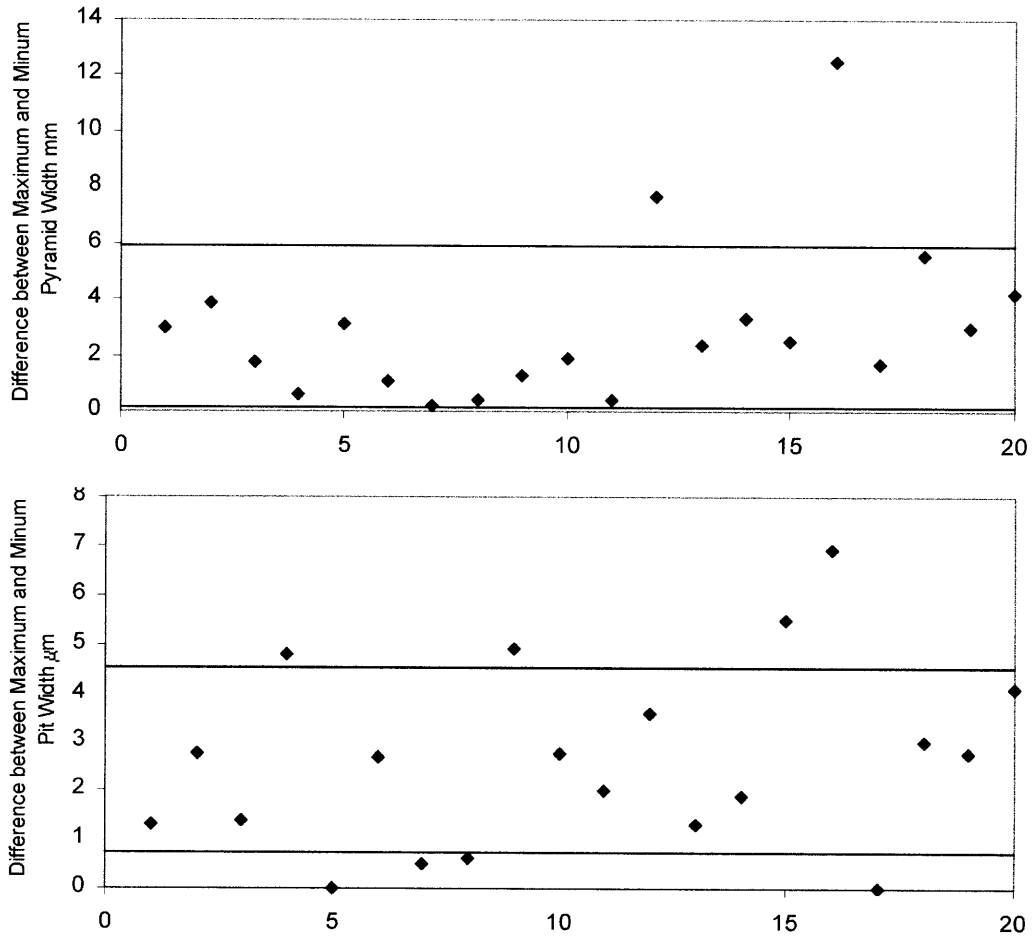

Figure 4-22: Top: The difference between the longest and shortest dimension of twenty pyramids. Bottom: The difference between the longest and shortest dimension of twenty pits.

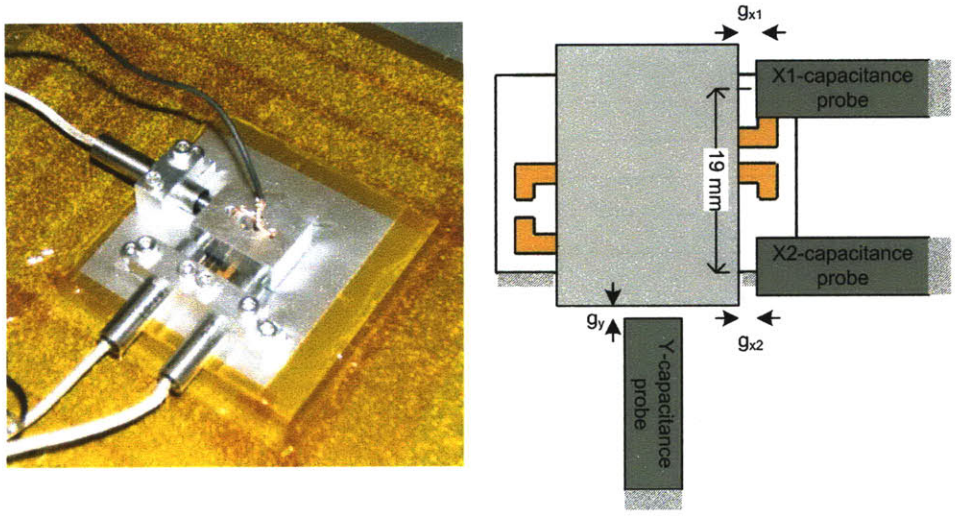

Figure 4-23: The test setup used to measure XY repeatability.

the entire system. In order to truly predict this error, a Monte Carlo simulation was run. In this simulation, thirty two pits and thirty two pyramids were given a random width difference based on a normal distribution of the measured width differences and standard deviations. The smallest translational error at these thirty two pyramid and pit interfaces was taken to be the actual translational error. This simulation was run 25,000 times. According to the simulation, the translational error will have an average value of 0.48 μm with a standard deviation of 0.58 μm and a maximum error of 3.29 μm.

The actual translational error was then measured using the test setup shown in Figure 4-23.

In this test setup, an aluminum target was mounted on top of a top coupon using super glue. This aluminum target had a wire which grounded it. The bottom coupon was glued to a mount which contained three capacitance probes which could measure the gap distance between the end of the probe and the aluminum target on the top samples. The coupons were assembled, and the capacitance probes were positioned within range. Two bottom coupons were assembled with three top coupons in each of the six possible ways. For each of these six configurations, the coupons were assembled and disassembled 50 times. The gaps at the X-capacitance probes, g_{x1} and

	Standard Deviation e_X μm	Maximum e_X μm	Standard Deviation e_Y μm	Maximum e_Y μm
Bottom 1, Top 1	0.169	0.471	0.300	0.884
Bottom 1, Top 2	0.182	0.677	0.126	0.344
Bottom 1, Top 3	0.271	0.778	0.439	1.468
Bottom 2, Top 1	0.140	0.360	0.145	0.401
Bottom 2, Top 2	0.257	0.691	0.255	0.822
Bottom 2, Top 3	0.173	0.435	0.177	0.424
Overall	0.199	0.778	0.241	1.486
Predicted	0.58	3.29	0.58	3.29

Table 4.7: The maximum and standard deviations of translational error in six cases.

g_{x2}, and the gap at the Y-capacitance probe, g_y, were recorded after each reassembly. Since this gap was a function of how close the capacitance probe was set up to the target initially, the average x1-gap, the average x2-gap and the average y-gap were subtracted from the raw data to get the gap fluctuation around the average. The true x-gap fluctuation was taken to be the average of the fluctuation of the x1-gap and the fluctuation of the x2-gap. The results of this data are shown in Figure 4-24.

The standard deviation and maximum translational error for each of these cases as well as the overall standard deviation and maximum translational error for both the x and y directions are shown in Table 4.7, which also displays the predicted values.

The actual measured translational errors were approximately twice as small as those predicted by the Monte Carlo simulation. In the Monte Carlo simulation, is was assumed that the pyramids and pits would slide to the end of their possible travel. In reality, they could stay closer to the middle. Therefore it makes sense that the measured error is smaller than the predicted error.

Rotational Error

Rotational error occurs because the translational error allows some rotation about the center of the coupons. The theoretical rotational error is therefore defined as

$$e_\theta = \arctan \frac{e_{XY}}{D_{cp-min}} \tag{4.8}$$

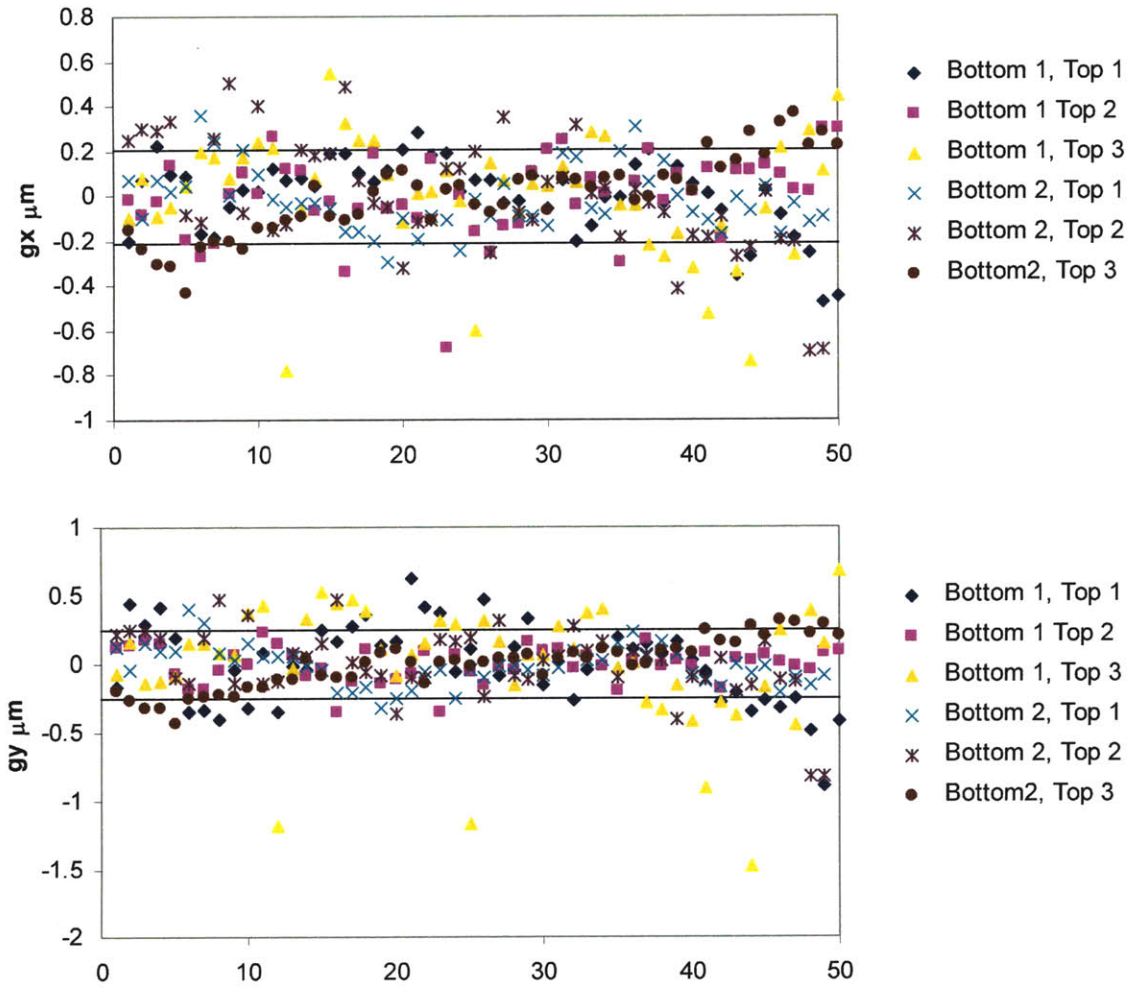

Figure 4-24: The translational repeatability of the second generation kinematic coupling two-coupon system.

	Standard Deviation of e_θ μrad	Maximum e_θ μrad
Bottom 1, Top 1	12.93	56.33
Bottom 1, Top 2	15.75	65.32
Bottom 1, Top 3	11.01	30.83
Bottom 2, Top 1	14.35	39.32
Bottom 2, Top 2	15.89	33.77
Bottom 2, Top 3	7.27	21.27
Overall	12.87	65.32
Predicted	70	380

Table 4.8: The standard deviation and maximum rotational error repeatabilites seen in six different top-bottom coupon combinations compared to predicted values.

where e_{XY} is the translational error, D_{cp-min} is the distance between the center and the closest pyramid/pit interface, shown to be 8.49 mm in Figure 4-19. The rotational error will be greatest when e_{XY} is greatest. The maximum and standard deviation for rotational error can be calculated by using the maximum and standard deviation values for translational error in Equation 4.8. The translational error values come from Table 5.10. At the maximum measured translational error of 3.29 μm, the maximum rotational error is 0.38 mrad. The x-translational error had a standard deviation of 0.58 μm. Therefore the rotational error will have a standard deviation of 0.07 mrad. The minimum possible rotational error is zero. Rotational error was measured using the test setup shown in Figure 4-23. Rotational error was defined to be

$$e_\theta = \arctan \frac{[g_{x1} - \bar{g_{x1}}] - [g_{x2} - \bar{g_{x2}}]}{19000} \tag{4.9}$$

where g_{x1} and g_{x2} are the gaps at the X1-capacitor and X2-capacitor in μm and 19,000 is the distance in μm between the centers of the X1-capacitor and X2-capacitor. As in the translational tests, two bottoms and three tops were assembled and disassembled in all six possible configurations 50 times. The rotational error for each of these was recorded. The raw data is shown in Figure 4-25 and the standard deviations and maximum errors are shown in Table 4.8.

The rotational error had a standard deviation of 12.87 μrad and a maximum of 65.32 μrad. This is quite small even compared to the predicted values for standard deviation and maximum of 70 and 380 μrad respectively. This is because the maxi-

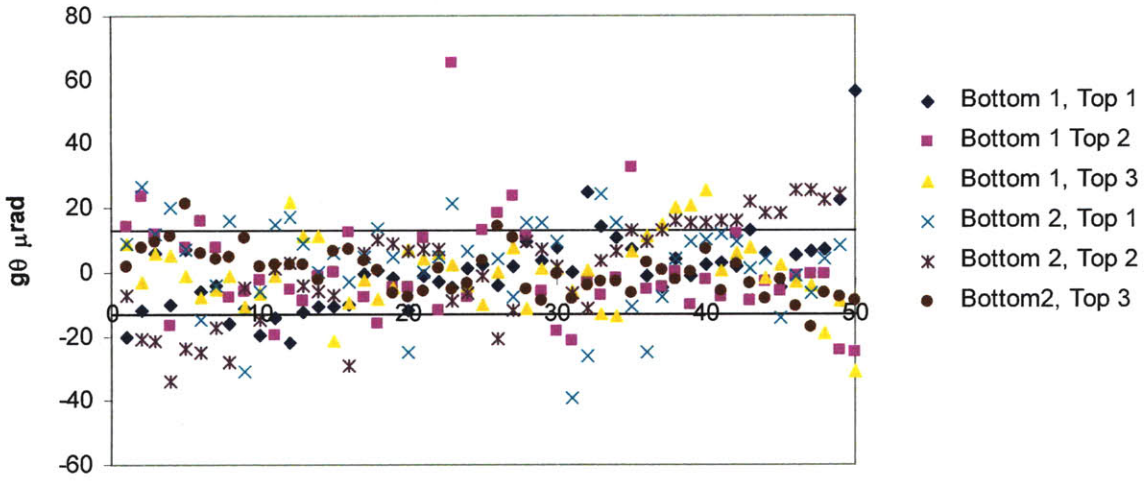

Figure 4-25: The rotational repeatability of the pyramid/pit two-coupon system.

mum translational value would have to be the same on every pyramid/pit interface. In reality, even one very good pyramid/pit interface with almost to translational error would keep the entire system from rotating. That is why the measured values for rotational error are so small.

4.3.3 Error Summary

All of the actual values for each of the errors (translational, rotational, gap error, and parallelism error) are displayed in Table 4.9

4.3.4 Error Interpretation

This section briefly analyzes the effects of the repeatability errors in the pyramid/pit two-coupon system. There are two areas affected by errors. The translational errors affect asperity level contacts. The second area affected is that membrane tilt and parallelism error have an effect on the applied force.

In the pyramid/pit two-coupon design, the standard deviation of translational repeatability was 0.241 μm. The asperities in many MEMS fabricated contacts are on the order of 1 μm [22]. Therefore, for all assemblies/disassembles falling within one

	Different Sets of Coupons			Assembly/Disassembly		
	Average	Standard Deviation	Maximum Absolute	Average	Standard Deviation	Maximum Absolute
G/e_g μm						
Predicted	8/-17	N/A	0.1/24.9	N/A	N/A	N/A
Measured	19.4/-5.6	4.5	12.4/12.6	N/A	2.4	7.4
e_ϕ mrad						
Predicted	0	N/A	14.3	N/A	N/A	14.3
Measured	0.42	0.21	1.15	N/A	0.25	0.81
e_{XY} μm						
Predicted	N/A	0.58	3.29	N/A	0.58	3.29
Measured	N/A	0.241	1.486	N/A	0.241	1.486
e_θ μrad						
Predicted	0	70	380	0	70	380
Measured	N/A	12.87	65.32	N/A	12.87	65.32

Table 4.9: The predicted and measured accuracy of the pyramid/pit two-coupon system

standard deviation from the average, the top and bottom portions of the contacting asperities will overlap by at least 76% of a diameter. At the maximum measured error, none of the original asperities are in contact. Therefore improved translational repeatability is needed.

In the pyramid/pit design, the worst case membrane tilt error was 800 μrad. The worst parallelism error was 65.32 μrad. These errors can sum, leading to the actual force on the contact being slightly less than the measured force. This is shown in Figure 3-28. For the worst case scenario, where the sum of the two contributing errors is 865 μrad, the actual contact force will be 99.9999% of the measured contact force. This is less than the accuracy of the mechanism used to measure the force.

4.3.5 Proof of Concept Testing

The pyramid/pit two-coupon system was tested using the custom instrumentation described in Chapter 6. A sample of the force vs. displacement curve is shown in Figure 4-26.

In Zone 1 the probe has not yet reached the top coupon, so the displacement of probe increases; but force is essentially zero. The force does drift a bit due to sensor

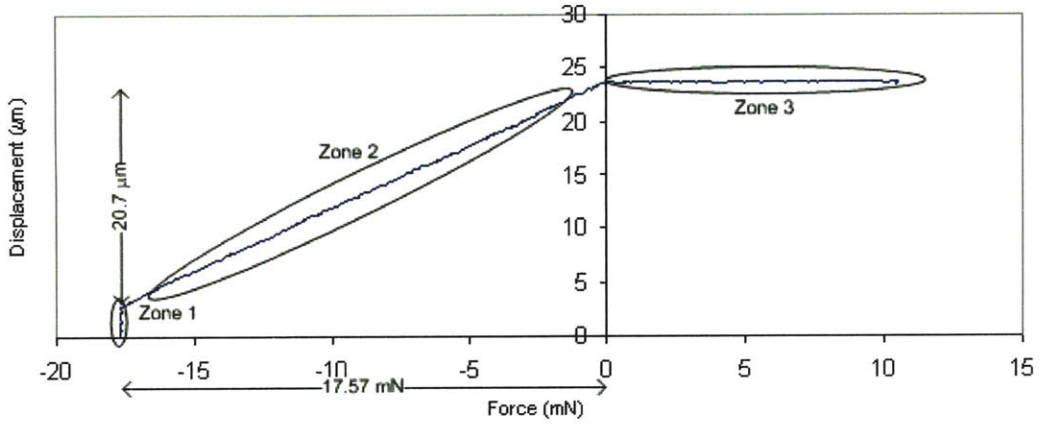

Figure 4-26: Force vs. displacement for the pyramid/pit two-coupon system

drift. In Zone 2 the probe displacement increases linearly with the force. This is the area when the membrane is being deflected, but the top coupon has not made contact with the bottom coupon. At the beginning of Zone 3, the top coupon bottoms out on the bottom coupon. Force continues to increase, but the probe stops moving. The stiffness of the membrane is measured as 0.85 mN/μm very near the predicted stiffness of 0.88 mN/μm.

One major problem with the testing was that the design had to be preloaded. Since contact was made through 32 individual pyramid/pit interfaces, the force on each of these interfaces was not enough to ensure stable contact. Additionally, some of these interfaces did not make contact at all. That is because the pits were etched over an SOI layer. When this was metalized, there was not good coverage across this SOI layer, so the bottom of the pits were not electrically connected to the top of the pits or the metal traces. An example showing an incomplete breakdown of the metalization at the SOI layer is shown in Figure 4-27. The solution to this problem was to preload the the top coupon to the bottom coupon by using tape. This worked, but was not ideal as it created a very difficult setup procedure.

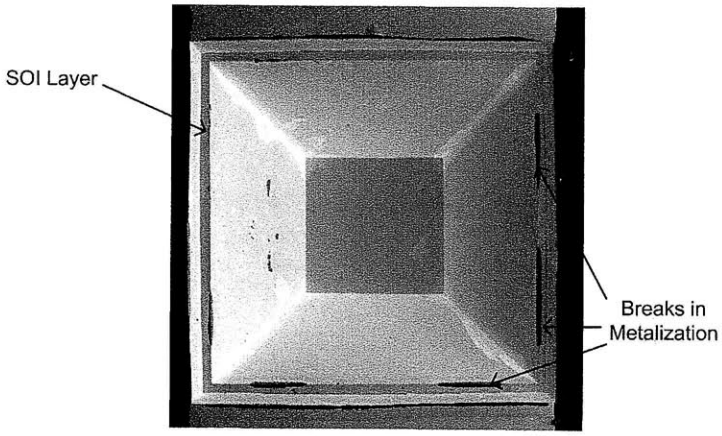

Figure 4-27: The SOI layer creating a break in the metalization of the pits.

4.3.6 Design performance compared to the functional requirements

Table 4.10 summarizes how the pyramid/pit two-coupon system's performance compared to the performance dictated by the functional requirements.

4.3.7 Summary and Improvement Opportunities

This chapter detailed the design, fabrication, and testing of a two-coupon system using an elastic averaging arrangement of of pyramids and pits for alignment. This alignment mechanism allowed for excellent repeatability between the top and bottom samples. The two-coupons were also electrically connected through the pyramid/pit interfaces. The electrical connection was not always made because there was not a lot of force on each individual pyramid/pit interface. Multiple opportunities for improvement were found in this initial design. These are all issues which are addressed in the final version of the two-coupon system.

The first design opportunity is the non conductivity between the pyramids and pits. This was due to both the small amount of force on each pyramid/pit interface and the metalization issues of the pits that occurred because the gold did not adhere well to the exposed SOI layer.

The second design opportunity is the membrane. The 20 μm membrane is quite

Functional Requirement	**Performance of 1st generation two-coupon system**
Measure contact resistance in the mΩ range.	Not Achieved, conductivity issue between pyramids and pits
Measure contact force in the 100 μN.	Achieved
Bring contacts together in a parallel manner.	Achieved. Parallelism error standard deviation of 0.21 mrad and maximum of 1.15 mrad.
Measure multiple cycles.	Achieved
Assembly/disassembly repeatability better than 1μm.	Achieved. Translational repeatability of 0.241 μm. Maximum of 1.486 μm.
Allow for the observation of the physical changes to the contact between cycles using metrology including, but not limited to, the SEM and AFM.	Achieved
Use no more than 50 mN of force to deflect membrane	Achieved. Uses 17.57 mN of force.
No more than 25μm of displacement to deflect membrane	Achieved. Average deflection of 19.4 μm.
Robust fabrication process which would not have the significant yield loss seen during the hot phosphoric acid step in the first process.	Achieved by not removing nitride.
Membrane fabrication which would not use a KOH-etch.	Achieved using DRIE.
No wiring to the top coupon.	Achieved by making contact through the pyramid/pit interface.
No ball handling.	Achieved using pyramids and pits.

Table 4.10: The performance of the pyramid/pit two-coupon system compared to its original functional requirements.

fragile and breaks with handling. A more robust membrane needs to be designed.

The final two-coupon system design addresses these design opportunities and also incorporates additional functionalities. This final two-coupon design is discussed in Chapter 5.

Chapter 5

Final Two-Coupon Design with Scrubbing and Three-Dimensional Tip Attachment Capabilities

List of Symbols	
A	Contact Area
D	Ball diameter
D_b	Distance between balls
D_c	Distance between a ball and the center of the coupon
D_{max}	Maximum possible ball diameter
D_{min}	Minimum possible ball diameter
δ	Probe displacement
$\delta_{SF=3}$	Membrane displacement when actual stress is one-third of the yield stress
Δbdv	Allowable ball diameter variation
Δdsf	Deviation from spherical form for balls
$\Delta sraa$	Surface roughness arithmetical average for balls
Δbdt	Basic diameter tolerance for balls
$\Delta aldv$	Allowable lot diameter variation for balls
Δmax	Total possible difference in diameter of largest ball and smallest ball

continued from previous page

List of Symbols	
e_g	Difference between measured gap and design gap
e_ϕ	Parallelism error
e_{theta}	Rotational error
e_x	Translational error in the x-direction
e_y	Translational error in the y-direction
$e_X Y$	Generalized Translational error
E	Young's Modulus
F	Force
$F_{contact}$	Force seen by the contact surfaces
$F_{measured}$	Force applied by the probe
$g_x 1$	Distance between target and x1-capacitance probe
$\bar{g_x} 1$	Average distance between target and x1-capacitance probe
$g_x 2$	Distance between target and x2-capacitance probe
$\bar{g_x} 2$	Average distance between target and x2-capacitance probe
g_y	Distance between target and y-capacitance probe
$\bar{g_y}$	Average distance between target and y-capacitance probe
G	Actual Gap
G_i	Design Gap
$\bar{G}$	Average of the gaps at each of the ball/pit interfaces. Taken to be the actual gap
G_{max}	Maximum gap at each of the three ball/pit interfaces
G_{min}	Minimum gap at each of the three ball/pit interfaces
h_t	Tip height
H	Characteristic height
I	Moment of inertia
k	Stiffness of the membrane
k_{arm}	Stiffness of one of the four arms of the in-plane flexure
$k_{segment}$	Stiffness of one of the two short segments that make up a flexure arm

continued from previous page

List of Symbols	
L	Cantilever arm length or thin film thickness
R_{add}	Resistance added by a titanium seed layer
ρ	Resistivity
σ_{max}	Maximum stress seen by the membrane
σ_y	Yield stress
t	Flexure thickness
t_c	Contact material thickness
t_{metal}	Metal trace thickness
t_p	Plating thickness
w	Flexure width
W	Nominal pit width
W_{max}	The longer of the two sides of a single pit
$W_{max-min}$	The difference in lengths of the two sides of a single pit
W_{min}	The shorter of the two sides of a single pit

The final two-coupon system for measuring and characterizing MEMS fabricated electrical contacts is presented in this chapter. This two-coupon system has all of the functionality of the systems presented in Chapters 3 and 4, but also allows contacts to be scrubbed relative to each other and allows for various types of three-dimensional tips to be tested. This chapter details the design, fabrication, error budget, and testing of the final two-coupon system.

5.1 Design

The following functional requirements were used to design final two-coupon system. These functional requirements were retained from the functional requirements of the previous designs:

1. Measure contact resistance in the mΩ range.

2. Measure contact force in the 100 μN range.

3. Bring contacts together in a parallel manner.

4. Measure multiple cycles.

5. Assembly/disassembly repeatability better than 1 μm.

6. Allow for the observation of the physical changes to the contact between cycles using metrology including, but not limited to, the SEM and AFM.

7. Use no more than 25 μm of displacement to deflect membrane.

8. Robust fabrication process which would not have the significant yield loss seen during the hot phosphoric acid step in the first process.

9. Membrane fabrication which would not use a KOH-etch.

10. No wiring to the top coupon.

11. No ball handling.

The instrumentation used to test these coupons had a force gauge with a larger range allowing for the requirements regarding the force used to deflect the membrane to be loosened.

12. Use no more than 300 mN of force to deflect the membrane.

Finally, new functional requirements were added to introduce new functionalities

13. Allow contacts to be scrubbed 20 μm.

14. Allow for the testing of multiple types of three-dimensional tips.

These functional requirements were achieved using a two-coupon system using a kinematic coupling configuration similar to the one presented in Chapter 3. The system has a silicon 21 mm x 32 mm bottom coupon containing a metal trace and three KOH-etched pits which contain stainless steel balls. Unlike the system presented

in Chapter 3, these balls are permanently attached to the coupon using conductive epoxy, which was done to avoid having to position the balls during each assembly. The pyramid/pit design presented in Chapter 4 achieved repeatable alignment without having balls; however, the electrical contact at the pyramid/pit interfaces was not good. The manufacturing of the pyramid/pit coupons was also far more complicated than a ball/pit design. Therefore, this alternative design using secured balls in pits was pursued. A three-dimensional tip can be epoxied or soldered onto the bottom coupon and 2.5 dimensional tips can be plated directly onto the coupon. Prior to the stainless steel balls being epoxied in place, the pits can be plated up to change the gap between the coupons to allow for tips of different heights. The balls are also plated with gold to increase conductivity. The top coupon is a 19 mm x 27 mm silicon rectangle. It contains a metal trace and three KOH-etched pits. These KOH-etched pits are on the metal trace. The top coupon also has a membrane similar in geometry to the membrane in the system presented in Chapter 4, but slightly thicker to make the coupon more durable. It also contains an in-plane flexure allowing the metal trace on the top coupon to move laterally relative to the bottom coupon. Lastly, the top coupon contains a retaining ring which allows a force probe to engage it and facilitate scrubbing. The coupons are assembled by placing the KOH-etched pits of the top coupon over the stainless steel balls of the bottom coupon. An integrated Kelvin structure runs through the gold plated stainless steel balls allowing contact resistance to be measured. When assembled, there is a gap between the two coupons equal to 25 μm plus the height of the tip. Therefore the distance between the tip and the top coupon is 25 μm. In order to test the sample, the membrane of the top coupon is deflected until the top coupon makes contact with the tip. Further increasing force will increase the load on the contact. The two sides of the contact can then be scrubbed against each other. The retaining ring holding the force probe keeps the center of the top coupon in one place. By moving the table underneath the bottom coupon, the bottom coupon can be moved relative to the top coupon. The in-plane flexure on the top coupon allows the balls to stay in contact with the KOH-etched pits by allowing the the section of the top coupon containing the KOH-

etched pits to move with the bottom coupon. This system and how force and scrub are imparted using this system are shown in Figure 5-1. The modules or this design are: the ball/pit interface, the in-plane flexure, the flexible membrane, the contact material, the contact tip, and the integrated Kelvin structure. Each of these are discussed in this section.

5.1.1 Ball/Pit Interface

The ball/pit interface has three functions. First, it provides a gap between the two coupons. Second, it allows for the repeatable assembly of the two coupons. Third, it provides electrical connections to the top coupon portion of the Kelvin structure. If this system is used to measure flat-on-flat contacts, as the systems presented in Chapters 3 and 4 were designed to do, the geometry of the ball/pit interfaces is relatively simple and shown in Figure 5-2. This ball and pit interface is almost identical to that of the ball and pit interface of the first generation two-coupon system presented in Chapter 3. One difference is that the pits are coated in metal and that the design gap is 25 μm instead of 5 μm.

Since the gap is now defined as the gap between the metal surfaces, pit width is independent of metal film thickness so long as the thickness of the metal on the pits is the same as the thickness of the metal on the contact surface. Equation 3.1 still applies. Therefore, to have a gap of 25 μm, the pit width needs to be 954.9 μm. The pits in Figure 5-2 do not terminate at a point. That is because they only need to be 397 μm deep to fit the balls. The target depth of these pits is 420 μm, assuming that by this point the critical pit width, 954.9 μm, has been achieved. Unlike the prior two versions of the two-coupon system, the final version of the system allows for the addition of contact material over the top metal trace and the addition of a contact tip on the bottom coupon. Therefore, the height between the coupons must be adjustable. This is done by plating the bottom pits with nickel cobalt. The thickness of the plating, t_p, is dependent on the height of the tip, h_t, and the contact material thickness, t_c. This geometry is shown in Figure 5-3. According to the geometry shown in Figure 5-3, the plating thickness of the nickel cobalt inside the

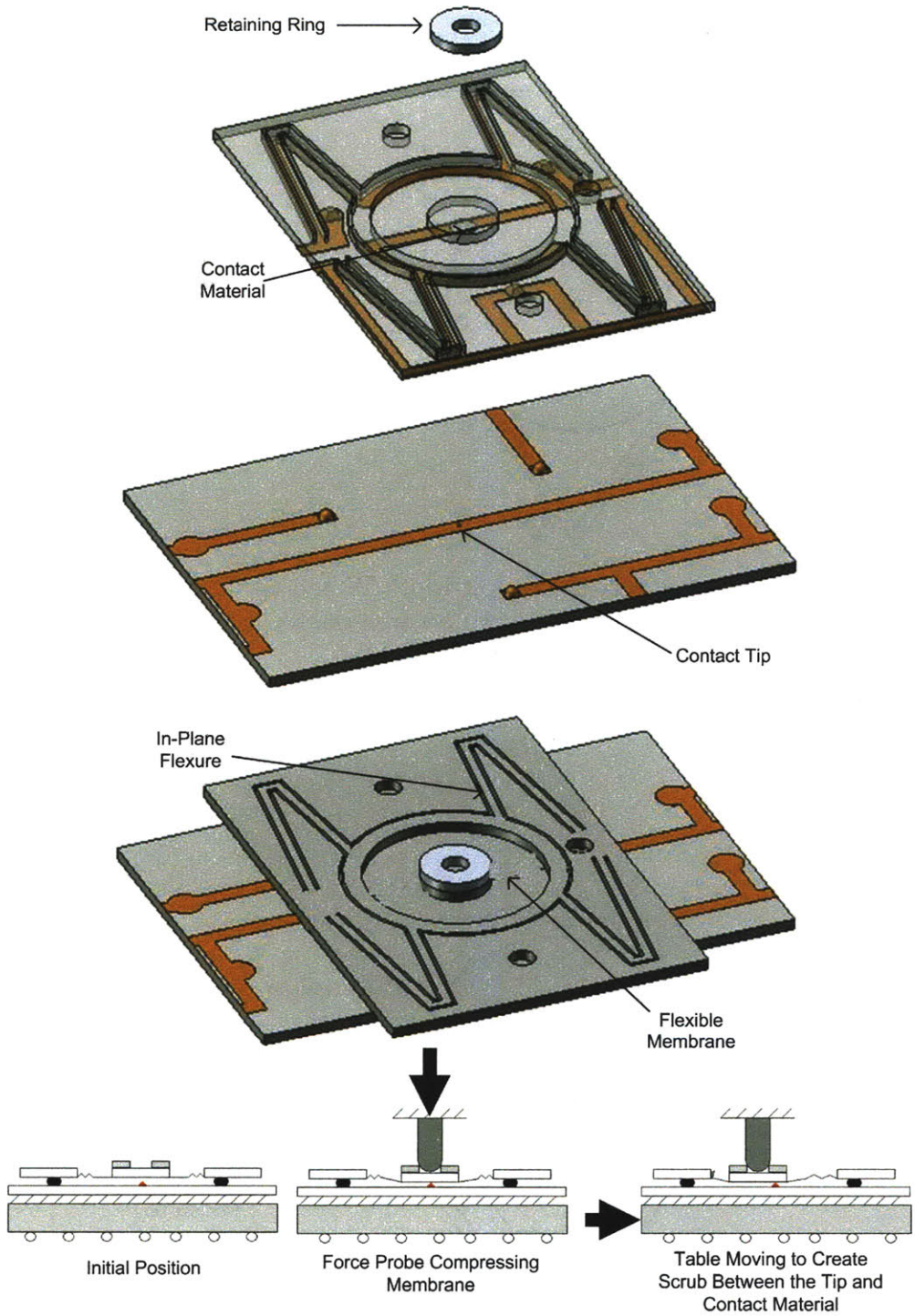

Figure 5-1: Top: An exploded view of the final two-coupon system. Middle: A collapsed view of the final two-coupon system. Bottom: A representative cross section showing how the two-coupon system imparts scrub and force. The in-plane flexure is represented as a simple spring in this depiction.

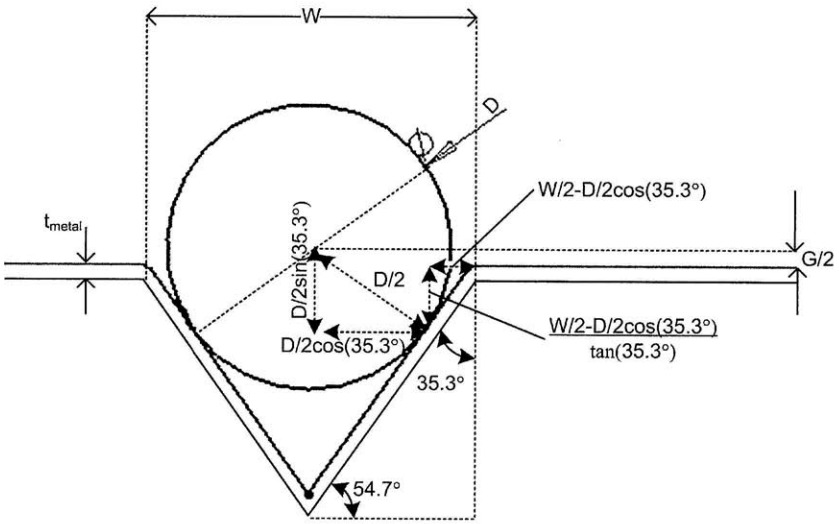

Figure 5-2: The geometry relating the pit width W and the ball diameter D to the gap height G. In this image, G/2 is shown because the top half of the coupon would be symmetrical, resulting in a total gap height of G.

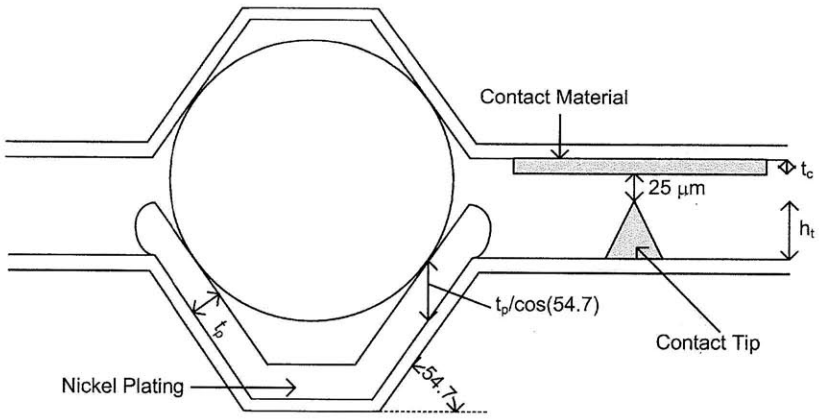

Figure 5-3: The geometry relating tip height H_t and contact material thickness t_c to the plating thickness of the nickel cobalt in the bottom pits.

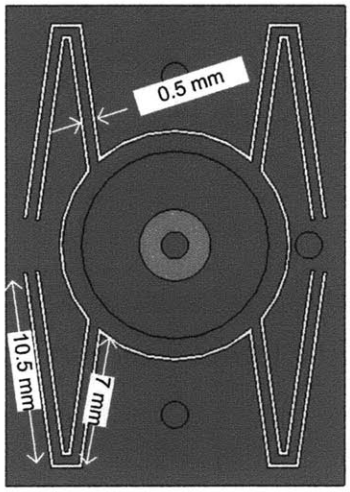

Figure 5-4: The in-plane flexure which allows relative movement between the top and bottom coupons.

pits required to maintain a gap of 25 μm between the tip and the contact material prior to membrane deflection is

$$t_p = \cos(54.7)[h_t + t_c]. \tag{5.1}$$

In the final two-coupon system, the balls are attached to the bottom coupon via conductive epoxy. The balls are also flash plated with gold to increase conductivity since stainless steel grows a non-conductive oxide. This flash coating of gold adds only 100 nm to the diameter of the ball so it does not significantly change gap height.

5.1.2 In-Plane Flexure

The in-plane flexure allows the tip on the bottom coupon to move relative to the contact material on the top coupon. The in-plane flexure is created by through etching 200 μm thick lines which release four flexural arms allowing the center of the top coupon to move independently from the outside of the top coupon. Since the etched lines are 200 μm across, the maximum travel of this flexure is 200 μm. This in-plane flexure is shown in Figure 5-4. The four arms of the flexure act like four springs in parallel. Each of the arms consists of two cantilever segments. These two

cantilever segments act as two springs in series. Each of the two cantilever segments acts as a cantilever beam with the slope at each end constrained at zero. The two segments have different lengths. One is 10.5 mm and one is 7.0 mm. The stiffness of one segment is

$$k_{segment} = \frac{12EI}{L^3} \tag{5.2}$$

where I is the moment of inertia of the segment, E is the Young's modulus of silicon which is 150 GPa, and L is the length of the segment. The moment of inertia is defined as

$$I = \frac{wt^3}{12} \tag{5.3}$$

where w is the width of the flexure and t is the thickness of the flexure. Both segments of the arms have the same moment of inertia because they have the same constant thickness and width. The width of each segment is 0.5 mm and the thickness of each segment is 0.67 mm, the thickness of the wafer. The stiffness of the two segments acting together as an arm is

$$k_{arm} = \frac{12EI}{L_1^3 + L_2^3} \tag{5.4}$$

where L_1 and L_2 are the thickness of each segment, 7.0 mm and 10.5 mm. Since there are four arms acting in parallel, the total stiffness of the in-plane flexure is

$$k_{arm} = \frac{48EI}{L_1^3 + L_2^3}. \tag{5.5}$$

Substituting in all values, the stiffness of the in-plane flexure is 60.1 mN/μm. Therefore, it would take about 120 mN of force to scrub a tip a 20 μm which is at the upper end of reasonable scrubbing distances and about 1200 mN of force to force the flexure through its full travel of motion. While these force numbers can easily be achieved using a piezo actuator, the flexure is stiff enough that small perturbations should not move it. The maximum stress in the flexure is

$$\sigma_{max} = \frac{FLt}{8I} \tag{5.6}$$

where t is the thickness of the flexure. For the 1200 mN of force needed to displace the flexure to the end of its range of motion, the maximum stress seen is 84 MPa, slightly less than the yield stress of silicon of 100 MPa. For the 120 mN needed for the maximum expected travel, the maximum stress seen is only 8.4 MPa, far less than the yield stress of silicon.

5.1.3 Membrane

The purpose of the membrane is to bridge the gap between the contact material of the top coupon and the contact tip on the bottom coupon in order to measure the contact resistance between them. This membrane is very similar to the membrane used in the pyramid/pit design presented in Chapter 4. It is a 10.5 mm diameter circular membrane with a 4 mm diameter stiff cylindrical boss in the center. In the pyramid/pit design, the membrane was 20 μm thick. This membrane was not very robust and broke frequently with handling. Therefore in this final version of the coupon, the membrane was designed with a 50 μm thickness. Equation 4.4 and Equation 4.5 can be used to calculate the stiffness of this membrane. The result is that the membrane has a stiffness of 13.75 mN/μm. However, in this case the membrane is not the only source of deflection. The in-plane flexure also deflects in the downward direction. Equation 5.5 determines the stiffness of this component. In this case the width of the flexure is 0.67 mm and the thickness of the flexure is 0.5mm. The stiffness of the in-plane flexure in the vertical direction is 33.5 mN/μm. Therefore the total stiffness of theses two items acting in parallel, the membrane and the in-plane flexure, is 9.75 mN/μm. Therefore, in order to bridge the 25 μm designed gap, 243.75 mN of force will have to be imparted on the membrane. This is less than the 300 mN of force maximum set in the functional requirements.

A finite element model was used to determine the effects of a non zero force angle of 5° and the effects of a 0.5 mm positional offset as well as verify the stiffness of the combination of the membrane and in-plane flexure. Force angle and positional offset are shown in Figure 3-6. Since the in-plane flexure has different stiffnesses in the x and y directions, the effect of force angle and positional offset in both directions was

Analysis Method	FEM	FEM	FEM	FEM	FEM	FEM	FEM	Num
Offset Direction	N/A	x	y	x	y	x	y	N/A
Center Offset (mm)	0	0	0	0.5	0.5	0.5	0.5	0
Force Angle (°)	0	5	5	0	0	5	5	0
Stiffness @ 10 mN (mN/μm)	15.06	15.11	15.02	14.76	13.73	14.40	13.33	9.75
Tilt @ 10 mN (mrad) 10 mN (mrad)	0	0	0	0.3	1.1	0.3	1.2	0
Displacement @ Safety Factor = 3 (μm)	23	23	23	19	20	16	18	Not given
Safety Factor @ 25 μm Displacement	2.76	2.76	2.76	2.28	2.4	1.92	2.16	Not given

Table 5.2: The calculated displacements and tilts for the combination of the membrane and in-plane flexure when 250 mN of force is applied.

investigated. The FEM results are shown in Figure 5-5 and summarized in Table 5.2.

The y-direction of the in-plane structure is more compliant than the x-direction therefore the errors from having positional or angle errors along the y-axis are greater than if the same errors were had along the x-axis. However, even in the worst case the tilt error is only about 1 mrad. In all cases the safety factor for maximum stress was between 1.92 and 2.76 at maximum travel. As with the earlier version of this membrane, membrane stiffness is proportional to the cube of membrane thickness. However, since this membrane is 50 μm thick as opposed to 20 μm thick, a 5 μm variation in membrane thickness will have a much smaller effect. If a membrane is designed to be 20 μm and is fabricated at 25 μm, the resulting membrane will be nearly twice as stiff as the designed membrane. If a membrane is designed to be 50 μm and is fabricated at 55 μm, the resulting membrane is only one-third stiffer than the designed membrane. In the membrane used in the pyramid/pit design presented in Chapter 4, an SOI wafer was used to control depth. However, this led to a break in the electrical connections where the pit metalization crossed the SOI layer. To avoid

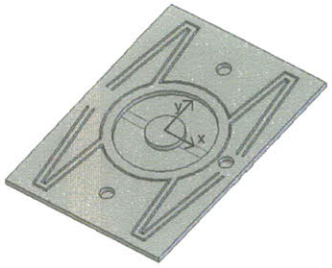

(a) coordinates

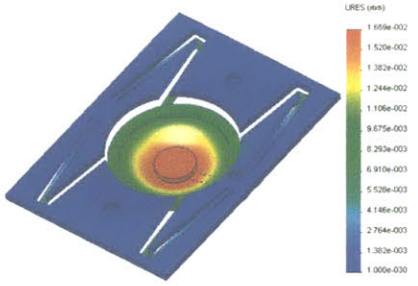

(b) 0 mm center offset; 0° force angle

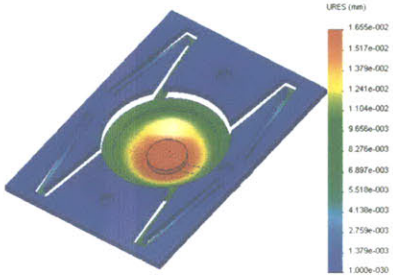

(c) 0 mm center offset; 5° force angle; x-direction

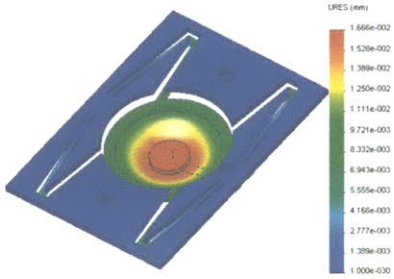

(d) 0 mm center offset; 5° force angle; y-direction

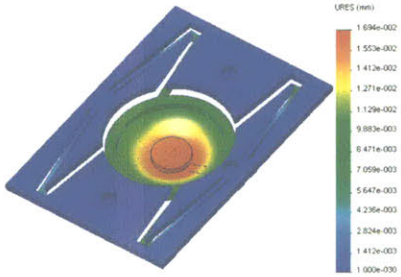

(e) 5 mm center offset; 0° force angle; x-direction

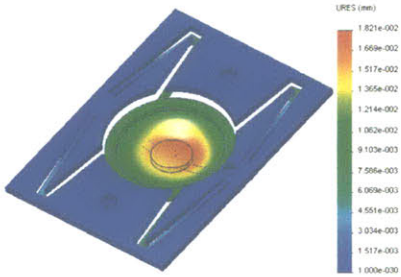

(f) 5 mm center offset; 0° force angle; y-direction

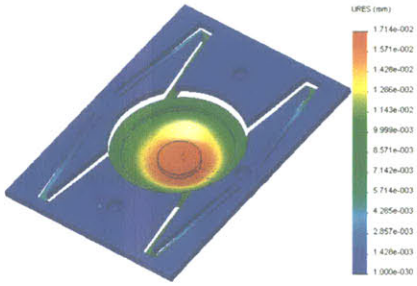

(g) 5 mm center offset; 5° force angle; x-direction

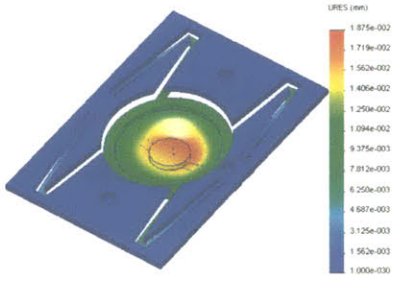

(h) 5 mm center offset; 5° force angle; y-direction

Figure 5-5: The FEM results for the DRIE-etched membrane when a force of 250 mN was applied.

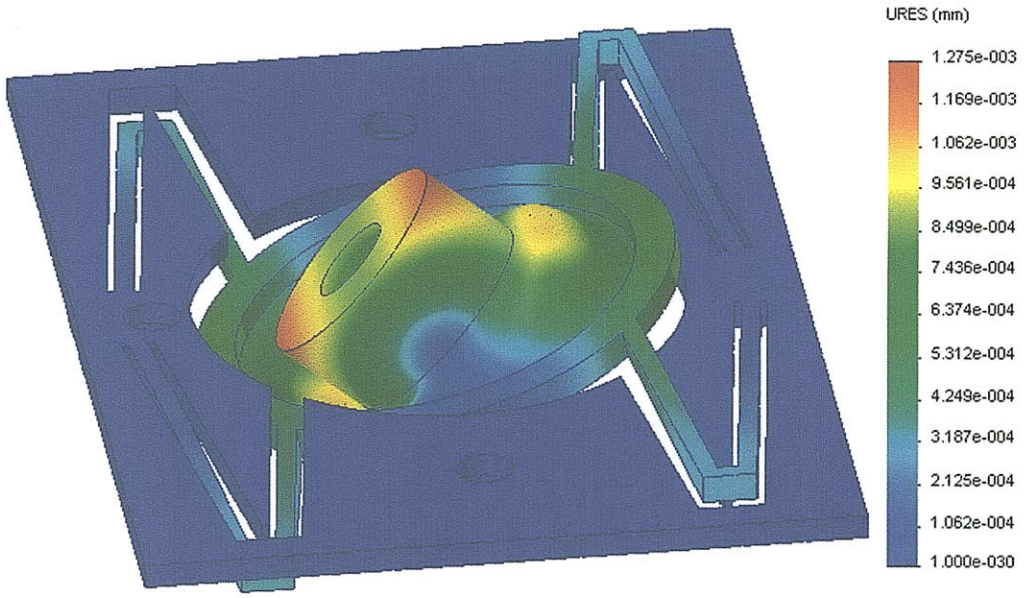

Figure 5-6: The effect of a moment on the angle of the top coupon contact surface.

this problem on the pits of this design, an SOI wafer is not used. Instead, a timed etch is used. This is detailed in the fabrication section of this chapter.

When the two contacts of the system are scrubbed, a moment is created on the top coupon. There are forces acting on the retaining ring and on the pits, but these forces are not aligned. This moment causes the in-plane flexure and membrane to twist, as shown in Figure 5-6. When the coupon is scrubbed to maximum displacement the effect of the moment is to tilt the top coupon contact surface 0.63 mrad.

5.1.4 Contact Material

In the final design of the two-coupon system, the contact material is independent from the metal trace on the top coupon. The metal trace is gold and the contact material can be anything. This is because the contact material may be something that grows a non conductive oxide layer, such as aluminum. If the entire contact trace was aluminum than the area in the pits would also be covered in a non conductive oxide layer which would not allow current to be conducted through the balls to the

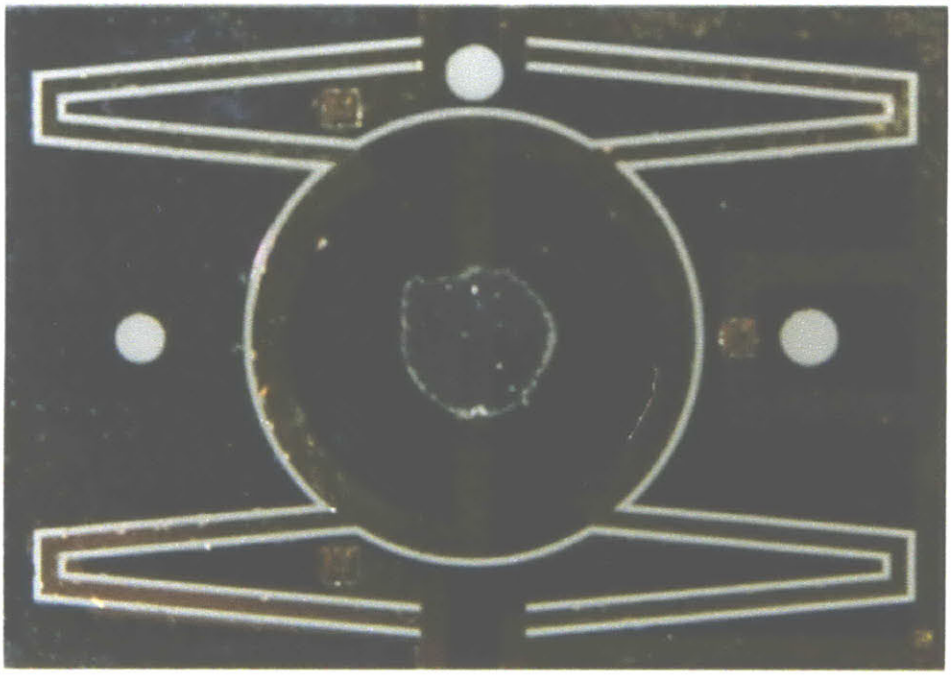

Figure 5-7: A top coupon with a gold metal trace and aluminum contact material in the center of the coupon.

top metal trace. An image of a top coupon with aluminum contact material at the center is shown in Figure 5-7.

5.1.5 Contact Tip

The final two-coupon system allows any number of tips to be tested. These tips are all attached to the center of the bottom coupon. If no tip is attached, then a flat-on-flat geometry can be tested. A tip can be plated directly onto the coupon to test a 2.5 dimensional tip. A glass ball can be embedded into the coupon and sputtered or plated over. Lastly, independently made third party tips cab be attached to the coupon using conductive epoxy or solder. These four types of "tips" are shown in Figure 5-8.

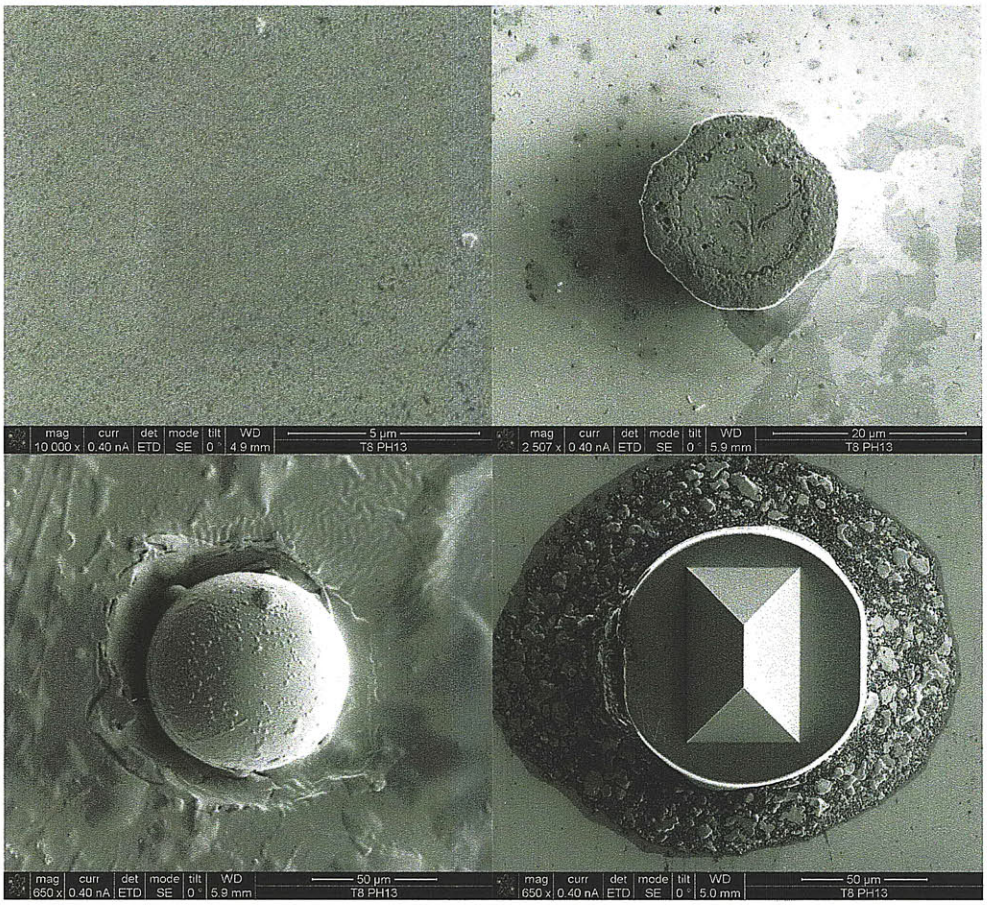

Figure 5-8: Top Left: A flat contact surface. Top Right: A 2.5 dimensional plated tip. Bottom Left: A sputtered and plated glass ball. Bottom Right: A third party tip attached to the coupon using conductive epoxy.

5.1.6 Kelvin Structure

The final two-coupon system has an integrated Kelvin structure similar to those used in the previous versions of the two-coupon system presented in Chapters 3 and 4. However, the geometry of the traces is more complicated. This is because these traces must wrap around the through etches used to release the in-plane structure. The Kelvin structure travels through two of the gold plated stainless steel balls so that all wiring can be done to the bottom coupon. The Kelvin structure is shown in Figure 5-9.

5.2 Fabrication

This section describes the fabrication of the final two-coupon system. The top and bottom coupons are fabricated on different wafers using different masks. The top coupons are fabricated from 670 μm thick double side polished silicon wafers while the bottom coupons are fabricated from 670 μm thick single side polished wafers. The fabrication of the top coupon varies somewhat depending on if the contact material is sputtered or evaporated gold, a sputtered or evaporated non-gold material, or a material deposited in a different manner such as plating.

5.2.1 Top Coupon Common Steps for Fabrication

The fabrication of the top coupon varies depending on the contact material being deposited onto the top coupon. Regardless of the contact material, each top coupon wafer will undergo the same first seven steps. These first seven steps are shown in Figure 5-10. These first seven steps are described in this section.

Step 1: Alignment Marks

This step is identical to the first step of the fabrication of the first generation ball/pit design. The first step in fabrication is placing alignment marks near the centers of the wafers. This step is identical for both top and bottom coupon wafers. The wafers are

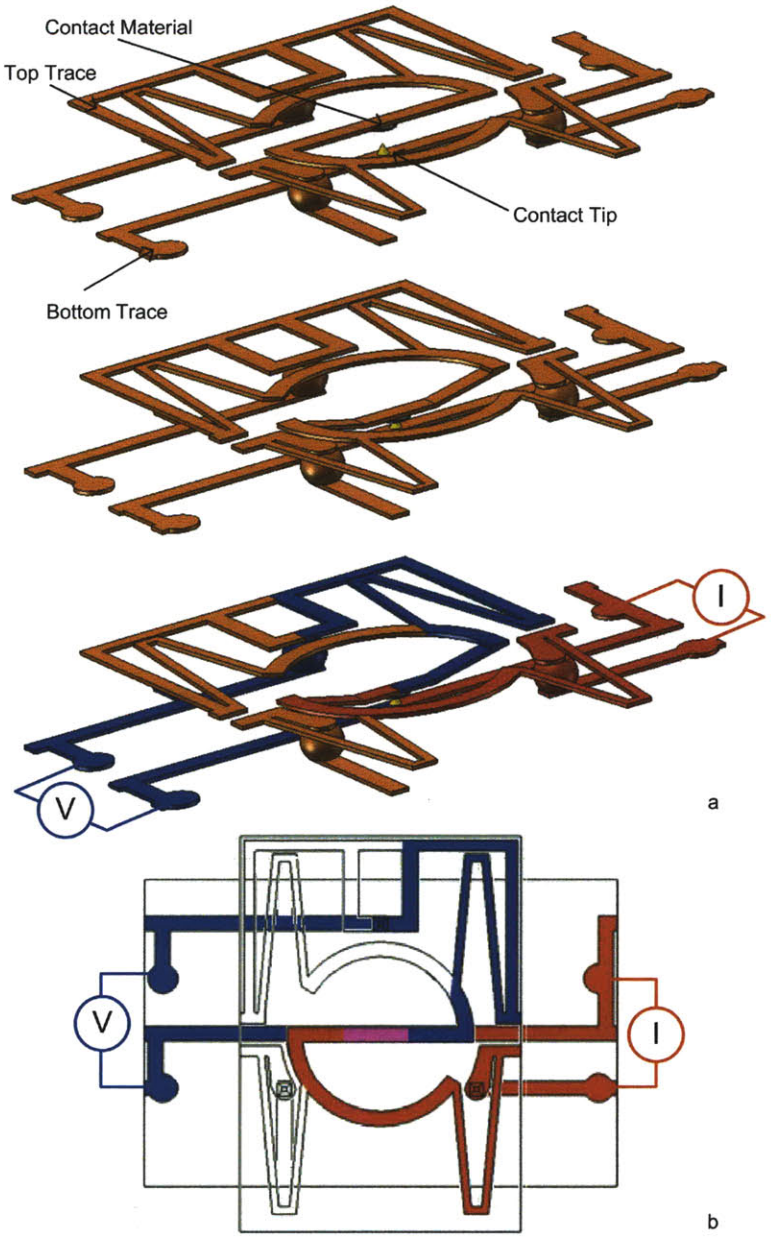

Figure 5-9: The integrated Kelvin structure of the final two-coupon system. a) The metal traces without the silicon coupons to clarify how the Kelvin structure works. In these images the size of the balls, tip, and gap is enlarged for clarity. The top image is the traces before the membrane is deflected. The next image is the traces after the membrane is deflected. The third image colorizes the traces to show the Kelvin structure. b)The colorized traces and coupons in transparency.

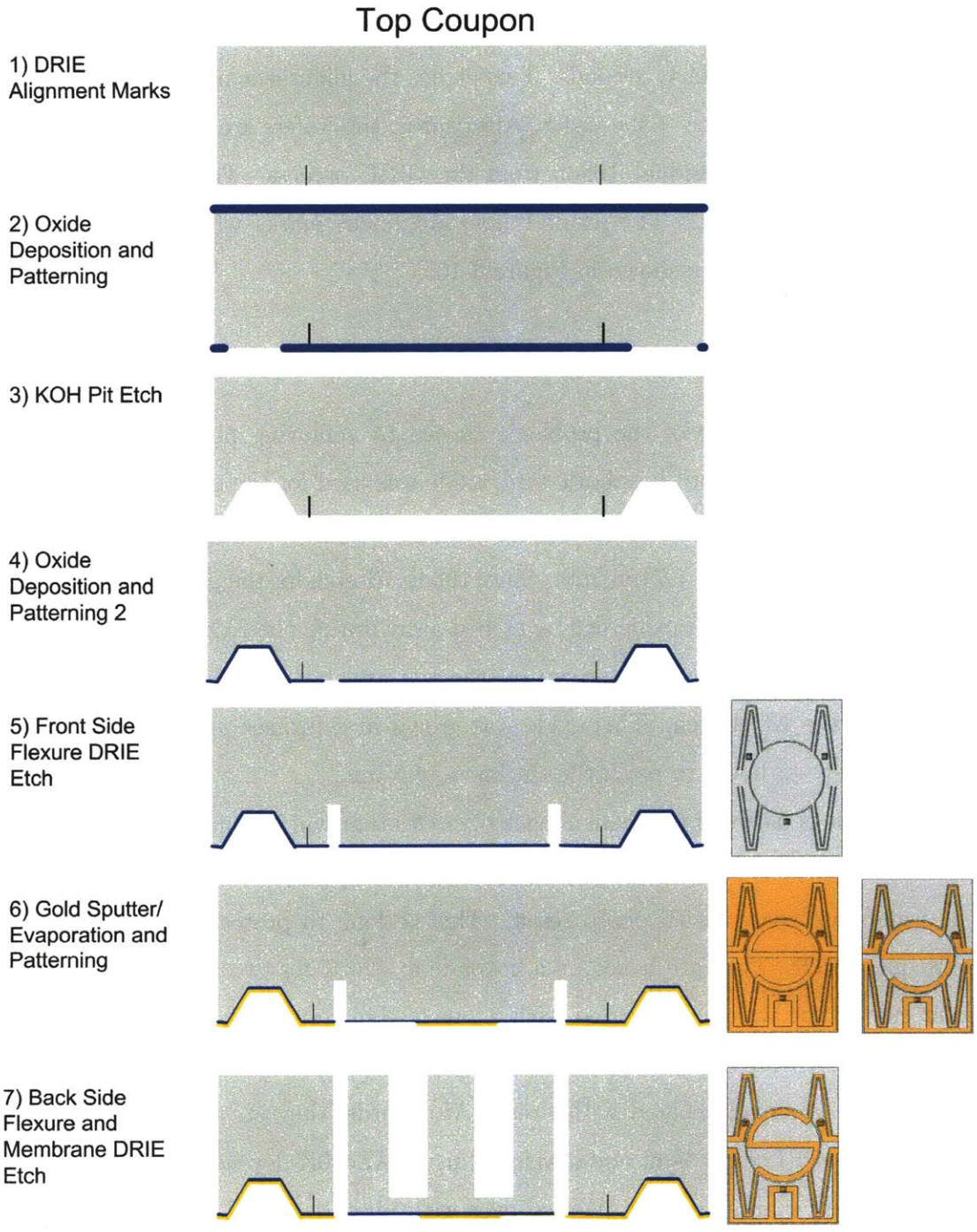

Figure 5-10: The seven common steps of fabrication used for all types of top coupons.

coated with HDMS to improve the adhesion of photo resist. The wafers are coated with 2μm of thin positive resist which is then patterned using standard lithography methods. The wafers are then etched in the STS deep reactive ion etcher (DRIE) using SF_6 plasma for thirty seconds. This etches the alignment mark pattern about 1 micron into the surface of the wafer. Afterwards, the wafers are placed in an oxide asher to remove any residual Teflon from the DRIE process. The wafers are then stripped of photo resist. The result is two alignment marks whose structure and location on the wafer are shown in Figure 3-10.

Step 2: Oxide Deposition and Patterning

In order to avoid some of the problems caused by removing nitride, such as the breakage of wafers in hot phosphoric acid, oxide was used for the mask for the KOH-etched pits. Nitride has an etch rate of virtually 0 nm/min in KOH, however, oxide has an etch rate of about 7.7 nm/min. Since the KOH-etch for the pits is 368 minutes, 2833 nm, or 2.833 μm, of oxide will be etched away during the KOH etch. Therefore 3 μm of oxide were thermally grown on the top and bottom coupons to serve as a mask for the KOH etch. This oxide was grown in a furnace at 1100 C. It takes approximately 18 hours to reach the thickness of 3 μm.

The oxide is pattered to create a mask of circles that will become the KOH-etched pits. The masks are different for the top and bottom coupons. First the backs of the wafers are coated with photo resist. This is done to protect them during the subsequent BOE. They are baked on a hotplate at 120°C for two minutes. Next, the front side of the wafers are coated with 2 μm of thin resist. They are then placed in a 100°C oven for 15 minutes. A hot plate can not be used because the backside of the wafer is already coated with resist. Afterwards, they are exposed through a mask under 100 J of UV light and developed using AZ400K developer for 40 seconds. The alignment marks are then painted over with photo resist. The wafers are then backed in a 120°C for 20 minutes. The exposed oxide is then etched using 32° 6:1 BOE. It takes 30 minutes to etch through the 3 μm of oxide. The photo resist was then stripped.

Step 3: KOH Pit Etch

The top and bottom wafers are etched in 80°C 30% KOH in order to etch the pits. The etch rate is 1.08 μm/min. The target etch depth is 420 μm and the target etch width was 955 μm. Therefore, the etch lasts approximatley 389 minutes. The lateral dimensions of the KOH-etched pits are checked to ensure that they are approximatley 955 μm across. After the etch, the wafers are cleaned by soaking in 45° HCL for five minutes. After the KOH-etch, a thin layer of oxide remains. This is removed with a 5 minute 32° 6:1 BOE dip.

Step 4: Oxide Deposition and Patterning 2

The top coupons all contain a through etched flexure. Part of this flexure is etched from the front of the wafer and the rest from the back of the wafer at the same time the membrane is etched. The purpose of this step is to first deposit a barrier layer of oxide and second to remove the oxide on the front side of the wafer where the flexure will be etched and to remove all the oxide from the backside of the wafer. The wafers are returned to the oxide furnace where 0.5 μm of oxide is thermally grown at 1100°C. This takes approximately 39 minutes not including temperature ramp up and ramp down time. The wafers are coated with HMDS to improve resist adhesion. The front side of the wafers are then coated with 4 μm of thin resist which is patterned using conventional lithography techniques. The alignment marks are painted over. The mask used creates 200 μm thick lines which will be etched in the DRIE in the next step. This mask is shown in Figure 5-11. The oxide covering these lines is then etched during a five minute 6:1 32° BOE. This also removes all of the oxide from the backside of the wafer. The wafer is then rinsed in DI wafter but the photo resist is not stripped.

Step 5: Front Side Etch Flexure DRIE Etch

The flexure which allows for the scrubbing motion of the contacts is a through etch. The flexible membrane requires an almost through etch (620 μm out of a 670 μm

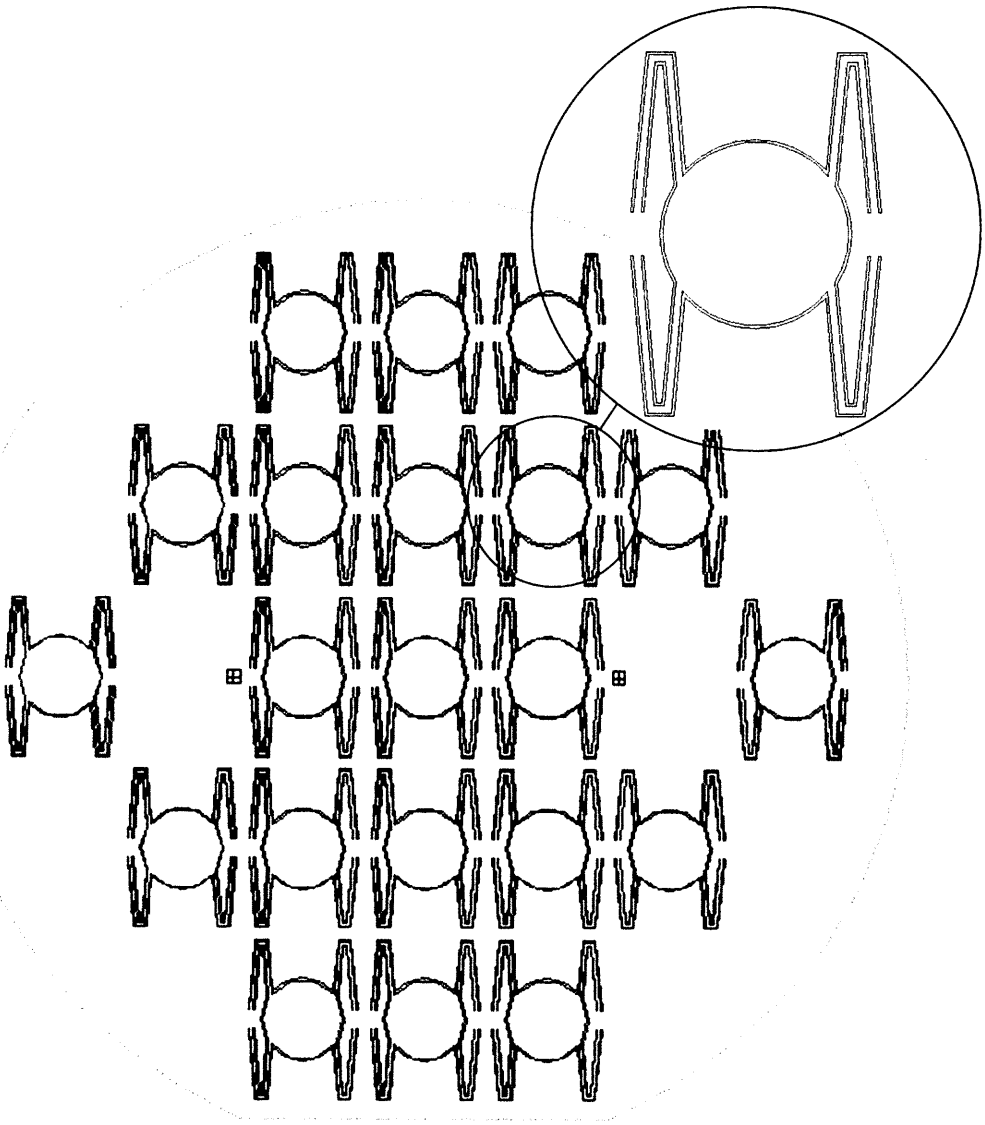

Figure 5-11: The mask used to create the in-plane flexures.

wafer.) Rather than perform a complete through etch and then another near through etch, these etches are performed together. This requires a separate etch from the front to etch the remainder of the in-plane flexure. This short etch is done before the long etch because the wafer is sturdier at that point. In the previous step, the photo lithography defining this flexure is performed. The flexure is etched in the DRIE chamber by alternating the etching SF_6 gas with the passivating CH_4 gas to create vertical sidewalls. The flexure is etched 100 μm deep which takes approximately 40 minutes. Afterwards the wafer is placed in an oxide plasma to remove any residual Teflon and then the photo resist is stripped.

Step 6: Gold Sputter/Evaporation and Patterning

In this step either sputtered gold or evaporated gold can be deposited. First, a 300 Å adhesion layer of titanium is deposited. Next 1000 Å of gold is deposited unless sputtered or evaporated gold is the contact material. In that case, the desired thickness of the contact material should be deposited. The front side of the wafers are then coated with 4 μm of thin resist which is patterned using conventional lithography techniques. The alignment marks are painted over. The mask used defines the metal trace and also leaves a ring of metal on the outside of the wafer. This mask is shown in Figure 5-12. The gold and titanium are then etched and the photo resist is stripped.

Step 7: Backside Flexure and Membrane DRIE Etch

This step finishes the through etch of the in-plane flexure and etches the 50 μm thick membranes. The wafers are coated with HMDS and the backside of the wafers are coated with 15 μm of thick positive resist. This resist is then exposed through two masks. First, the mask which creates the in-plane flexures, shown in Figure 5-11 and second, the mask which creates the membranes, shown in Figure 4-12. The wafers are then mounted to quartz wafers so that vacuum is not broken after the through etch of the in-plane flexures. The membranes and flexures are then etched in the DRIE alternating the etching SF_6 gas with the passivating CH_4 gas to create vertical sidewalls. The etch rate of the membranes is about 2.5 μm/min so this etch takes

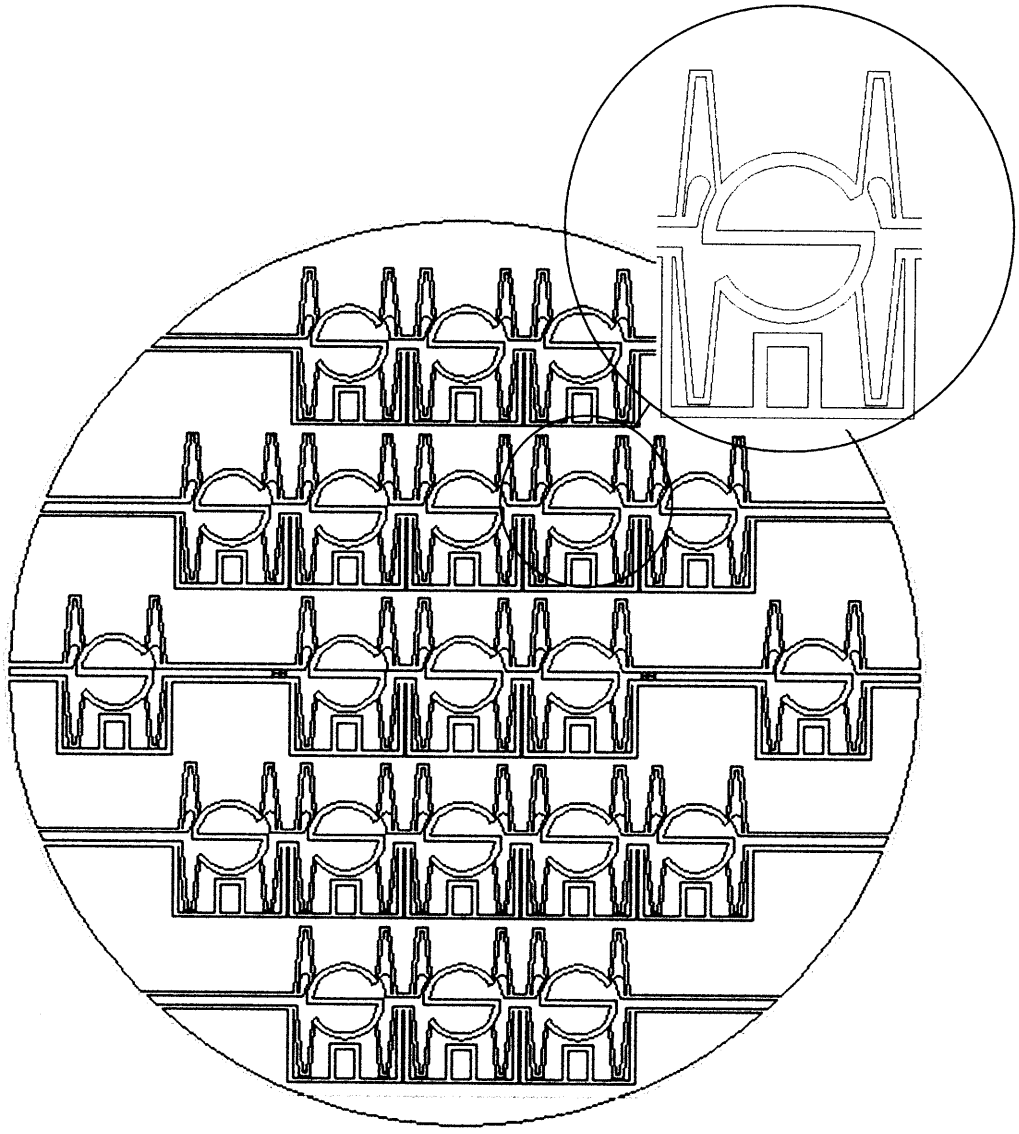

Figure 5-12: The mask used to metalize the top coupon wafers.

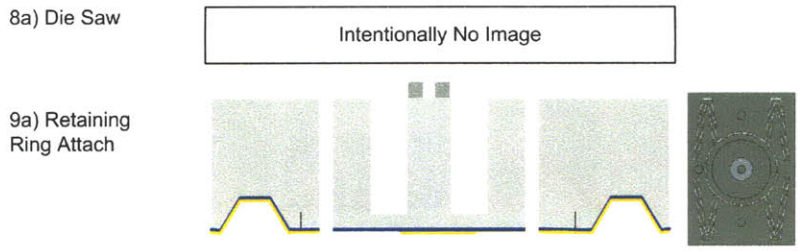

Figure 5-13: The last two steps in the fabrication of top coupons with sputtered or evaporated gold as the contact material.

approximately 248 minutes. During this process, the flexures etch slightly slower than the membranes which is why they were etched 100 μm from the front side instead of only 50 μm. This ensures that when the membranes are done etching the flexures have through etched.

5.2.2 Top Coupon Additional Steps for Sputtered or Evaporated Gold Contact Material

If sputtered or evaporated gold is the contact material, this fabrication process for the top coupons is very simple. That is because while depositing the gold metal traces, the contact material is also deposited. Therefore, after the seven common fabrication steps for top coupons, these types of coupons only have two additional fabrication steps. These are shown in Figure 5-13. These two steps are detailed in this subsection.

Step 8a: Die Saw

In this step the top coupons are diced. Each top coupon wafer contains 21 dies. Since the thin membranes can not be put under vacuum and since the through etched in-plane flexure cannot support a vacuum, the wafer is secured to a dummy wafer gold side up using crystal bond and than diced with a die saw. The crystal bond is then removed using 80°C deionized water.

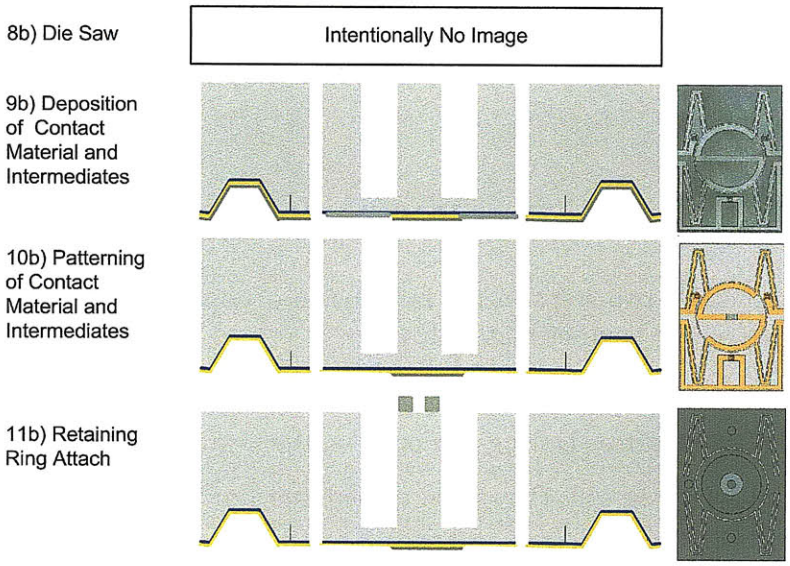

Figure 5-14: The last four steps in the fabrication of top coupons with a sputtered or evaporated non-gold contact material.

Step 9a: Retaining Ring Attach

In this step, the washer which acts as a retaining ring for the force probe is attached to the stiff cylindrical boss of each top coupon. This is done using Krazy Glue. The retaining rings used have a 5/32" OD a 1/16" ID, and a thickness of 1/32". They are aligned by hand.

5.2.3 Top Coupon Additional Steps for Sputtered or Evaporated non-Gold Contact Material

If a sputtered or evaporated non-gold is the contact material, four additional fabrication steps are required after the initial seven common fabrication steps for top coupon wafers. These are shown in Figure 5-14. These steps are detailed in this subsection.

Step 8b: Die Saw

In this step the top coupons are diced. Each top coupon wafer contains 21 dies. Since the thin membranes can not be put under vacuum and since the through etched in-plane flexure cannot support a vacuum, the wafer is secured to a dummy wafer gold

side up using crystal bond and than diced with a die saw. The crystal bond is then removed using 80°C deionized water. The wafer is diced before the contact material is applied because the die saw is typically a relatively dirty machine and can contaminate the contact material. Therefore not exposing the contact material to the die saw is preferable.

Step 9b: Deposition of Contact Material and Intermediates

In this section, the desired contact material is evaporated or sputtered. Intermediate layers may be required. For example, aluminum should not be sputtered onto gold because an intermetallic can form. A thin layer of titanium, around 300 Å should be sputtered between the aluminum and gold. There is a small increase in the resistance due to this addition. For a 300 Å layer of titanium between an aluminum contact and a gold trace having a contact area of 225 μm^2, the increase in contact resistance cab be calculated from the following equation:

$$R_{add} = \frac{\rho L}{A} \tag{5.7}$$

where L is the thickness of the contact, A is the area of the contact, and ρ is the resistivity of titanium which is 4.2x10^{-}7 Ωm. The increased resistance from the titanium in this case would be 56 μΩ. Low, stable values of contact resistance tend to be in the 10s of mΩ range, so this contribution is negligible.

Step 10b: Patterning of Contact Material and Intermediates

After the sputtering or evaporation of the final contact material and any intermediates, a small drop of photo resist is placed on the center of each coupon. This photo resist is baked in an oven at 100°C for fifteen minutes. Then the contact material and any intermediates are etched away using appropriate chemicals. The photo resist is stripped leaving a top coupon with a gold trace and a small amount of contact material in the center. This is shown in Figure 5-15.

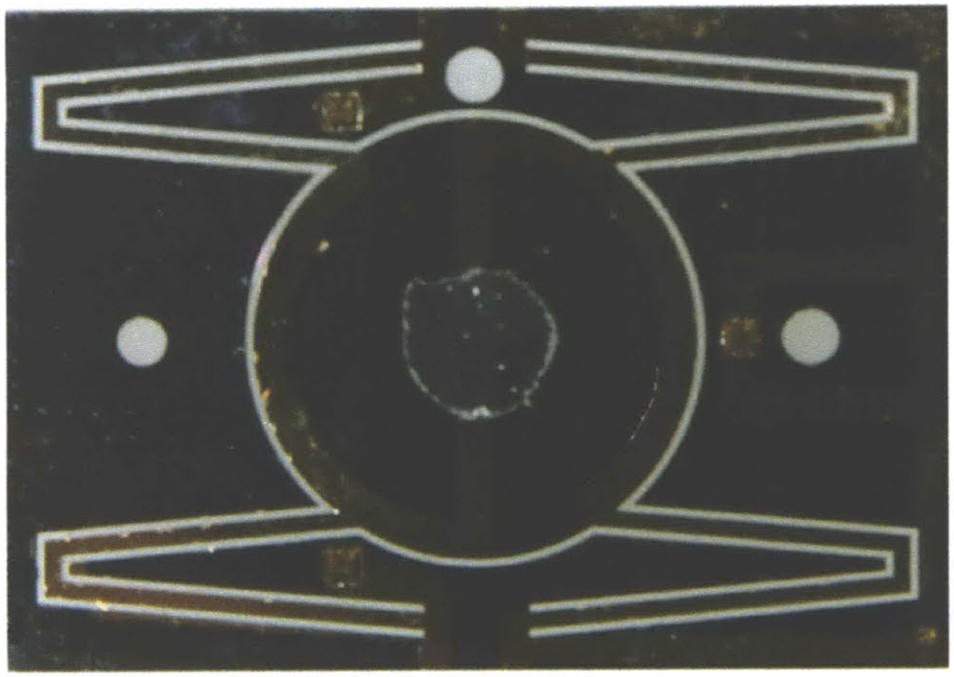

Figure 5-15: Contact material on a single top coupon.

Step 11b: Retaining Ring Attach

In this step, the washer which acts as a retaining ring for the force probe is attached to the stiff cylindrical boss of each top coupon. This is done using Krazy Glue. The retaining rings used have a 5/32" OD a 1/16" ID, and a thickness of 1/32". They are aligned by hand.

5.2.4 Top Coupon Additional Fabrication Steps for Plated Contact Material

If the contact material on the top coupon is plated, five additional fabrication steps are required after the initial seven common fabrication steps for top coupon wafers, which are shown in Figure 5-10. The five additional steps are shown in Figure 5-16. These steps are detailed in this subsection.

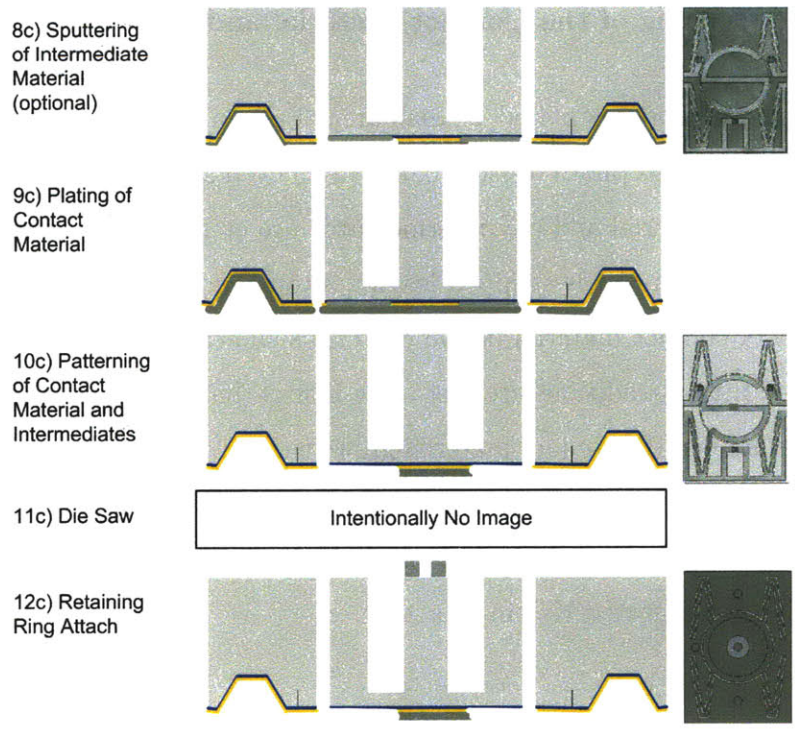

Figure 5-16: The last five steps in the fabrication of top coupons with a plated contact material.

Step 8c: Sputtering of Intermediate Material (Optional)

This step depends on the material being plated. Gold can be plated directly onto the gold trace. However, copper forms an intermetallic with gold and should not be platted directly onto gold. Instead, a thin layer of titanium and a thin layer of copper should be sputtered and the copper plated onto that.

Step 9c: Plating of Contact Material

In this step, the contact material is plated. If an intermediate layer is used, the entire wafer is plated. If no intermediate layer is used, only the gold trace is plated. The pattern of the gold trace, shown in Figure 5-12, allows the entire wafer to be plated easily because all the gold traces are connected.

Step 10c: Patterning of the Contact Material and Intermediates

After the contact material is plated, a small area of photo resist is painted on the center of each coupon. This photo resist is baked in an oven at 100°C for fifteen minutes. Then the contact material and any intermediated are etched away using appropriate chemicals. The photo resist is stripped leaving a top coupon with a gold trace and a small amount of contact material in the center, as shown in Figure 5-15. This step can be skipped if two conditions are met. The first is that no intermediate layers are used. The second is if the contact material grows either no oxide or grows a relatively conductive oxide, such as platinum metal groups oxides and specific rhodium oxides [35]. In this case the contact material can be left on the trace because it will not interfere with the integrated Kelvin structure.

Step 11c: Die Saw

In this step the top coupons are diced. Each top coupon wafer contains 21 dies. Since the thin membranes can not be put under vacuum and since the through etched in-plane flexure cannot support a vacuum, the wafer is secured to a dummy wafer gold side up using crystal bond and then diced with a die saw. The crystal bond is then removed using 80°C deionized water. For plated contact materials, the coupons are diced after plating so that all the plating can be done at once and does not have to be done on the individual die level.

Step 12c: Retaining Ring Attach

In this step, the washer which acts as a retaining ring for the force probe is attached to the stiff cylindrical boss of each top coupon. This is done using Krazy Glue. The retaining rings used have a 5/32" OD a 1/16" ID, and a thickness of 1/32". They are aligned by hand.

5.2.5 Top Coupon Wafers Additional Fabrication Steps for Other Contact Materials

Other contact materials not specifically addressed in this chapter can also be deposited onto the top coupon. For example, solder can be flowed over the center of the gold trace to test the contact resistance of a tip on solder. Whenever depositing a new type of contact material, attention must be paid to the height of the contact material because of the effect on the gap between the contact material and contact tip. Attention must also be paid to any intermediate layers to assure the have no measurable effect on contact resistance.

5.2.6 Bottom Coupon Wafers Common Steps for Fabrication

For bottom coupons having a flat contact area, a plated tip, or an externally fabricated tip, the first five fabrication steps are the same. Flat contact area coupon wafers go through an additional five fabrication steps, plated tip coupon wafers go through an additional six fabrication steps, and externally fabricated tip coupon wafers go through an additional seven fabrication steps. Bottom coupon wafers which contain embedded glass spheres go through a different fabrication process which is discussed after the fabrication processes for flat contact area, a plated tip, or an externally fabricated tip bottom coupon wafers. For bottom coupon wafers having a flat contact area, a plated tip, or an externally fabricated tip, the first five fabrication steps are shown in Figure 5-17. Each of these five steps is discussed in this subsection.

Step 1: Alignment Marks

This step is identical to the first step of the fabrication of the first generation ball/pit design. The first step in fabrication is placing alignment marks near the centers of the wafers. The wafers are coated with HDMS to improve the adhesion of photo resist. The wafers are coated with 2 μm of thin positive resist which is then patterned using standard lithography methods. The wafers are then etched in the STS deep reactive ion etcher (DRIE) using SF_6 plasma for thirty seconds. This etches the alignment

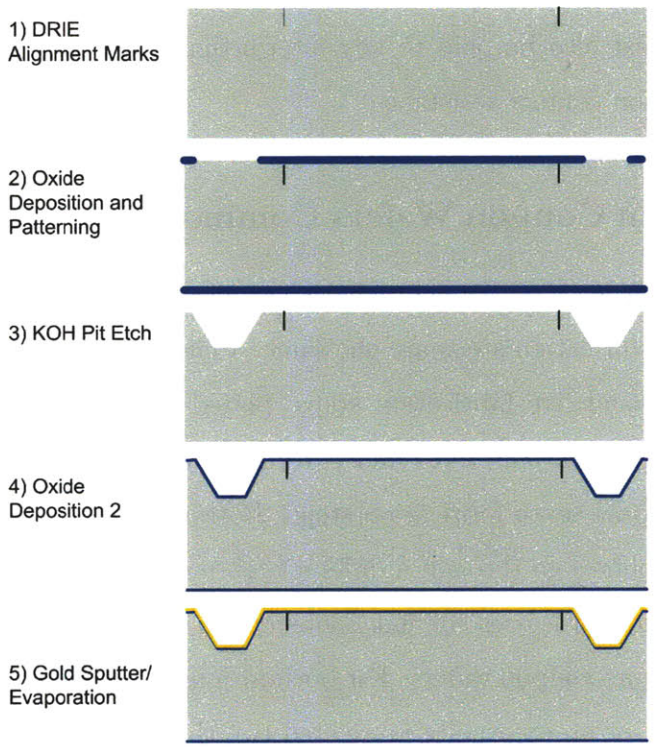

Figure 5-17: The five common steps of fabrication used for bottom coupon wafers having a flat contact area, a plated tip, or an externally fabricated tip.

mark pattern about 1 micron into the surface of the wafer. Afterwards, the wafers are placed in an oxide asher to remove any residual Teflon from the DRIE process. The wafers are then stripped of photo resist. The result is two alignment marks whose structure and location on the wafer are shown in Figure 3-10.

Step 2: Oxide Deposition and Patterning

In order to avoid some of the problems caused by removing nitride, such as the breakage of wafers in hot phosphoric acid, oxide was used for the mask for the KOH-etched pits. Nitride has an etch rate of virtually 0 nm/min in KOH, however, Oxide has a an etch rate of about 7.7 nm/min. Since the KOH-etch for the pits is 368 minutes, 2833 nm, or 2.833 μm, of oxide will be etched away during the KOH etch. Therefore 3 μm of oxide are thermally grown on the wafers to serve as a mask for the KOH etch. This oxide is grown in a furnace at 1100 C. It takes approximately 18 hours to reach the thickness of 3 μm.

The oxide is pattered to create a mask of circles that will be come the KOH-etched pits. First the backs of the wafers are coated with photo resist. This is done to protect them during the subsequent BOE. The are baked on a hotplate at 120°C for two minutes. Next, the front side of the wafers are coated with 2 μm of thin resist. They are then placed in a 100°C oven for 15 minutes. A hot plate cannot be used because the backside of the wafer is already coated with resist. Afterwards, they were exposed through a mask under 100 J of UV light and developed. The alignment marks are then painted over with photo resist. The wafers are then backed in a 120°C oven for 20 minutes. The exposed oxide is then etched using 32° 6:1 BOE. It takes 30 minutes to etch through the 3 μm of oxide. The photo resist is then stripped.

Step 3: KOH Pit Etch

The top and bottom wafers are etched in 80°C 30% KOH in order to etch the pits. The etch rate is 1.08 μm/min. The target etch depth is 420 μm and the target etch width is 955 μm. Therefore, the etch lasts approximatley 389 minutes. The lateral dimensions of the KOH-etched pits are checked to ensure that they are approximatley

955 μm across. After the etch, the wafers are cleaned by soaking in 45° HCL for five minutes. After the KOH-etch, a thin layer of oxide remains. This is removed with a 5 minute 32° 6:1 BOE dip.

Step 4: Oxide Deposition 2

The purpose of this step is to deposit a barrier layer of oxide between the silicon and the metal traces. The wafers are returned to the oxide furnace where 0.5 μm of oxide is thermally grown at 1100°C. This takes approximately 39 minutes not including temperature ramp up and ramp down time.

Step 5: Gold Sputter/Evaporation

In this step either sputtered gold or evaporated gold can be deposited. First, a 300 Å adhesion layer of titanium is deposited. Next 1000 Å of gold is deposited unless sputtered or evaporated gold is the contact material. In that case, the desired thickness of the contact material should be deposited.

5.2.7 Bottom Coupon Wafers Additional Fabrication Steps for Flat Contact Areas

For bottom coupon wafers with flat contact areas (as opposed to plated or externally fabricated and attached tips), five additional steps are needed after the five common steps to complete fabrication. These are shown in Figure 5-18. These five steps are discussed in this subsection.

Step 6a: Gold Trace Patterning

In this step, the gold and titanium are etched using appropriate chemistries to create the gold traces on the bottom coupon. First, 2 μm of thin positive resist is spun on the wafer. It is patterned using standard lithography techniques. The gold and titanium layers are etched using appropriate chemistries. Finally, the photo resist is stripped.

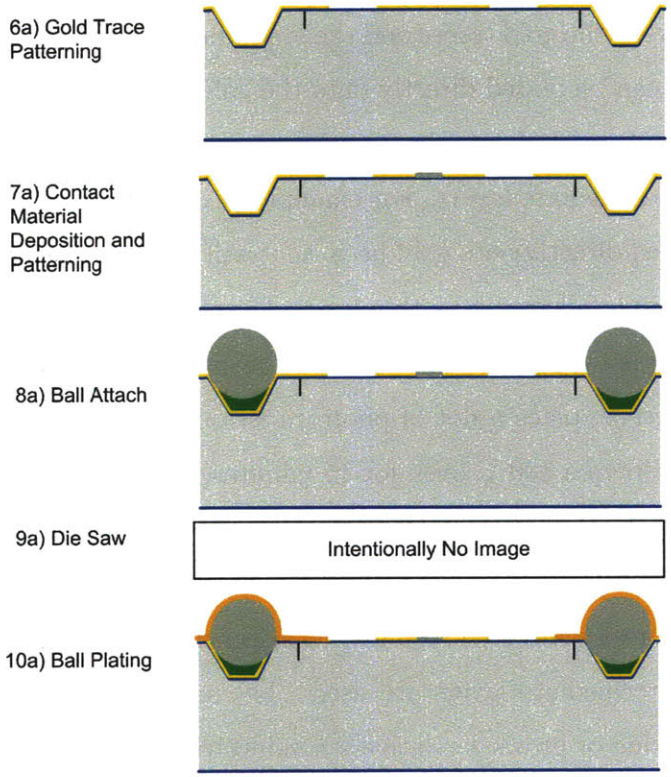

Figure 5-18: The five additional steps needed to fabricate bottom coupons having flat contact areas.

Step 7a: Contact Material Deposition and Patterning

In this step, the contact metal is applied assuming that sputtered or evaporated gold is not the contact material. If sputtered or evaporated gold is the contact material, skip this step. For sputtered or evaporated contact materials, blanket coat the wafer with the contact material and any intermediates. Intermediates are applied to prevent the formation of intermettalics. For example, if aluminum is sputtered directly onto gold, it will form a resistive intermettalic. Therefore a thin layer of titanium should be sputtered between the gold traces and the aluminum. For plated contact materials, certain materials can be plated directly onto the gold traces. For example, most gold and gold alloys can be plated directly onto the traces. However, some plated materials need sputtered intermediate layers. For example, if copper is the contact material it cannot be sputtered directly onto gold because it will form an intermetallic. Instead a thin layer of titanium followed by a thin layer of copper should be sputtered onto the wafer. The copper is then plated onto the thin layer of sputtered copper. To pattern any of these materials, place a dot of photo resist on the center of each coupon and then bake the wafers in a 100°C oven for 15 minutes. Then etch the contact material and any intermediates and strip the photo resist. This will leave gold traces and a small area of contact material in the center of each coupon. If the contact material is plated, this photo resist and etch step can be skipped if two conditions are met. The first is that no intermediate layers are used. The second is if the contact material grows either no oxide or grows a relatively conductive oxide, such as platinum metal groups oxides and specific rhodium oxides [35]. In this case the contact material can be left on the trace because it will not interfere with the integrated Kelvin structure.

Step 8a: Ball Attach

This step secures the precision 1/32" stainless steel balls inside the KOH-etched pits. First, a small amount of Norland conductive epoxy NCA 130 is placed in each pit. Then a ball is placed in each pit. The amount of conductive epoxy should be small enough that when the balls are pressed into the pits, no epoxy is forced out of the

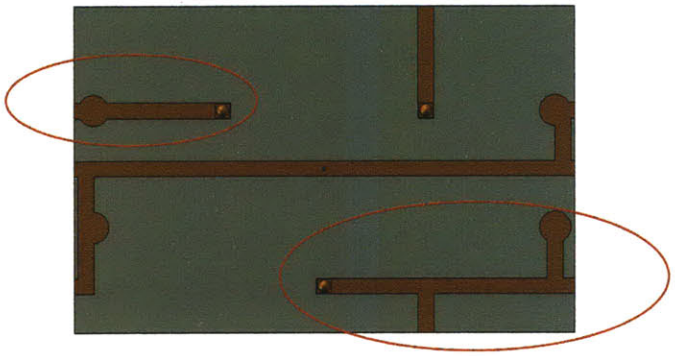

Figure 5-19: The two areas which are plated to ensure good conductivity between the balls and the top coupon.

pits. The wafers are then baked in a 125°C oven for two hours to cure the epoxy.

Step 9a: Die Saw

The wafers are diced conventionally. Each bottom coupon wafer contains 16 individual coupons.

Step 10a: Ball Plating

On each bottom coupon, two balls are part of the integrated Kelvin structure, as shown in Figure 5-9. These two balls are flash plated with 400 Å of gold to improve the electrical connection between the balls and the KOH-etched pits of the top coupon. This is done by attaching an alligator clip to the end of each of the two traces containing these balls and lowering them into gold plating solution. The plating current is approximately 2 mA and the time to plate is about 15 seconds. The two metal traces requiring plating are shown in Figure 5-19.

5.2.8 Bottom Coupon Wafers Additional Fabrication Steps for Plated and Externally Fabricated Tips

The fabrication processes for bottom coupon wafers with plated tips and those with externally fabricated tips are very similar. Both begin with the five common steps for bottom coupon wafer fabrication shown in Figure 5-17. They each have a different

sixth step. Then they go through 4 additional identical steps. Finally, the bottom coupon wafers having externally fabricated tips go through one additional step. These steps are shown in Figure 5-20. These steps are detailed in this subsection.

Step 6b: Tip Target Plating

This step is performed only on bottom coupon wafers which will have externally fabricated tips attached. The purpose of this step is to plate a 100 nm target on the center of the coupon. This target is later used to visually align the externally fabricated tips to the coupon before attaching them. First, 2 μm of thin positive resist is spun onto the wafer. It is patterned using standard lithography techniques. Then the target is plated onto the wafers in Nickel Cobalt. This is a very fast plate and is done at 1 mA and takes only six seconds. The result is a truncated circle 100 nm tall that can be used to orient the externally fabricated tips. This is shown in Figure 5-21. The photo resist is then stripped.

Step 6c: Tip Plating

This step is performed only on bottom coupon wafers with plated tips. 2 μm of thin positive resist is spun onto each wafer. It is patterned using standard lithography techniques. Each bottom coupon wafer contains 16 bottom coupons or dies. A tip is patterned in the center of each of these 16 coupons. The mask has four different tip types: an 84 μm diameter circle, a 42 μm diameter circle, a square diamond having 15 μm sides and 90° angles, and an elongated diamond having 23.7 μm sides, two 127° angles, and two 53° angles. Each of these four tip types appears four times on the wafer. Therefore each bottom coupon wafer will produce four coupons with each type of tip. These tip geometries are shown in Figure 5-22. These tips are then plated to the desired height. This is typically on the order of 5 μm. Any material can be used. Typically, this tip itself might be made of a hard material and then coated with another material with better contact resistance characteristics, such as a conductive oxide or lack of an oxide. Both the bulk material plating and the coating of the tip with any additional materials are performed during this step. The photo

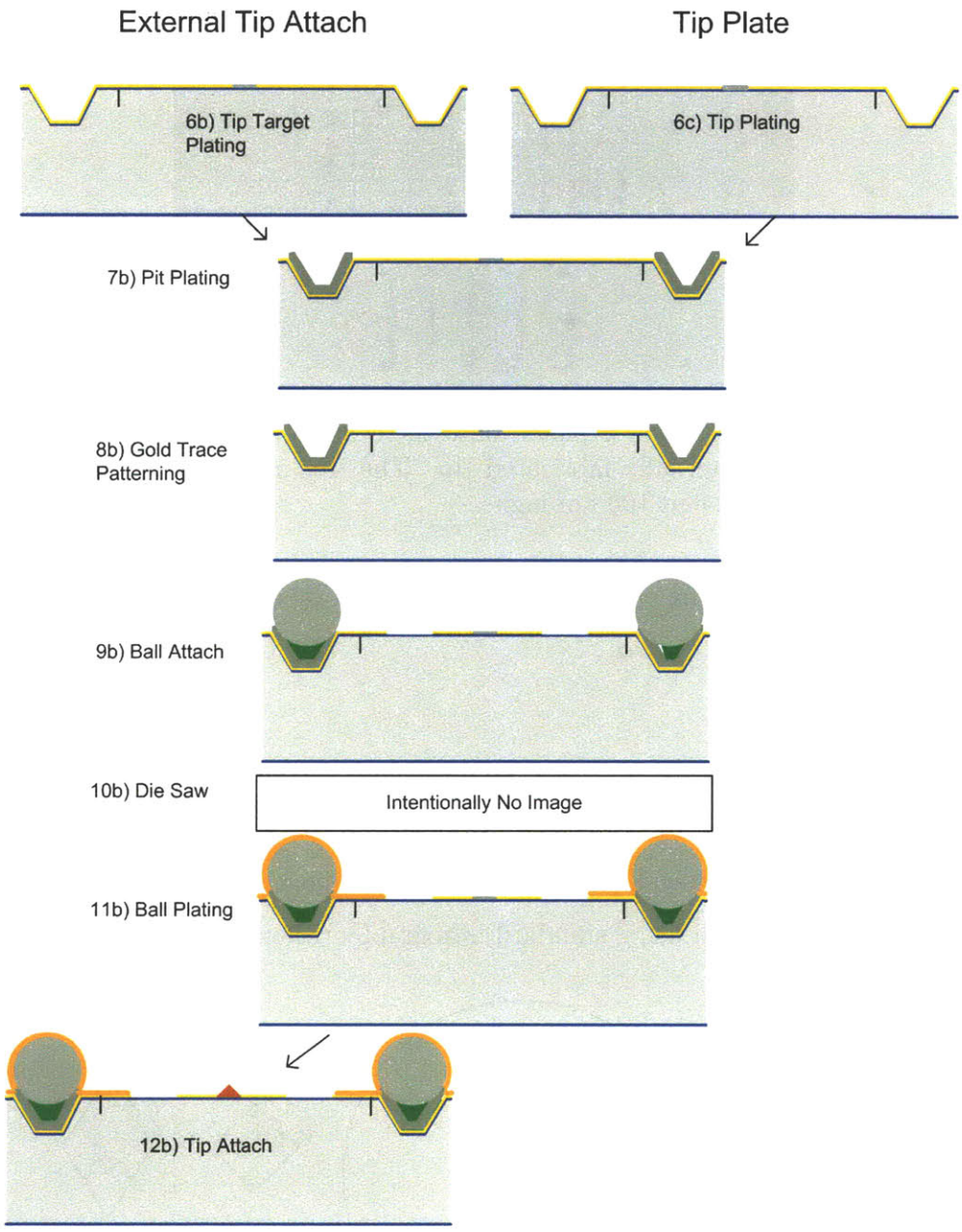

Figure 5-20: The additional fabrication steps for bottom coupon wafers having plated tips or externally fabricated attached tips.

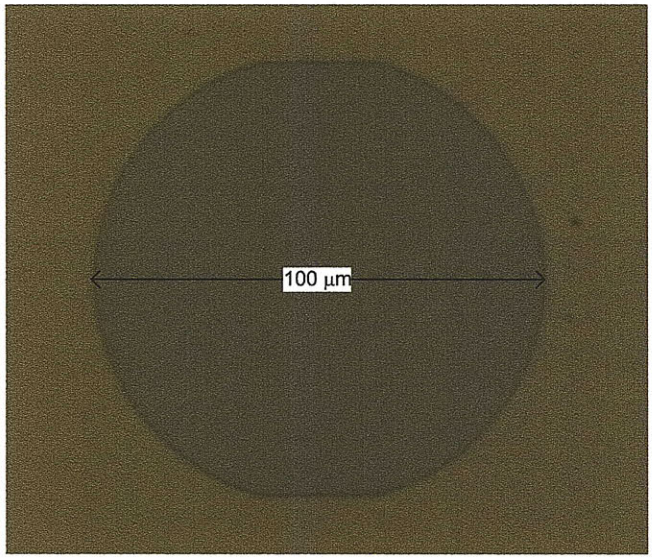

Figure 5-21: The target which is plated onto the center of each coupon to facilitate the alignment of an externally fabricated tip. The tips are visually aligned to the target. This target is plated 100 nm high.

resist is then stripped. Any other tips could be plated by changing the mask.

Step 7b: Pit Plating

In this step, the KOH-etched pits are plated with nickel cobalt to compensate for the height of the contact tip as well as the height of the contact material. The plating thickness is calculated using Equation 5.1. 2 μm of thin positive resist is spun onto the wafer. It is patterned using standard lithography techniques. The mask used to

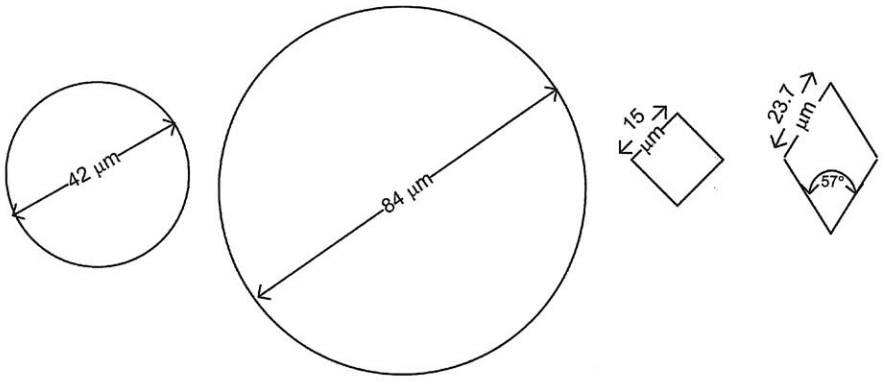

Figure 5-22: The four types of 2.5 dimensional tips which are plated directly onto the bottom coupon wafers.

pattern the oxide prior to the KOH-etch is also used in this step. The pits are plated to the desired thickness. The photo resist is then stripped.

Step 8b: Gold Trace Patterning

In this step, the gold traces are patterned. This is done after the plating steps because the plating is more uniform if there is a blanket seed layer on the wafer. 2 μm of thin positive resist is spun onto the wafer. It is patterned using standard lithography techniques. The gold and titanium are then etched using appropriate chemistries. The photo resist is then stripped.

Step 9b: Ball Attach

This step secures the precision 1/32" stainless steel balls inside the KOH-etched pits. First, a small amount of conductive epoxy is placed in each pit. Then a ball is placed in each pit. The amount of conductive epoxy should be small enough that when the balls are pressed into the pits, no epoxy is forced out of the pits. The wafers are then baked in a 125°C oven for two hours to cure the epoxy.

Step 10b: Die Saw

The wafers are diced conventionally. Each bottom coupon wafer contains 16 individual coupons.

Step 11b: Ball Plating

On each bottom coupon, two balls are part of the integrated Kelvin structure, as shown in Figure 5-9. These two balls are flash plated with 400 Å of gold to improve the electrical connection between the balls and the KOH-etched pits of the top coupon. This is done by attaching an alligator clip to the end of each of the two traces containing these balls and lowering them into gold plating solution. The plating current is approximately 2 mA and the time to plate is about 15 seconds. The two metal traces requiring plating are shown in Figure 5-19. At this point, the bottom wafer coupons containing the plated tips are complete.

Step 12b: Tip Attach

If externally are to be attached to the bottom coupon wafers, it is done in this last step. The tip is aligned to the plated target shown in Figure 5-21. The tip is then rigidly attached using conductive epoxy, solder, or another type of conductive adhesion method. Conductive epoxy tends to provide better control over flatness. This assembly steps tends to be more or an art form than a standard process and requires skill on the part of the operator.

5.2.9 Bottom Coupon Wafers Additional Fabrication Steps for Embedded Glass Sphere Tips

If the tips on the bottom coupon wafers consist of embedded glass spheres which are then coated with contact material, then the fabrication process is slightly different that that for flat, plated, or externally fabricated tips. The first three steps of common fabrication are performed, which are shown in Figure 5-17. Ten additional fabrication steps are then performed which are shown in Figure 5-23. These steps are detailed in this subsection.

Step 4d: DRIE Trench Etch

In order to embed the glass spheres in the coupons, trenches are etched equal to one half of the diameter of the glass spheres which will be embedded. The glass spheres are then potted in epoxy inside these trenches. This step etches those trenches. First, 2 μm of thin positive resist is spun onto the wafer. It is patterned using standard lithography techniques. The mask used to pattern the trenches is actually the same mask used to create the tip target feature used when attaching externally fabricated tips to the bottom coupon wafers. The shape pattered in the photo resist is shown in Figure 5-21. This shape is plated to create the target structure for the externally fabricated tips. However in this case, the shape is etched into the wafer using DRIE. The etch depth is equal to one-half of the sphere diameter. For 84 μm and 42 μm spheres, the etch depths are 42 μm and 21 μm respectively. The etch rate is around

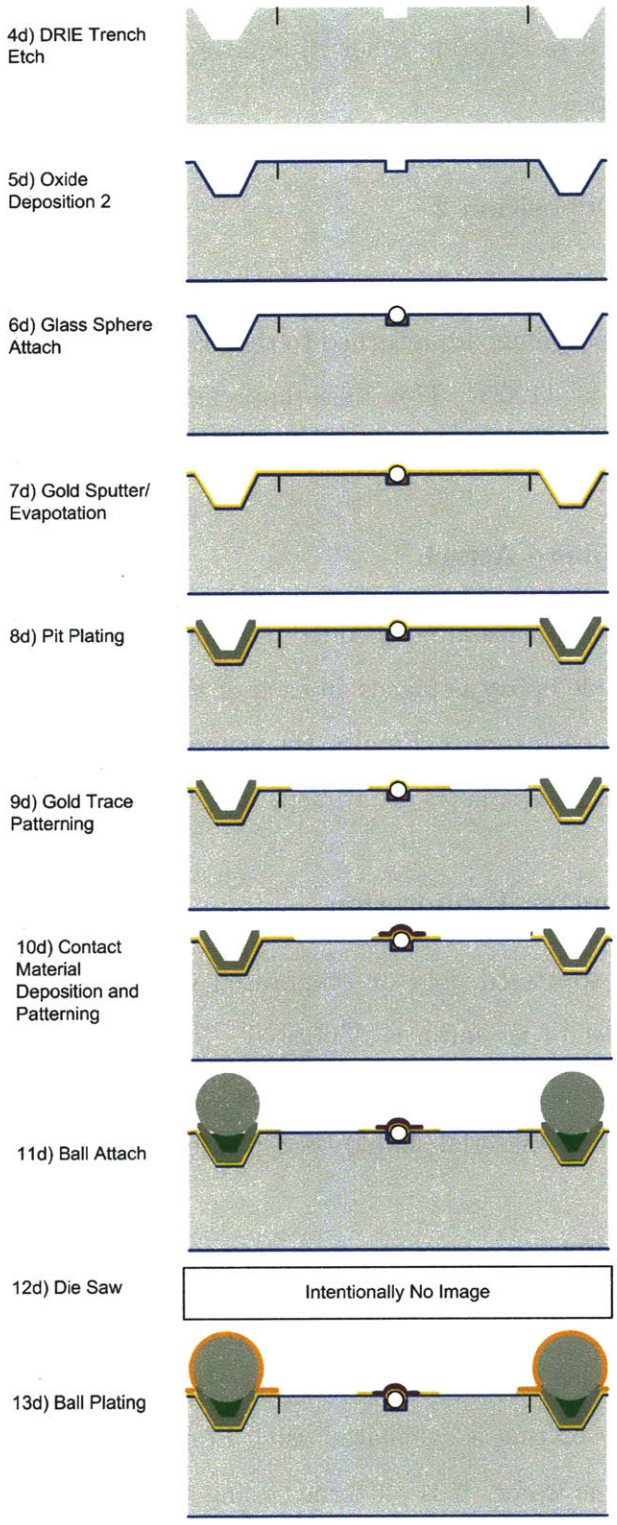

Figure 5-23: The final ten steps of fabrication for bottom coupon wafers having embedded glass tips.

2.5 μm/min, so this etch takes between 8 and 17 minutes. After the etch is complete, the wafers are placed in an oxide asher to remove any residual Teflon. Finally, the photo resist is stripped.

Step 5d: Oxide Deposition 2

The purpose of this step is to deposit a barrier layer of oxide between the silicon and the metal traces. The wafers are returned to the oxide furnace where 0.5 μm of oxide is thermally grown at 1100°C. This takes approximately 39 minutes not including temperature ramp up and ramp down time.

Step 6d: Glass Sphere Attach

In this step, the glass spheres are embedded into the bottom coupon wafers. A small amount of UV curable epoxy is placed in each of the center trenches. Next, a glass sphere is dropped in each trench. Finally, the wafers are placed in a UV oven to cure the epoxy. Since the glass spheres are transparent, the epoxy beneath them is cured.

Step 7d: Gold Sputter/Evaporation

In this step either sputtered gold or evaporated gold can be deposited. First, a 300 Å adhesion layer of titanium is deposited. Next 1000 Å of gold is deposited unless sputtered or evaporated gold is the contact material. In that case, the desired thickness of the contact material should be deposited.

Step 8d: Pit Plating

In this step, the KOH-etched pits are plated with nickel cobalt to compensate for the height of the embedded glass sphere as well as the height of the contact material. The thickness of the plating is calculated using Equation 5.1. 2 μm of thin positive resist is spun onto the wafer. It is patterned using standard lithography techniques. The mask used to pattern the oxide prior to the KOH-etch is also used in this step. The pits are plated to the desired thickness. The photo resist is then stripped.

Step 9d: Gold Trace Patterning

In this step, the gold traces are patterned. This is done after the plating step because the plating is more uniform if there is a blanket seed layer on the wafer. 2 μm of thin positive resist is spun onto the wafer. It is patterned using standard lithography techniques. The gold and titanium are then etched using appropriate chemistries. The photo resist is then stripped.

Step 10d: Contact Material Deposition and Patterning

In this step, the contact metal is applied assuming that sputtered or evaporated gold is not the contact material. If sputtered or evaporated gold is the contact material, skip this step. For sputtered or evaporated contact materials, blanket coat the wafer with the contact material and any intermediates. Intermediates are applied to prevent the formation of intermettalics. For example, if aluminum is sputtered directly onto gold, it will form a resistive intermettalic. Therefore a 300 Å layer of titanium should be sputtered between the gold traces and the aluminum. For plated contact materials, certain materials can be plated directly onto the gold traces. For example, most gold and gold alloys can be plated directly onto the traces. However, some plated materials need sputtered intermediate layers. For example, if copper is the contact material it cannot be sputtered directly onto gold because it will form an intermetallic. Instead 300 Å of titanium followed by 1000 Å of copper should be sputtered onto the wafer. Copper can then be plated onto the thin layer of sputtered copper. To pattern any of these materials, place a dot of photo resist over the glass sphere tip and then bake the wafers in a 100°C oven for 15 minutes. Then etch the contact material and any intermediates and strip the photo resist. This will leave gold traces and a small area of contact material over the embedded glass sphere. If the contact material is plated, this photo resist and etch step can be skipped if two conditions are met. The first is that no intermediate layers are used. The second is if the contact material grows either no oxide or grows a relatively conductive oxide, such as platinum metal groups oxides and specific rhodium oxides [35]. In this case the contact material can be left

on the trace because it will not interfere with the integrated Kelvin structure.

Step 11d: Ball Attach

This step secures the precision 1/32" stainless steel balls inside the KOH-etched pits. First, a small amount of conductive epoxy is placed in each pit. Then a ball is placed in each pit. The amount of conductive epoxy should be small enough that when the balls are pressed into the pits, no epoxy is forced out of the pits. The wafers are then baked in a 125°C oven for two hours to cure the epoxy.

Step 12d: Die Saw

The wafers are diced conventionally. Each bottom coupon wafer contains 16 individual coupons.

Step 13d: Ball Plating

On each bottom coupon, two balls are part of the integrated Kelvin structure, as shown in Figure 5-9. These two balls are flash plated with 400 Å of gold to improve the electrical connection between the balls and the KOH-etched pits of the top coupon. This is done by attaching an alligator clip to the end of each of the two traces containing these balls and lowering them into gold plating solution. The plating current is approximately 2 mA and the time to plate is about 15 seconds. The two metal traces requiring plating are shown in Figure 5-19.

5.2.10 Fabrication of Bottom Coupon Wafers having other Types of Contact Tips

It is possible to create bottom coupon wafers having contact tips not specifically described in this section. For example, carbon nanotubes can be grown directly onto the surface of these coupons or diamond chips can be implanted into the gold traces. The fabrication of different types of tips would vary, but would be largely similar to the fabrication methods described in this section.

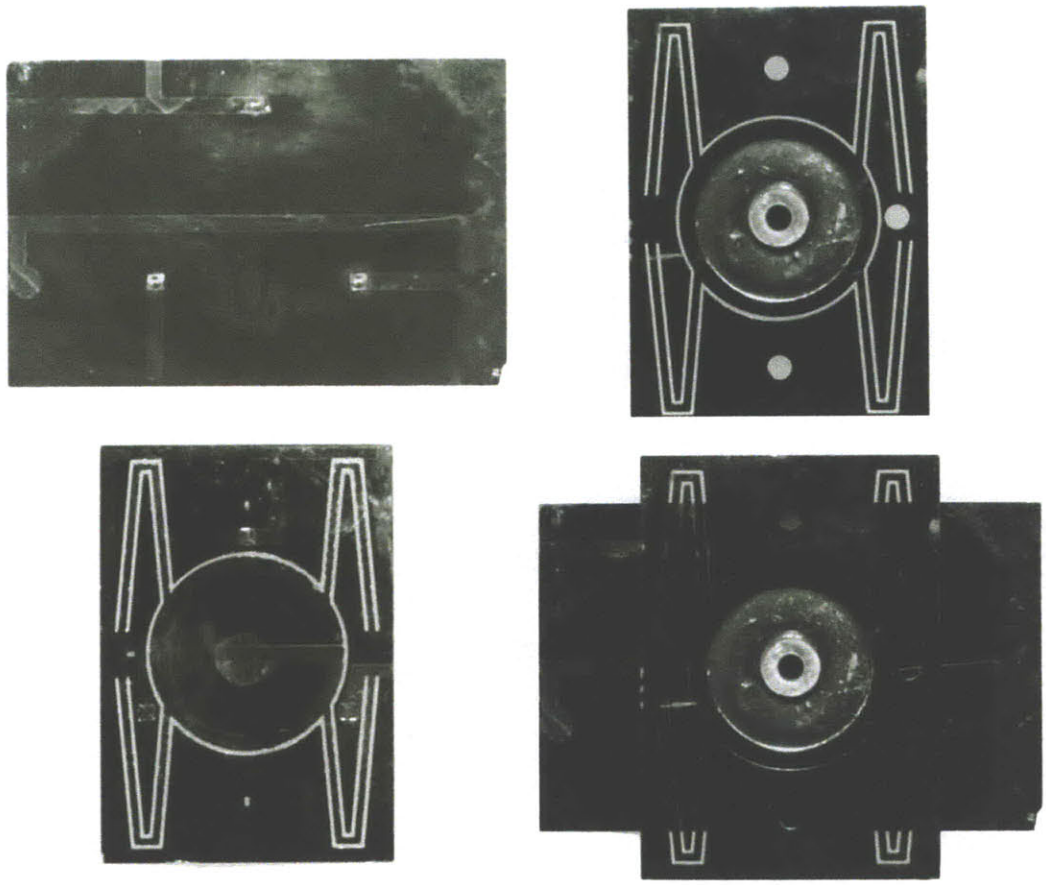

Figure 5-24: The final two-coupon system

5.2.11 Finished Coupons

The completed final two-coupon system is shown assembled and disassembled in Figure 5-24.

5.3 Position Error Analysis and Measurement

One of the important functional requirements of this two-coupon system is that it be able to be taken apart, so the contact surfaces can be analyzed, and put back together in a repeatable manner, so that tests can resume. This repeatability is limited by certain aspects of the system which are not entirely repeatable. There are four errors that can occur: gap height error, parallelism error, translational error, and rotational

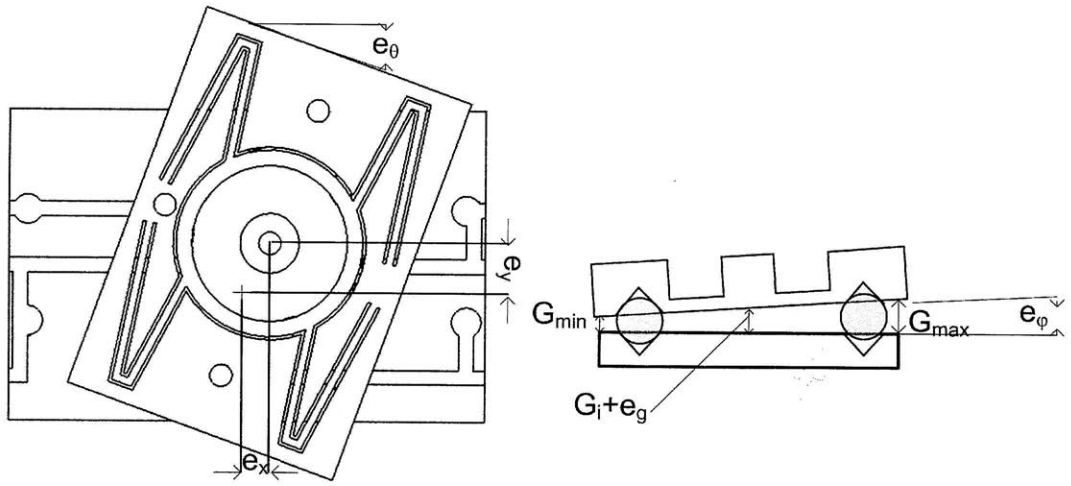

Figure 5-25: The four measurable errors of the final two-coupon system: translational, e_x and e_y; rotational, e_θ; gap, e_g, and parallelism, e_ϕ.

error. These errors are shown in Figure 5-25.

5.3.1 Gap Height Error

As shown in Figure 5-26, the gap, and therefore gap error, are determined by a combination of the pit width, the ball diameter, the plating up of the pits, and any error caused by the conductive epoxy. Since the bottom coupon is plated, it is difficult to optically measure the pit width. Therefore an alternative method of approximating the gap was found. The important dimensions for this alternative method are ball diameter, D, pit width of the top coupon, $W_{pit-min}$, and the characteristic height between the top of the ball and the top surface of the bottom coupon, H. This measured characteristic height H incorporates all of the errors from the width of the bottom coupon pits, the plating, and the conductive epoxy. These dimensions are shown in Figure 5-27. It should be noted that H was measured throughout the process. It remained the same before and after the conductive epoxy step, meaning that the conductive epoxy added no measurable error. The total gap G can be described by the geometry in Figure 5-27 as

$$G = H - \frac{D}{2} + \frac{D \sin 35.3}{2} - \frac{W_{pit-min} - D \cos 35.3}{2 \tan 35.3} \tag{5.8}$$

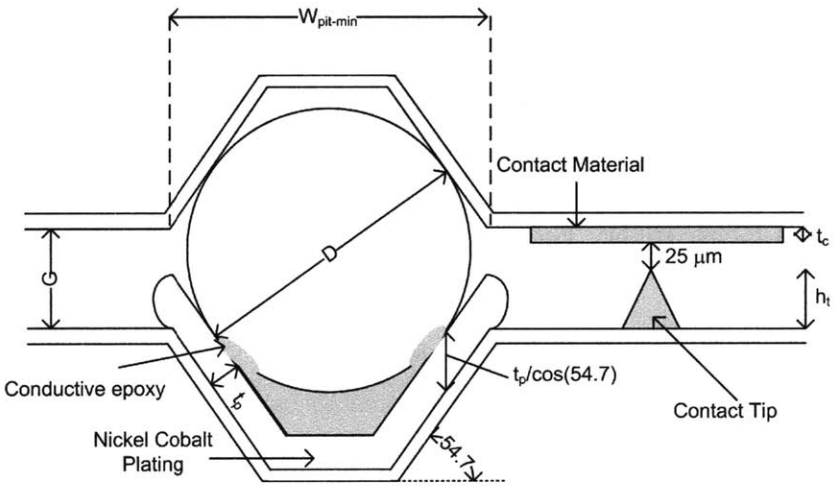

Figure 5-26: The contributors to the gap between the coupons G.

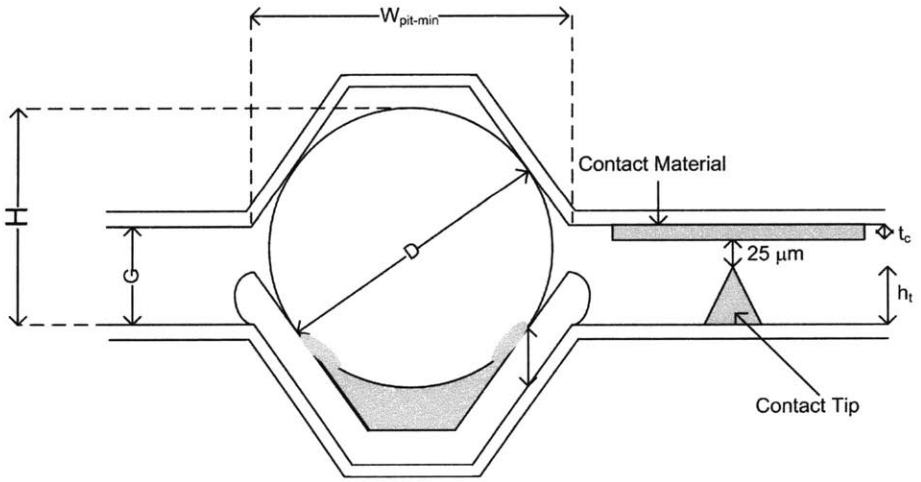

Figure 5-27: Additional contributors to the gap between the coupons G.

Figure 5-28: Left: Focus on the metal surrounding the pit. Center: The top of the ball just out of focus. Right: The top of the ball in focus.

The characteristic height H is very easy to measure. It is done by focusing on metal deposited on the wafer surface and then focusing on the top of the ball and subtracting the focal heights. That top of the ball can be found very easily by bringing the focus upwards. The focused area on the ball will become a smaller and smaller circle until only a small spot on the top of the ball is in focus. This is shown in Figure 5-28. It is crucial that the z-axis focus be calibrated correctly during these measurements

The gap error, e_g, is the difference between the design gap, G, and the actual gap, G_i, as shown in the following equation.

$$e_g = \bar{G} - G_i \tag{5.9}$$

In the final version of the two-coupon system, the design gap varies based on the tip which will be placed on the coupon. The error analysis was completed for a coupon containing a 42 μm tip which therefore had a design gap of 67 μm. This leaves a 25 μ gap between the contact tip and the top coupon. In order to predict the error, the error from the three components, ball diameter, characteristic height, and top coupon pit width, were examined.

The balls used are precision stainless steel balls, but are still not perfect spheres. They are Grade 25 balls with a target diameter or 1/32", or 794 μm. In the first version of the two-coupon system, Grade 3 balls were used. Grade 3 balls are expensive, \$12 each, but in the first design the same set of balls could be used on multiple

	μ"	μm
Allowable Ball Diameter Variation Δ_{bdv}	25	0.635
Deviation from Spherical Form Δ_{dsf}	25	0.635
Surface Roughness Arithmetical Average Δ_{sraa}	2	0.0508
Basic Diameter Tolerance Δ_{bdt}	+/- 100	+/- 2.54
Allowable Lot Diameter Variation Δ_{aldv}	50	1.27

Table 5.3: Tolerances of Grade 25 Balls

Minimum Average Lot Diameter D_{max}	791.21 μm
Maximum Average Lot Diameter D_{min}	796.29 μm
Maximum Diameter Variation Within a Lot Δ_{max}	2.59 μm

Table 5.4: Variations in Grade 25 Ball Geometry

coupons. In the final two-coupon system, the balls are permanently attached to each coupon, so many more balls had to be purchased. The final version of the two-coupon system also has a 25 μm gap between the tip and the contact material whereas the first version of the system only had a 5 μm gap. Therefore the tolerances of the balls could be slightly looser. That is why Grade 25 balls, which are only \$0.18 each, were chosen. The various tolerances of Grade 25 balls in both micro-inches and microns are listed in Table 5.3.

Within one lot of balls, the difference between the smallest diameter at any point on any ball and the largest diameter at any point on any ball is defined by Equation 3.9. The minimum average ball diameter is defined by Equation 3.10. The maximum average ball diameter is defined by Equation 3.11. These values are summarized in Table 5.4

The characteristic height was measured on 48 ball/pit interfaces after plating and epoxy. The raw data is shown in Figure 5-29. The average, maximum, minimum, and standard deviation of this data is shown in Table 5.5.

As with the first generation two-coupon system, if the pit is non-square, the important dimension for gap height is the shorter of the two sides of the pit. Twenty pits were measured and their minimum pit width and the difference between their maximum and minimum pit widths were recorded. This raw data is shown in Figure 5-30 and the statistics of this data are shown in Table 5.6.

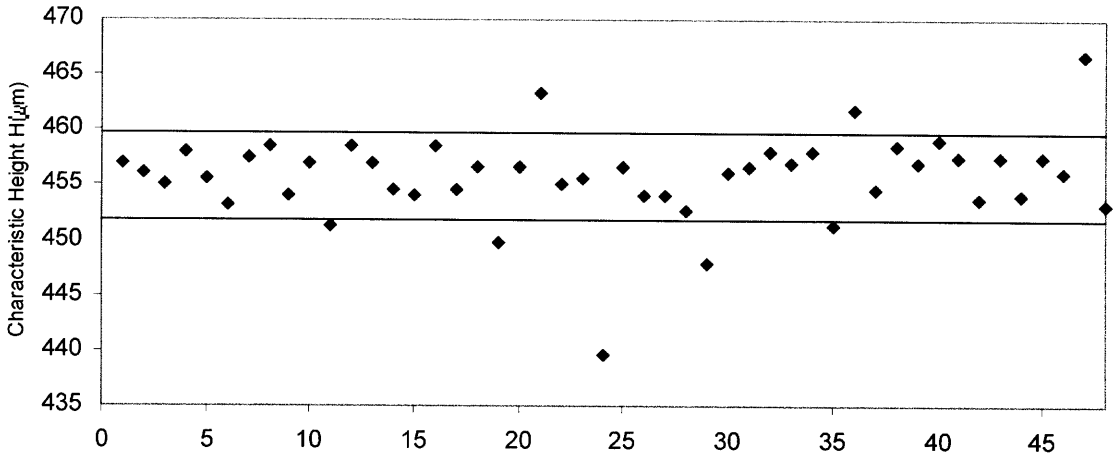

Figure 5-29: The characteristic height H measured on 48 ball/pit interfaces with the use of Grade 25 balls.

	H μm
Average Value	455.8
Standard Deviation	3.9
Maximum Value	466.7
Minimum Value	439.7

Table 5.5: Variability of the Characteristic Height

	W_{min} μm	$W_{max} - W_{min}$ μm
Average Value	957.3	5.36
Standard Deviation	8.5	3.91
Maximum Value	978	12.50
Minimum Value	946.4	0.00

Table 5.6: Variability of Pit Geometry

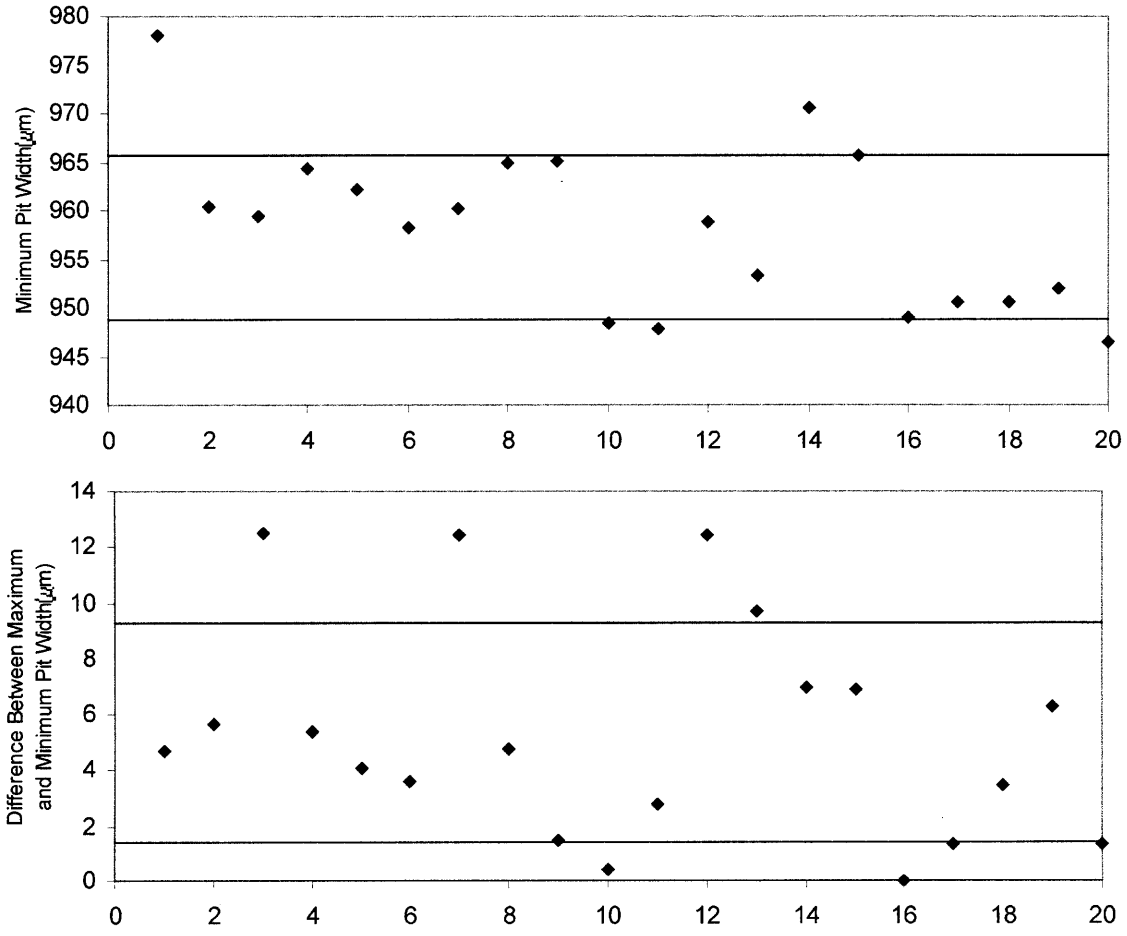

Figure 5-30: The minimum pit width and difference between maximum and minimum pit widths for twenty pits.

	Minimum Case	Maximum Case	Average Case
Ball Diameter μm	789.9	797.6	793.8
Characteristic Height μm	439.7	466.7	455.7
Minimum Pit Dimension μm	978	946.4	957.3
Gap Height μm	38.3	91.3	71.2
Gap Error μm	-28.7	+24.3	+4.2

Table 5.7: The maximum and minimum possible gap heights in the final two-coupon system.

The overall gap height will be highest when the characteristic height and ball diameter are greatest and the pit width is the smallest. The overall gap height will be smallest when the characteristic height and ball diameter are smallest and the pit width is largest. The average gap case, maximum gap case, and minimum gap case are shown in Table 5.7.

All of these calculations were for the total gap between the two coupons. When the 42 μm tall tip is in place, the gap between the tip and the contact material will be this total gap minus the height of the tip. According to the values in Table 5.7, the average gap between the tip and the contact material would be 29.2 μm and in the maximum possible case would be 49.3 μm. However, in the minimum possible gap case, there would actually be an interference between the tip and the coupon of 3.7 μm. However, this case is unlikely to occur as it would require all dimensions being at the absolute end of their tolerance spectrum.

In order to test the predictions for gap height error as well as determine the assembly/disassembly error, gap height was experimentally measured. Gap error was tested by measuring the height difference between the bottom coupon and top coupon at four different places. The thickness of the top coupon, which was measured with micro-meters, was subtracted to get the true gap at each of these four places. This is shown in Figure 5-31.

The gap distance was taken as the average height difference at each of the four locations minus the thickness of the top coupon. This height was measured by focusing on the top coupon and then focusing on the bottom coupon and recording the difference in focal heights. Three sets of coupons were assembled and disassembled five

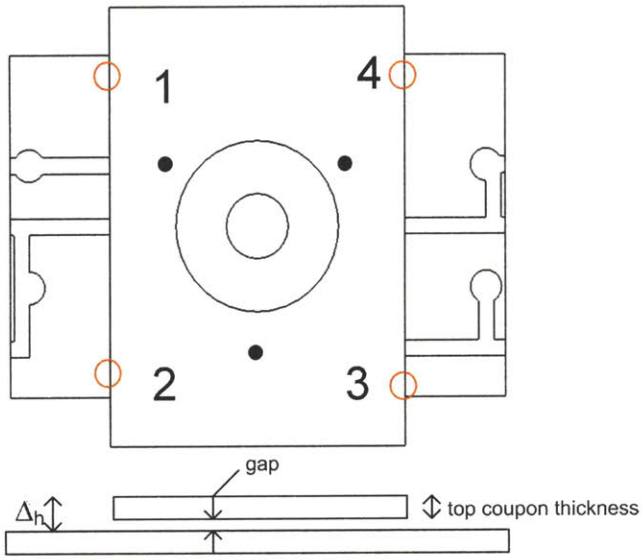

Figure 5-31: The four places gap height was measured for the final two-coupon system.

		Predicted	Measured
Different Sets of Coupons	Average Gap Height/Error μm	71.2/4.2	67.5/0.5
	Minimum Gap Height/Error μm	38.3/-28.7	55.6/-11.4
	Maximum Gap Height/Error μm	91.3/24.3	83.1/16.1
	Standard Deviation Gap Error μm	N/A	9.3
Assembly/ Disassembly	Standard Deviation μm	N/A	0.9
	Maximum Deviation from Average μm	N/A	1.7

Table 5.8: The maximum and minimum gap heights in the final two-coupon system.

times and their gaps recorded. An additional seven sets of coupons were assembled and disassembled once and their gap recorded. The raw data for these experiments is shown in Figure 5-32.

Table 5.8 displays the measured minimum gap height, maximum gap height, and average gap height compared to those predicted in Table 5.7. It also displays the statistics relating to assembly and disassembly.

The measured gaps ranged from 55.6 μm to 83.1 μm. This range of errors is slightly better than what was predicted by the error budget. The standard deviations of gap height for the three sets of coupons that were assembled and disassembled five times were 1.4 μm, 0.4 μm, and 0.8 μm, which averaged to 0.9 μm. It should be noted

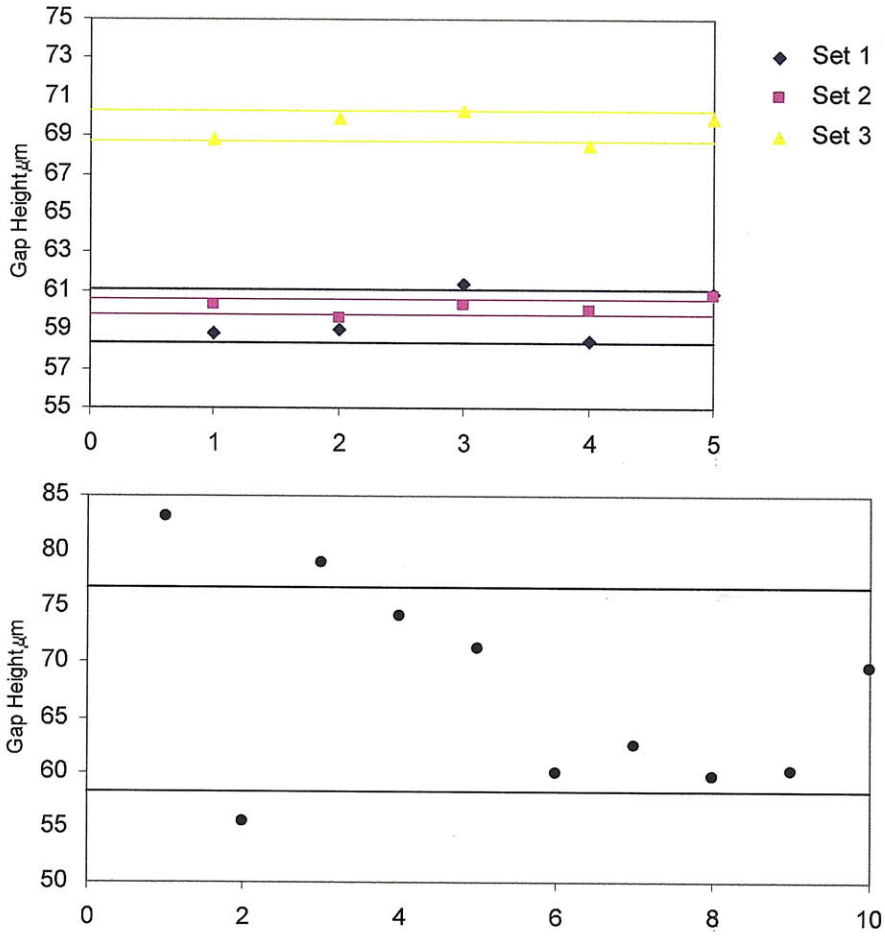

Figure 5-32: Top: The repeatability of the average gap for three coupons. Bottom: The average gap of ten coupons.

that these gap heights were measured with an optical microscope with a resolution of about 1 μm. The errors were found to be around the resolution of the microscope, so the actual repeatability may be better than recorded.

5.3.2 Parallelism Error

From Figure 5-25 it can be determined that the parallelism error is

$$e_\theta = \arctan \frac{G_{max} - G_{min}}{D_b} \tag{5.10}$$

where G_{max} is the largest ball/pit interface gap, G_{min} is the smallest ball/pit interface gap, and D_b is the distance between these two ball/pit interfaces. This parallelism error would be largest when D_b and G_{min} are as small as possible and G_{max} is as large as possible. The balls form an equilateral triangle, so the distance between them D_b is always 8.39 mm, as shown in Figure 5-33. The maximum G_{max} is 91.3 μm and the minimum G_{min} is 38.3 μm. These are given in Table 5.7. The leads to a maximum parallelism error of 6.3 mrad. The minimum parallelism error would be zero and would occur when all ball/pit interfaces had the same gap height.

The parallelism error was calculated using the same data used to measure gap error. The gap at positions 1, 2, and 3, shown in Figure 5-31, were used to determine the angle of the top coupon relative to the bottom coupon. The equations relating these three heights to parallelism error are Equation 3.13 and Equation 3.14. Ten sets of coupons had their parallelism error measured once, while 3 sets of coupons were each taken apart and put back together five times to determine parallelism error. This data is shown in Figure 5-34.

The actual parallelism error measurements are compared to the predicted parallelism error in Table 5.9.

Overall, the parallelism error is very low, with the maximum error being on the order of 1 mrad. Between the ten different sets of coupons, the standard deviation of parallelism error is 0.42 mrad. For the three sets of coupons which were assembled and disassembled, the assembly and disassembly standard deviations were 0.38 mrad,

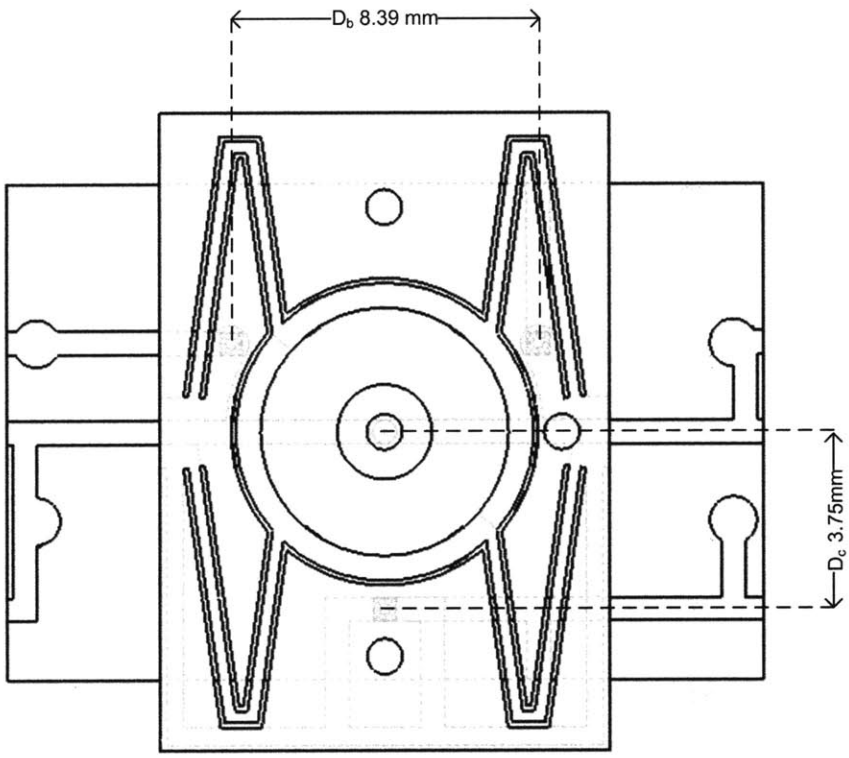

Figure 5-33: Dimensions between the balls and between the balls and the center of the final two-coupon system.

		Predicted	Measured
Different Sets of Coupons	Average Error mrad	N/A	0.34 mrad
	Minimum Absolute Error mrad	0	0.20 mrad
	Maximum Absolute Error mrad	6.3	0.69 mrad
Assembly/ Disassembly	Standard Deviation mrad	N/A	0.38 mrad
	Maximum Deviation from Average mrad	N/A	1.02 mrad

Table 5.9: The parallelism error e_ϕ in the final two-coupon system.

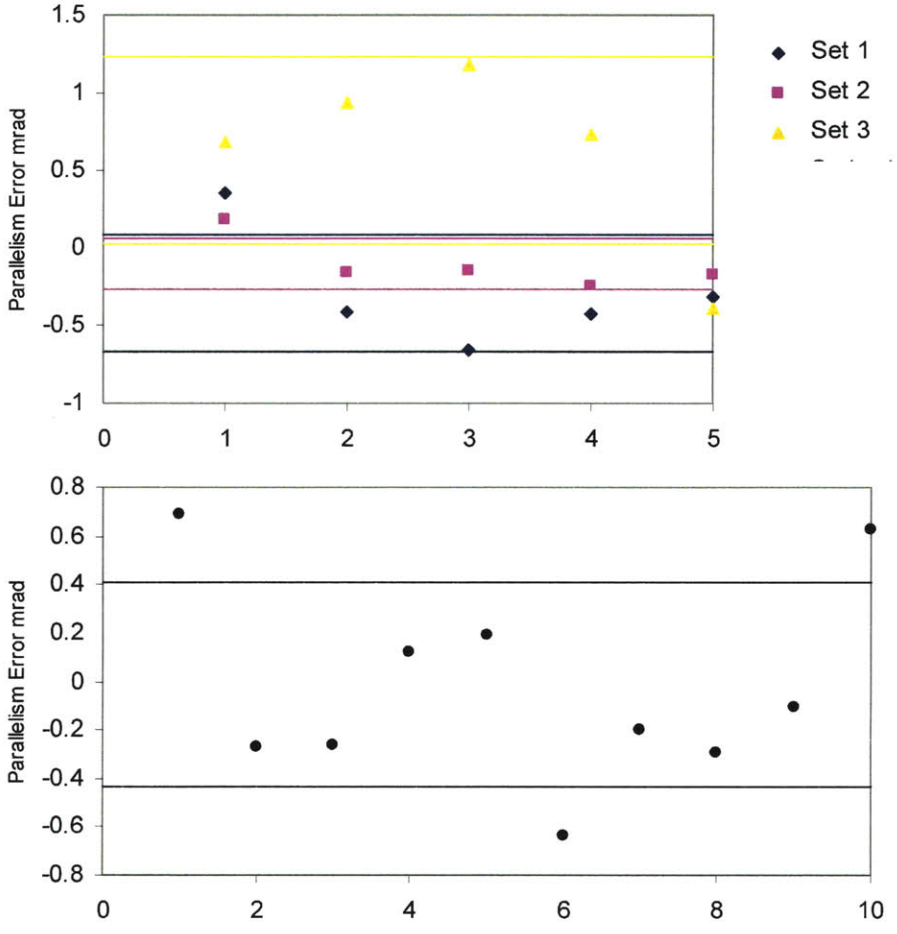

Figure 5-34: Parallelism error, e_ϕ, raw data for the final two-coupon system.

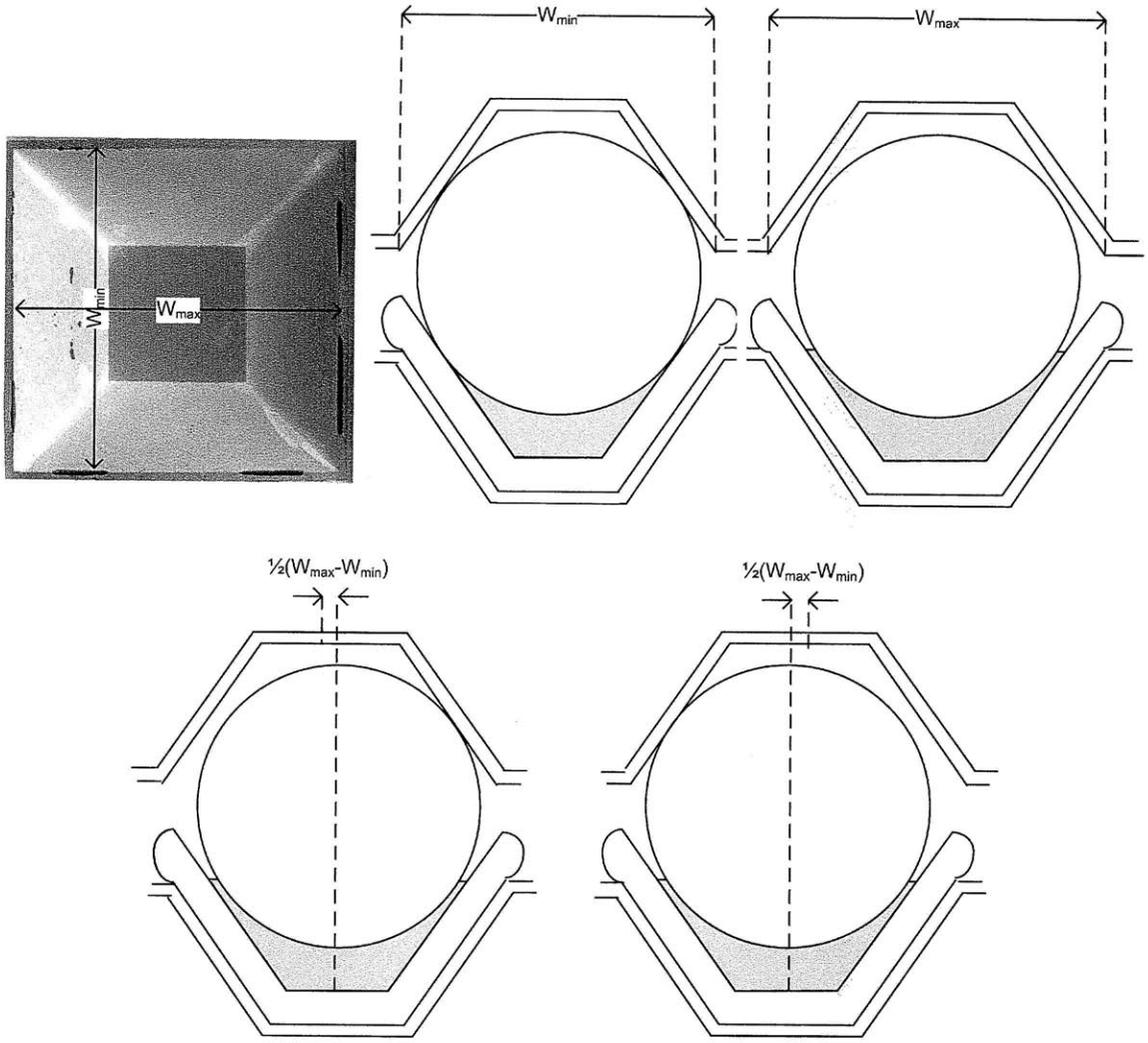

Figure 5-35: The effect of the non-square nature of the top pit on translational error.

0.16 mrad, and 0.60 mrad which average to 0.38 mrad.

5.3.3 Translational Error

The only error affecting the translational errors, e_x and e_y is the non-squareness of the pits.

From Figure 5-35, one can see that the total translational error is equal to one-half the maximum difference between the long dimension of the top coupon pit, W_{max} and

the short dimension of the top coupon pit W_{min}. Therefore

$$e_{XY} = +/- \frac{W_{max} - W_{min}}{2} \tag{5.11}$$

This is only one-half the error of the original kinematic coupling two-coupon system because in this case, the ball is secured to the bottom coupon, preventing rolling at that interface. According to data for pit geometry variability in Table 5.6, the maximum value for this error is +/- 6.3 μm and the average value for this error is 2.68 μm. These results were obtained using only gravity as a preload.

The accuracy of this error estimation was then tested. Translational error was measured using the test setup shown in Figure 4-23.

In this test setup, an aluminum target was mounted on top of a top coupon using super glue. This aluminum target had a wire which grounded it. The bottom coupon was glued to a mount which contained three capacitance probes which could measure the gap distance between the end of the probe and the aluminum target on the top samples. The coupons were assembled, and the capacitance probes were positioned within range. Three different bottom coupons were tested with three different top coupons. For each of these three pairs, the coupons were assembled and disassembled 50 times. The gaps at the X-capacitance probes, g_{x1} and g_{x2}, and the gap at the Y-capacitance probe, g_y, were recorded after each reassembly. Since this gap was a function of how close the capacitance probe was set up to the target initially, the average x1-gap, the average x2-gap and the average y-gap were subtracted from the raw data to get the gap fluctuation around the average. The true x-gap fluctuation was taken to be the average of the fluctuation of the x1-gap and the fluctuation of the x2-gap. The results of this data are shown in Figure 5-36.

In the x-direction, the standard deviation of the x-gap data was 0.53 μm. The maximum offset between the average gap and a single point in the "+" direction was 0.84 μm while the maximum offset between the average gap and a single point in the "-" direction was 1.55 μm. In the y-direction, the standard deviation of the y-gap data was 0.42 μm. The maximum offset between the average gap and a single point

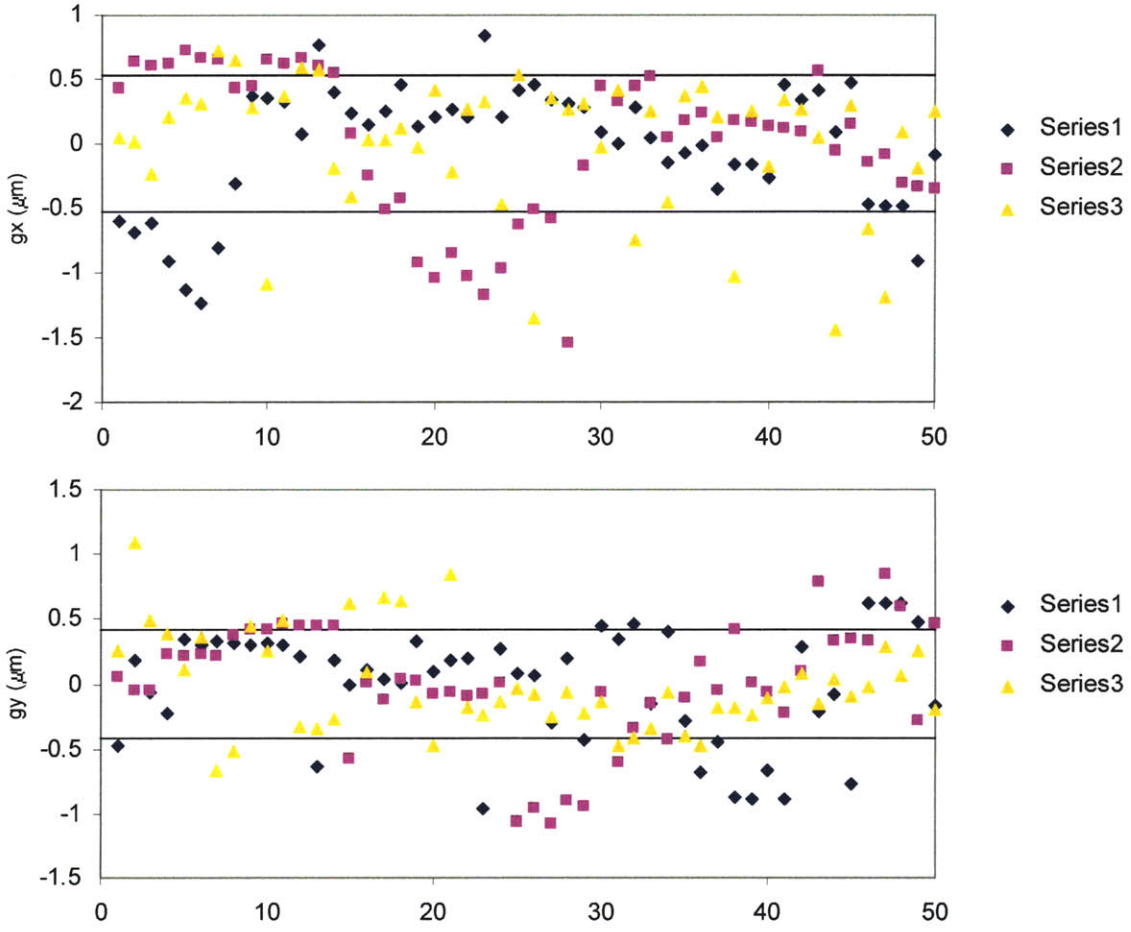

Figure 5-36: The translational repeatability of the final two-coupon system.

	Predicted e_{XY}	Measured e_X	Measured e_Y
Standard Deviation of Error (μm)	2.68	0.53	0.42
Maximum "+" Error (μm)	6.25	0.84	1.09
Maximum "-" Error (μm)	6.25	1.55	1.08

Table 5.10: Translational accuracy in the final two-coupon system.

in the "+" direction was 1.09 μm while the maximum offset between the average gap and a single point in the "-" direction was 1.08 μm. These results are summarized in Table 5.10. The translational repeatability was also analyzed to see if repeatability improved after many cycles. This was done as often kinematic couplings will wear together and become more repeatable. However, there was no evidence of this for any of the data analyzed.

The measured maximum error was less than one-fourth of the predicted maximum error. That is because for the maximum error to occur, each of the three pits on the coupon would have to have the maximum amount of non-squareness in the same direction, and the chances of this happening are very low.

5.3.4 Rotational Error

The rotational error comes from the coupon being able to rotate slightly as a result of non-square nature of the pits. This error is shown in Figure 5-37.

The rotational error can be described in terms of the translational error by the equation

$$e_\theta = \tan \frac{e_{XY}}{D_c} \tag{5.12}$$

where e_θ is the rotational error and e_{XY} is the translational error. The rotational error will be greatest when e_{XY} is greatest. D_c is 3.75 mm, as shown in Figure 5-33. The maximum and standard deviation for rotational error can be calculated by using the maximum and standard deviation values for translational error in Equation 5.12. The translational error values come from Table 5.10. At the maximum measured translational error of 6.25 μm, the maximum rotational error is 1.7 mrad. The x-

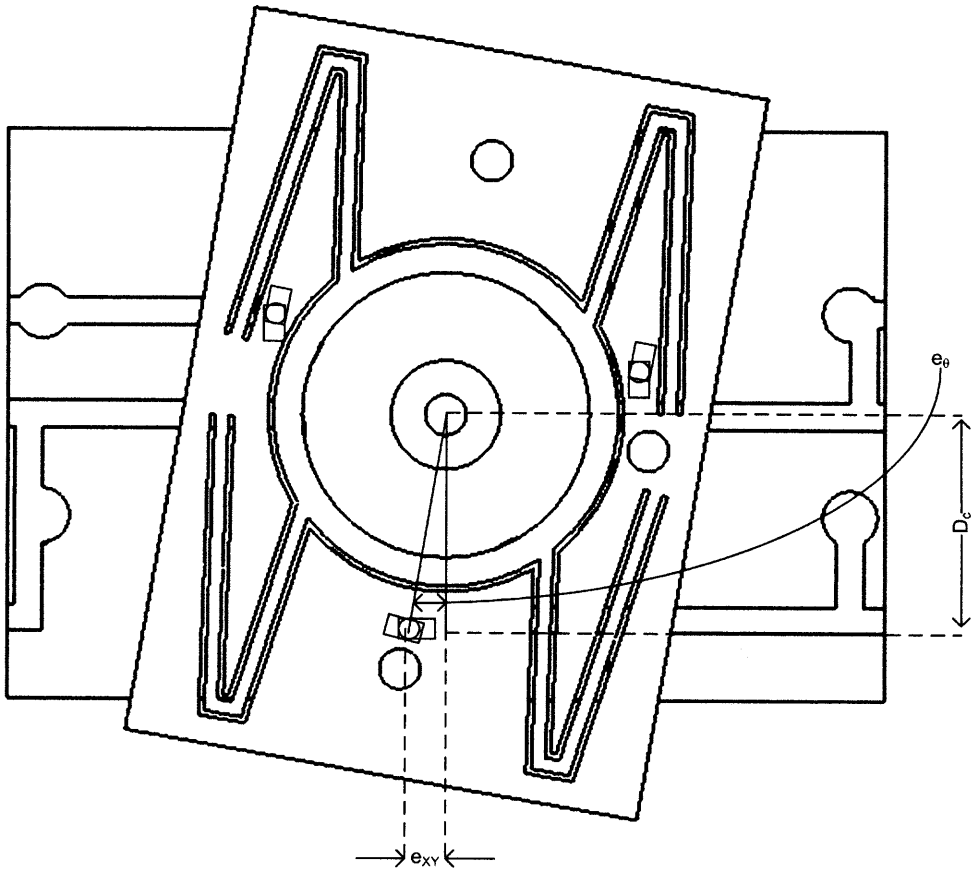

Figure 5-37: Effect of non-square pits on rotational error.

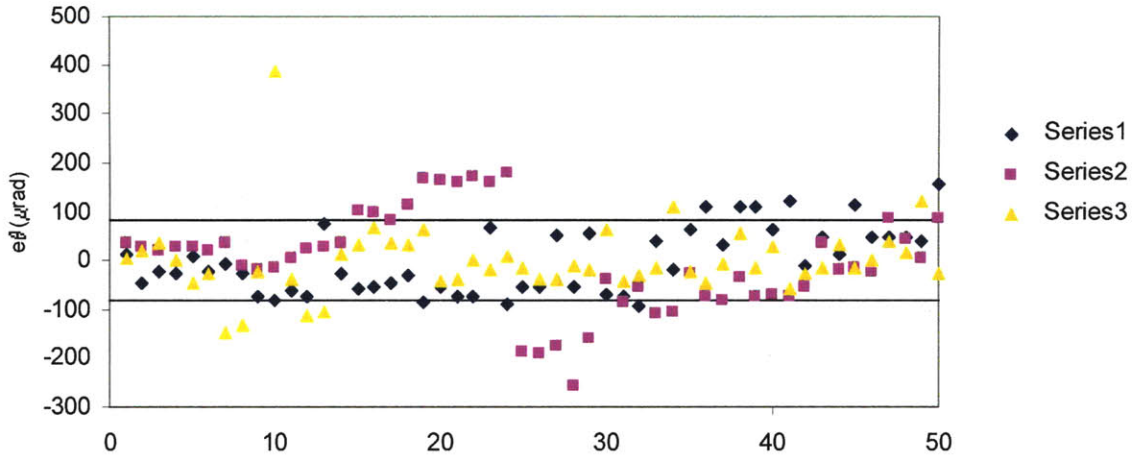

Figure 5-38: The rotational repeatability of the final two-coupon system.

	Predicted e_θ	Measured e_θ
Standard Deviation of Error (mrad)	.140	0.083
Maximum "+" Error (mrad)	1.7	0.389
Maximum "-" Error (mrad)	1.7	0.256

Table 5.11: The rotational error in the final two-coupon system.

translational error had a standard deviation of 0.53 μm. Therefore the rotational error will have a standard deviation of 0.14 mrad. The minimum possible rotational error is zero. Rotational error was measured using the test setup shown in Figure 4-23. Rotational error was defined to be

$$e_\theta = \arctan \frac{[g_{x1} - \bar{g_{x1}}] - [g_{x2} - \bar{g_{x2}}]}{19000} \tag{5.13}$$

where g_{x1} and g_{x2} are the gaps at the X1-capacitor and X2-capacitor in μm and 19,000 is the distance in microns between the centers of the X1-capacitor and X2-capacitor.

As in the translational tests, three pairs of top and bottom coupons were assembled and disassembled 50 times. The rotational error for each of these was recorded. The raw data is shown in Figure 5-38 and the standard deviation and maximum error are shown in Table 5.11.

The rotational error had a standard deviation of 82.2 μrad and a maximum of

	Different Sets of Coupons			Assembly/Disassembly		
	Average	Standard Deviation	Maximum Absolute	Average	Standard Deviation	Maximum Absolute
G/e_g μm						
Predicted	71.2/4.2	N/A	91.3/24.3	N/A	N/A	N/A
Measured	67.5/0.5	9.3	83.1/16.1	N/A	0.9	1.7
e_ϕ mrad						
Predicted	0	N/A	6.3	N/A	N/A	N/A
Measured	-0.014	0.42	0.69	N/A	0.38	1.02
e_{XY} μm						
Predicted	N/A	2.68	6.25	N/A	2.68	6.25
Measured	N/A	0.53	1.55	N/A	0.53	1.55
$e_\theta mrad$						
Predicted	0	0.14	1.7	0	0.14	1.7
Measured	N/A	0.83	0.389	N/A	0.83	0.389

Table 5.12: The predicted and measured accuracy of the final two-coupon system

388.5 μrad. This is quite small.

5.3.5 Error Summary

All of the actual values for each of the errors (translational, rotational, gap error, and parallelism error) are displayed in Table 5.12

5.3.6 Error Interpretation

This section briefly analyzes the effects of the repeatability errors in the final two-coupon system. There are two areas affected by errors. The translational errors affect asperity level contacts. The second area affected is that membrane tilt, scrub induced moment tilt, and parallelism error have an effect on the applied force.

In the final two-coupon design, the standard deviation of translational repeatability was 0.53 μm. The asperities in many MEMS fabricated contacts are on the order of 1 μm [22]. Therefore, for all assemblies/disassembles falling within one standard deviation from the average, the top and bottom portions of the contacting asperities will overlap by at least 47% of a diameter. One potential way of improving this repeatability is to use a harder metal on the inside of the pits and to plate the balls.

This would lessen the deformity of the metals increasing repeatability. Another way to improve repeatability is to use a nitride mask instead of an oxide mask to pattern the pits. In the first generation kinematic coupling two-coupon system, a nitride mask was used. The standard deviation of the minimum pit width created with a nitride mask was 2.9 μm as opposed to 8.5 μm acheived with an oxide mask. The fabrication was switched from nitide masks to oxide masks because it is far easier to remove oxide. However, the alignment benefits of the nitride mask may outweight the manufacturing benefits of the oxide mask.

In the final two-coupon design, the worst case membrane tilt error was 1.2 mrad. The worst parallelism error was 0.388 mrad. The worst case scrub induced moment parallelism error was 2.22 mrad. These errors can sum, leading to the actual force on the contact being slightly less than the measured force. This is shown in Figure 3-28. For the worst case scenario, where the sum of the two contributing errors is 1.588 mrad, the actual contact force will be 99.9998% of the measured contact force. This is less than the accuracy of the mechanism used to measure the force.

5.4 Proof of Concept Testing

The proof of concept testing demonstrates the three main functionalities of the two-coupon system: measure contact resistance as a function of force and scrub, measure displacement as a function of force, and impart a scrub. These three experiments are described in this section.

The first proof of concept testing for this coupon consisted of testing 5 μm of plated gold contacting 5 μm of plated gold. The resistance measurements were then compared to Holm Theory. This is shown in Figure 5-39. The resistance measured is very close to that predicted by Holm theory. The slight deviations at the beginning of the touchdown could be due to the two flats "settling" against each other. The samples might have rocked until they were truly flat-on-flat. Contact resistance on a pair of 5 μm of plated gold flat-on-flat contacts were also tested, disassembled, reassembled, tested a second time, disassembled, reassembled, and tested a third

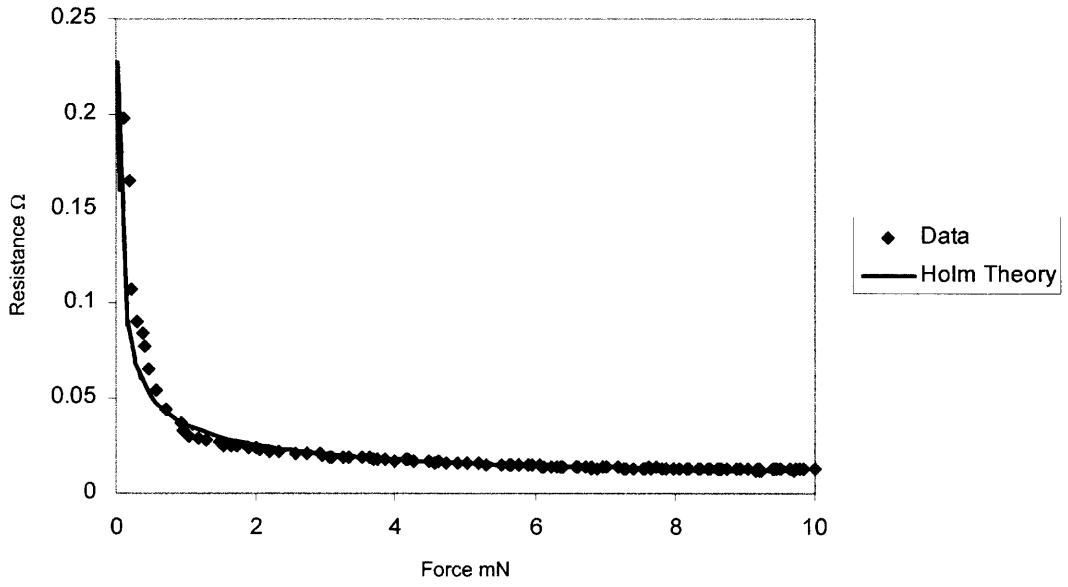

Figure 5-39: 5 μm gold flat-on-flat contact test compared to Holm theory.

time. The results of these multiple touchdowns are shown in Figure5-40. There are small deviations between the contact resistances of each of the three runs. This can be expected as the asperities plastically deform. However, each of the three data sets are very similar and very close to Holm theory.

The stiffness of the membrane was also examined. Figure 5-41 shows the force and displacement relationship for the final two-coupon system.

In Zone 1 of Figure 5-41, the force probe is moving but has not yet hit the top coupon. In Zone 2, the membrane is being deflected. This takes 280.23 mN and 32.88 μm displacement. This means the gap between the coupons was 32.88 μm, near the 25 μm design gap. The stiffness of the membrane is 8.52 mN/μm. The predicted membrane stiffness was 9.75 mN/μm. However, this predicted stiffness was based on the thickness of the membrane cubed, so control of the membrane stiffness was not precise. However, it is not necessary to have precise control of the membrane stiffness because it can be measured during the resistance test.

In order to prove the contacts could create scrub, a 25 μm blade tip was scrubbed 15 μm. The force on the tip was very small, 2 mN. The surface the tip was contacting

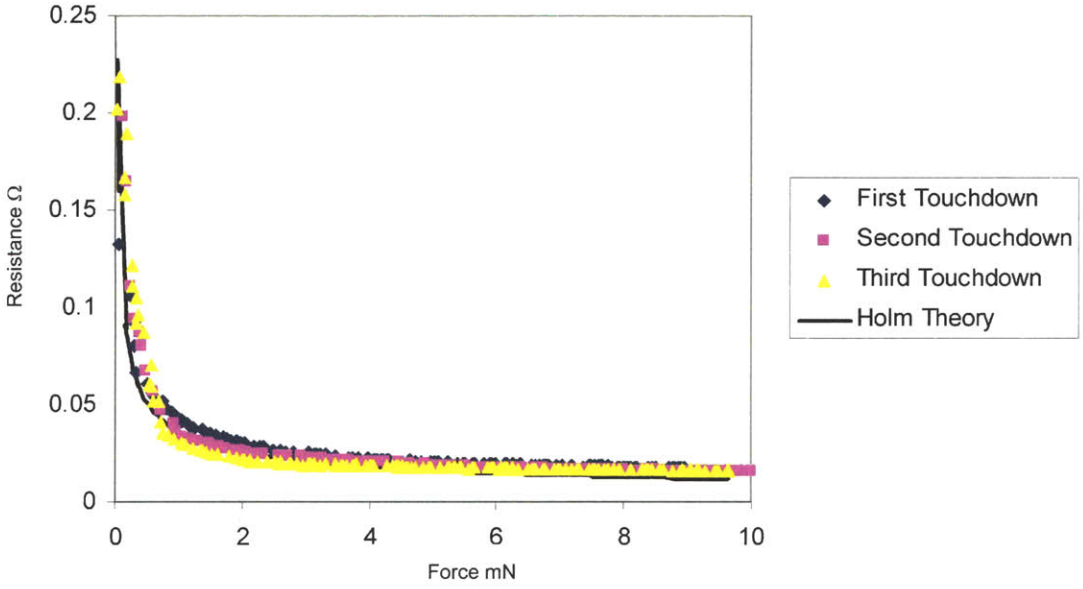

Figure 5-40: The repeatability of contact resistance for plated gold flat-on-flat contacts.

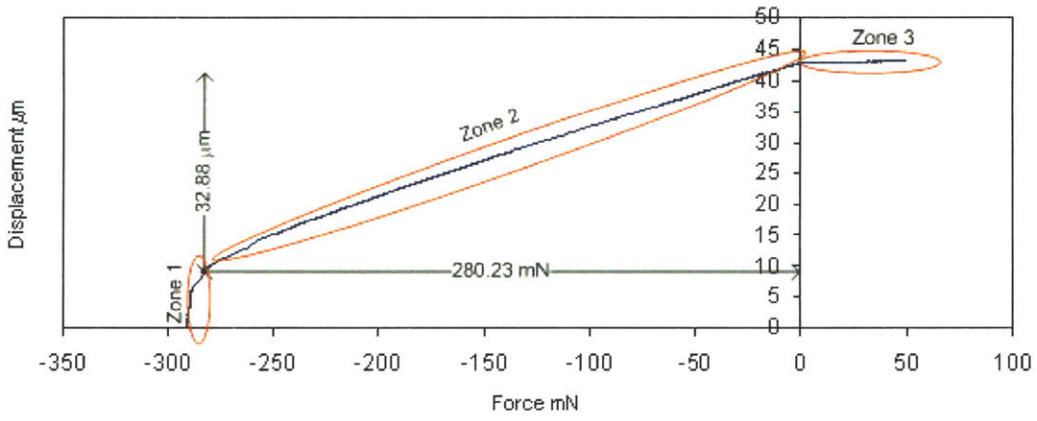

Figure 5-41: Displacement v. force for the final two-coupon system.

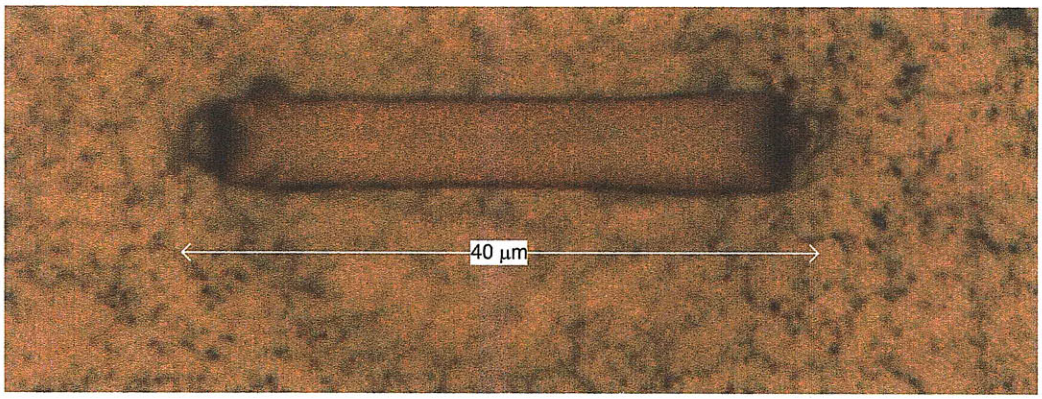

Figure 5-42: A proof of concept scrub mark made on a surface colored using a Sharpie marker.

was gold which had been coated with Sharpie marker. The Sharpie was scrubbed away from the area the tip contacted. The full area which was scrubbed clean was 40 μm, the sum of the tip length and the scrub length. The instrumentation used to impart this scrub is described in Chapter 6. This proof of concept scrub is shown in Figure 5-42.

Additionally, the repeatability of scrub was examined visually. The 25 μm blade tip was scrubbed 15 μm across a surface seven times. Between each scrub, the coupons were assembled and disassembled. Images were taken after the first and seventh scrub. The results are shown in Figure 5-43.

5.4.1 Design performance compared to the functional requirements

Table 5.13 summarizes how the two-coupon system's performance compared to the performance dictated by the functional requirements.

Functional Requirement	**Performance of 1st generation two-coupon system**
Measure contact resistance in the mΩ range .	Achieved
Measure contact force in the 100 μN.	Achieved
Bring contacts together in a parallel manner.	Achieved a parallelism error standard deviation 0.42 mrad of and a maximum of 0.69 mrad.
Measure multiple cycles.	Achieved
Assembly/disassembly repeatability better than 1 μm.	Achieved a translational error standard deviation of 0.53 μm and a maximum of 1.55 μm .
Allow for the observation of the physical changes to the contact between cycles using metrology including, but not limited to, the SEM and AFM.	Achieved
No more than 25 μm of displacement	Not achieved. The coupons use an average of 25.5 μm of displacement.
Robust fabrication process which would not have the significant yield loss seen during the hot phosphoric acid step in the first process.	Achieved using an oxide mask instead of a nitride mask.
Membrane fabrication which would not use a KOH-etch.	Achieved using DRIE
No wiring to the top coupon.	Achieved by making electrical contact through the ball/pit interfaces.
No ball handling.	Achieved by securing balls to the bottom coupon.
Use no more than 300 mN of force to deflect the membrane.	Achieved. Uses 280.23 mN of force.
Allow contacts to be scrubbed 20 μm.	Achieved.
Allow for the testing of multiple types of three-dimensional tips.	Achieved. Tested flat, plated, and spherical tips.

Table 5.13: The performance of the final two-coupon system compared to its functional requirements..

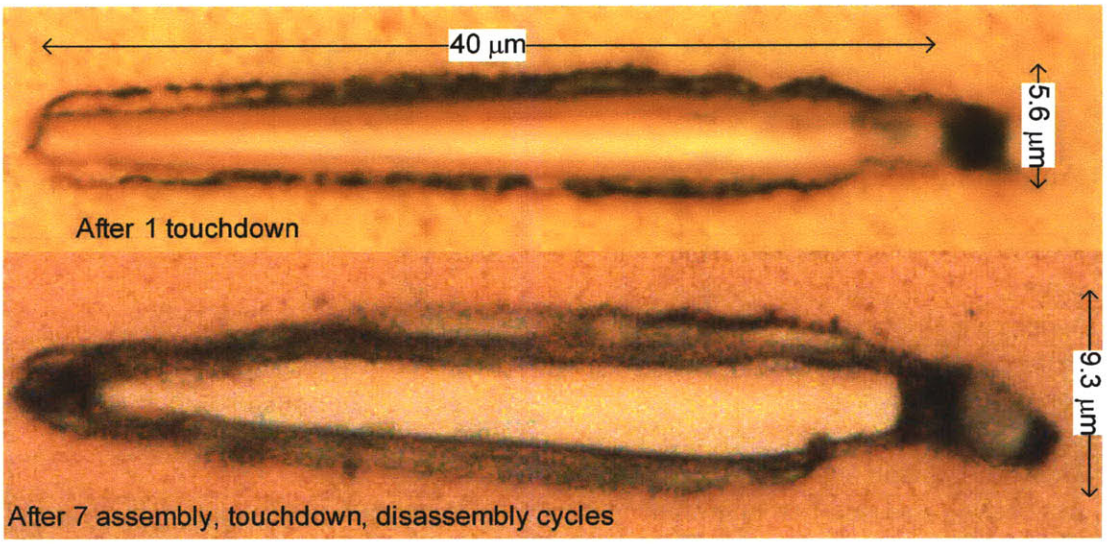

Figure 5-43: A surface after being scrubbed with a blade tip once and again after the seventh applied scrub.

5.5 Summery, Future Capabilities, and Improvement Opportunities

This chapter presented a two-coupon system capable of imparting force and scrub onto many types of contacts. Two coupon systems were built for flat-on-flat contacts, sphere-on-flat contact, and plated contacts. The repeatability of the assembly of the coupons was measured and found to be on the order of an asperity diameter. There are several improvement opportunities and potential future capabilities for the two-coupon system.

The first improvement opportunity exists because the coupons have an average gap between the tip and the contact material of 25.5 μm. The functional requirements desire that this displacement be no more than 25 μm. This can be easily rectified by having a slightly thinner membrane.

The next design opportunity would expand the testing functionality of the two-coupon system. Creating a top-coupon with a rotary flexure would allow the contacts to be scrubbed rotationally. Other types of flexures might allow for out of plane tip rotation.

Another improvement opportunity would be replacing the Krazy glue attached retaining ring with a microfabricated feature. This would ensure the feature was centered on the device by taking advantage of the excellent alignment capabilities of microfabrication processes.

The next opportunity would be a change to the system. Potentially, the contacts could be fabricated on a very simple contact blank which would contain only parts of a Kelvin structure, alignment and assembly features, and the contacts. This could then be inserted into a device which would allow the contacts to be scrubbed and have force imposed. This way, the membranes and flexures would not have to be fabricated for every coupon.

Chapter 6

Instrumentation

List of Symbols	
$\delta_{membrane}$	Flexure deflection
E	Young's modulus
F	Force
I	Moment of inertia
k	Flexure stiffness
L	Flexure segment length
σ	Stress
σ_y	Yield stress
t	Flexure thickness
w	Flexure width
x_c	Gap sensed by capacitance probe
x_m	Position of force probe
x_t	Total membrane deflection

Custom instrumentation was designed to test the two-coupon systems presented in Chapters 3, 4, and 5. This chapter first describes a simple proof of concept design of this custom instrumentation and then describes the final instrumentation. The final custom instrumentation allows for the imparting of any force and scrub profile within the limits of the machine while measuring contact resistance. It also has an interface

to mount the two-coupon system.

6.1 Proof of Concept Instrumentation

This original instrumentation was designed to test only the flat-on-flat non scrubbing coupons described in Chapter 3. This section describes the design and testing of this proof of concept instrumentation. The functional requirements of this instrumentation were:

1. Apply and measure force of at least 60 mN.
2. Force accuracy of at least 100 μN.
3. Measure resistance on the order of mΩ.
4. Measure the displacement of the membrane with an accuracy of 10 nm.
5. Work with the kinematic coupling two-coupon system presented in Chapter 3.

These functional requirements were achieved using the simple design shown in Figure 6-1. The system consists of a base, precision scale, frame, capacitance probe, and linear micro-stepper motor. Resistance is measured using a Keithley 2420 source-measure unit. A schematic view of these components is shown in Figure 6-2.

Since this test setup tested the original kinematic coupling two-coupon system, lead wires must first be attached to the top and bottom coupons, as shown in Figure 3-29. The bottom coupon is then taped onto the center of the scale. The Grade 3 stainless steel balls are placed inside the KOH-etched pits of the bottom coupon. The top coupon is then placed over the balls. The wires of the top and bottom coupon are then taped to the top of the scale to minimize the amount they will pull on the scale, which affects the force reading. The lead wires are then clipped to larger wires which connect to the Keithley 2420 source-measure unit. The frame, to which the linear micro-stepper motor and capacitance probe are mounted, is then placed onto the base, by mating the conical ends of the three frame legs into the the three

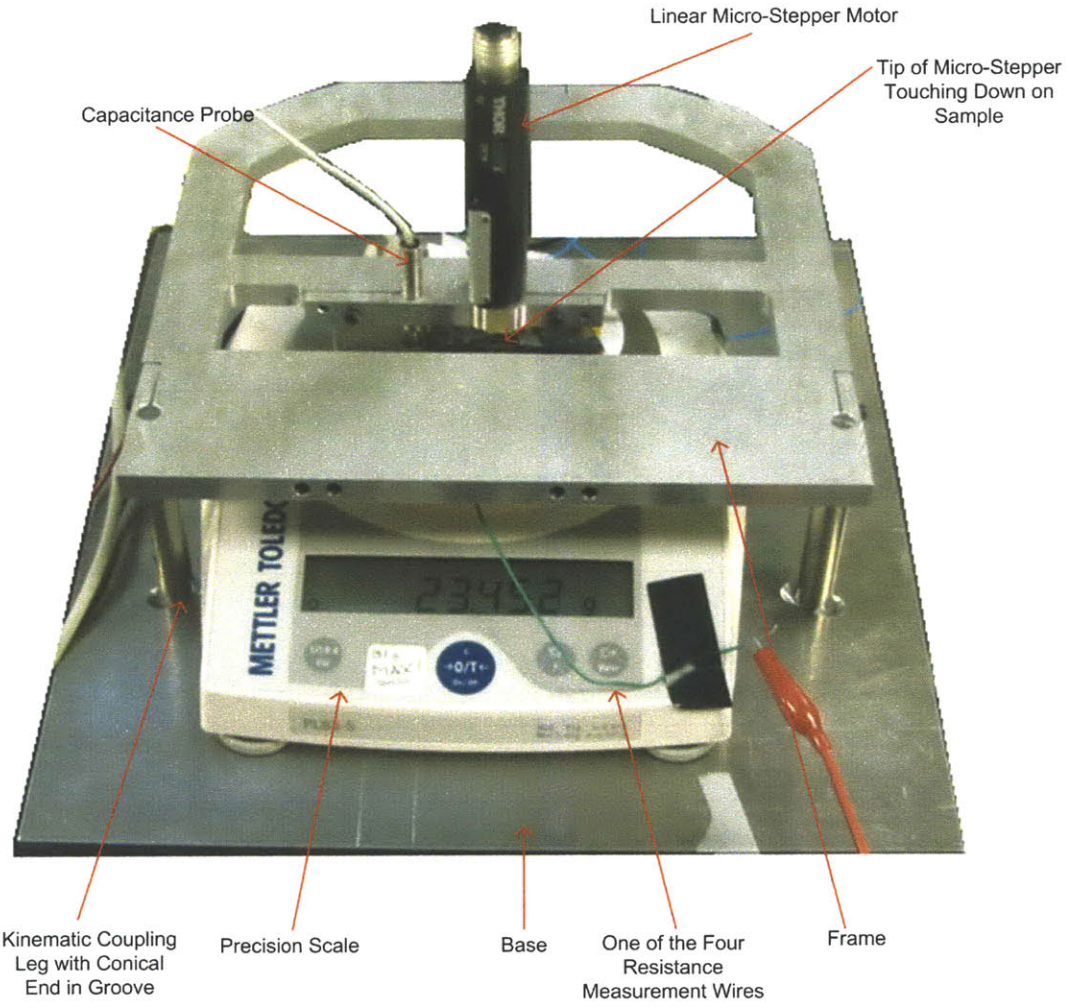

Figure 6-1: The proof of concept instrumentation used to measure the original kinematic coupling two-coupon design.

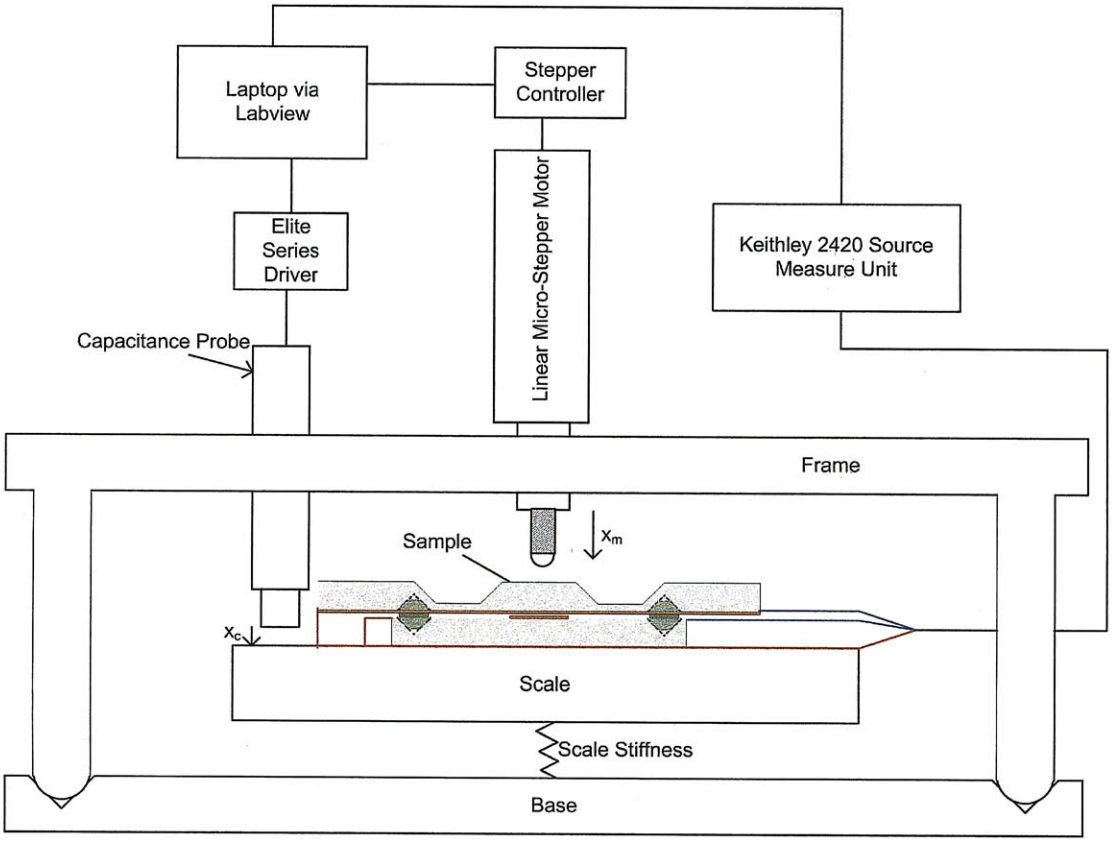

Figure 6-2: The elements of the proof of concept instrumentation used to measure the original kinematic coupling two-coupon design.

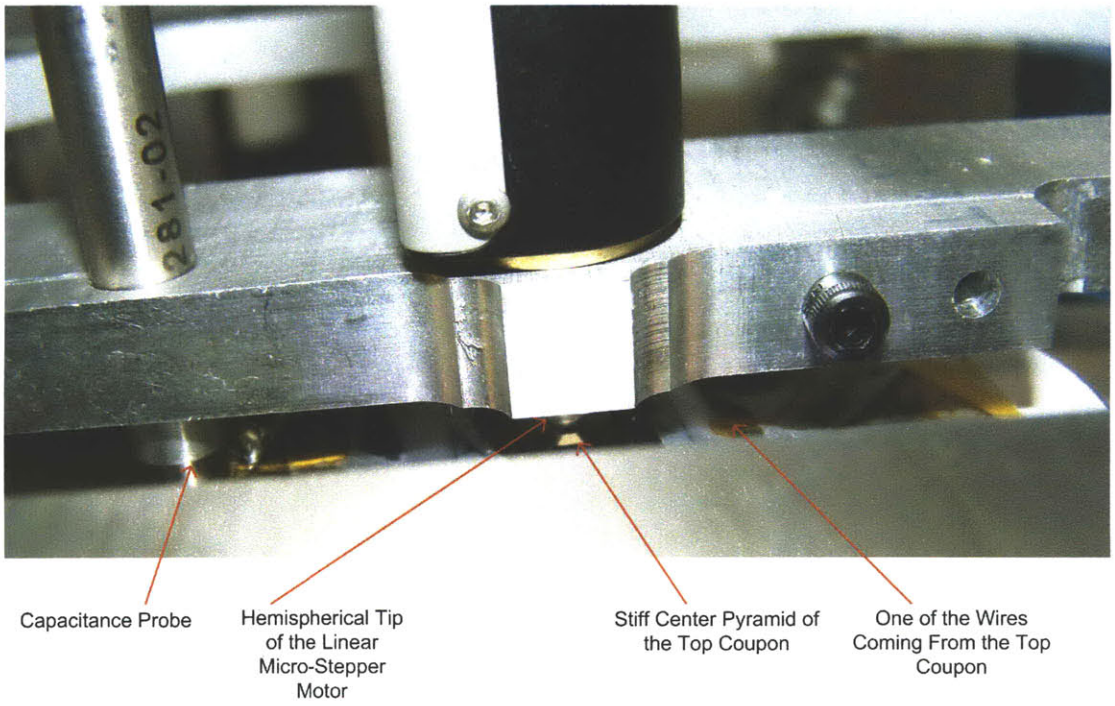

Figure 6-3: The hemispherical tip of the linear stepper making contact with the top coupon's stiff center pyramid.

grooves on the base. The linear micro-stepper motor is then advanced until it makes contact with the stiff center pyramid of the top coupon, which will cause the scale to read an increase in force. The hemispherical tip of the linear stepper motor contacting the stiff center pyramid of the top coupon is shown in Figure 6-3. The linear stepper continues to advance, first deflecting the membrane and then increasing the force on the contact. The compliance of the scale allows the linear stepper motor to advance without dislodging the frame. As the stepper motor advances, the position of the stepper motor is recorded, the gap measured by the capacitance probe is recorded, the force read by the scale is recorded, and contact resistance is measured and recorded by the Keithley 2420 source-measure unit. Current is sourced at 10 mA.

The linear micro-stepper motor used is a ThorLabs ZST6 micro-stepper, which has a resolution of 2.5 nm incremental linear steps over a 6 mm range. This actuator essentially uses a stepper motor to advance a lead screw. The end of the lead screw is a 2.5 mm diameter hemisphere, which makes contact with the sample. The forward

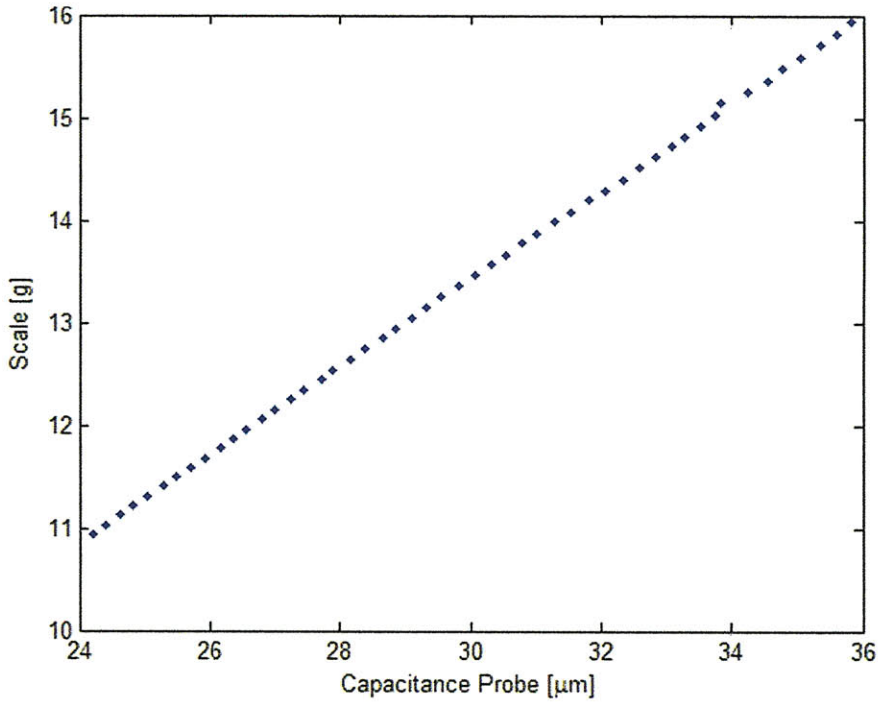

Figure 6-4: Force measured by the scale versus the deflection of the scale.

motion of this micro-stepper is the sum of the deflection of the top coupon membrane and the deflection which results from the scale having a finite stiffness. This forward motion is labeled x_m in Figure 6-2.

In order to measure the scale's stiffness, a Lion Capacitive Sensor with a 50 μm range and 2 nm resolution is mounted to the frame and measures the deflection of the scale as the linear stepper deflects it. The stiffness of the scale can then be measured by plotting the change in the gap measured by the capacitance probe versus the force recorded by the precision scale. This data is shown in Figure 6-4. The stiffness of the scale was measured to be 0.428 g/μm or 4.19 mN/μm.

A Mettler-Toledo PL83-S precision balance was chosen to measure force. It has a range of 80 g (784 mN) and a resolution of 0.1 g (0.98 mN).

The deflection of the membrane can then be calculated as

$$\delta_{membrane} = x_m - \frac{F}{K} \tag{6.1}$$

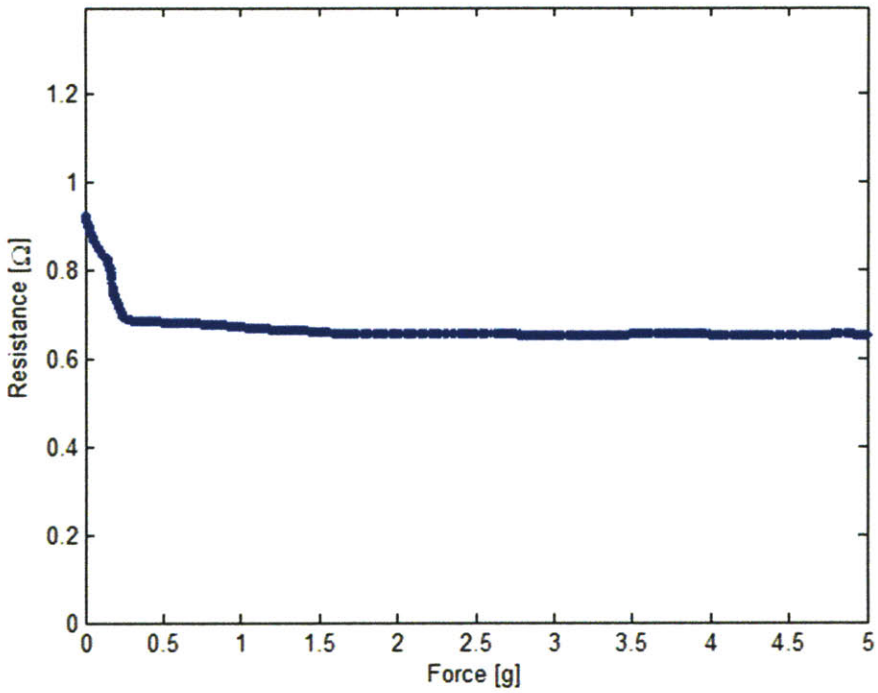

Figure 6-5: Force vs. contact resistance of evaporated gold contacts measured using the proof of concept instrumentation.

where F is the force read by the scale and K is the stiffness of the scale.

This proof of concept test setup was used to measure the contact resistance of evaporated gold flat-on-flat contacts. Contact resistance as a function of force is shown in Figure 6-5.

This proof of concept instrumentation measured contact resistance at a few grams (a few 10s of mN) on the order of 650 mΩ. According to Holm theory, and the initial testing of these devices using the Tribometer, resistance at this force should be on the order of 10 mΩ. This large bulk resistance could have been a result of several things. First, the wires attaching to the top coupon could have acted like a spring, pushing the top and bottom coupons apart and therefore reducing contact resistance. Second, taping the wires to the leads required excessive handling of the two coupons. The contact surfaces may have become contaminated during this procedure.

6.1.1 Design Opportunities

The following design opportunities were discovered during the design and testing of the proof of concept instrumentation.

The first design opportunity comes from mounting the coupons on the scale. This is a concern because the four wires coming off the sample can push or pull on the scale and interfere with the readings. The platform to which the samples are mounted needs to be rigid and the force gauge should be connected to the force probe and come from above the sample.

Second, the wiring of the coupons is a major difficulty when measuring a sample. The final two-coupon system described in Chapter 5 allows for all wiring to be done to the bottom coupon. For ease of use, the instrumentation should have a sample mount which can make contact to the four wire pads without tape or solder.

Third, in the proof of concept instrumentation, the coupon was placed in the center of the scale by hand. There should be an alignment mechanism to ensure the coupons are directly underneath the force probe and held in place without the use of tape.

Fourth, the original proof of concept instrumentation does not have a way of scrubbing the coupons. Scrubbing capability should be added.

6.2 Final Instrumentation

This final instrumentation was designed to test the final two-coupon system described in Chapter 5. The functional requirements of this instrumentation were derived from those required to measure and actuate the two-coupon system and from the design opportunities discovered during the building and testing of the proof of concept instrumentation. The final functional requirements for the instrumentation were:

1. Apply and measure force of at least 500 mN.
2. Force accuracy of at least 100 μN.
3. Measure resistance on the order of mΩ.

4. Measure the displacement of the membrane with an accuracy of 10 nm.

5. Work with the final two-coupon system presented in Chapter 5.

6. Contain a mount for the bottom coupon which will accurately position it as well as hold it in place.

7. Contain a quick attach wiring system which could connect the four leads of the bottom coupon to the Keithley source-measure unit.

8. Have a method of imposing scrub on the two-coupon system.

These functional requirements were achieved using the simple design shown from the front in Figure 6-6 and from the side in Figure 6-7. A schematic view of these components is shown in Figure 6-8.

This section describes the components of the instrumentation, the procedures used during testing done performed using this instrumentation, and design opportunities discovered during the building and testing of this instrumentation.

6.2.1 Components

There are two major assemblies in the instrumentation: the base assembly and the frame assembly. In this subsection, the components of these two assemblies are described. The integration of these two assemblies is also discussed. The two flexure components and the scrubbing components are then discussed in detail.

Base Assembly

The base portion includes the base, a lead screw with linear plain bearing and carriage module, two spacer plates, a linear ball bearing, a piezo with coarse and fine motion, a vacuum plate, and a mounting plate with four aluminum arms to make electrical connections. A solid model of the base assembly components is shown in Figure 6-9.

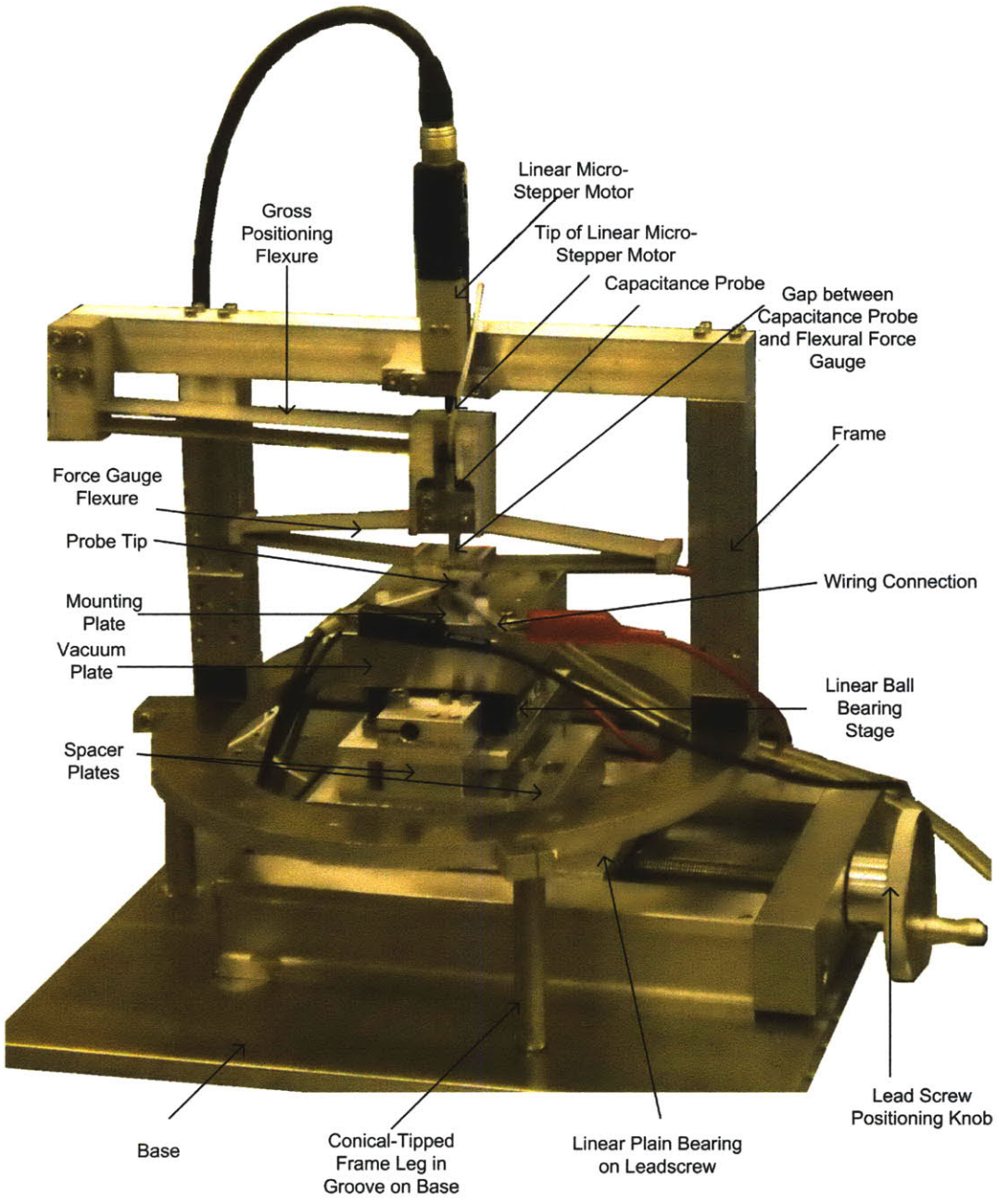

Figure 6-6: The final instrumentation system (front view).

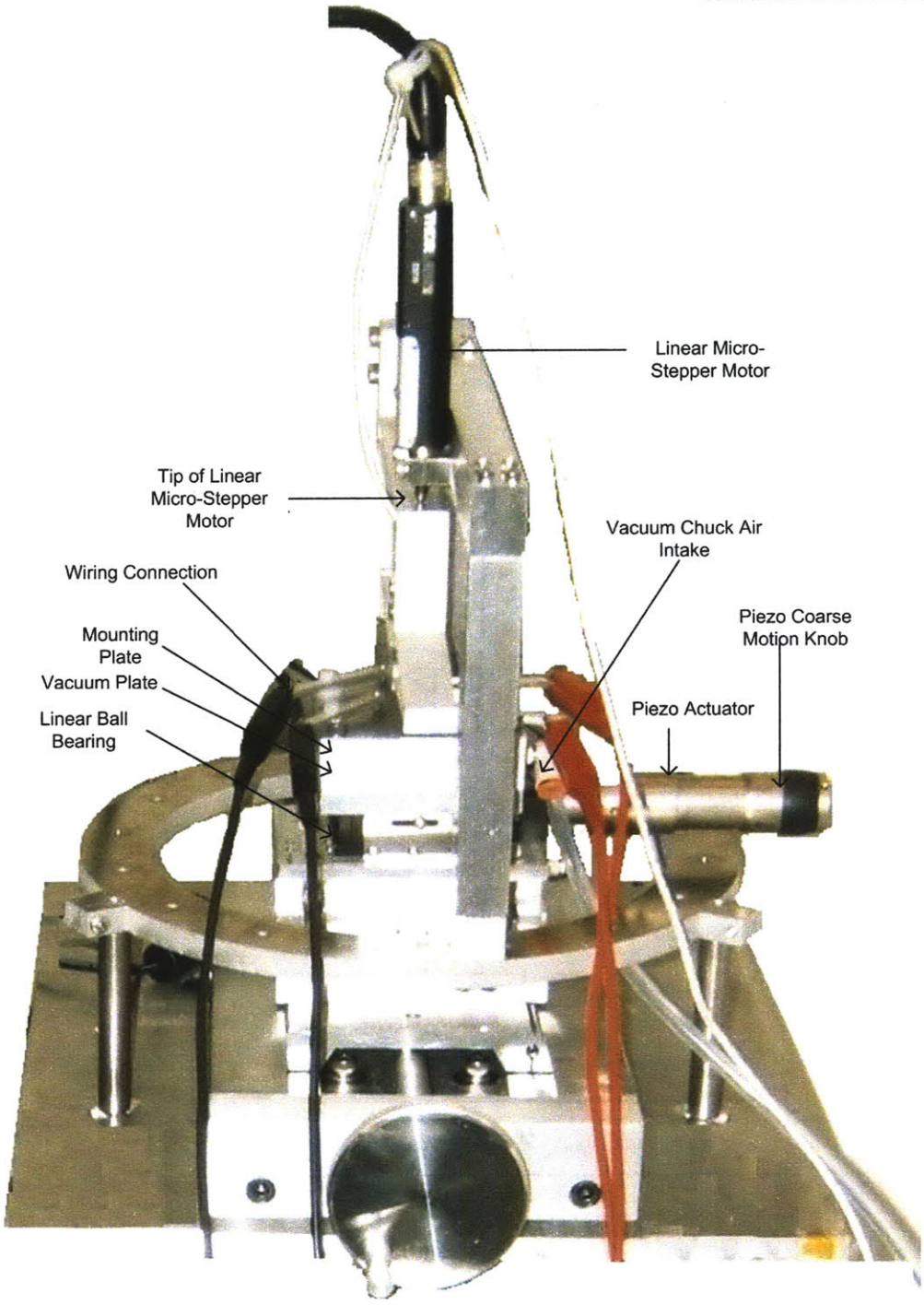

Figure 6-7: The final instrumentation system (side view).

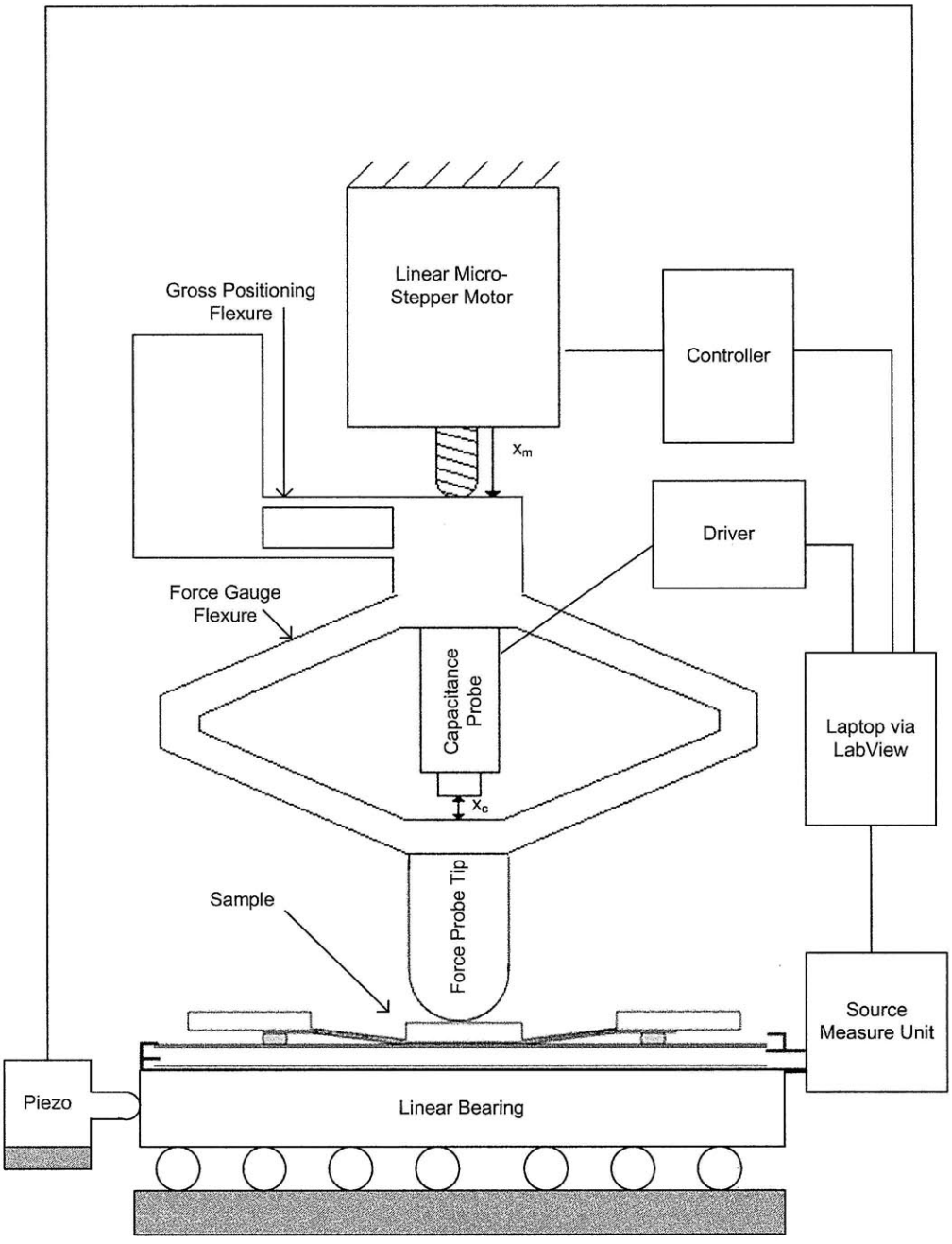

Figure 6-8: Schematic of the final instrumentation system.

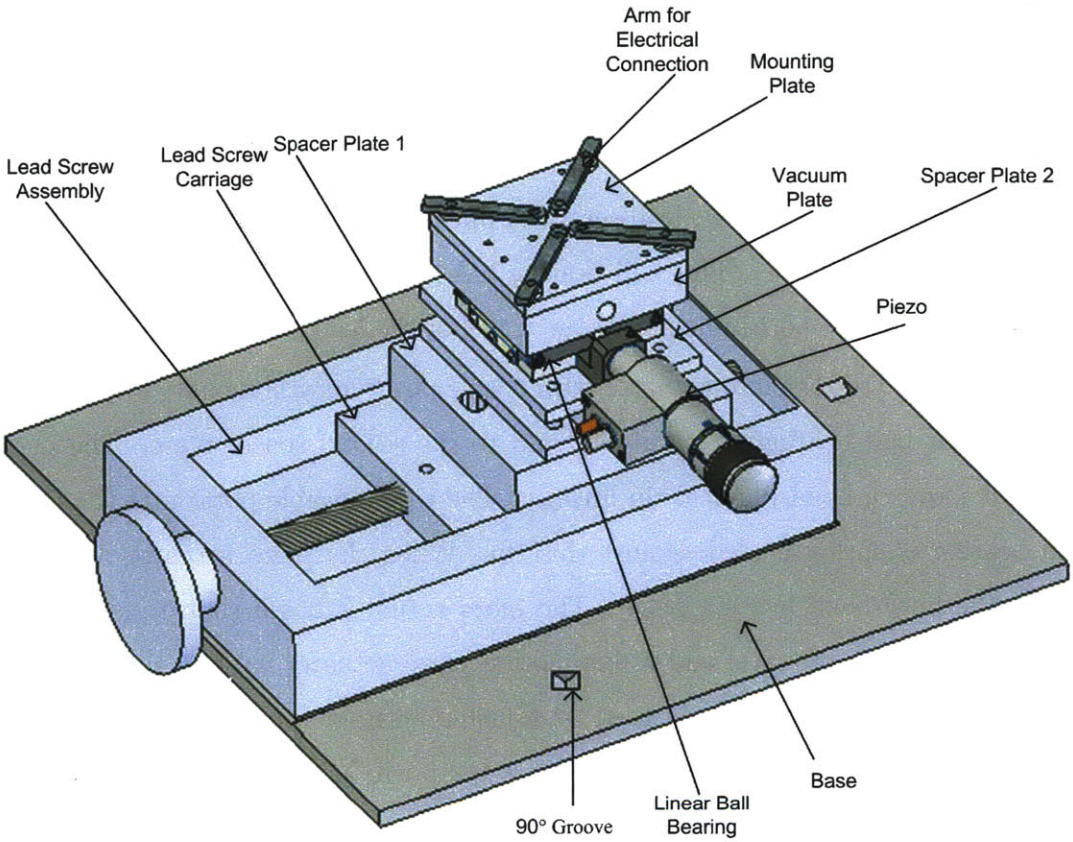

Figure 6-9: The components of the base assembly.

The base of the instrumentation is an aluminum plate 300 mm by 325 mm. It contains three 90° angled grooves. These grooves are spaced in a circular pattern each 120° apart and 130 mm from the center of the plate.

The lead screw with linear bearing is bolted to the base plate. This is a stand alone unit consisting of a lead screw, carriage on plain bearings, and a knob to turn the lead screw. This lead screw is used for the gross positioning of the sample in one direction. It has a total travel of 75 mm, but in reality only about 1 mm of the travel is ever used. The long length of the lead screw was chosen in case the samples tested were ever changed to consist of multiple samples on a single wafer. This would require large amounts of translation to move from sample to sample. Two spacer plates are mounted to the carriage of the lead screw. A linear ball bearing stage is mounted on top of these spacer plates. This ball bearing has 15 mm of travel. The travel of the linear ball bearing is perpendicular to the travel of the lead screw.

A Thorlabs DV517 piezo actuator with coarse positioning is mounted to the base of the linear ball bearing which is mounted to the second spacer plate. The piezo actuator moves a hemispherical tip linearly. The top, movable portion of the linear ball bearing is spring loaded against this tip. When the piezo actuator moves, it moves the linear ball bearing stage. The piezo actuator has a coarse motion lead screw with 15 mm of travel and a fine motion piezo actuator with 25 μm of travel. The coarse motion lead screw is used to adjust the sample position manually. The fine motion piezo actuator is used to impart the scrub as controlled by a LabView program.

A 3/4" aluminum vacuum plate is mounted to the top portion of the linear ball bearing stage. This plate has a fitting for a vacuum line and a circular opening in the top center portion of the plate through which vacuum can be pulled.

A 1/4" aluminum mounting plate is bolted over the 3/4" aluminum plate with the vacuum fitting. This smaller plate also has a hole in the center for pulling vacuum. This aluminum plate has three cylindrical pins near its center. It also has four arms which make electrical contact to the sample. This is shown in Figure 6-10. The process for mounting the samples is described later in this chapter.

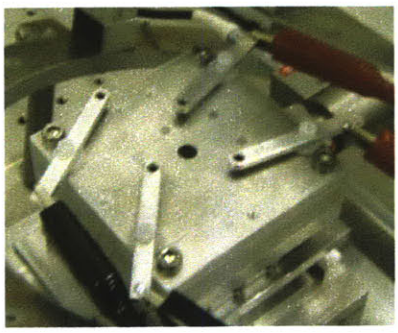

Figure 6-10: The three alignment pins and four arms for making electrical contact on the mounting plate.

Frame Assembly

The frame assembly includes a frame having three legs, a linear micro-stepper motor, a capacitance probe, gross positioning flexure, force gauge flexure, and changeable tip which makes contact with the sample. The solid model of the frame assembly is shown in Figure 6-11.

The frame is the largest object in the frame assembly. It consists of a circular ring with three legs. The bottoms of these legs are machined to have a conical profile. Attached to the circular frame are two vertical supports, each 133 mm tall. On top of this is a cross bar which is 300 mm across. The flexures and linear micro-stepper motor each attach to the cross bar of the frame.

The force gauge flexure and gross positioning flexure are both contained on a solid piece of 3/4" aluminum. The gross positioning flexure allows for the gross positioning of the force gauge flexure and more importantly the tip on the force gauge flexure. This is a double bar cantilever flexure. The force gauge flexure allows a capacitance probe to measure the amount of force imparted by the flexure. This is a symmetrical flexure comprised of four cantilever flexures in a diamond configuration. These two flexures are shown in Figure 6-11.

The ThorLabs ZST6 micro-stepper, which has a resolution of 2.5 nm linear steps over a 6 mm range, is mounted to the cross bar of the frame. It is positioned directly in line with the center of the of the symmetrical force gauge flexure. It is positioned at the end of the double bar cantilever gross positioning flexure.

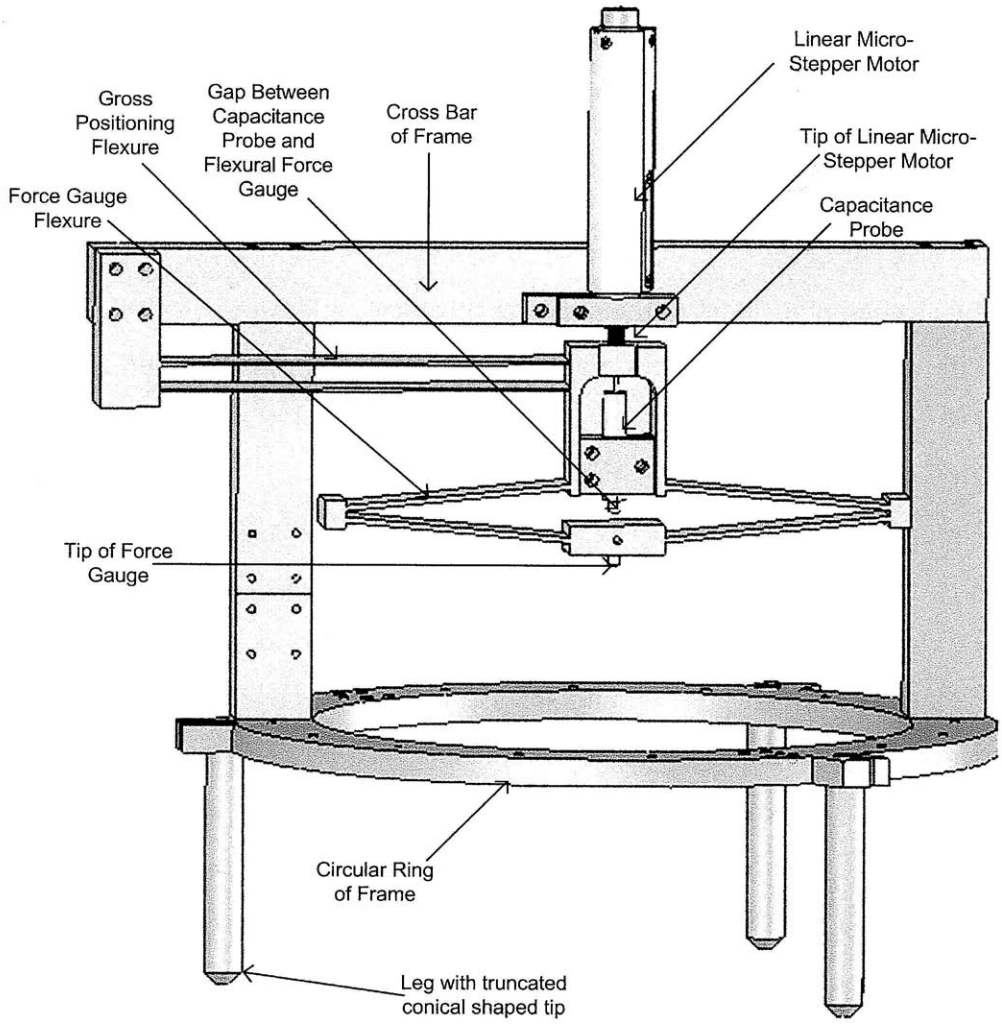

Figure 6-11: The components of the frame assembly.

A Lion Capacitive Sensor with a 50 μm range and 2 nm resolution is mounted directly over the flexural force gauge. When the symmetrical flexure is compressed, the gap between the end of the capacitance probe and the flexure changes. This is detailed later in this chapter.

On the bottom of the symmetrical flexural force gauge, there is an M4 threaded hole. This allows multiple tips to be placed on the end of the force gauge. For the experiments described in this thesis, a hemispherical tip with a radius of 1.25 mm is used. This tip is directly in line with the capacitance probe and the micro-stepper.

Alignment of the Base Assembly to the Frame Assembly

The base assembly and the frame assembly are aligned to each other using a kinematic coupling configuration. In Chapter 5, it was shown that the position of the probe only needs to be accurate to within 0.5 mm and 5°. Kinematic coupling configurations are accurate on the order of microns, so the alignment between the base and the frame is adequate. The conical ends of the three legs of the frame make contact at six points with the three 90° grooves on the base. The legs are stainless steel and the base is aluminum. This positions the tip of the force gauge flexure over the center of the mounting plate. The exact position of the mounting plate relative to the tip can be adjusted using the large lead screw in one direction and the coarse piezo leadscrew in the other direction. A solid model of the complete assembly is shown in Figure 6-12.

Details of the Force Gauge Flexure and Gross Positioning Flexure

The relative motions of the gross positioning flexure and the force gauge flexure allow force imparted at the tip of the force gauge flexure and the total displacement of that tip to be measured. Before any force is applied, the tip of the micro-stepper sits just on top of the flexure. The tip of the force gauge is not touching anything. The capacitance probe measures the gap between the tip of the capacitance probe and the force gauge flexure. The micro-stepper is then advanced. This flexes the gross positioning flexure. This also advances the tip of the force gauge flexure. However,

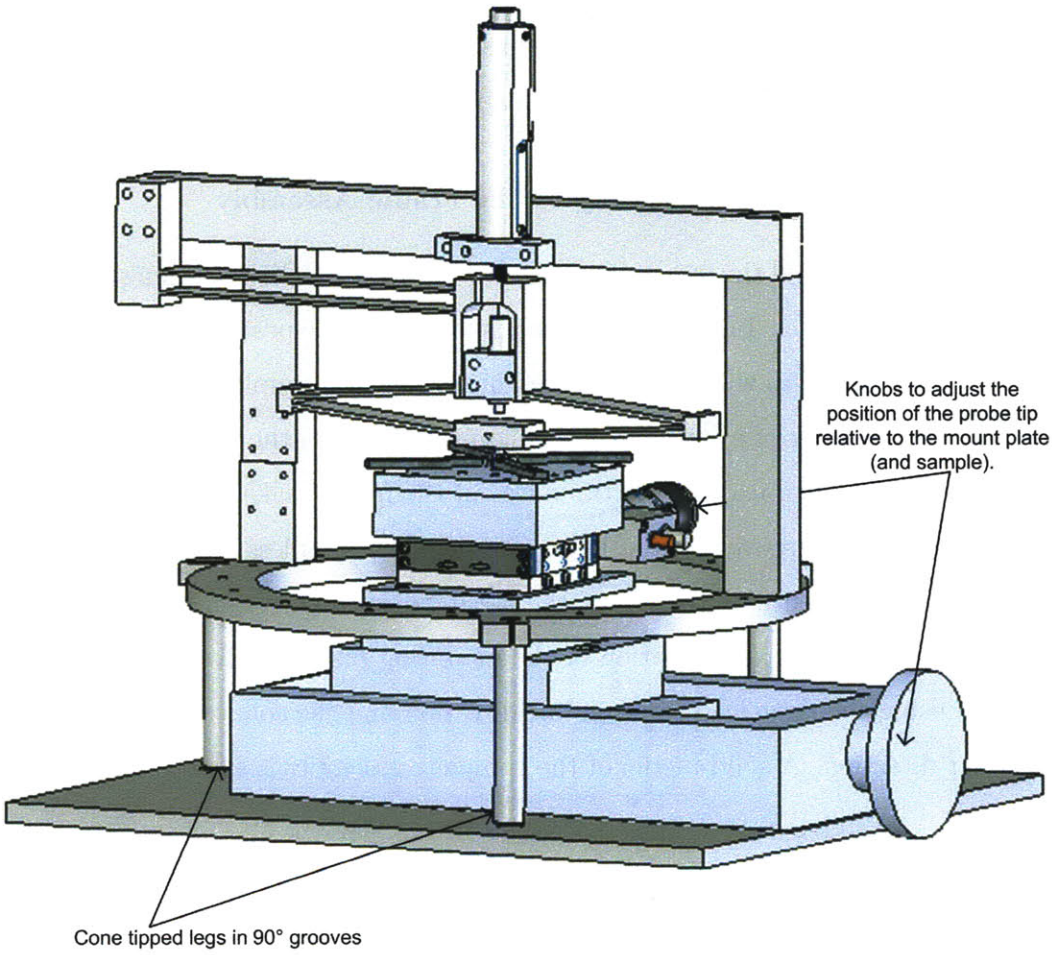

Figure 6-12: The base and frame assemblies aligned using a kinematic coupling configuration.

the gap between the capacitance probe and the force gauge flexure remains unchanged because there is no force applied to the tip of the force gauge. This continues until the tip of the force gauge makes contact with something that can impart a force. If the contacting surface is rigid, the tip of the force gauge can no longer move. However, the micro-stepper can continue to advance. This means that as the micro stepper advances a certain amount, the gap between the capacitance probe and the force gauge flexure will change by that same amount. If the contacting surface has a finite stiffness, as with the membrane of the top coupon of the two-coupon system described in Chapter 5, then the tip of the force gauge flexure will continue to advance. The amount it will continue to advance is the difference between the the forward motion of the micro-stepper and the change in gap between the capacitance probe and the force gauge flexure. The flexures meeting a rigid contact surface are shown in Figure 6-13. The forward motion of the linear micro-stepper is x_M, the change in the gap between the capacitance probe and the force gauge flexure is x_c, and the total displacement of the tip on the force gauge flexure is x_t. These three displacements are related by the following equation:

$$x_t = x_m - x_c. \tag{6.2}$$

The change in gap between the capacitance probe and the force gauge flexure is directly proportional to the force imparted by the flexure. The flexure consists of four cantilever beams with the slope of each beam fixed at zero at either end. These four beams form two pairs of of beams in series. These two pairs are themselves in parallel. Since the stiffness of two beams in series is half of one beam and the stiffness of two beams in parallel is twice of one beam, the overall stiffness of the force gauge flexure is the same as one beam. This stiffness of the force gauge and the individual cantilever beams having a zero-degree slope condition at both ends is

$$k_{fg} = \frac{12EI}{L^3} \tag{6.3}$$

where I is moment of inertia, E is young's modulus of aluminum, and L is the length

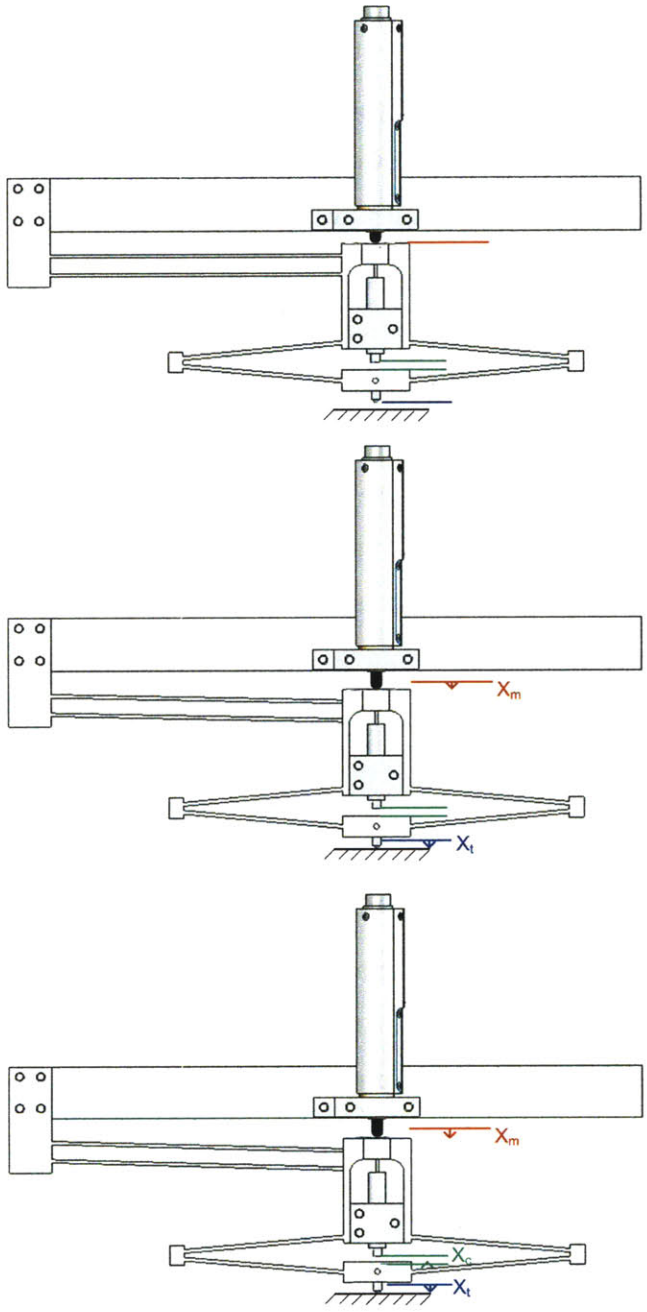

Figure 6-13: Top: The original position of all of the flexural elements. Middle: The micro-stepper displacing the gross positioning flexure. Bottom: The micro-stepper continuing to displace the gross positioning flexure while the force gauge flexure is compressed against a rigid surface.

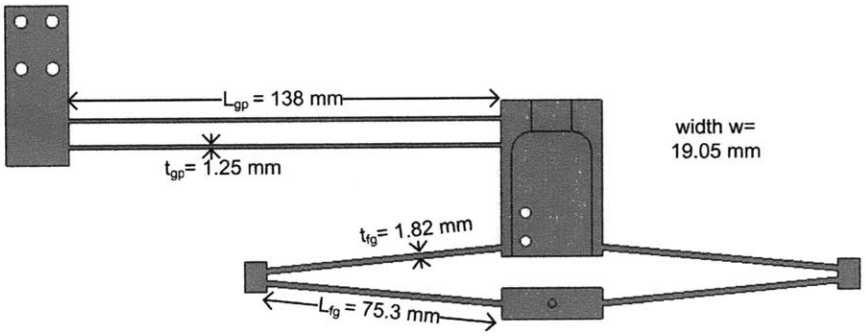

Figure 6-14: The geometry of the gross positioning and the force gauge flexures

of the flexure. The dimensions of the force gauge flexure, as well as of the gross positioning flexure, are shown in Figure 6-14. For a rectangular beam, the moment of inertia is

$$I = \frac{wt^3}{12} \tag{6.4}$$

Where w is the width of the flexure and t is the thickness of the flexure. Therefore, the moment of inertia for the force gauge flexure having a width of 19.05 mm and a thickness of 1.82 mm is 9.57 mm^4. The stiffness of the force gauge flexure having individual cantilever beam lengths of 75.3 mm is therefore 18.8 mN/μm. The range of the force gauge is dependent on the range of the capacitance probe. Since the capacitance probe can only measure gap changes of up to 50 μm, the total measurable force range is 941.1 mN. The resolution of the force gauge is dependent on the resolution of the capacitance probe. The resolution of the capacitance probe is 2 nm, so the resolution of the force gauge is 37.7 μN. A stiffer force gauge could offer larger forces with larger resolution while a more flexible force gauge would offer smaller maximum forces with better resolution. The two-coupon system described in Chapter 5 requires 243.75 mN to deflect the membrane. This is force taken out of the force range that can be applied to the contact. Therefore using the two-coupon system described in Chapter 5 and this force gauge, the maximum measurable force on the contact would be 697.35 mN of force. This is far more than most contacts would require. Many MEMS fabricated electrical contacts have forces of less than 10 mN. However, assembly applications may have higher force requirements. The maximum stress seen in

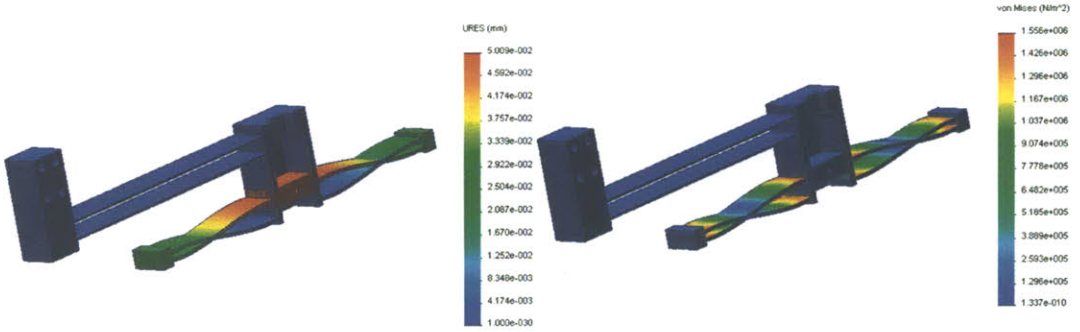

Figure 6-15: The results of an FEM of the force gauge flexure when 941.1 mN of force is applied. The deflection shown in this figure is exaggerated. The actual deflection is very small.

the flexure is described by the following equation:

$$\sigma = \frac{FLt}{8I}. \tag{6.5}$$

At the maximum force of 941.1 mN, the maximum stress in the force gauge flexure will be 1.69 MPa, far less than the yield strength of aluminum, 207 MPa. This stiffness was tested using a finite element model. In this model, the gross positioning flexure was restrained so that all force and displacement were taken up by the force gauge flexure. 941.1 mN of force were applied and the displacement of the flexure and the maximum stress seen were recorded. The maximum displacement seen was 50.09 μm, nearly exactly the predicted displacement of 50 μm. The maximum stress seen was 1.56 MPa, slightly less than the 1.69 MPA predicted stress. These results are shown in Figure 6-15. It should be noted that the FEM program used shows an extremely exaggerated geometry. The actual deflections are quite small. The actual flexure was calibrated using weights to determine the the real stiffness of the device. The capacitance probe was adjusted so that when no external forces were acting on the force gauge flexure, the capacitance probe would see the smallest possible gap. Then, plates machined to fit on the bottom of the force gauge flexure were added, as shown in Figure 6-16. These plates were weighed on a precision scale. After the weights were added, the gap was measured using the capacitance probe. A plot of

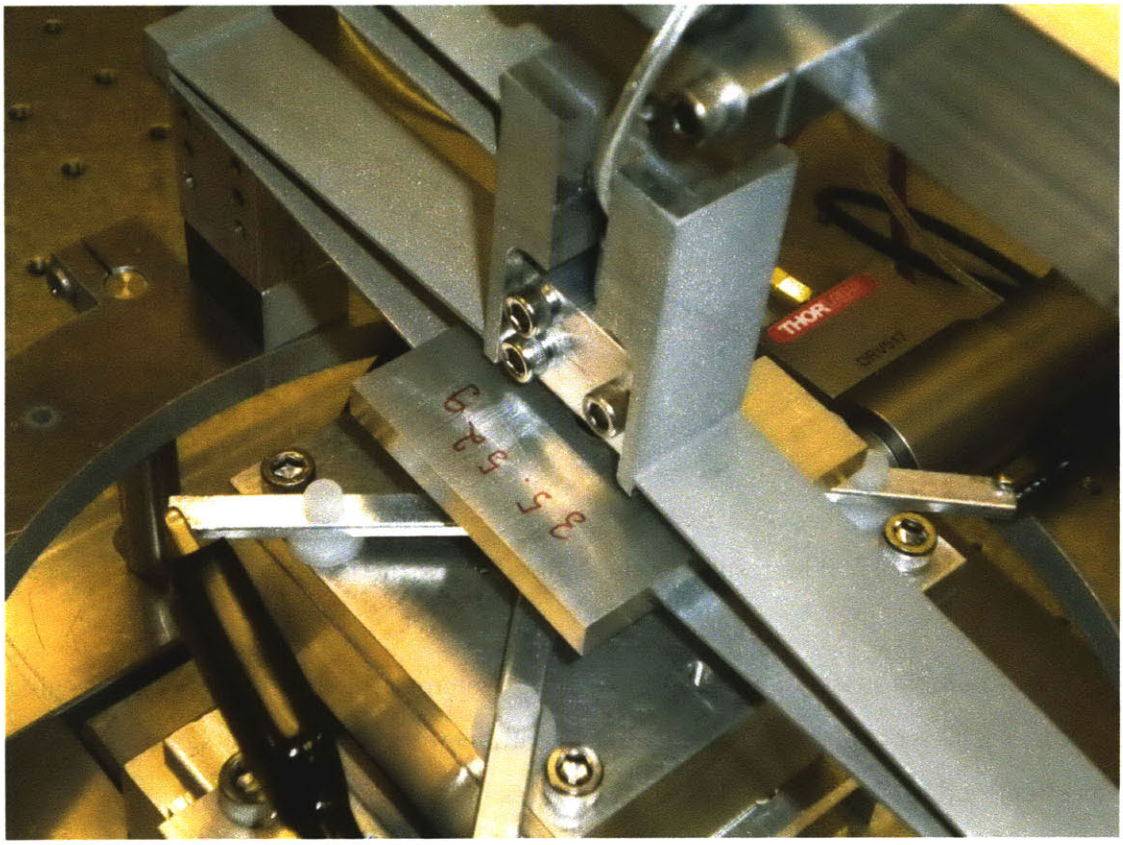

Figure 6-16: Plates of a known mass being used to deflect the force gauge flexure.

the deflection of the flexure versus the weights of the plates is shown in Figure 6-17. This calibration shows the stiffness of the flexure to be approximately 16 mN/μm. It also shows that stiffness is constant throughout the deflection of the flexure, as the R^2 value of the calibration data fitted to a linear function is 0.9999. The 16 mN/μm is slightly less than the 18.8 mN/μm which was predicted. This is because the waterjet cutter used to fabricate the flexures did not have precise tolerances on the thickness of the flexure and the sidewalls of the flexure were slightly tapered.This means the maximum force value the gauge can read is 800 mN not 941.1 mN and the resolution of the force gauge is 32 μN not 37.7 μN. Later on the calibration factor is referred to having units of mN/V. The capacitance probes actually output a voltage. One volt is equal to 2.5 μm. Therefore the calibration factor can be stated as 40 mN/V.

The gross positioning force gauge has no effect on the force measured. The maximum displacement of the gross positioning force gauge is limited by the yield strength

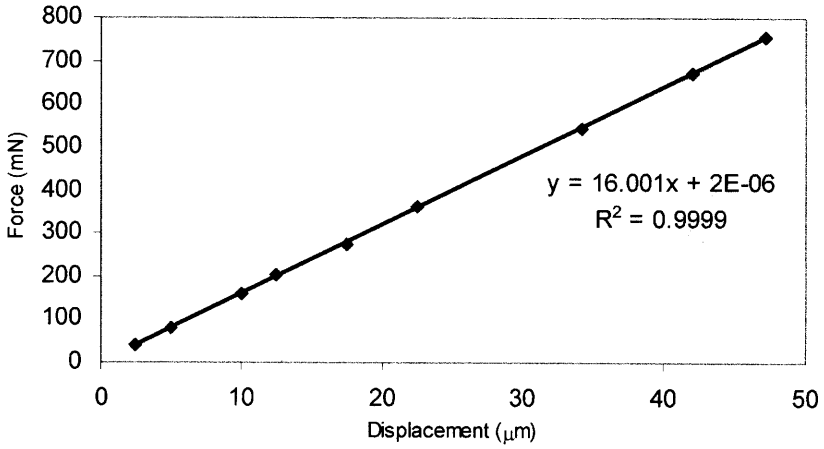

Figure 6-17: The results of the calibration of the force gauge flexure.

of the aluminum material and the travel of the micro-stepper. This gross positioning flexure consists of two cantilever flexures in parallel restrained by zero-slope conditions at either end of the flexure. The total stiffness of this flexure is

$$\frac{24EI}{L^3} \tag{6.6}$$

The geometry of this flexure is shown in Figure 6-14. Moment of inertia is defined in Equation 6.4. With a length of 138 mm, a thickness of 1.25 mm, and a width of 19.05 mm, this flexure has a moment of inertia of 3.1 mm^4 and a stiffness of 1.982 $mN/\mu m$. The micro-stepper has a maximum travel of 6 mm. The force that this maximum travel would impart on the flexure would be 11.9 N. The maximum stress occurs at

$$\sigma = \frac{FLt}{8I}. \tag{6.7}$$

At the maximum travel of 6 mm and the corresponding force of 11.9 N, the maximum stress seen in the gross positioning flexure would be 82.7 MPa. The yield strength of aluminum is approximately 207 MPa. Therefore at the maximum travel of the micro-stepper, the safety factor for yield stress is 2.5. A finite element model was created to check the results of this analysis. A force of 11.9 N was imparted onto the

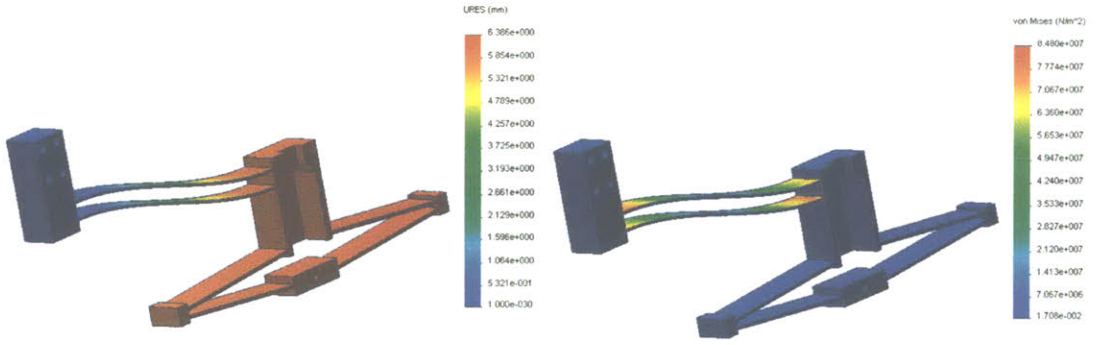

Figure 6-18: The FEM results for the gross positioning flexure when a force of 11.9 N is applied. Deflection is exaggerated.

gross positioning flexure and displacement and maximum force were recorded. These results are shown in Figure 6-18. At this force, the FEM showed a displacement of 6.37 mm, slightly more than the 6 mm predicted. The stress seen was 84.8 MPa, slightly more than the 82.7 MPa predicted, but still well less than the yield strength. Most importantly, the FEM showed no measurable tilt when the maximum force was applied. Therefore the force gauge should apply a completely vertical force.

Details of the Scrubbing Module

The scrubbing module is quite simple: the piezo is mounted to the base of the linear ball bearing stage. When the piezo is extended the top portion of the stage translates. Since the vacuum plate, the mounting plate, and the bottom coupon are all attached to the top portion of the linear ball bearing, they move as well. The force gauge tip stays in the same position. It is engaged with the retaining ring preventing center of the top coupon from moving. The in-plane flexure allows the outside of the top plane coupon to move with the bottom coupon. The 243 mN of force it takes to close the gap between the coupons preloads the ball/pit interfaces. Therefore, the center of the top coupon with the contact material stays stationary, while the tip on the bottom coupon translates the same distance that the piezo extends. This is shown in Figure 6-19. As discussed in Chapter 5, in order to prove the contacts could create scrub, a 25 μm blade tip was scrubbed 15 μm. The force on the tip was very small, 2 mN. The surface the tip was contacting was gold which had been coated with Sharpie

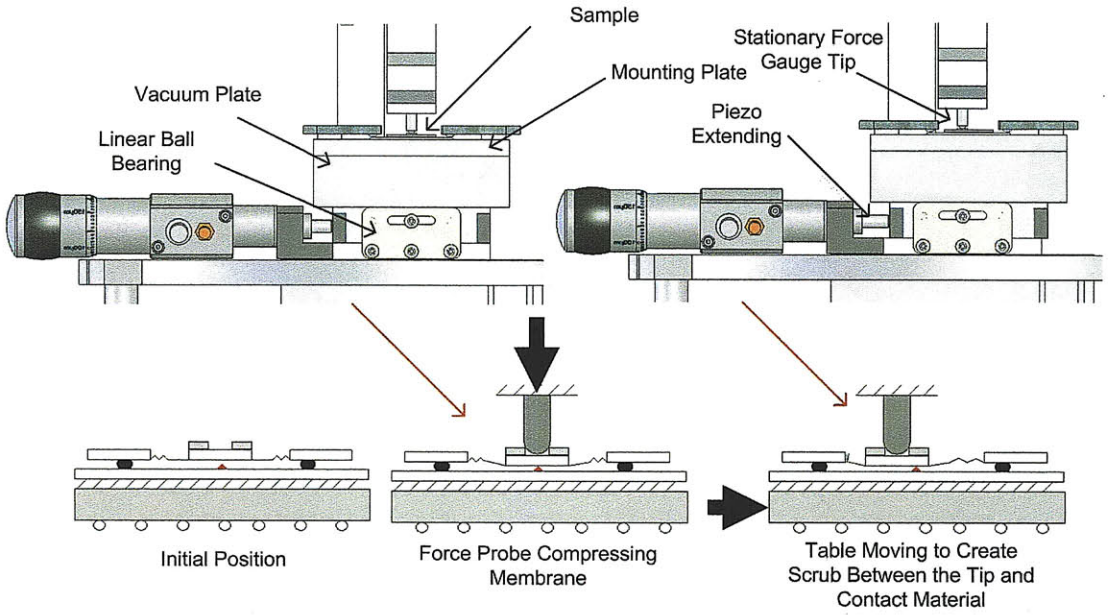

Figure 6-19: The scrubbing motion of the instrumentation. The gap height and the scrub distance are exaggerated.

marker. The Sharpie was scrubbed away from the area the tip contacted. The full area which was scrubbed clean was 40 μm, the sum of the tip length and the scrub length. This proof of concept scrub is shown in Figure 6-20, which is also shown in Chapter 5.

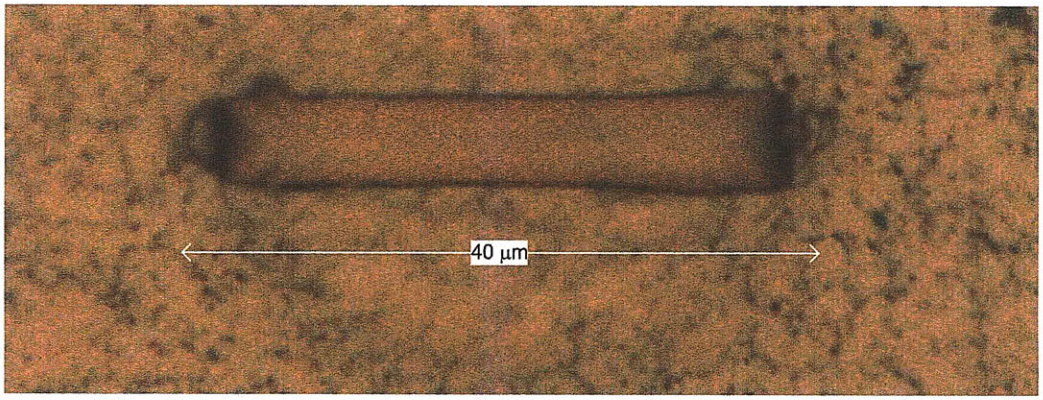

Figure 6-20: A proof of concept scrub mark made using sharpie marker.

6.2.2 Testing Procedure

This section details the calibration of the machine, the setup of a two-coupon system, and the programs used to test the two coupon system.

Calibration

Prior to placing the sample on the instrumentation, the force gauge flexure should be calibrated. This is done to ensure the accuracy of the measurement. In normal operation, when nothing is making contact with the force gauge flexure, the capacitance probe is positioned so that it is measuring maximum gap; hence, when the probe pushes on a sample, the gap gets smaller and the maximum range of the capacitance probe is utilized. When the capacitance probe is in this position, it has an output of about -9.5 V. If the voltage is -10 V, then the capacitance probe is out of range. The in range voltage ranges from -10 to 10 V which correspond to gaps of -25 μm to 25 μm. The force gauge flexure is calibrated by placing a 35.25 g (345.45 mN) plate on the flexure as shown in Figure 6-16. With the capacitance probe in its standard position, adding this weight would cause the gap to be too large and out of range. This can be avoided by adjusting the zero of the offset. The Elite Series Driver has a knob which can adjust the offset of the gap. This is shown in Figure 6-21. When this knob is turned all the way clockwise, the voltage output from the capacitance probe changes from -9.5 to -0. At that point, a LabView program is run, entitled "Two Point Calab." This program prompts the user to hit measure when no weight it applied to the system and then again after the 345.45 mN weight has been applied to the system. After each measure, the program waits until the signal is stable, because taking weights on and off can induce vibrations, and then measures the voltage output from the capacitance probes. It then uses these two points to find the calibration factor, which should be around 40 mN/V. The weight is then removed and the zero knob on the capacitance probe driver is adjusted again until the output voltage reads approximately -9.5 V. This calibration factor is used later on when setting up the sample and when running the programs which take measurements.

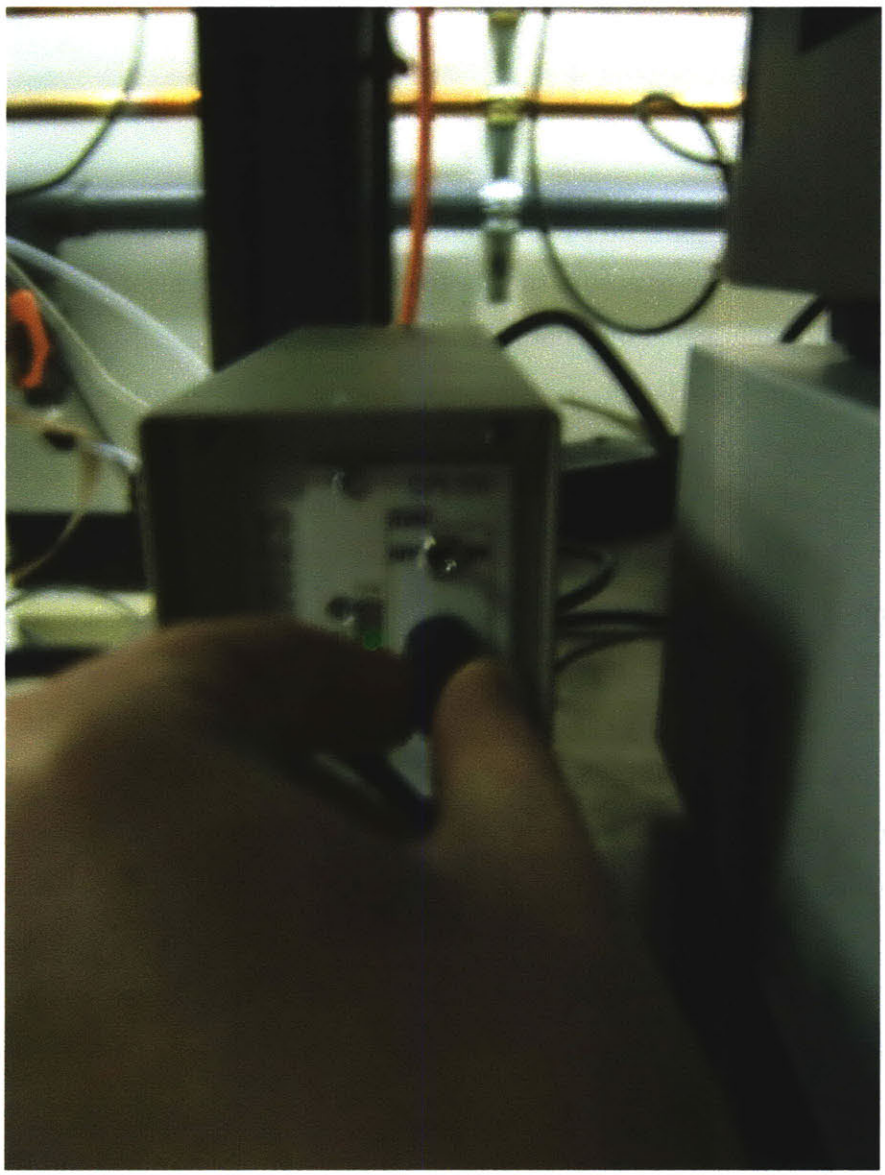

Figure 6-21: The knob on the Elite capacitance driver which adjusts the zero position of the output voltage. This is turned all the way clockwise before calibration and adjusted to have an output of -9.5 volts for normal use when no force is applied to the force gauge flexure.

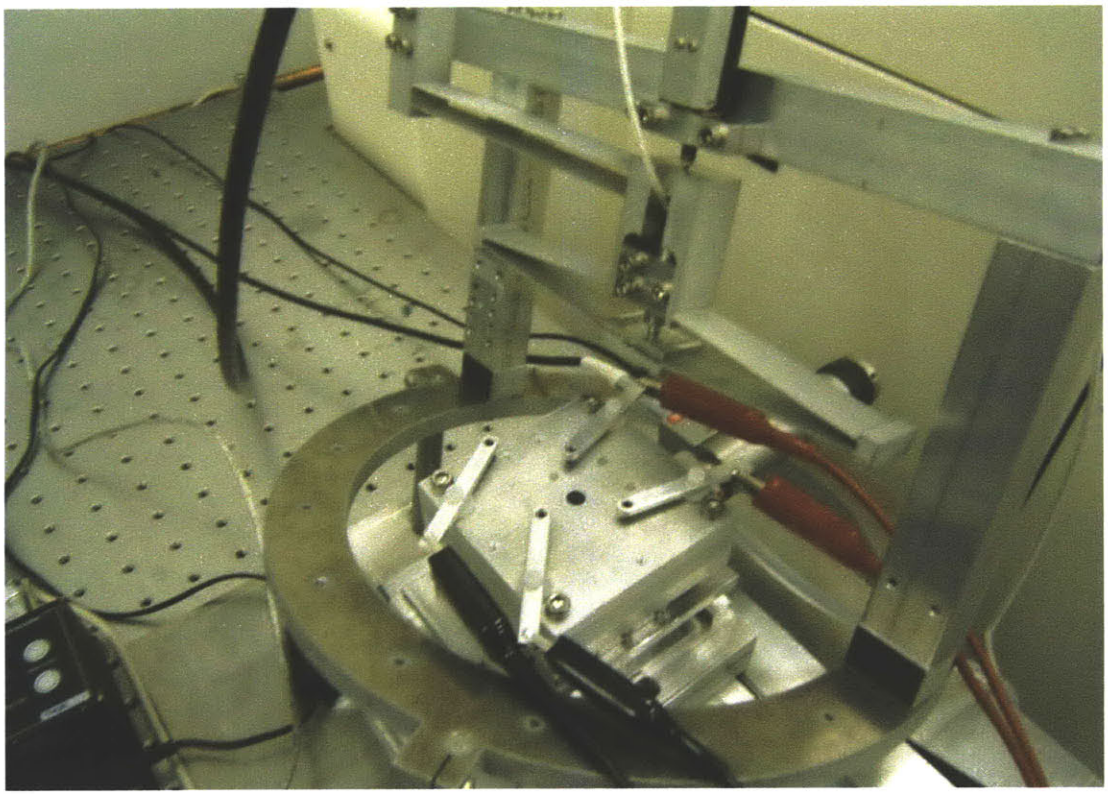

Figure 6-22: The frame assembly tilted away from the base assembly to expose the mounting plate.

Sample Alignment

The instrumentation contains hardware which aligns the two-coupon system to the instrumentation and makes electrical contact to the bottom coupon. First, the frame assembly is tilted away from the base assembly to gain access to the mounting plate. This is shown in Figure 6-22. Then, the bottom coupon is placed on the mounting plate. The mounting plate has three cylindrical pins in the center. These are used to align the bottom coupon to the mounting plate. The bottom coupon is pressed against these three pins and the vacuum is turned on to keep the coupon in place. This is shown in Figure 6-23.

After the vacuum has been turned on, electrical connections are made to the bottom coupon. The four bond pads of the bottom coupon are contacted by four sphere tipped detent spring set screws located at the end of four aluminum arms.

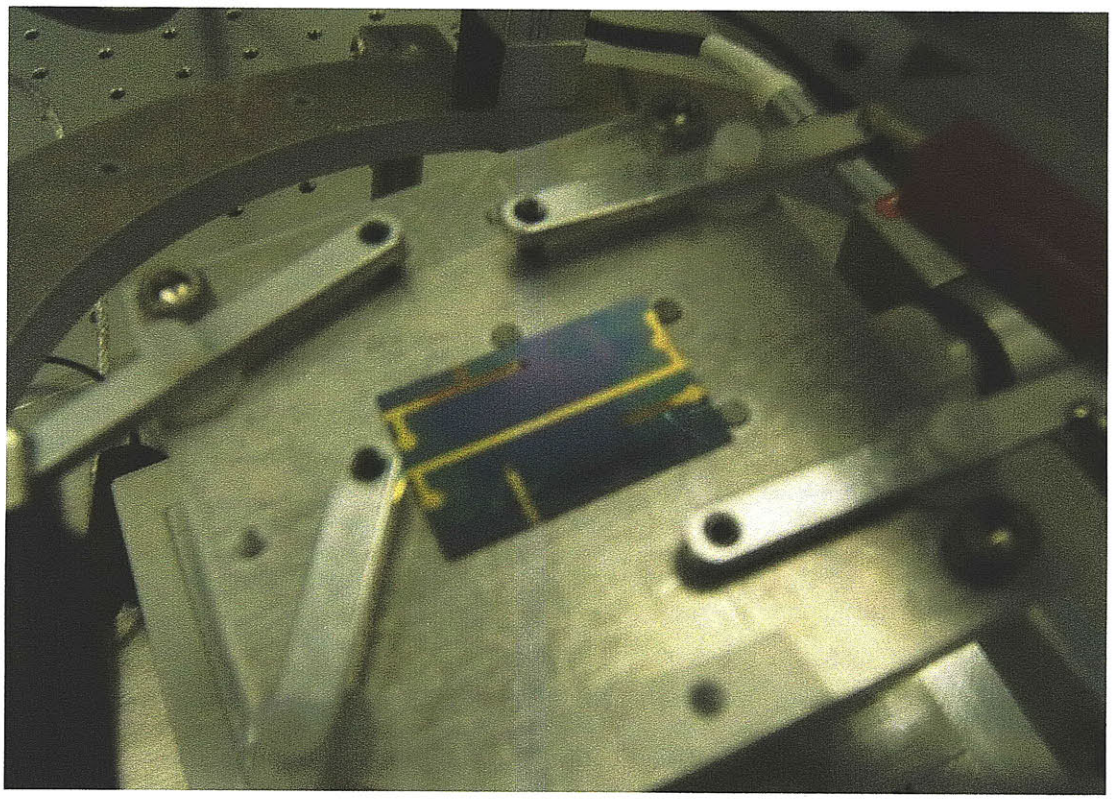

Figure 6-23: The bottom coupon aligned to the mounting plate using the three alignment pins on the mounting plate.

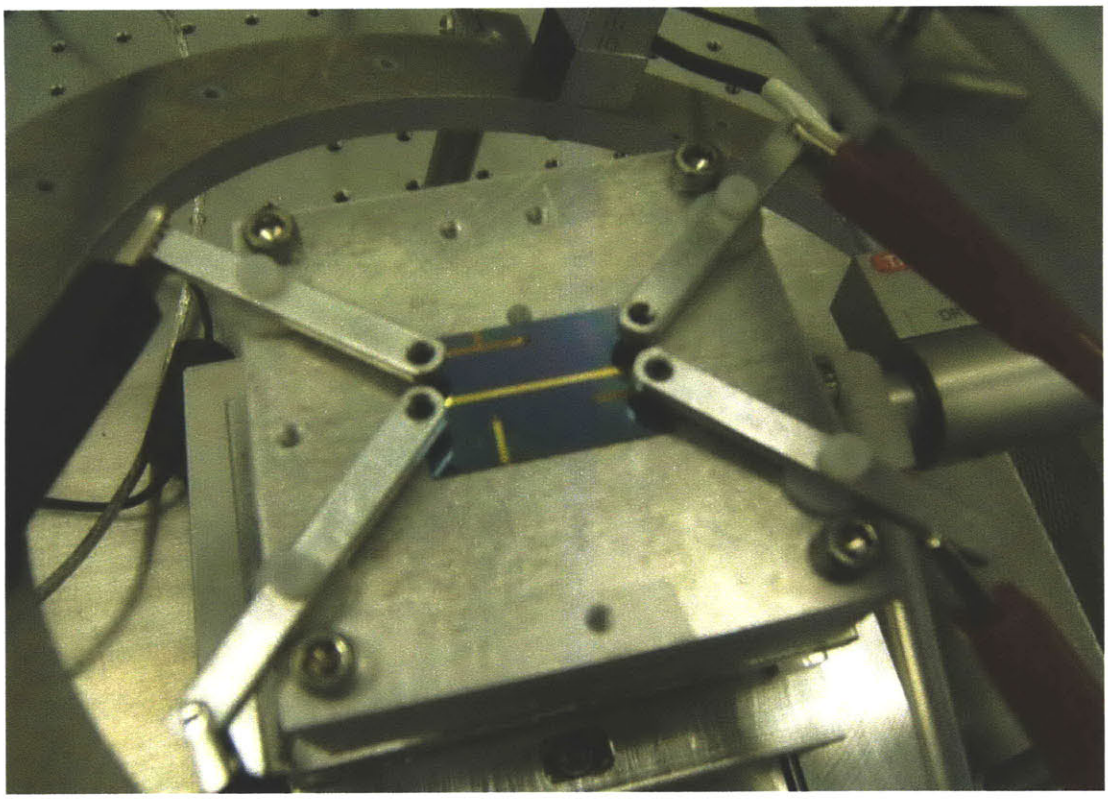

Figure 6-24: The bottom coupon after electrical connections have been made to each of the four bond pads through the aluminum arms with detent spring set screws.

These aluminum arms are bolted to the corners of the mounting plate using nylon springs and have nylon washers separating the aluminum arms from the mounting plate. That way, the arms are electrically insulated from the mounting plate and each other. The ends of the arms are positioned over the four bond pads of the bottom coupon, and the detent spring sphere tipped set screws are tightened against the bond pads using a hex key. Wires from the Keithley 2420 source-measure unit are attached to the aluminum arms using banana clips. This is shown in Figure 6-24.

The top coupon is then assembled onto the bottom coupon, as is shown in Figure 6-25.

Next, the retaining ring on the top coupon is positioned directly below the force gauge probe. A manual alignment is performed first. The gross piezo lead screw and the large lead screw must be adjusted so that the force gauge probe is approximately over the center of the retaining ring. Next, the linear micro-stepper is advanced until

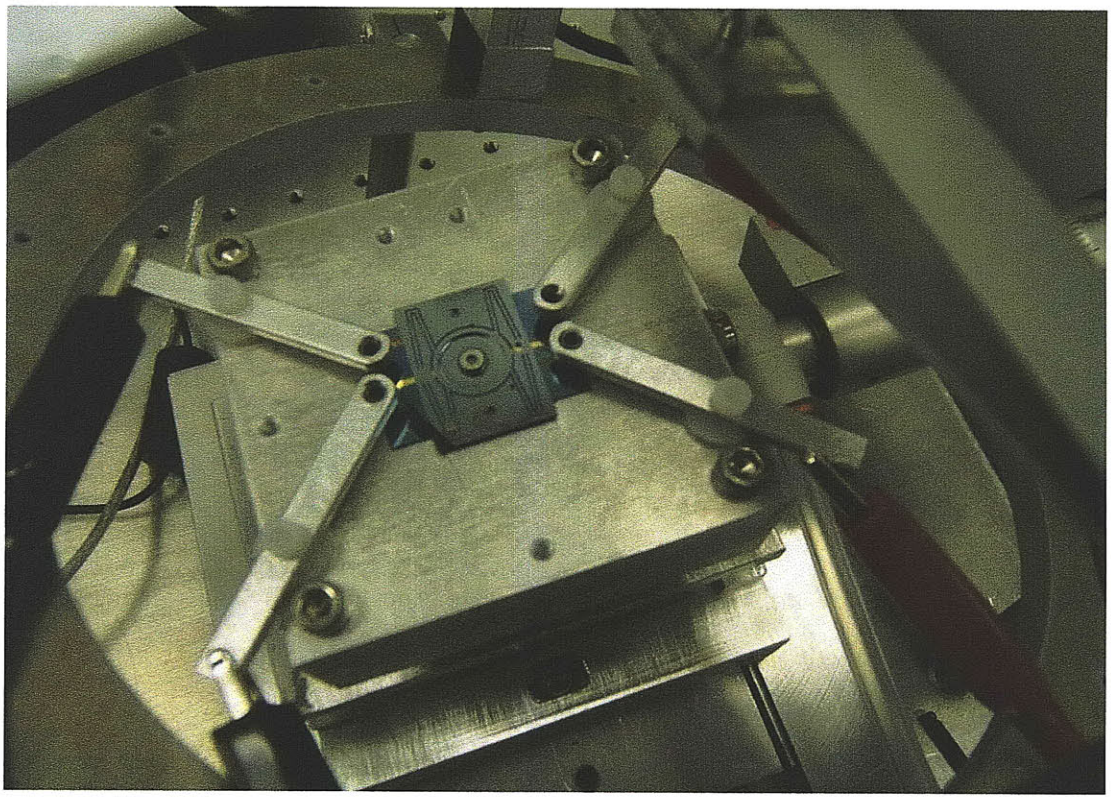

Figure 6-25: The top and bottom coupons in place on the mounting plate of the instrumentation.

Figure 6-26: From left to right: the micro-stepper motor controller with the manual positioning knob circled, moving the micro-stepper motor manually to adjust the vertical position of the tip of the force gauge, moving the piezo gross positioner manually, moving the large lead screw manually.

the tip of the force gauge is just above the retaining ring. The linear micro-stepper is advanced by using the manual controls on the motor controller. These three manual controls are shown in Figure 6-26. The tip of the force gauge approximately centered is shown in Figure 6-27.

A LabView program assists in finding the exact center of the retaining ring. The program "Manual Position" asks the use to input the calibration factor. The program then advances the force gauge tip until it makes contact with the retaining ring at a force of 100 mN. This is less than the 243.75 mN needed to close the gap between the top and bottom coupons. The program then graphically displays the voltage output of the capacitance probe. It will be at about -8 V at this point (a change from -9.5 V when the program was started). The user then manually adjusts the large lead screw and piezo gross positioning knobs. As the user adjusts these knobs, the voltage either goes up or down. When the user is in the exact center of the retaining ring, the voltage will go up when the knobs are turned in either direction. This is because when the ring is in the center of the probe, moving it in any direction will cause the tip run up the sides of the retaining ring, compressing the force gauge flexure. If the retaining ring is very off center, then the user may not see a low point in voltage. Instead, the voltage may return to -9.5 V when the user has moved the probe off of the side of the retaining ring and into the center of the retaining ring. At this point the tip is no longer contacting the retaining ring. The program is run again to place a force of 100 mN on the retaining ring and the process is repeated until a low point in voltage

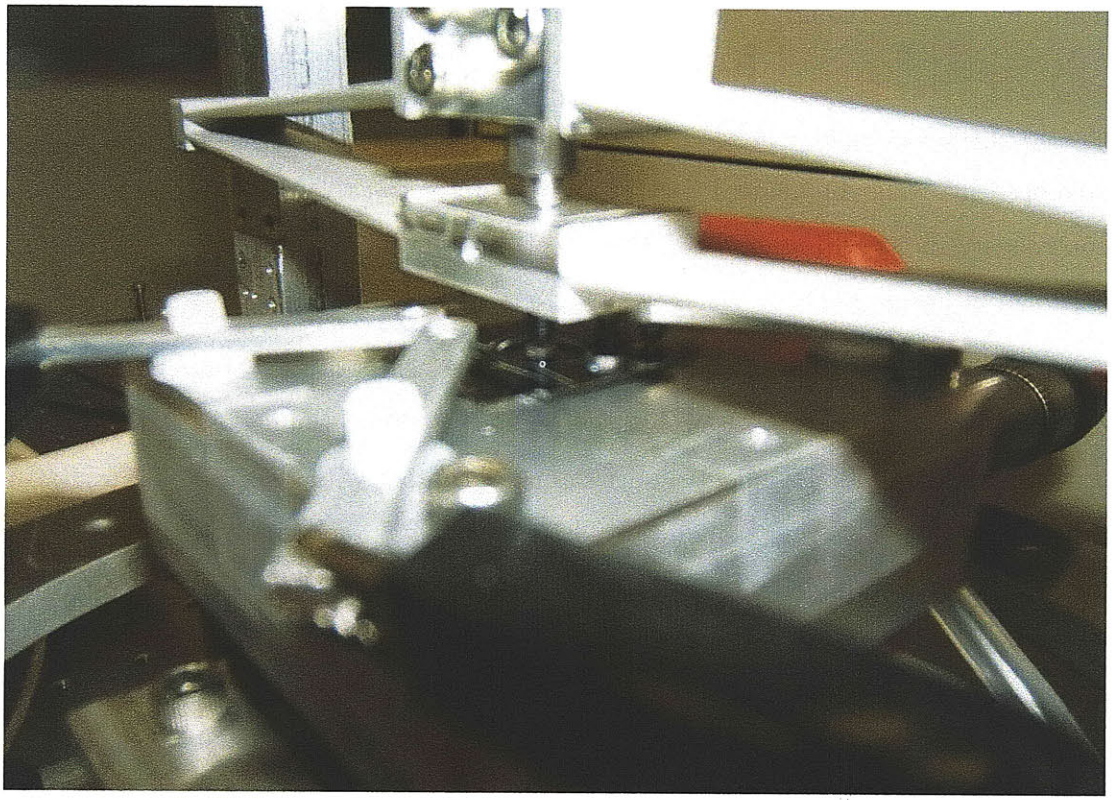

Figure 6-27: The tip of the force gauge after manual centering.

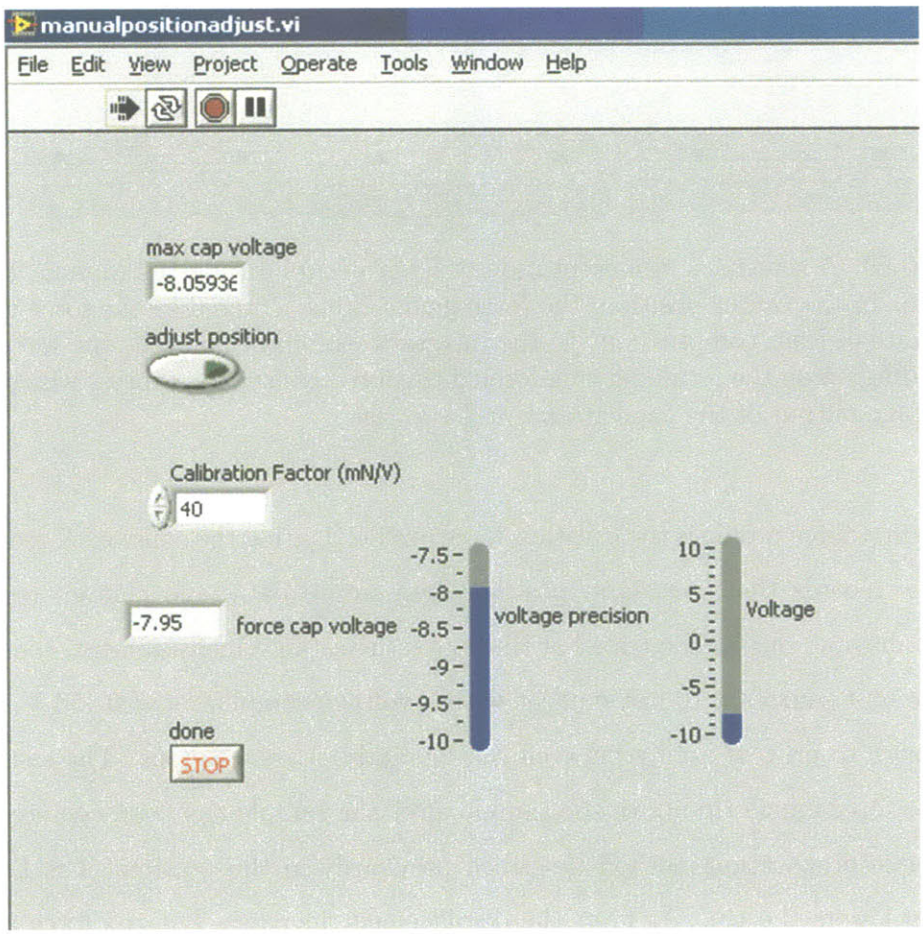

Figure 6-28: The user interface for the Manual Position program. The blue voltage indicators help the user find the voltage low point.

is found. At this point the retaining ring is centered and the force tip is retracted so that it is no longer making contact and the output voltage from the capacitance probe is once again -9.5 V. At this point the sample is positioned and ready for testing. The user interface for the LabView program Manual Position is shown in Figure 6-28. A schematic of what this program controls is shown in Figure 6-29.

Data Acquisition

This instrumentation allows any profile or force to be combined with any profile of scrub. This thesis concentrates on two types of force scrub profiles. LabView programs run each of the two force profiles.

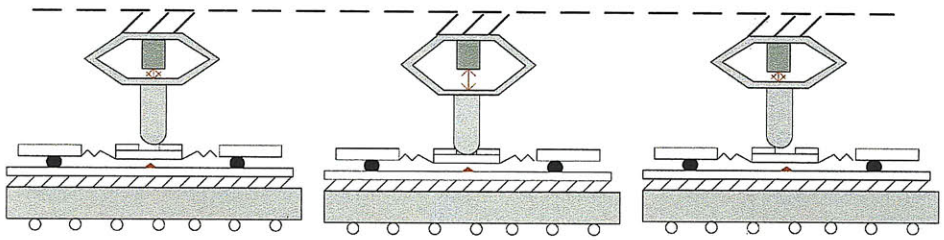

Figure 6-29: A schematic representation of what occurs during the Manual Position program. In the center position, the force gauge tip is centered so the force gauge is in its state of least compression. In the images to the right and left, the force gauge tip is riding up on the retaining ring forcing the force gauge to compress which causes the voltage output of the capacitance probe to rise.

The first force profile is the constant force profile. During the constant force profile, LabView records the force data, position data, scrub data, and contact resistance data at all times during the test. For the contact resistance measurement, the source-measure unit sources a 10 mA current with a voltage compliance of 0.150 V. This is low enough to prevent arcing between the top and bottom coupons. The test begins with the force gauge tip above the sample after the sample has been centered using the sample preparation method described previously in this section. The LabView program lowers the tip. At first, the displacement increases but the force remains constant on the tip because it has not made contact with anything. This is called Zone 1. Next, the tip makes contact with the retaining ring of the top coupon. Then force increases linearly with displacement according to the stiffness of the membrane and in-plane flexure in the top coupon. This is called Zone 2. Finally, the top coupon's contact material touches down on the tip of the bottom sample. This is the point where the contact sees no force. Any additional force will be taken up by the contact because the membrane can no longer flex and can therefore no longer transmit any additional force. As the micro-stepper continues to advance, the total displacement remains constant because the tip has made rigid contact with the sample. The force continues to increase. This is called Zone three. An example of the three zones of the force and displacement relationship is shown in Figure 6-30. The force increases until the maximum contact force defined by the user is reached. At that point, the piezo begins to scrub the contact. A feedback loop ensures that the force on the contact

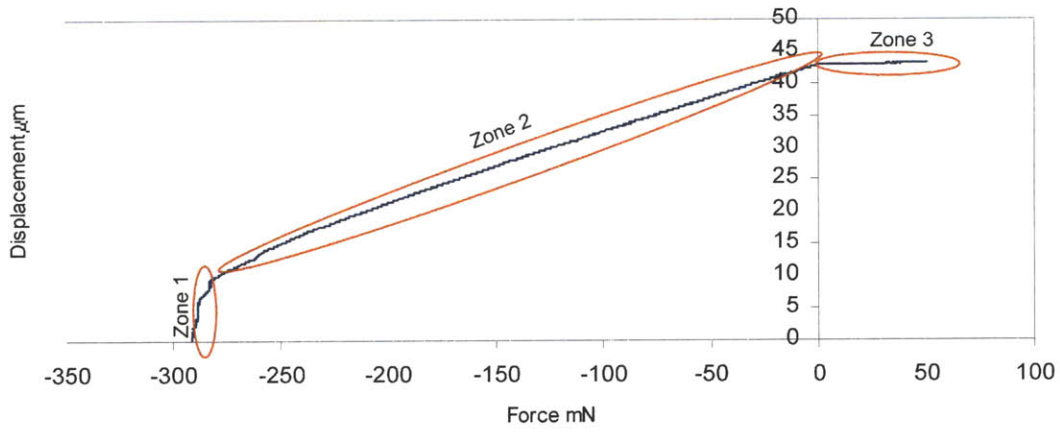

Figure 6-30: The three zones of force and displacement during both the constant and linear force profiles.

stays constant as the piezo scrubs. This piezo advances to the maximum travel of dictated by the user. Once the sample has reached maximum force and scrub, a voltage sweep is run to test the contact resistance at various voltages ranging from zero to the maximum voltage set by the user. The user interface of the program used to run a constant profile test, "Force then scrub then fritt voltage," is shown in Figure 6-31.

When using the program "Force then scrub then fritt voltage," the user inputs the calibration factor; the force step size, which is the increment of force between each measurement; the total force after touchdown, which is the force on the contact; the scrub step size, which is the increment of scrub between each measurement; the total scrub length; the dry circuit current, which is the current sourced through the four-wire resistance measurement and is typically 10 mA; the dry circuit compliance voltage, which is the maximum voltage allowed in the four-wire resistance measurement before current is decreased and is typically 150 mV; the step size for the voltage sweep, which is the increment voltage is increased between measurements during the voltage sweep; the voltage sweep maximum voltage; and the file name where the output will be saved. The program outputs the force, displacement, resistance, voltage, current, and scrub data at all points during the measurement. At the end of the test

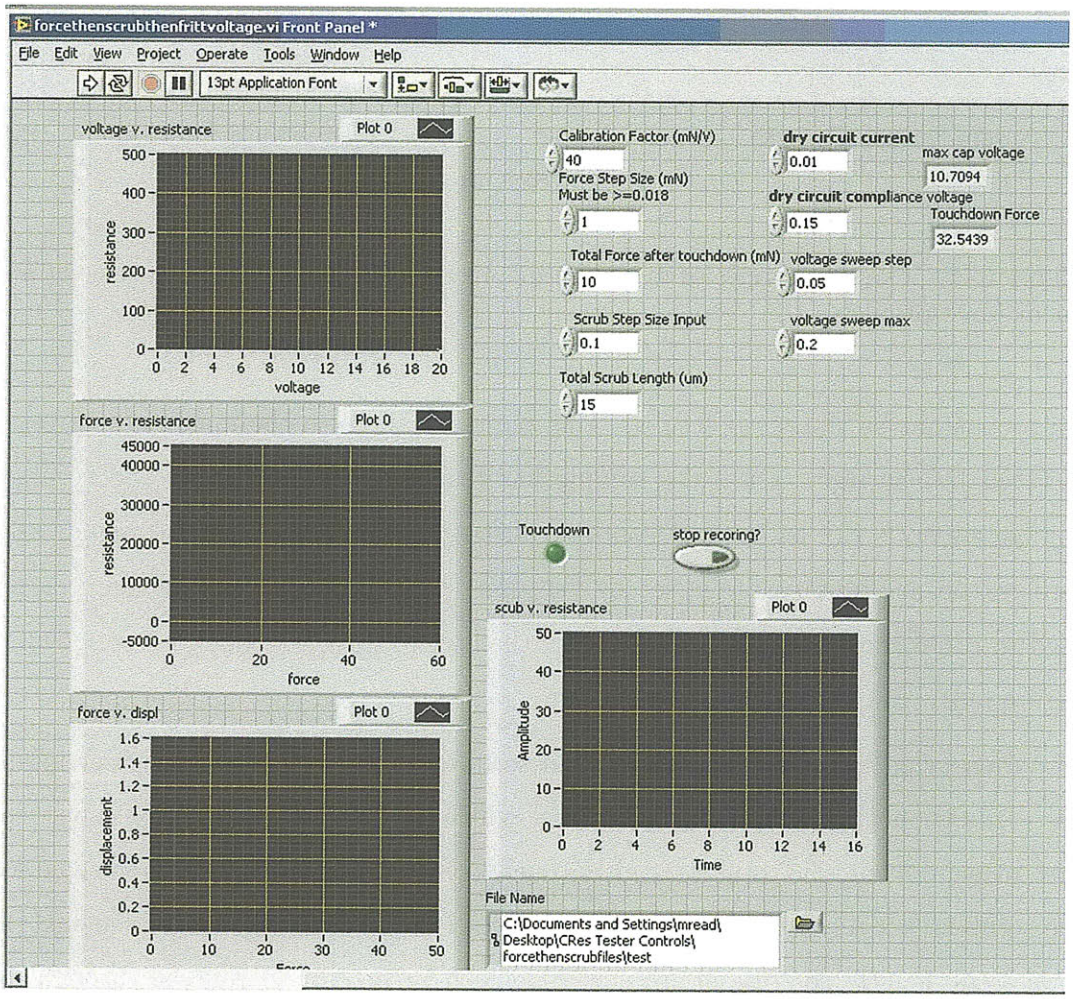

Figure 6-31: The user interface used to perform a constant force profile measurement using the "Force then scrub then fritt voltage" program.

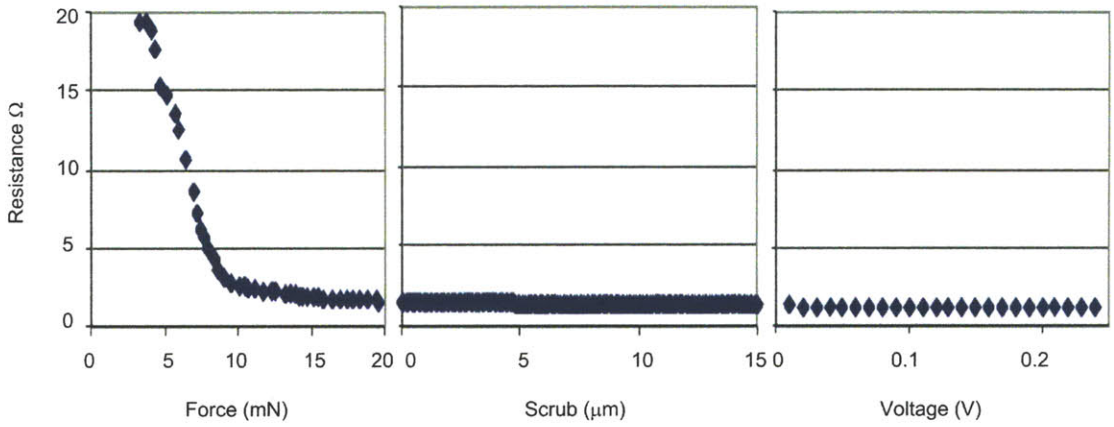

Figure 6-32: A profile of contact resistance as force is increased, followed by scrub, followed by voltage. This is a constant force profile.

the force gauge tip retracts allowing the user to remove the sample. An example of the effect of increased force, scrub, and voltage have on contact resistance is shown in Figure 6-32

The second force profile is the linear profile. During the linear profile, LabView records the force data, position data, scrub data, and contact resistance data at all times just as with the constance profile test. The first portion of the test is identical to tests made using constance force profiles. The test begins with the force gauge tip above the sample after the sample has been centered using the sample preparation method described previously in this section. The LabView program lowers the tip. At first, the displacement increases but the force remains constant on the tip because it has not made contact with anything. This is called Zone 1. Next, the tip makes contact with the retaining ring of the top coupon. Then force increases linearly with displacement according to the stiffness of the membrane and in-plane flexure in the top coupon. This is called Zone 2. Finally, the top coupon's contact material touches down on the tip of the bottom sample. At this point, the contact is at its zero force point. Then force and scrub are increased lineally at the same time. The rates of increasing force and scrub are such that the maximum scrub length is achieved at the same time as the maximum force. This occurs during Zone 3. An example of the three zones of the force and displacement relationship is shown in Figure 6-30. After

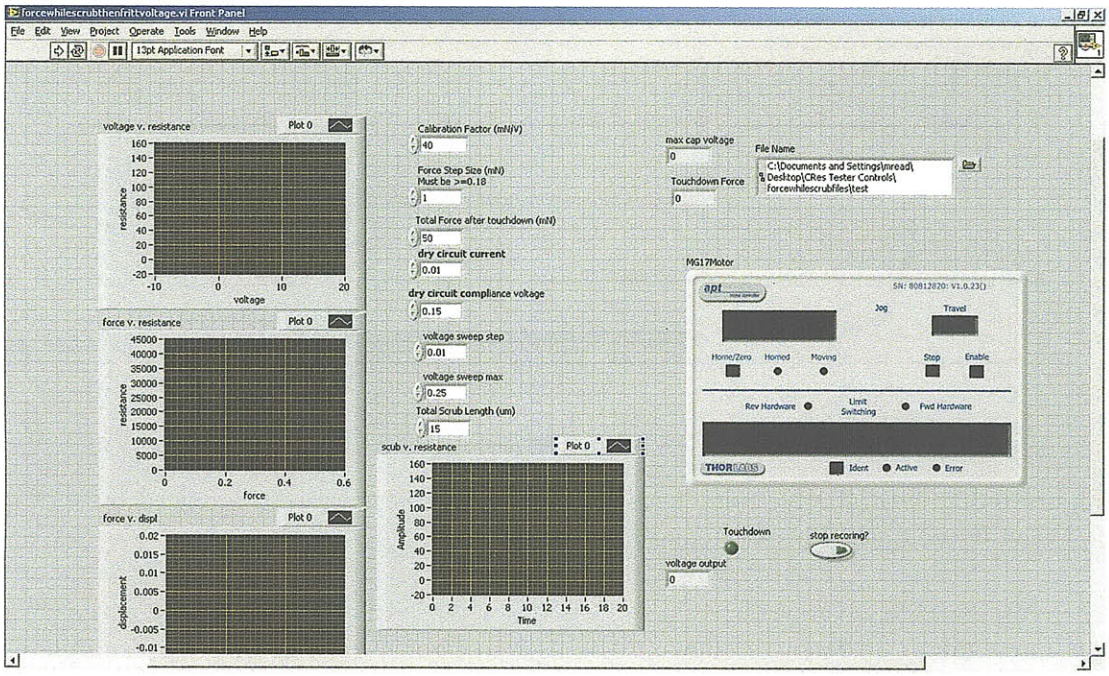

Figure 6-33: The user interface used to perform a linear force profile measurement using the program "Force while scrub then fritt voltage."

these maximum are achieved, a voltage sweep is performed ranging from 0 V to the maximum voltage dictated by the user. The user interface of the program used to run a linear profile test, "Force while scrub then fritt voltage," is shown in Figure 6-33.

When using the program "Force while scrub then fritt voltage," the user inputs the calibration factor; the force step size, which is the increment of force between each measurement; the total force after touchdown, which is the force on the contact; the total scrub length; the dry circuit current, which is the current sourced through the four-wire resistance measurement and is typically 10 mA; the dry circuit compliance voltage which is the maximum voltage allowed in the four-wire resistance measurement before current is decreased and is typically 150 mV; the step size for the voltage sweep, which is the voltage increment between measurements during the voltage sweep; the voltage sweep maximum voltage; and the file name where the output will be saved. The scrub step size is not inputted because it is calculated. The ratio of scrub size to total scrub length is the same as the ratio of force step size and maximum force. The program outputs the force, displacement, resistance, voltage,

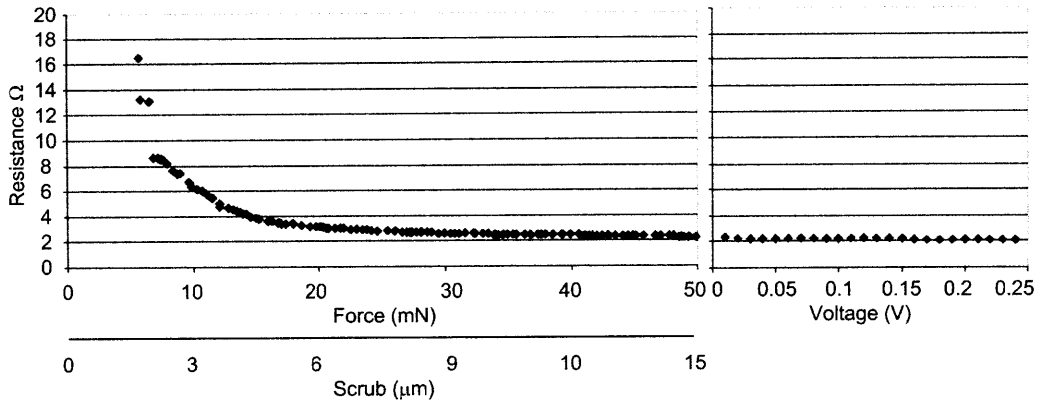

Figure 6-34: A profile of contact resistance as force and scrub are increased, followed by voltage. This is a linear force profile.

current, and scrub data at all points during the measurement. At the end of the test the force gauge tip retracts allowing the user to remove the sample. An example of the effect of increased force, scrub, and voltage have on contact resistance is shown in Figure 6-34

6.2.3 Design Opportunities

Several design opportunities were discovered during the building and use of this instrumentation.

First, the instrumentation could be improved by motorizing the gross translational axes currently controlled manually with knobs. This would allow the sample centering to be done entirely by the LabView program.

Second, the maximum force achieved using the load cell, about 556 mN, is far above what most MEMS applications need. This could be replaced with a softer load cell which has a lower maximum force but better resolution.

The third design opportunity is linked to the coupons themselves. If more of the coupon functionality, such as the in-plane flexure allowing for scrub and the membrane allowing for vertical displacement, were shifted to the instrumentation then the coupons themselves could be made faster and easier.

6.3 Chapter Summary and Conclusions

This chapter presented a proof of concept instrumentation used to test the two-coupon system presented in Chapter 3 and the final instrumentation used to test the final two-coupon system presented in Chapter 5. The final instrumentation system imparts force and scrub to the two-coupon system. This instrumentation could also be used to impart force and scrub onto other devices, although the current mounting plate is customized for the two-coupon system. It measures force with a resolution of 32 μN and displacement with a resolution of 2.5 nm. Contact resistance is measured on the order of mΩ and scrub can be imparted with an accuracy of several nm. All of the tests described in Chapters 7 and 8 were performed using this instrumentation using either the constant or linear profile. For the non-scrubbing, non-voltage sweeping tests, the maximum scrub and the maximum voltage sweep values were set to zero.

Chapter 7

Contact Resistance in Flat Thin Films

List of Symbols	
a	Asperity radius
α	Holm radius
b	Outer boundary radius of contact
F	Force
H	Vicker's hardness GPa
J_1	Bessel function of the first kind of order 1
l	Length of the apparent contact area
k_1	A correction factor of units μm^{-1}
k_2	1 μm
L	Film thickness
L_p	Film thickness of plated layer
L_s	Film thickness of sputtered layer
λ_n	Argument of Bessel function of the first kind of order 1
R_a	Additional contact resistance resulting from a seed layer
R_{ac}	Additional resistance added by the transition from the plated region to the sputtered region

continued from previous page

List of Symbols	
R_{bp}	Fraction of current that actually travels in the bulk
R_c	Contact resistance
R_m	Measured contact resistance of the film and seed layer stackup
R_N	Normalized contact resistance. Measured resistance divided by the resistance predicted by Holm theory
ρ	Resistivity
ρ_p	Resistivity of the plated layer
ρ_s	Resistivity of the seed layer
w	Width of the apparent contact area

The two-coupon system presented in Chapter 5 along with the instrumentation test system presented in Chapter 6 were used to test the contact resistance of a variety of materials, deposition methods, and tip geometries. This chapter presents the data obtained from testing the contact resistance between flat, thin films. The contact surfaces in MEMS-fabricated electrical contacts are commonly two flat surfaces coming into contact [64]. Modeling their contact force/resistance relationship can be difficult because much of the theory on contact resistance was developed for macro-scale contacts [18], and contact properties for MEMS-scale contacts do not always agree with those predicted by this theory [59]. One contribution to this disagreement is that when the dimensions of the contact thickness are on the order of the contact asperity dimensions, the spreading resistance is affected [60]. The two-coupon system and instrumentation presented in this thesis is uniquely capable of investigating the contact resistance between flat thin films because it allows thin sputtered, evaporated, or plated films to be brought together in a parallel manner.

Contact resistance is a resistance in addition to bulk resistance. It occurs between two separate surfaces in contact as a current is passed through them. The increase in contact resistance occurs because the two surfaces are not making contact with all of their apparent area. They are instead making contact at only small asperities.

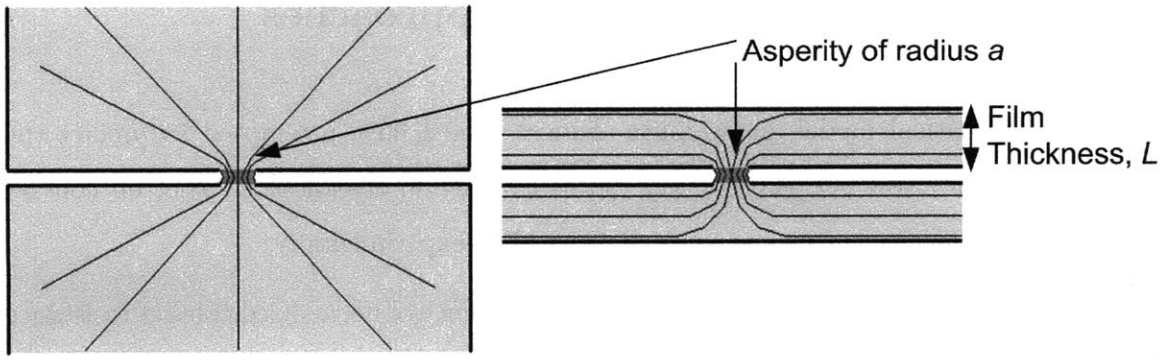

Figure 7-1: Right:A typical contact and current lines as modeled by Holm. Left: A thin film contact and current lines, which have to curve more rapidly than those seen in the Holm model.

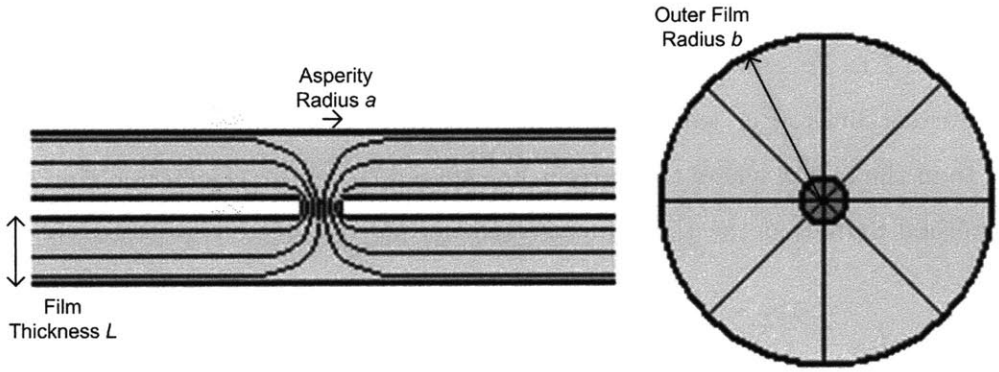

Figure 7-2: The geometry of a thin cylindrical contact.

The current lines must curve into and out of these asperities creating an increase in contact resistance. This is described in detail in Chapter 2. In Holm theory, contact resistance between two surfaces meeting at a single asperity of radius a is defined by the equation

$$R_c = \frac{\rho}{2a} \tag{7.1}$$

where ρ is the resistivity of the contact surface. However, in thin films, where the film thickness L is on the order of the contact spot radius a, the geometry of the contact limits the current lines from spreading in all directions. Instead, the current lines must curve fairly rapidly. Current lines in a non-thin film contact and current lines in a thin film contact are compared in Figure 7-1.

7.1 Theoretical Modeling Approaches

A mathematical model and a finite element model have attempted to predict the effect of the ratio between contact radius a and film thickness L, a/L, on contact resistance, however, this had never been studied experimentally.

The mathematical model predicts the dependence of normalized contact resistance on the ration between contact radius a and film thickness L, a/L. Normalized contact resistance is defined as

$$R_N = \frac{R_c}{\frac{\rho}{2a}} \tag{7.2}$$

where R_c is the actual contact resistance and $\rho/2a$ is the contact resistance predicted by Equation 7.1. This method theorizes that thin film geometry causes the spreading of the current lines after leaving an asperity to be constrained to a much smaller region than the region where the current line spreading takes place in non-thin films. This method finds that the thin film affected normalized contact resistance is given by [60].

$$R_N = \frac{4}{\pi}\sum_{n=0}^{n=\infty}\left(\frac{\coth\left(\lambda_n L/b\right)\sin\left(\lambda_n a/b\right)}{(J_1(\lambda_n)\lambda_n)^2}\right) - \frac{2(a/L)}{\pi}\ln(a/b) \tag{7.3}$$

where b is the outer film radius for a cylindrical contact. The geometry of a cylindrical contact are defined in Figure 7-2. In Equation 7.3 the argument for the Bessel function of the first kind of order 1, λ_n, is

$$\lambda_n = \frac{\beta}{4}\left[1 + \frac{2}{\beta^2} - \frac{62}{3\beta^4} + \frac{15116}{30\beta^6}\right] \tag{7.4}$$

where β is

$$\beta = \pi(4n - 1). \tag{7.5}$$

These calculations were based on assumptions which were only valid where $0 \leq a/L \leq 0.5$ [60]. The effects of this on normalized contact resistance are shown in Figure 7-3. For very low values of a/L there is no effect on contact resistance. As a/L increases, the normalized contact resistance decreases. At a/L= 0.5, the maximum valid value of these equations, the normalized contact resistance is approximately 0.52. The outer

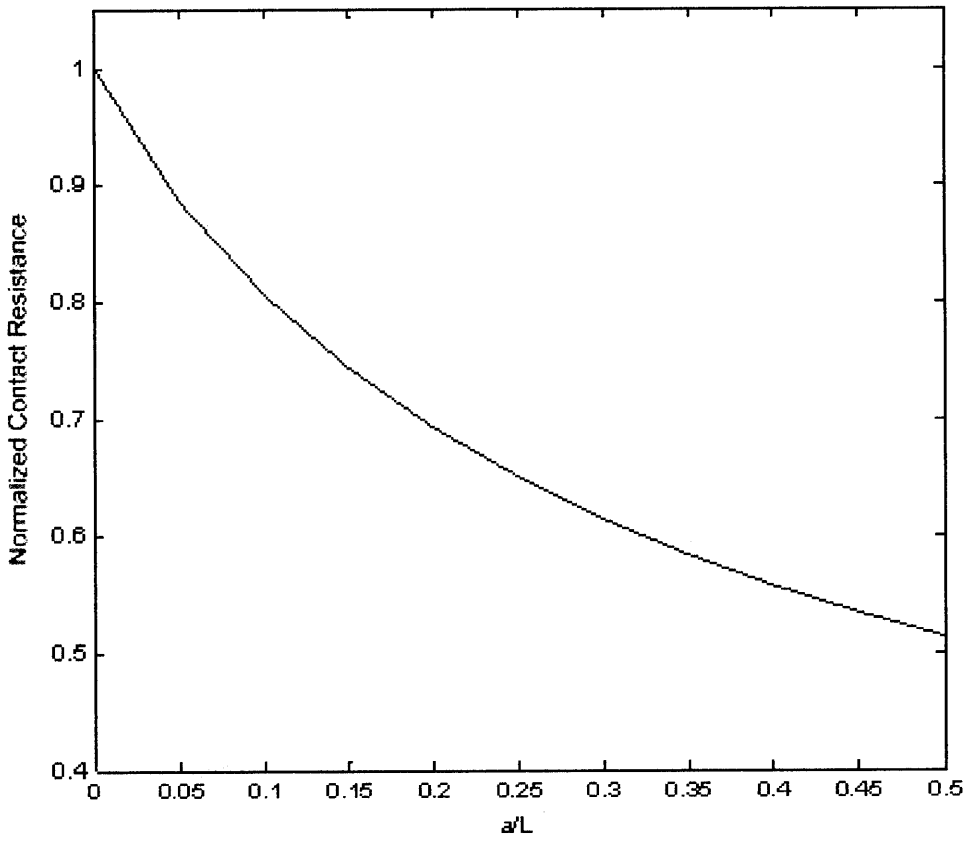

Figure 7-3: Normalized contact resistance as a function of the ratio a/L as predicted by [60].

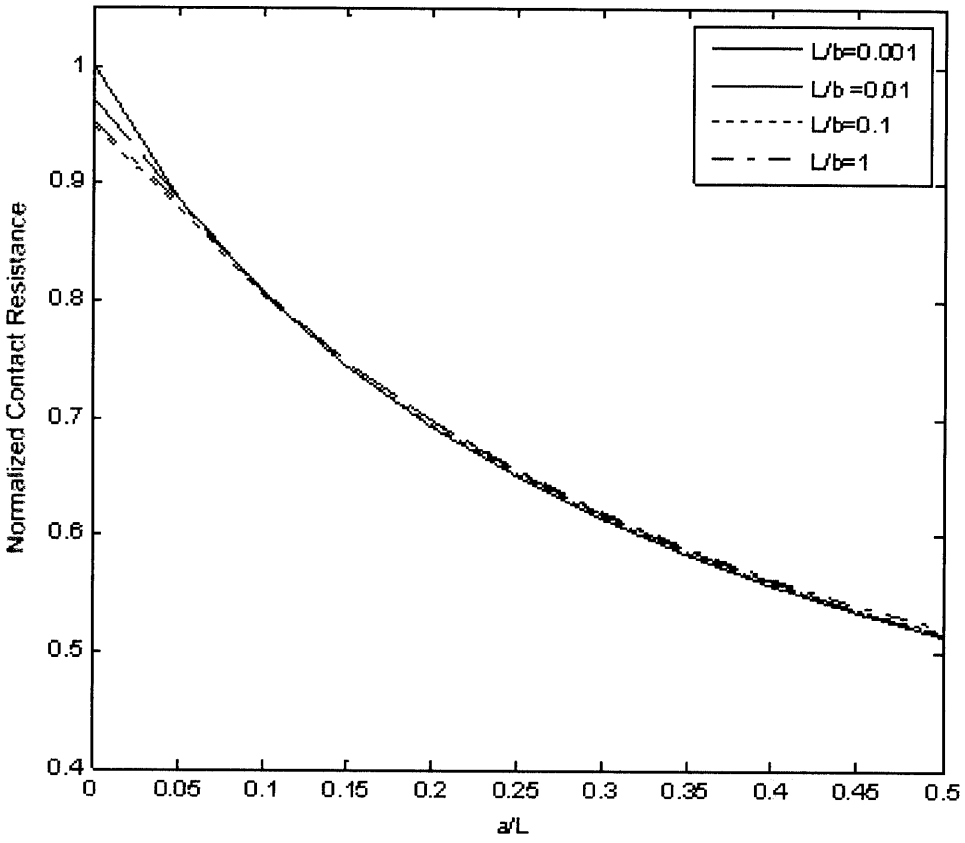

Figure 7-4: The effect of the ratio L/b, film thickness to outer film radius, on normalized contact resistance.

film radius b only affects the contact resistance if this value is on the order of the film thickness L. If the film outer radius is on the order of the asperity radius or the film thickness, than this truncated outer film radius can change the contact resistance by influencing the current lines. However, as long as this outer film radius is sufficiently greater than both the film thickness and the asperity radius, it should not have an effect. To show this, normalized film thickness as a function of a/L for L/b= 0.001, 0.01, 0.1, and 1 is plotted in Figure 7-4. This shows the ratio b/L to be insignificant at values anywhere except at values of $a/L < 0.05$ and even at that range contact resistance is only changed by a maximum of 5%.

When a force is applied to two thin films in contact, many asperities make contact.

If the contact areas of each of these asperities are summed, then according to Holm theory, the Holm radius of equivalent contact, α, is given by the formula

$$\alpha = \sqrt{\frac{F}{\pi H}} \tag{7.6}$$

where F is force and H is hardness. This is detailed in Chapter 2. Film thickness is not a factor in this equation; therefore, films having identical compositions but different film thicknesses will have identical values of Holm radius α for a given applied force F. In traditional Holm theory, this value α can be substituted for the constriction radius a when determining contact resistance. Assuming this also holds in thin films, then the a/L values for any given applied force will decrease as film thickness increases. According to Figure 7-3, when a/L decreases, normalized contact resistance will increase. Therefore, in this model, normalized contact resistance increases as film thickness increases. This effect was calculated for plated gold films having thicknesses of 0.1, 0.3, and 0.5 μm. The hardness of plated gold was assumed to be 1 GPa [39]. This effect of film thickness on normalized contact resistance is shown in Figure 7-5. Assumptions made in the mathematic model used to predict the contact resistance values shown in Figure 7-5 were only valid for values of $a/L < 0.5$. For the three thicknesses of plated gold values of normalized contact resistance were calculated for, this corresponded to a maximum valid contact force of 7.9 μN, 70.7 μN, and 196.3 μN. The data shown in Figure 7-5 is normalized contact resistance, which is the actual resistance divided by the resistance predicted by Holm theory from Equation 7.1 and Equation 7.6. The predicted thin film effects on absolute contact resistance are shown in Figure 7-6.

Other work suggests that Holm theory actually underestimates contact resistance for thin films. In [38], it is pointed out that in the derivation of Equation 7.1, Holm assumes the depth of an asperity making contact between two surfaces is equal to the radius of that same asperity. However, this is not applicable in films where the Holm radius is on the order of the film thickness. In [38], an finite element model was developed to look at the contact geometry shown in Figure 7-7. The FEM

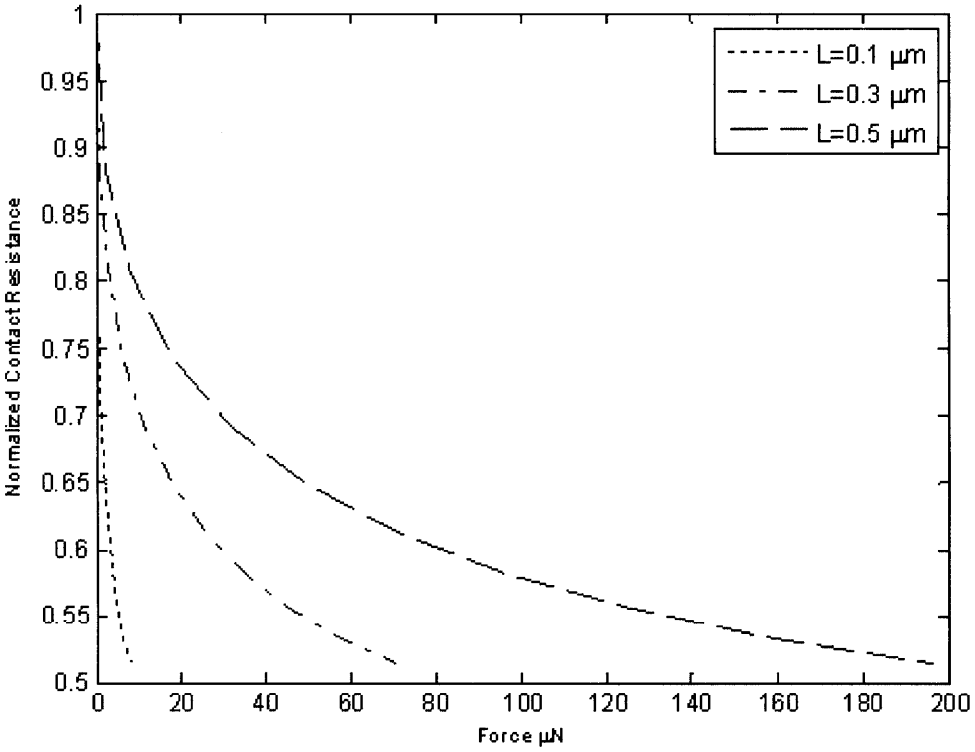

Figure 7-5: The effect of film thickness on normalized contact resistance.

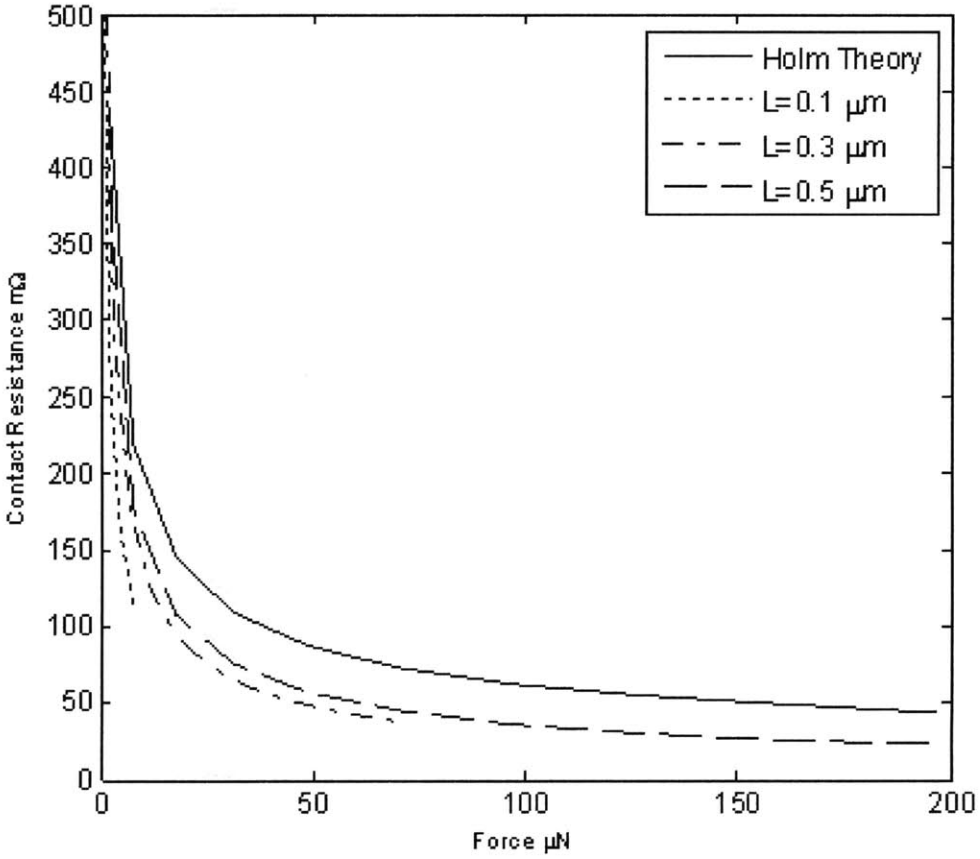

Figure 7-6: The effect of film thickness on absolute contact resistance.

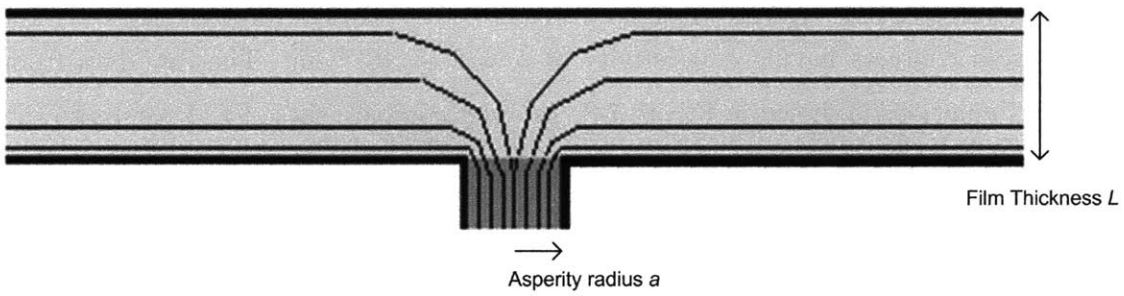

Figure 7-7: Geometry used in an FEM model of contact resistance

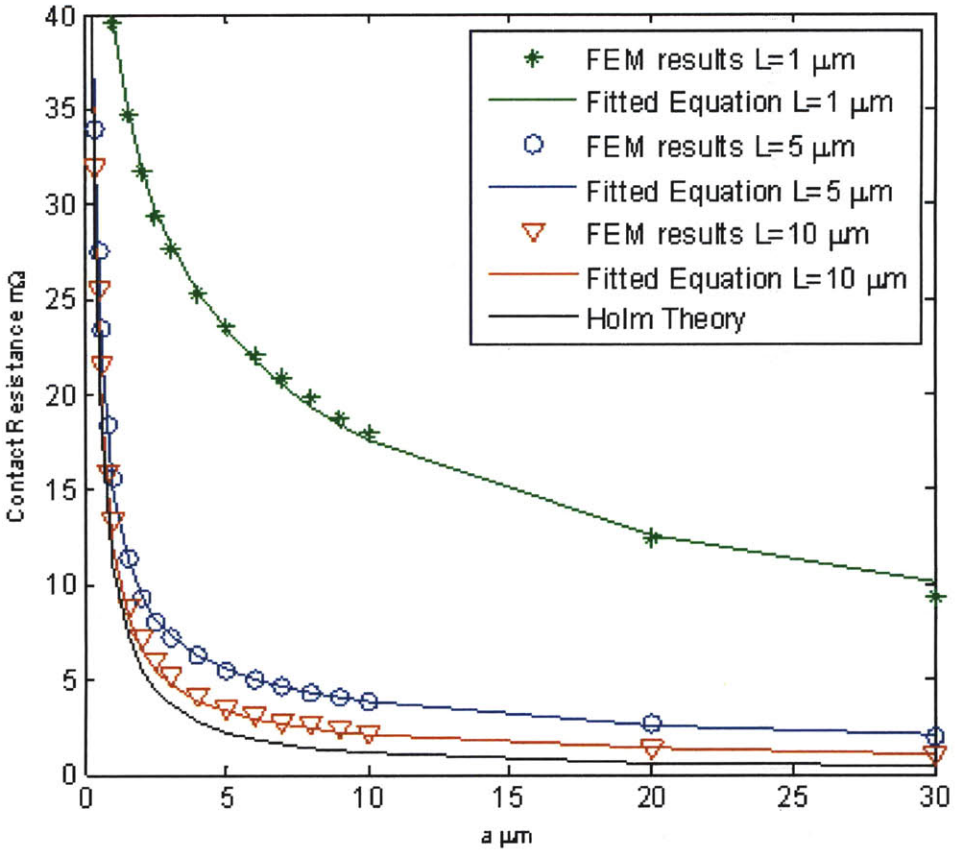

Figure 7-8: FEM results of contact resistance as a function of contact radius a for film thickness of 1, 5, and 10 μm.

simulations in [38] were performed on film thicknesses of 1, 5, and 10 μm and found that contact resistance decreased as film thickness increased over the range of L= 1-10 μm. This contact resistance was plotted as a function of radius of actual contact a for gold contacts having a resistivity of $\rho = 2.18x10^{-8}\Omega$m. The raw data from these simulations is shown in Figure 7-8. In order compare these FEM results to the mathematical model, this author fitted curves to the data presented in [38] which are also shown in Figure 7-8. The curve fitted to the FEM data from [38] is defined as

$$R_c = \frac{\rho}{2a}\left[\frac{1.45}{Lk_1}(\ln(a/k_2+1))^2 + \left(\frac{3.13}{Lk_1} - .29\right)\ln(a/k_2+1) + 1\right] \qquad (7.7)$$

where R_c is contact resistance in mΩ, and L is film thickness in μm, and k_2 is a

constant where $k_2 = 1\mu$m. The constant k_1 is a correction factor used to account for contact geometry and surface roughness. For all of the FEM simulations, $k_1 = \mu$ m^{-1}. The FEM data was given as a function of contact radius a. Contact force was then calculated from the following equation:

$$F = a^2 \pi H. \tag{7.8}$$

The contact resistance as a function of force then becomes

$$R_c = \frac{\rho}{2\sqrt{\frac{F}{\pi H}}} \left[\frac{1.45}{Lk_1} \left(\ln \left(\sqrt{\frac{F}{\pi H k_2^2}} + 1 \right) \right)^2 + \left(\frac{3.13}{Lk_1} - .29 \right) \ln \left(\sqrt{\frac{F}{\pi H k_2^2}} + 1 \right) + 1 \right] \tag{7.9}$$

The FEM predicted contact resistance as a function of force as well as the force predicted by Equation 7.7 are shown in Figure 7-9. These results were also shown as a function of the ratio of contact area radius to film thickness a/L. This is shown in Figure 7-10. Normalized contact resistance was also plotted as a function of force and the ratio a/L. These are shown in Figure 7-11 and Figure 7-12. The fitted equations for normalized contact resistance as a function of force and a/L are

$$R_c = \left[\frac{1.45}{Lk_1} \left(\ln \left(\sqrt{\frac{F}{\pi H k_2^2}} + 1 \right) \right)^2 + \left(\frac{3.13}{Lk_1} - .29 \right) \ln \left(\sqrt{\frac{F}{\pi H k_2^2}} + 1 \right) + 1 \right] \tag{7.10}$$

and

$$R_c = \left[\frac{1.45}{Lk_1} (\ln(a/k_2 + 1))^2 + \left(\frac{3.13}{Lk_1} - .29 \right) \ln(a/k_2 + 1) + 1 \right]. \tag{7.11}$$

The force values studies by the FEM, up to 2800 mN, were incredibly high for MEMS fabricated devices. The a/L values investigated went as high as 30. At a force of 12.6 mN, which is on the order of the force seen in some larger-scale MEMS devices, the contact resistances for the 1, 5, and 10 μm thick films were 5.8, 1.7, and 1.3 times that predicted by Holm theory respectively. At 1.13 μN of force, the contact resistances for the 1, 5, and 10 μm thick films were 2.7, 1.3, and 1.2 times that predicted by Holm theory respectively.

The mathematical model suggests that contact resistance increases with increasing

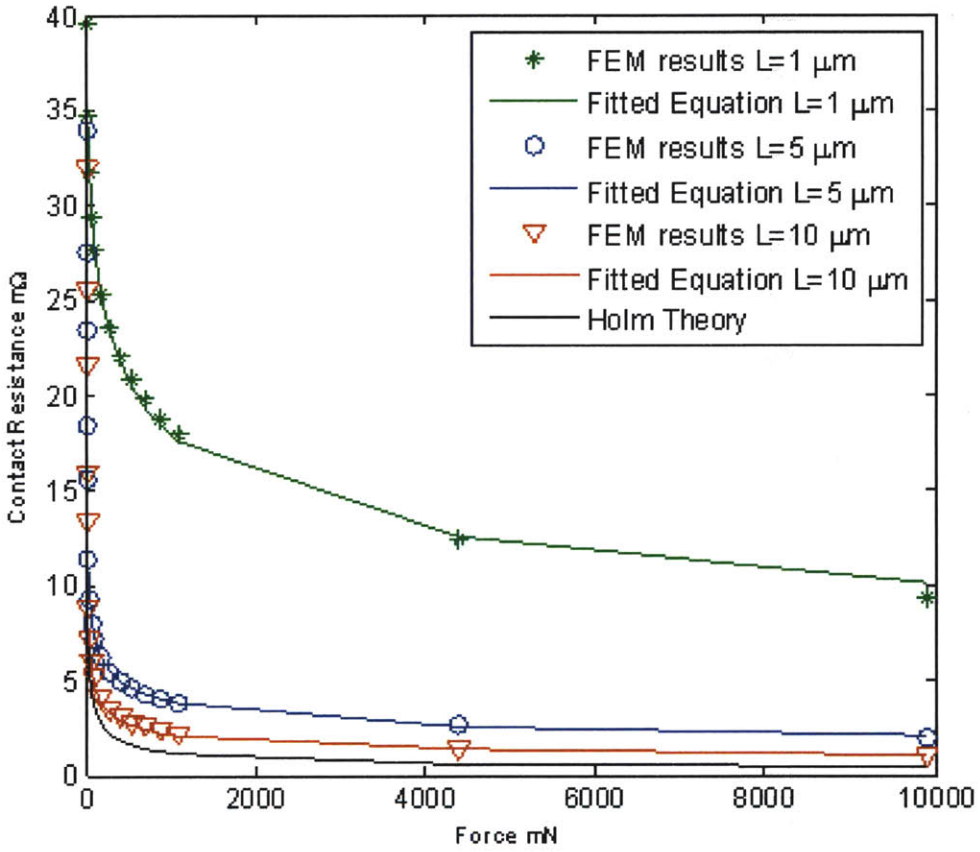

Figure 7-9: FEM results of contact resistance as a function of force for film thickness of 1, 5, and 10 μm.

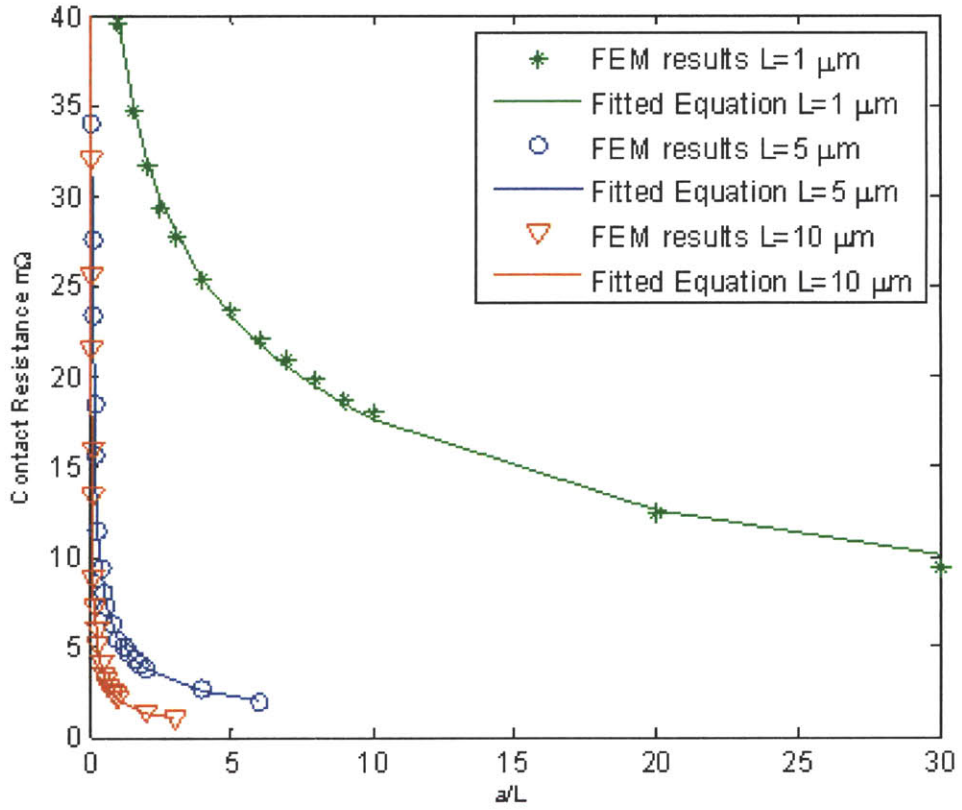

Figure 7-10: FEM results of contact resistance as a function of a/L for film thickness of 1, 5, and 10 μm.

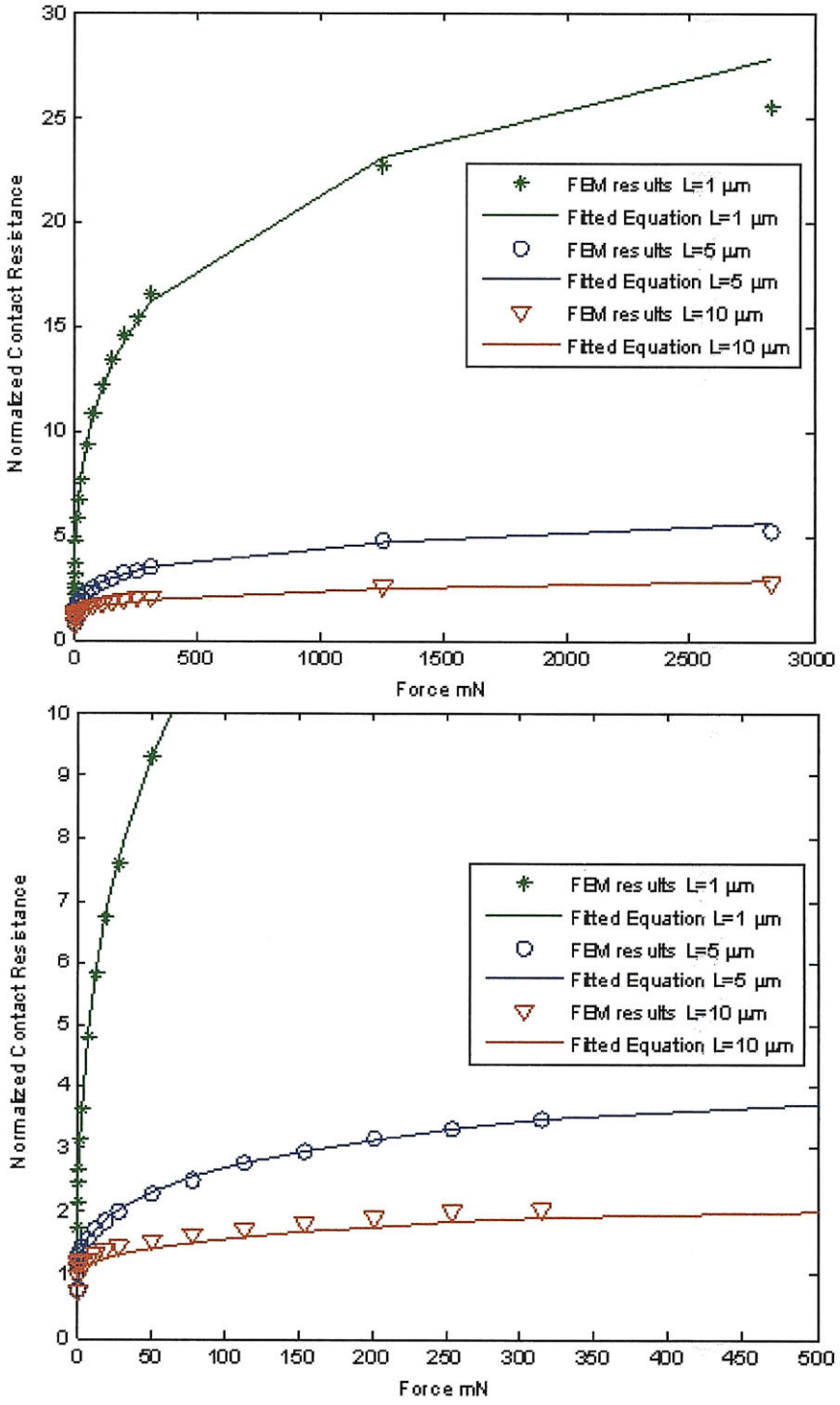

Figure 7-11: FEM results of normalized contact resistance as a function of force for film thickness of 1, 5, and 10 μm.

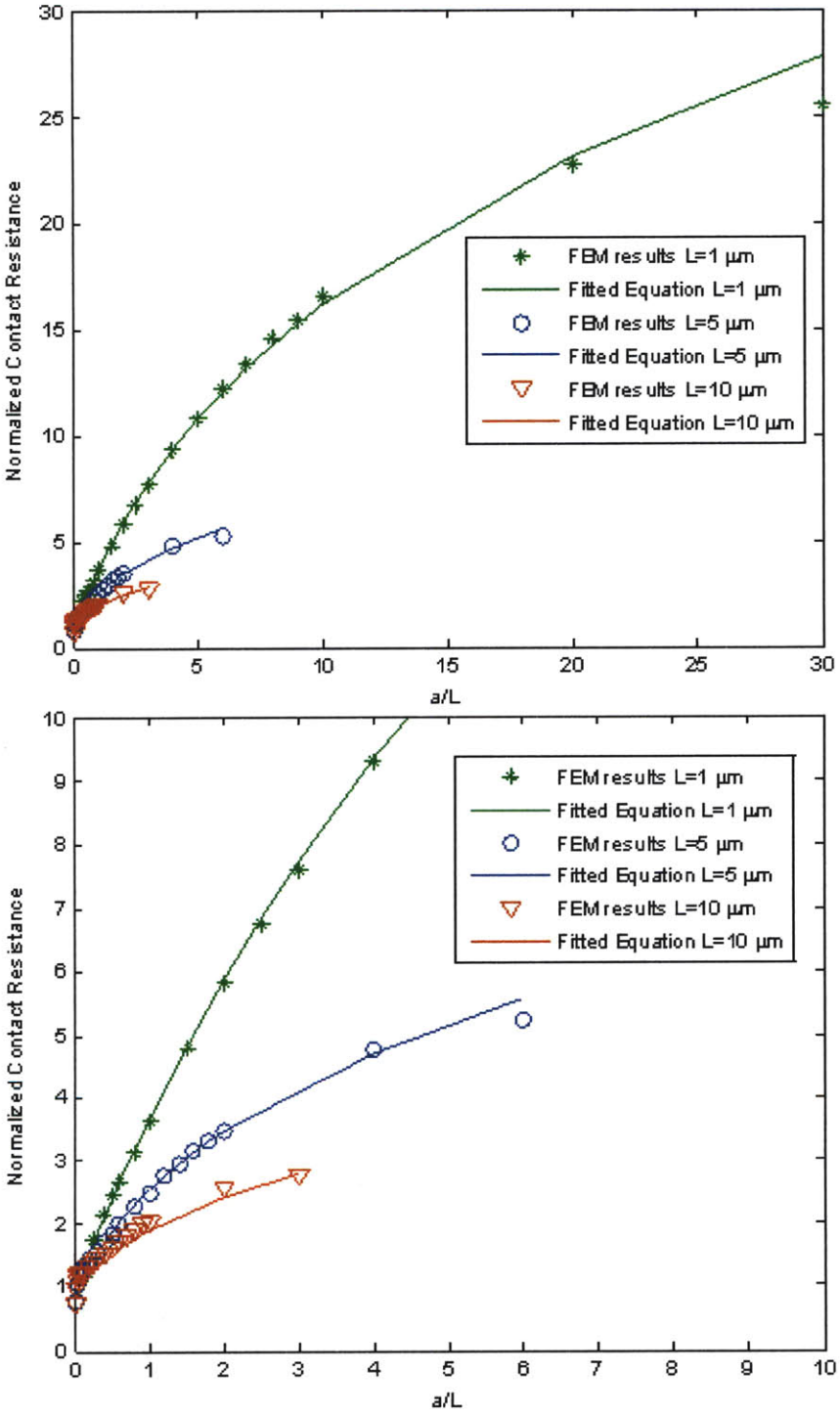

Figure 7-12: FEM results of normalized contact resistance as a function of a/L for film thickness of 1, 5, and 10 μm.

film thickness, whereas the FEM suggests that contact resistance decreases as film thickness increases. Additionally, the mathematical model predicts contact resistance in thin films will be below that predicted by Holm theory whereas the FEM predicts contact resistance will be greater than Holm theory. However, these two models looked at very different ranges. The mathematical model was limited to $a/L < 0.5$ whereas the FEM looked at much higher a/L values. The FEM only looked at film thicknesses where $L > 1$ μm and many MEMS fabricated contacts have dimensions smaller than this. Additionally, in the mathematical model normalized contact resistance was a function of a/L but not film thickness, L independent of contact radius a. However, in the FEM, normalized contact resistance was a function of both a/L and L. It is not immediately obvious how either of these models would perform outside of the ranges presented. Therefore, measurements were performed on film thicknesses of L = 0.1, 0.3, 0.5 μm and a/L= 0-17 using the two-coupon system presented in Chapter 5 and the instrumentation presented in Chapter 6.

7.2 Test Setup

The two-coupon system and instrumentation presented in Chapters 5 and 6 was used to test the contact resistance properties of sputtered and electroplated gold films in thicknesses of 0.1, 0.3, and 0.5 μm. The version of the two-coupon system used to test these samples was a slight variant on the final two-coupon system presented in Chapter 5. Since these tests did not require scrubbing capabilities, the in-plane flexure was not etched.

The contact materials for the bottom coupons and top coupons were prepared in the same way. The sputtered coupons were prepared by sputtering a 300 Å adhesion layer of titanium onto the 0.25 μm barrier layer of oxide on the coupons followed by the appropriate thickness of sputtered gold, either 0.1, 0.3, and 0.5 μm. The metal was patterned using standard lithography techniques. The plated coupons were prepared by sputtering a 300 Å adhesion layer of titanium, then a 1000 Å seed layer of gold. The appropriate thickness of gold was then plated onto the coupons, either 0.1, 0.3,

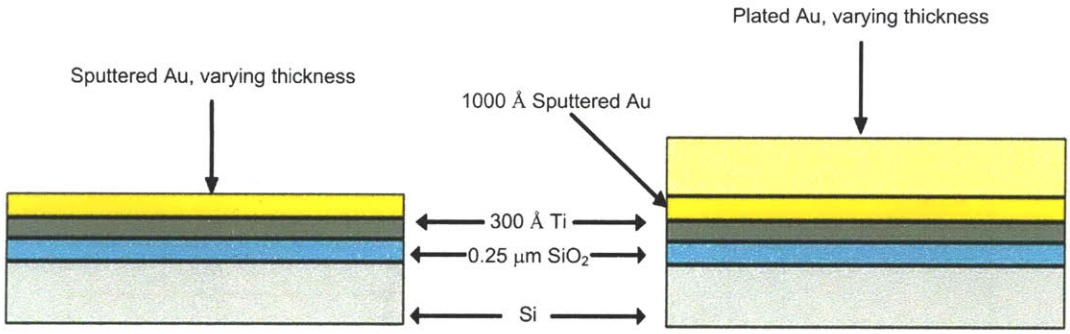

Figure 7-13: The metal stackups on both the sputtered and plated gold coupons.

and 0.5 μm. These metal stackups are shown in Figure 7-13.

The apparent contact area in this case of the two-coupon system is a 1 mm x 4 mm rectangle. However, the actual contact area is much small and made up of many small asperities. In the mathematical and finite element models, the contact area is a single asperity. In the two-coupon system, it is reasonable to believe that the many individual contact spots are round. A not-to-scale drawing of a few individual contact spots in relation to the rest of the trace is shown in Figure 7-14. For the experimental set up, the contact length was 4mm and the contact width was 1mm making the apparent area of contact 4 mm^2. However, the Holm radius corresponding to the actual area of contact is on the order of 1-10 μm. It is hypothesized that even though the macro-geometry is rectangular, the contact spots act locally much like those in the mathematical and finite element models. This is because $\alpha << w$ and $\alpha << l$. Because of this inequality of scale, it is unlikely that the current flow lines immediately around the contact spots will be affected by the macro geometry. However, it is acknowledged that this is an assumption and that there might be a small effect on contact resistance caused by the macro geometry which is not accounted for.

Also considered was the true flatness of the contact. In designing of this fixture, achieving flatness was a top priority. The maximum measured angle between the coupons was 1.6 mrad, which means that there is a possibility of the contact rocking immediately after touchdown. No physical evidence of this rocking was seen under normal conditions; however, when a current greater than one Ampere was forced through the contact, the contact did tend to fail along one edge, suggesting that the

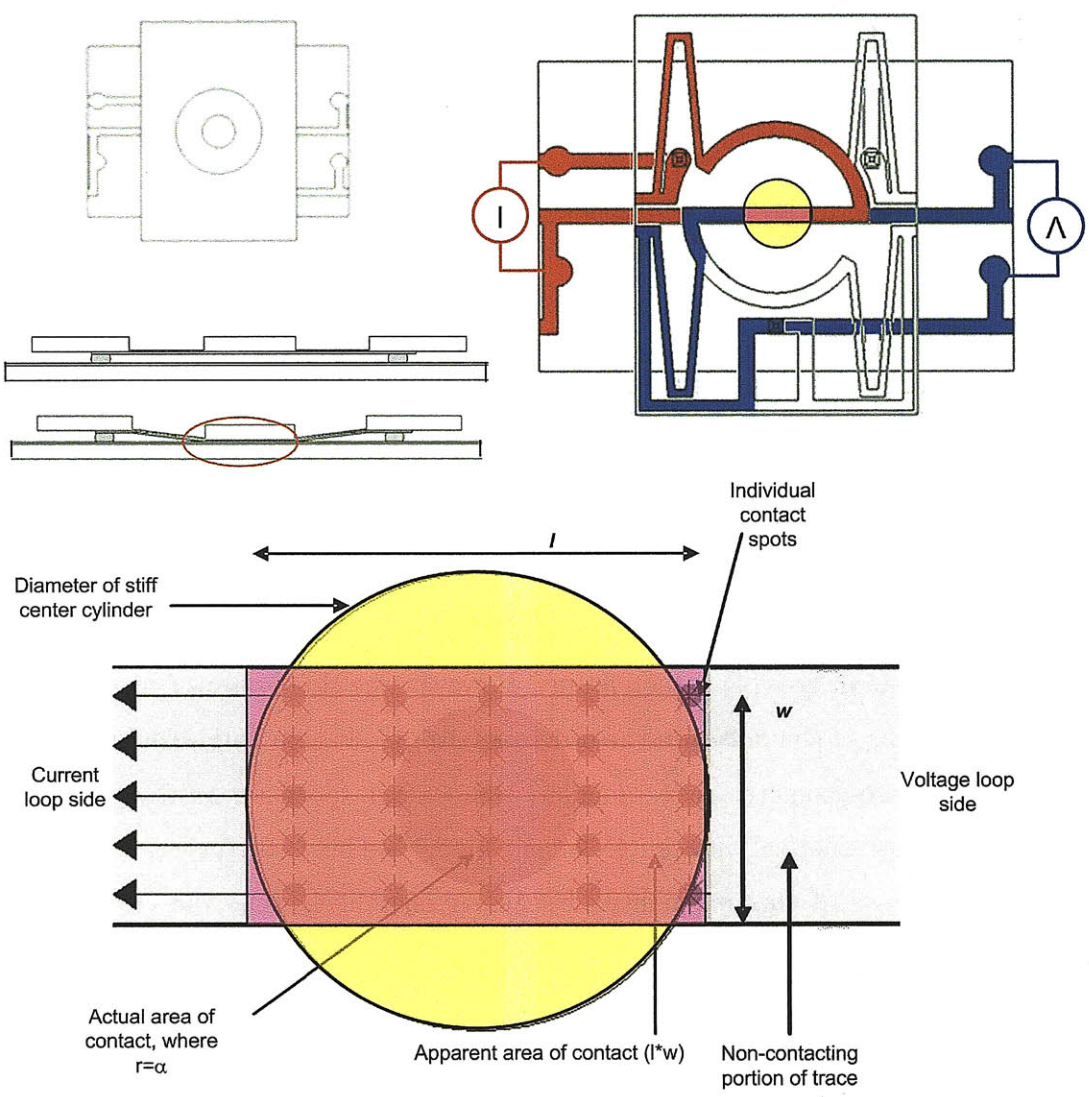

Figure 7-14: The actual contact area and apparent contact area in the two-coupon system.

pressure may have been higher on that edge.

Due to the difficulty in measuring the hardness of films with thicknesses less than 1 μm, the hardnesses of the sputtered and plated films were approximated from literature values as 3.5 and 1 GPa respectively [25, 39]. The surface roughness of the sputtered films was found to be about 6 nm while the surface roughness of the electroplated films was found to be about 14 nm.

The resistivity of the sputtered samples was measured as $4.27\text{x}10^{-8}$ Ωm. This value was consistent across all three thicknesses of the sputtered film samples. This is significantly higher than the bulk resistivity of Au. Sputtered films are known to have a higher than bulk contact resistivity [46]. Resistivity can be affected by various mechanisms such as temperature, electron surface scattering, impurities, intragranular defects, and scattering at grain boundaries [46]. It has also been shown that in thin sputtered Au films with an adhesion layer of Ti, the Au and Ti can form an alloy of significantly higher resistivity [17]. The resistivity of the electroplated samples was also measured. Taking into account the resistivity of the seed layer as a parallel resistance, the resistivity of the bulk was found to be $2.18\text{x}10^{-8}$ Ωm, consistent with literature values for Au resistivity.

7.3 Testing Procedure

During the experiment, a force gauge compressed the top membrane bringing the two metal traces into contact. The overall displacement of the membrane, the force, and the contact resistance were recorded throughout the test. When the membrane stopped moving, contact was made. This also corresponded to the first time finite contact resistance was seen since no oxides or films impeded current flow. This is the point where the contact sees zero force. After this point, force was further increased to 10 mN. The current was sourced at 5 mA and 4-wire resistance was measured using a Keithely 2420 source measure unit. The instrumentation used to measure force, displacement, and contact resistance is described in Chapter 6.

7.4 Results

This section discusses the results of contact resistance tests performed on sputtered and plated gold films. The results are often discussed with respect to the Holm radius of equivalent contact , α, which is the radius of the equivalent actual contact area between samples. Both the mathematical approach and the FEM model a single contact having a radius of a. In macro-scale contact theory, these two variables are often interchangeable. In order to compare the theoretical results to the data obtained from testing, theory derived using a single contact point of radius a is compared to data having a Holm equivalent radius of contact α. In this section, when referring to a single point of contact the variable a is used but when referring to the Holm equivalent radius of contact, the variable α is used.

7.4.1 Sputtered Film Results

Three thicknesses of sputtered gold film were tested. The contact resistance of these tests as a function of force is shown in Figure 7-15. Also shown are the predicted results from the FEM fitted equation, Equation 7.9 with the correction factor k_1=8 μm^{-1}, resistivity ρ= 4.27 x10^{-8} Ωm, and hardness H = 3.5 GPa. For the FEM results, k_1=1, however, this predicted a contact resistance four times higher than measured. The value k_1=8 was chosen because it gave the closest predictions from all three thicknesses, although there is still significant error between the measured data and FEM fitted equation. If hardness is changed to H = 1 GPa, the data is much closer to that predicted by Equation 7.9, as shown in Figure 7-16. This could mean that the sputtered gold is softer than thought, or that the fitted equation does not adequately describe the physics of the experiment. The fitted equation does however accurately describe the shape of the contact resistance curve and the trend of reduced contact resistance with increasing film thickness. The mathematical model predictions are not shown in Figure 7-15 or Figure 7-16 because they are only valid in the micro-Newton range.

In Figure 7-15 and Figure 7-16, the hardness of the films of all three thicknesses

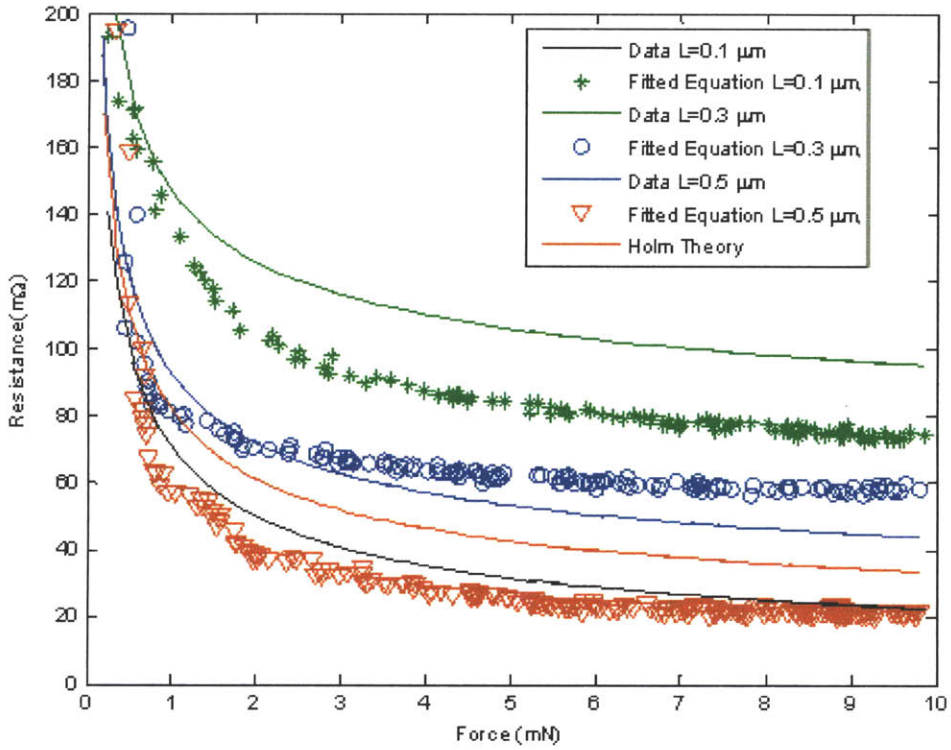

Figure 7-15: Contact resistance as a function of force for sputtered gold film thicknesses of 0.1, 0.3, and 0.5 μm. The raw data is shown as well as the predictions of Equation 7.9. Hardness was assumed to be 3.5 GPa and the correction factor was 8 μm^{-1}.

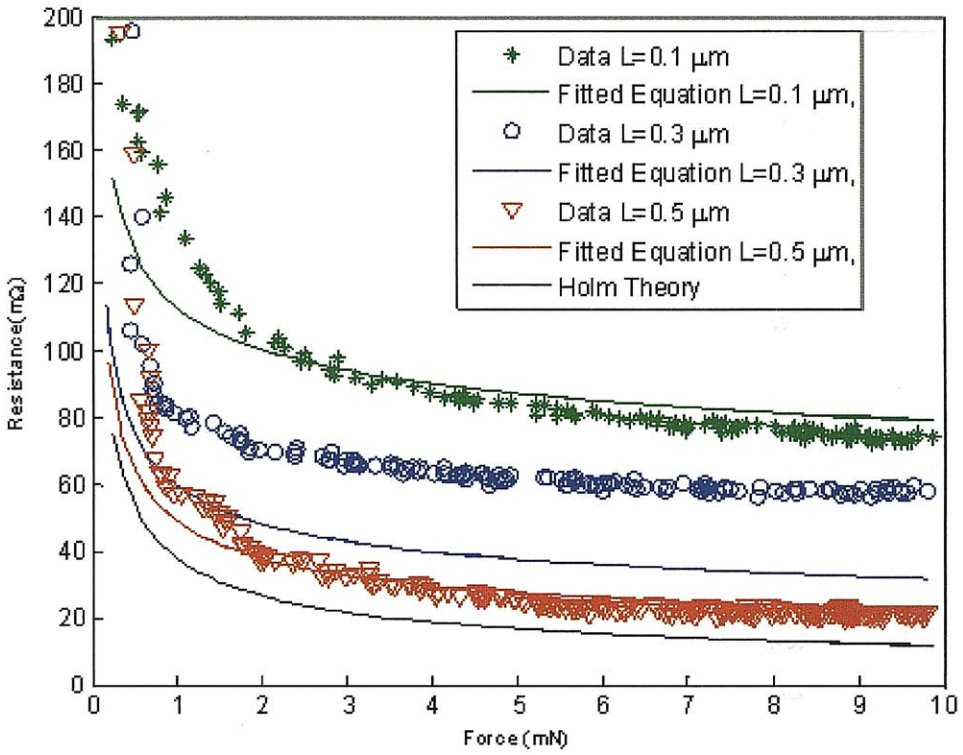

Figure 7-16: Contact resistance as a function of force for sputtered gold film thicknesses of 0.1, 0.3, and 0.5 μm. The raw data is shown as well as the predictions of Equation 7.9. Hardness was assumed to be 1 GPa and the correction factor was 8 μm^{-1}.

is assumed to be the same. In fact, very thin films have a hardness greater than that of the bulk material [48]. Hardness is thought to increase with decreasing film thickness. Figure 7-17 shows the data compared to the predictions of Holm theory only, not including the thin film effects predicted by the mathematical model or the FEM. The hardness of each film was defined as

$$H = \frac{1.5}{L} \tag{7.12}$$

where H is Hardness in GPa and L is film thickness in μm. This corresponds to the 0.1 μm film having a hardness of 15 GPa, the 0.3 μm film having a hardness of 5 GPa, and the 0.5 μm film having a hardness of 3 GPa. The resistance predicted by Holm theory is defined as

$$R_c = \frac{\rho}{2}\sqrt{\frac{\pi H}{F}}. \tag{7.13}$$

The predictions of Holm theory alone do not give the correct shape of the contact resistance data curve. However, if this increasing hardness with decreasing film thickness is combined with the thin film effects predicted by the FEM, then a very good prediction of contact resistance can be made for the 0.1 μm and 0.5 μm films. The data for the 0.3 μm film does not agree as well. Figure 7-18 shows the measured contact resistance and the values for contact resistance predicted by Equation 7.9 when constance k_1=16 μm^{-1}. Hardnesses was defined as

$$H = \frac{0.75}{L} \tag{7.14}$$

where H is hardness in GPa and L is film thickness in microns. This results in hardnesses of 7.5, 2.5, and 1.5 GPa for the 0.1, 0.3, and 0.5 μm films respectively. The data and predicted results shown in Figure 7-18 were then plotted as normalized contact resistance as a function of a/L, the ratio of contact radius to film thickness. The predicted results are from Equation 7.11. This is shown in Figure 7-19.

At values of α/L greater than one, the data shown in Figure 7-19 agrees nicely with that predicted by Equation 7.11 for the 0.1 and 0.5 μm films. The 0.3 μm film does

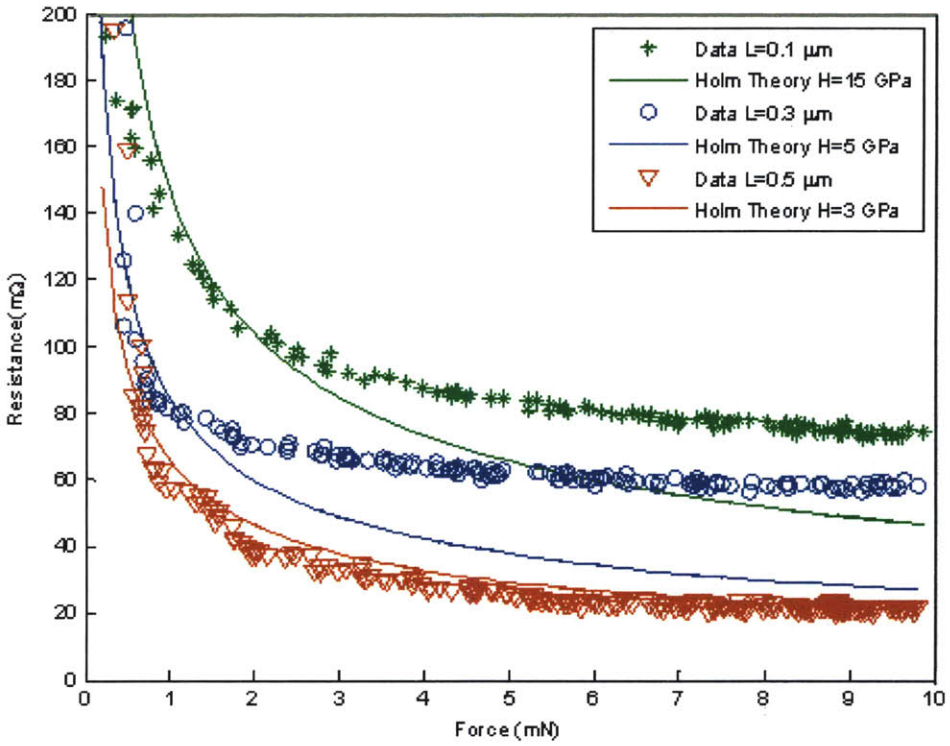

Figure 7-17: Contact resistance as a function of force for sputtered gold film thicknesses of 0.1, 0.3, and 0.5 μm compared to the Holm theory for films having hardnesses of of 15, 5 and 3 GPa.

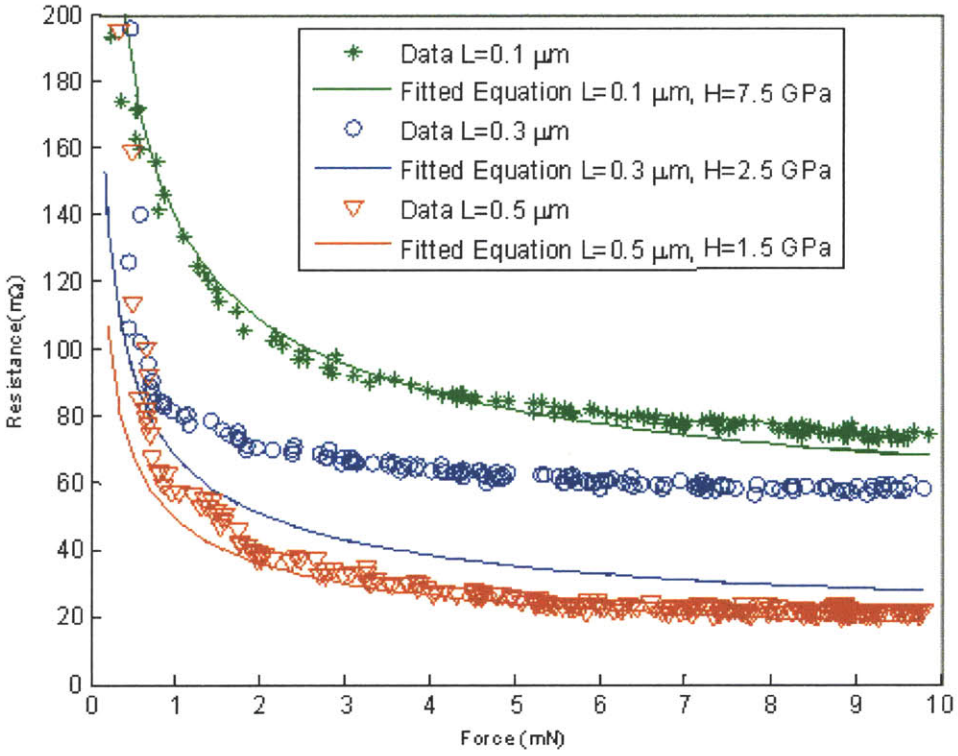

Figure 7-18: Contact resistance as a function of force for sputtered gold film thicknesses of 0.1 μm, 0.3 μm, and 0.5 μm. The raw data is shown as well as the predictions obtained from Equation 7.9 when k_1=16 μm^{-1} and hardnesses for the 0.1, 0.3, and 0.5 μm films are 7.5, 2.5, and 1.5 GPa respectively.

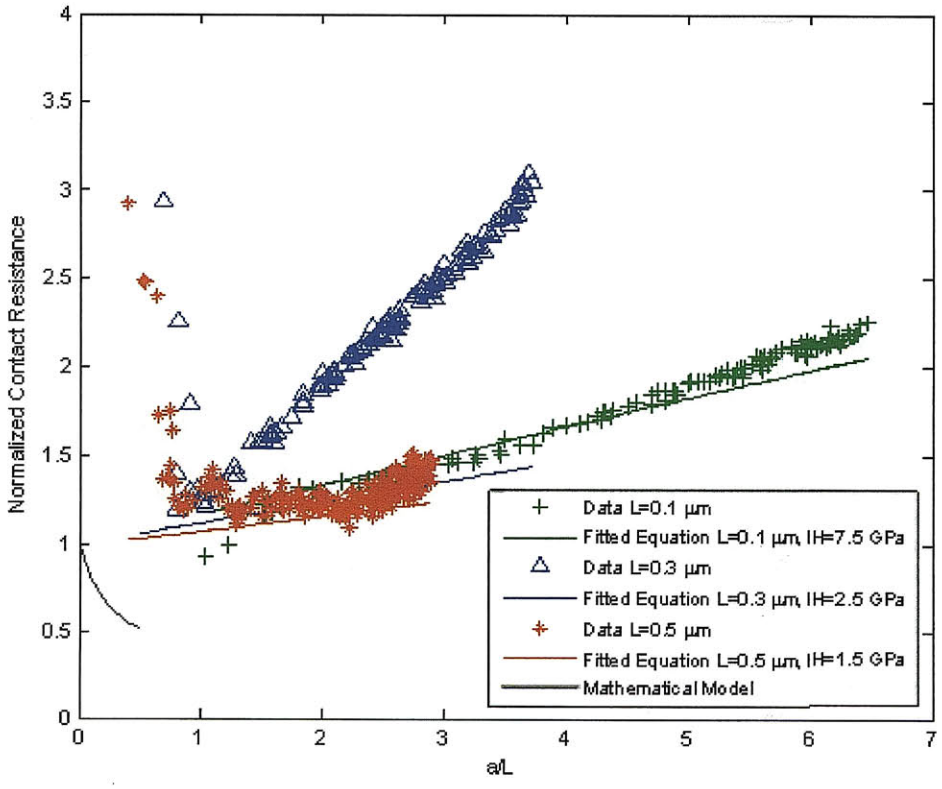

Figure 7-19: Normalized contact resistance as a function of a/L for sputtered gold film thicknesses of 0.1 μm, 0.3 μm, and 0.5 μm. The raw data is shown as well as the predictions obtained from Equation 7.9 when k_1=16 and hardnesses for the 0.1, 0.3, and 0.4 μm films are 7.5, 2.5, and 1.5 GPa respectively.

not agree in magnitude but does agree in trend. That trend is that normalized contact resistance increased with increasing α/L in a somewhat linear fashion. At values of α/L less than one, the normalized contact resistance decreased with increasing α/L. This agrees with the trend predicted by the mathematical model valid only at values of α/L less than 0.5. However the measured normalized contact resistance is about three times greater than that predicted by the mathematic model. These very low values of α/L, which correspond to very low values of force, are also the least accurate portion of the measurement.

7.4.2 Plated Film Results

When determining the contact resistance in the plated films, the effects of the sputtered seed layer have to be taken into account. Traditional contact resistance theory models this added resistance as shown in Figure 7-20a. However, this model assumes all of the current lines travel into the seed layer. In this test setup, as shown in Figure 7-20b, only a portion of the current flow lines travel into the seed layer. In traditional modeling, the additional resistance R_a of the transition from the electroplated Au into the sputtered seed layer would be [54]

$$R_a = (8/\pi)(\rho_p/\rho_s)(L_p/\alpha) \tag{7.15}$$

where ρ_p is the resistivity of the plated material, ρ_s is the resistivity in the seed layer, L_p is the thickness of the plated layer, and α is the Holm radius of contact. However, the fraction of current that actually travels in the bulk Rs_{bp} is defined as

$$R_{bp} = \frac{\rho_p w/L_p l}{\rho_p w/L_p l + \rho_s w/L_s l} = \frac{\rho_p/L_p}{\rho_p/L_p + \rho_s/L_s} \tag{7.16}$$

where w and l are the width and length of the bulk trace and L_s is the thickness of the seed layer. Therefore, an approximation of the additional resistance added by the

transition from the plated region to the sputtered region R_{ac} is

$$R_{ac} = R_a R_{bp} = (8/\pi)(\rho_p/\rho_s)(L_p/\alpha)\frac{\rho_p/L_p}{\rho_p/L_p + \rho_s/L_s} \tag{7.17}$$

and the portion of the contact resistance due to the film R_c as a function of the measured contact resistance of the film and the seed layer R_m is

$$R_c = R_m - R_{ac} = R_m - (8/\pi)(\rho_p/\rho_s)(L_p/\alpha)\frac{\rho_p/L_p}{\rho_p/L_p + \rho_s/L_s} \tag{7.18}$$

This contact resistance due to the plated film as a function of force for plated gold of 0.1, 0.3, and 0.5 μm thicknesses is shown in Figure 7-21. Also shown is the prediction of contact resistance using Equation 7.9 when the correction factor k_1=7.25 μm^{-1}. The resistivity of the samples was 2.18x10^{-8} Ωm and the hardness of the samples was assumed to be 1 GPa. The raw data was very close to the results predicted by Equation 7.9. The predicted results assumed that all the samples had a hardness of 1 GPa, regardless of thickness. In the sputtered film results, the match between data and theory was improved if hardness was assumed to increase with the inverse in film thickness. For the plated film results, this was not the case. The best results were seen when assumed hardness was kept constant across the samples. This type of discrepancy between the results of sputtered and plated films illustrates that current models for contact resistance in thin films are often inadequate and the method for measuring contact resistance outlined in this thesis is necessary.

The results presented in Figure 7-21 were then plotted as normalized contact resistance as a function of the ratio a/L. This is shown in Figure 7-22. The mathematical model for determining normalized contact resistance as a function of a/L is also shown. At values where α/L is greater than one, the normalized contact resistance predicted by Equation 7.11 is very close to the measured contact resistance. At values where α/L is less than one, the predicted normalized contact resistance actually decreases with increasing α/L, the opposite of what Equation 7.7 predicts. However, the shape of this portion of the curve is very similar to the shape of the mathematical model used to predict normalized contact resistance as a function of

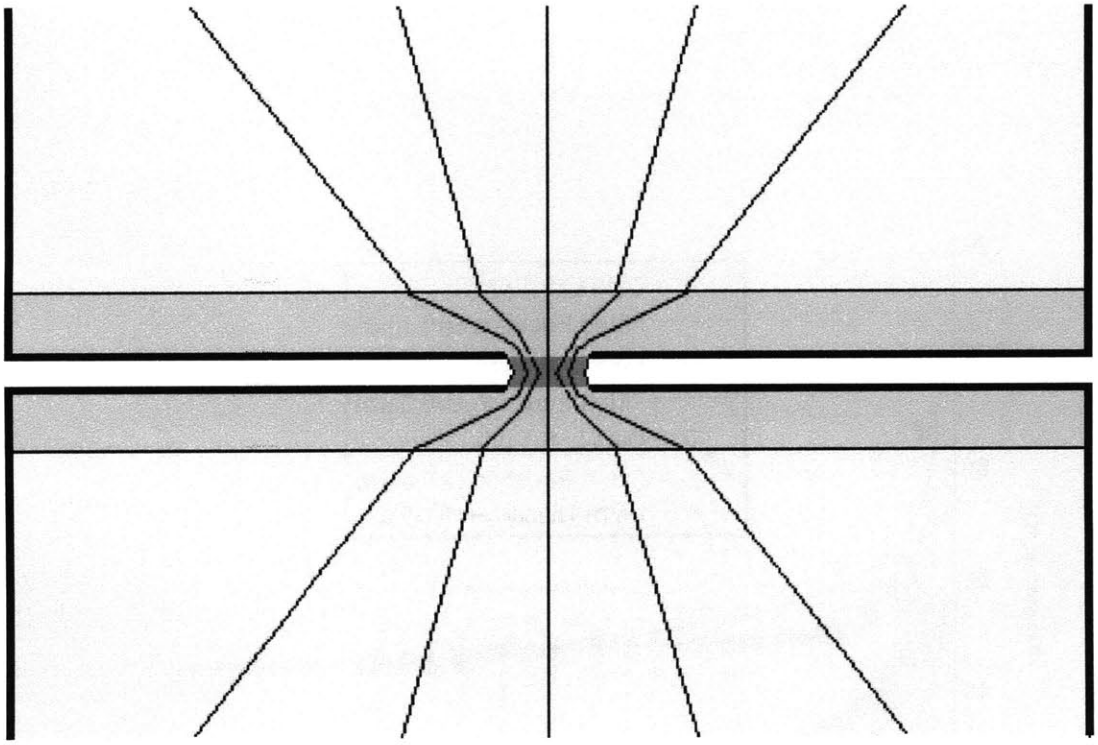

(a)

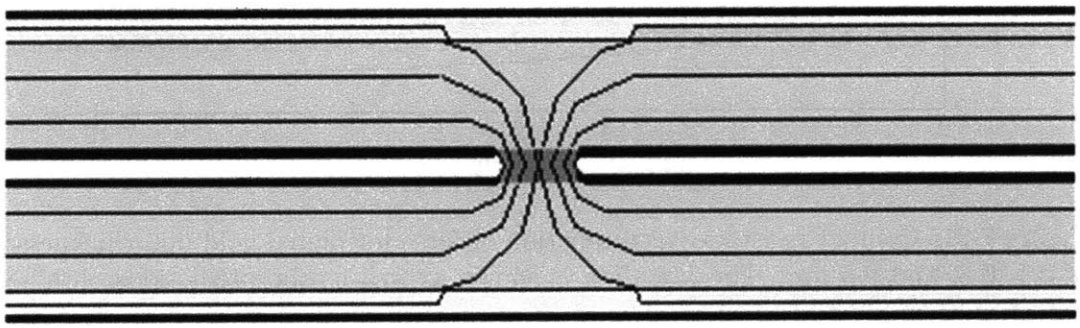

(b)

Figure 7-20: (a)Current lines between layers in traditional film theory. (b)Current lines in a thin electroplated film on a sputtered seed layer. [54]

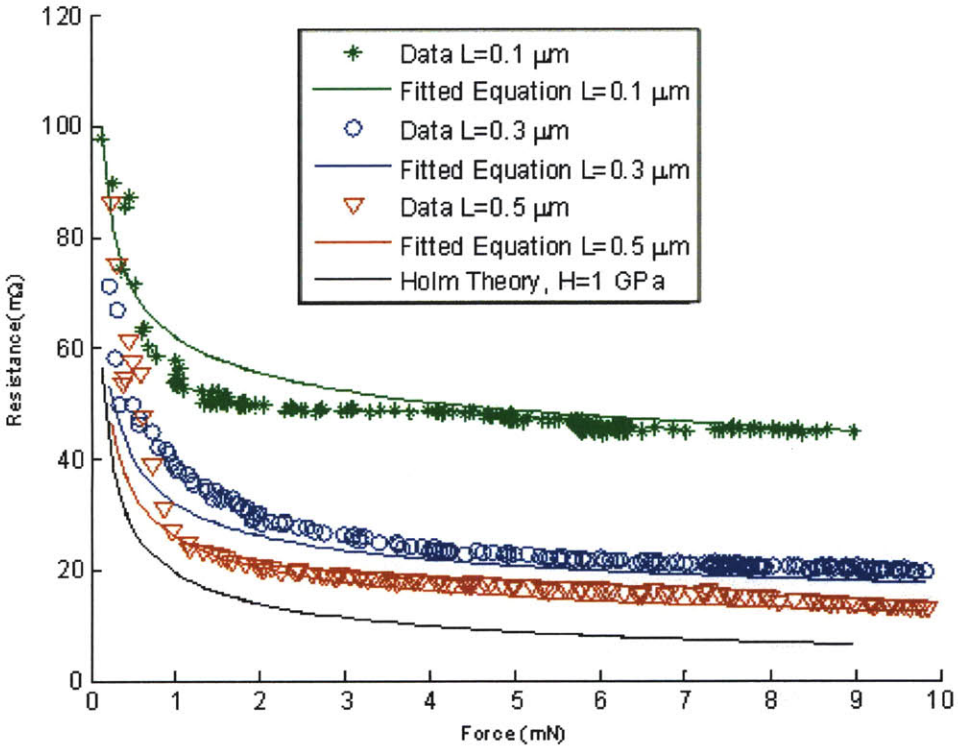

Figure 7-21: Contact resistance as a function of force for plated gold film thicknesses of 0.1, 0.3, and 0.5 μm. The raw data is shown as well as the predictions obtained from Equation 7.9 when constant k_1=7.25 μm^{-1} and hardness of all films was H=1 GPa.

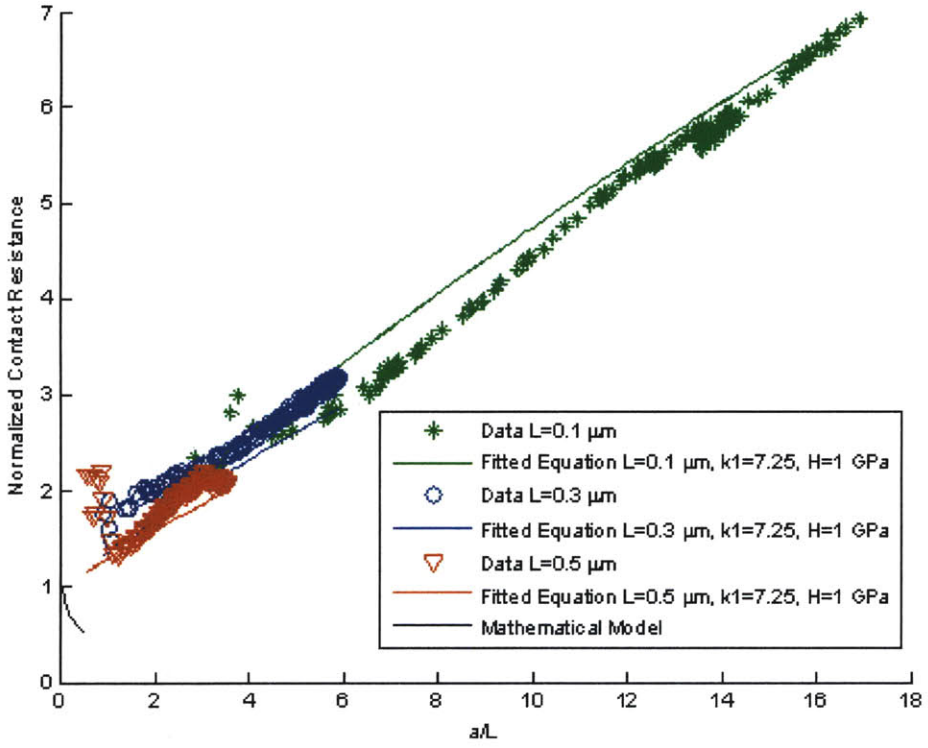

Figure 7-22: Contact resistance as a function of force for plated gold film thicknesses of 0.1, 0.3, and 0.5 μm. The raw data is shown as well as the predictions obtained from Equation 7.9 when constant k_1=7.52.

a/L for values of a/L less than 0.5 This suggests that the effects taken into account in the mathematical model, mainly the rapid curving of the current lines in the area immediately outside the asperity, dominate the contact resistance at low levels of α/L while the effects taken into account by the FEM model, mainly the fact that in the derivation of Holm theory asperity height is assumed to be equal to the asperity radius which inaccurate when asperity radius is on the order of film thickness, dominate contact resistance at higher vales of α/L. The transition between these regions occurs around $\alpha/L = 1$. At values below this transition, the Holm radius is less than the film thickness. However, at α/L values above this transition, the Holm radius is greater than the film thickness. This means in the lower range there is a net compression of current lines inside the contact areas but in the higher range their is a net expansion of current lines in the contact areas. Therefore it makes physical sense that a transition in the normalized contact resistance as a function α/L occurs around $\alpha/L = 1$.

7.4.3 Chapter Summary

The contact resistances of sputtered and plated films were found to be a function of both film thickness and force. Two models were looked at to explain this function: a mathematical model and a finite element model. The ratio between Holm radius of contact α and film thickness L was found to be important. At values of α/L less than one, the contact resistance decreased with increasing α/L. In this range, the contact resistance looked similar in shape to that predicted by the mathematical model. At values where α/L is greater than one, the normalized contact resistance resembled that predicted by the FEM. The FEM model was dependent on the hardness of the samples. The sputtered samples were determined to have increasing hardness with decreasing film thickness. The plated samples were determined to have a relatively constant hardness. A correction factor, k_1, was a part of the finite element model. In the FEM, $k_1 = 1\ \mu\ \mathrm{m}^{-1}$. In the sputtered films, $k_1 = 16\ \mu\mathrm{m}^{-1}$. In the plated films, In the FEM, $k_1 = 7.25\ \mu\ \mathrm{m}^{-1}$. One possible reason for this correction factor being necessary was that in the models, the contact was a single growing asperity

while in the actual data, many asperities were in contact. One possible reason for the difference between the correction factor of the plated and sputtered samples is the difference in surface roughness between the two samples. The sputtered surface had a roughness of 6 nm while the plated surface had a roughness of 14 nm. However, it is difficult to make a conclusion as to the exact reason for the varying correction factor.

Chapter 8

Contact Resistance Between Three-Dimensional Tips and Flat Surfaces

List of Symbols	
a	Asperity radius
A_n	Area of nickel plating
α	Holm radius
E_b	Young's modulus of the bottom contact
E_e	Equivalent Young's modulus
E_t	Equivalent Young's modulus of the top contact
F	Force
H	Vicker's hardness
$k_{thin-film}$	Thin film correction factor
k_1	A correction factor of units μm^{-1}
k_2	1 μm
L_b	Thickness of the bottom contact material
L_n	Thickness of the nickel plating
L_s	Thickness of the seed layer

continued from previous page

List of Symbols	
R	Sphere radius
R_b	Contact resistance of bottom contact
R_c	Total contact resistance
R_t	Contact resistance of top contact
ρ	Resistivity
ρ_b	Resistivity of the bottom contact material layer
ρ_n	Resistivity of the nickel layer
ρ_s	Resistivity of the seed layer
ρ_t	Resistivity of the top contact material
ν_b	Poisson's ratio of top contact material
ν_t	Poisson's ratio of bottom contact material

Often times, one or both sides of a contact may have three-dimensional geometry. Different geometries can be beneficial in different situations. For example, a sphere-on-flat contact geometry reduces the demand of parallelism between the contacts because the sphere will always be tangent to the flat. Pointed geometries can be used to break through oxides or push away contaminants. These types of contacts have more variables affecting contact resistance than their flat-on-flat counterparts. Therefore, experimentally measuring the contact resistance in three-dimensional contacts is very beneficial. This chapter first discusses some of the theory involved in sphere-on-flat contact and the composition of the sphere on flat contacts tested in this thesis. It then discusses three sphere on flat experiments: varying sphere diameter, varying force/scrub profile, and varying contact material. The composition and theory regarding plated experiments are then discussed followed by an experiment which looks at contact pressure when making contact with a surface coated in a non-conductive oxide.

8.1 Sphere on Flat Contact

One main advantage of electrical contacts which use a sphere-on-flat configuration is that the sphere always makes tangent contact with the flat. This eliminates the concern of the two contacts rocking against each other due to the parallelism errors which can occur in flat-on-flat contacts. The contacts described in this section consist of a metal coated sphere on one side and a flat metal contact area on the other side. The geometry of the metal coated sphere is shown in Figure 8-1. A glass sphere of radius 21 or 42 μm is glued into a recess in the oxide coated bottom silicon coupon. The glass spheres used were general purpose soda-lime glass microspheres from Whitehouse Scientific. The recess is one radius deep. The wafer is then sputtered with a 300 Å adhesion layer of titanium followed by a 1000 Å seed layer of gold. The metal traces on the bottom coupon are then patterned. The traces are then plated with 5 μm of nickel and 1 μm of either pure gold or chrome gold. The top coupon contact consists of one micron of pure gold or aluminum. Since this is a non symmetrical contact, the contact resistance of the two sides is determined separately. The contact resistance in the top coupon is

$$R_t = \frac{\rho_t}{4a} \tag{8.1}$$

where a is the radius of contact if contact occurs at one central, growing asperity or the Holm equivalent contact radius if contact is made at multiple asperities and ρ_t is resistivity of the top contact surface material. The contact resistance in the bottom coupon is the contact resistance at top contact material plus the resistance at contact material and nickel transition plus the resistance at the nickel and sputtered gold seed layer transition. The titanium layer is ignored because it is only 30 nm thick and has a relatively higher resistivity. The contact resistance in the bottom half of the coupon in therefore

$$R_b = \frac{\rho_b}{4a} + (4/\pi)(\rho_b/\rho_n)(L_b/a)\frac{\rho_b/L_b}{\rho_b/L_b + \rho_n/L_n + \rho_s/L_s}$$

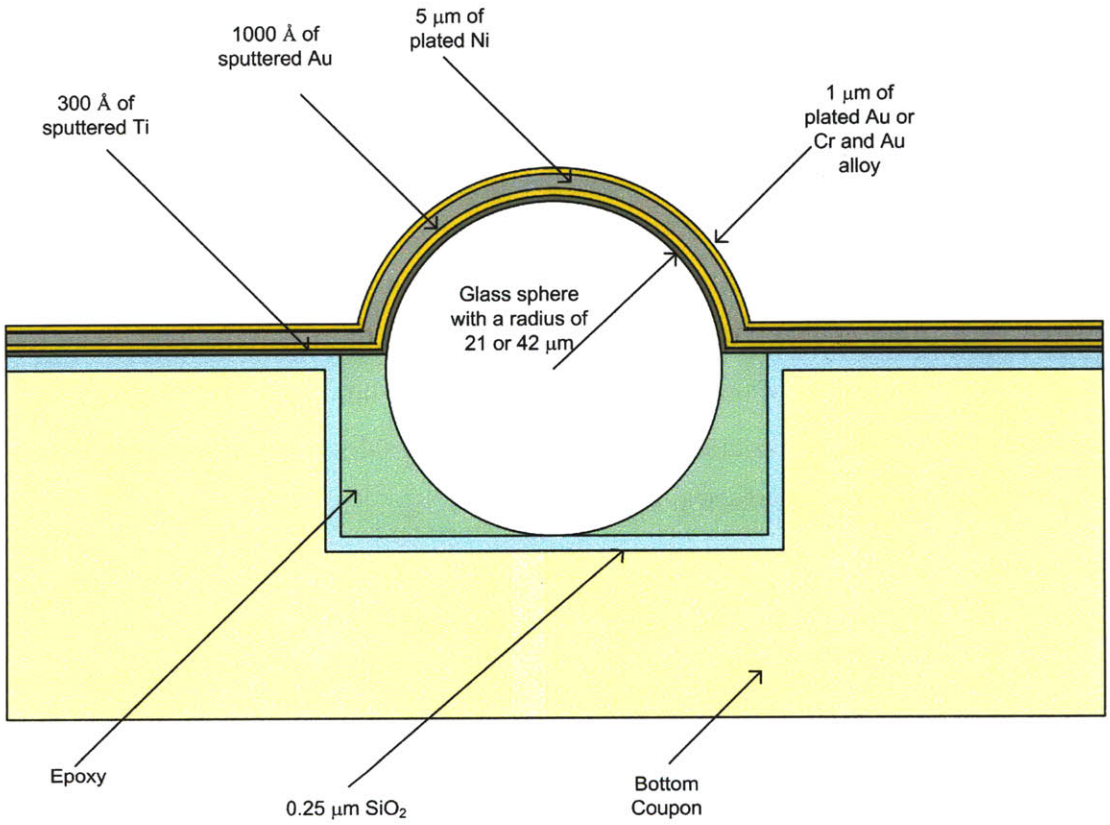

Figure 8-1: The geometry of the sphere side of the sphere-on-flat contacts.

$$+(4/\pi)(\rho_n/\rho_s)(L_n/a)\frac{\rho_b/L_b+\rho_n/L_n}{\rho_b/L_b+\rho_n/L_n+\rho_s/L_s} \tag{8.2}$$

where ρ_b is the resistivity of the outermost contact surface on the bottom coupon, which is either plated pure gold or plated chrome gold, ρ_n is the resistivity of the nickel , ρ_s is the resistivity of the sputtered gold seed layer, L_b is the thickness of the outermost contact surface on the bottom coupon, which is either plated pure gold or plated chrome gold, L_n is the thickness of the nickel, and L_s is the thickness of the sputtered gold seed layer. The total theoretical contact resistance of the sphere-flat contact geometry is then

$$\begin{aligned} R_c &= \frac{\rho_t}{4a}+\frac{\rho_b}{4a}+(4/\pi)(\rho_b/\rho_n)(L_b/a)\frac{\rho_b/L_b}{\rho_b/L_b+\rho_n/L_n+\rho_s/L_s}+ \\ &\quad (4/\pi)(\rho_n/\rho_s)(L_n/a)\frac{\rho_b/L_b+\rho_n/L_n}{\rho_b/L_b+\rho_n/L_n+\rho_s/L_s} \end{aligned} \tag{8.3}$$

There is a question as to how the radius of contact a is determined. In traditional contact theory, a would be equal to the Holm radius of equivalent contact area α defined as

$$\alpha=\frac{\rho}{2}\sqrt{\frac{\pi H}{F}}. \tag{8.4}$$

However, when dealing with a spherical tip, one must consider the effects of Hertzian contact stresses. When a sphere makes contact with a flat, the tip of the sphere is deformed into a flat circle. That circle has a radius of

$$a=\left(\frac{3FR}{4E_e}\right)^{1/3} \tag{8.5}$$

where F is the contact force, R is the radius of the sphere, and E_e is the equivalent modulus of elasticity of the system. The equivalent modulus of elasticity is given by

$$E_e=\frac{1}{\frac{1-\nu_t^2}{E_t}+\frac{1-\nu_b^2}{E_b}} \tag{8.6}$$

where E_t and ν_t are the Young's modulus and Poisson's ratio of the top flat contact surface and E_b and ν_b are the Young's modulus and Poisson's ratio associated with the

bottom contact sphere. Whether the Young's modulus and Poisson's ratio associated with the bottom contact sphere is that of the sphere's material or that of the metal coating the sphere depends on their relative Young's moduli. If the material in the sphere is softer than the relatively thick nickel plating, then the sphere will deform and the metals will conform around it. If the sphere is relatively stiff but the nickel is soft, then the sphere may not deform significantly but the nickel might. The gold or chrome gold on the outside of the sphere is relatively thin so it is assumed to be conformal. Assuming the top coupon contact material is gold then E_t= 78 GPa and ν_t=0.44. If the glass dominates the bottom coupon deflection then E_b=68.9 GPa and ν_b=0.21. This results in an equivalent modulus of elasticity of 41.3 GPa. If the nickel cobalt dominates the bottom coupon deflection then E_b=195 GPa and ν_b=0.31. This results in an equivalent modulus of elasticity of 43.08 GPa. Since using glass as the dominant material results in a slightly softer equivalent modulus of elasticity, glass is assumed to be dominant. If the top coupon contact material is aluminum, them E_t= 70 GPa, ν_t=0.35, and the equivalent modulus of elasticity is 37.9 GPa.

If the Hertz radius of contact found using Equation 8.5 is less than the Holm radius of equivalent contact round using Equation 8.4, then the Hertz radius of contact would be the actual radius of contact. If the Hertz radius of contact was found to be greater than the Holm radius of contact, then the Hertz radius is only the radius of the apparent contact area and the Holm radius would be the true radius of equivalent contact. In order to determine which s these radii is greater, Hertz and Holm radii are plotted for 21 and 42 μm glass spheres contacting aluminum or gold with spheres coated in pure gold or chrome gold. This is shown in Figure 8-2. The smaller of the two predicted radii will be the one which determines contact area. According to Figure 8-2, in these cases, the Holm radius is smaller at low forces but is larger than the Hertz radius for the 21 μm radius sphere at a force of about 10 mN. Additionally, these predictions are all dependent on the hardness of the contact materials, which is difficult to predict at small scales. Therefore the data will have to be evaluated with respect to both the Holm and Hertz radii.

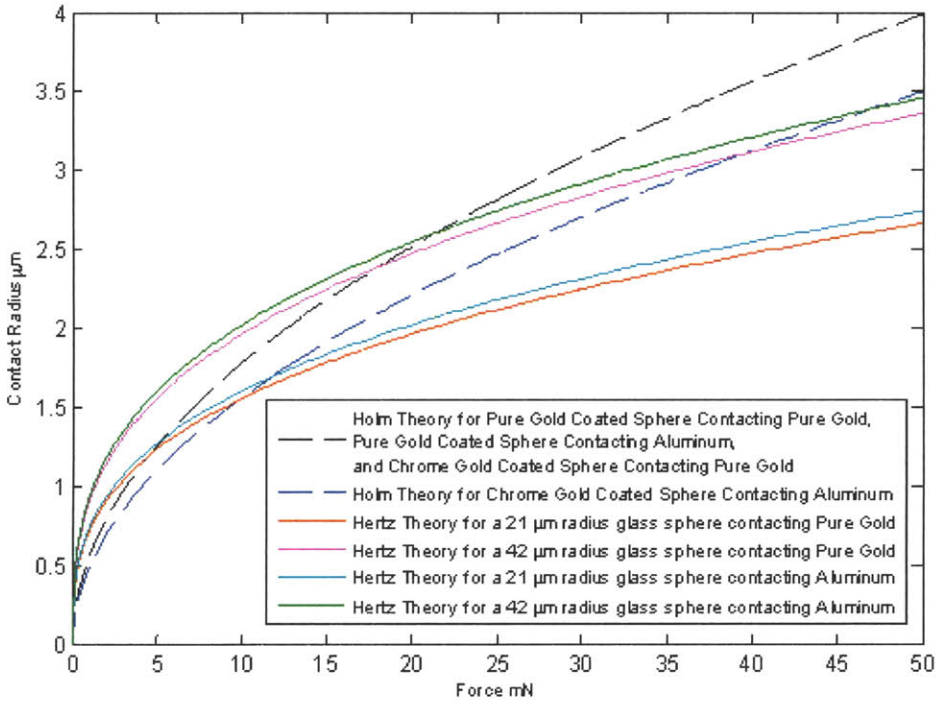

Figure 8-2: The predicted contact radii for Hertz and Holm theory.

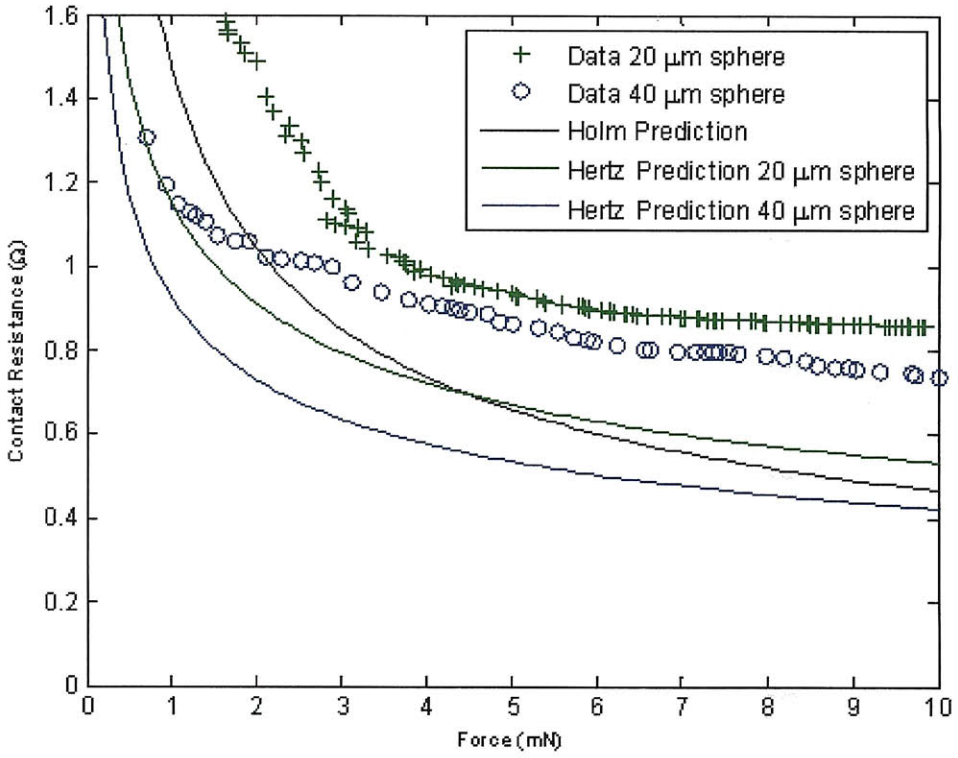

Figure 8-3: Contact resistance for sphere-on-flat contacts compared to Hertz and Holm theory.

8.2 Sphere on Flat Contact: Variation in Sphere Diameter

In order evaluate the dominance of Hertz and Holm radii, a 21 μm radius sphere coated in 1 μm of pure plated gold and a 42 μm radius sphere coated in 1 μm of pure plated gold were both contacted with 1 μm of pure sputtered gold. This data was compared to the resistance predicted by the Holm radius using Equation 8.3 and Equation 8.4 and the resistance predicted using the Hertz radius, using Equation 8.3 and Equation 8.5. This is shown in Figure 8-3. In this data, the 21 μm radius sphere does have a lower contact resistance than the 42 μm sphere; however these values are higher than both those predicted by Hertz and Holm. In Chapter 7 it was noted that flat thin films have a higher contact resistance than they would if they were thicker.

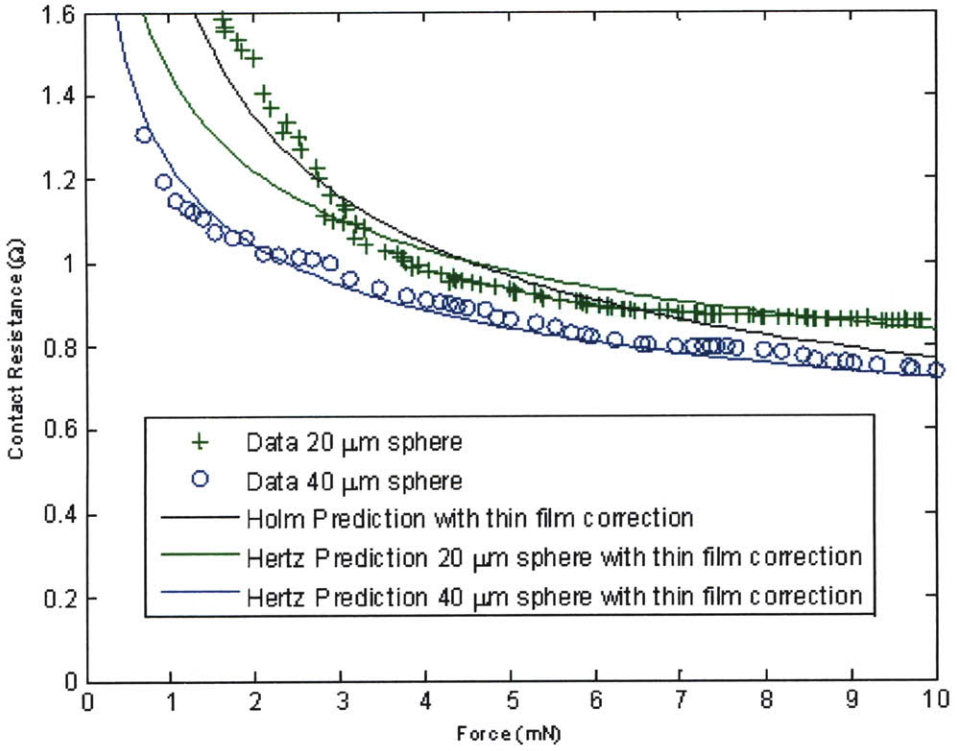

Figure 8-4: Contact resistance for sphere-on-flat contacts compared to Hertz and Holm theory including the thin film effect.

The actual resistance was the Holm predicted resistance multiplied by a thin film factor which was itself a function of contact radius a. This thin film factor was

$$K_{thin-film} = \left[\frac{1.45}{Lk_1}(\ln(a/k_2+1))^2 + \left(\frac{3.13}{Lk_1} - .29\right)\ln(a/k_2+1) + 1\right]. \qquad (8.7)$$

where k_1 is a correction factor which varied based on the geometry and roughness of the contact, a is the contact radius in microns, and k_2 is a constant equal to 1 μm^{-1}. When the Holm and Hertz predictions for contact resistance are multiplied by this thin film factor using a correction factor k_1= 5 μm^{-1}, the magnitudes of the predicted resistances are much closer to those of the data. These are shown in Figure 8-4.

In the 21 μm case, it appears as though Hertz theory dominates until about 3 mN at which point Holm theory dominates. In the 42 μm case, it appears as is though Hertz theory dominates the entire time.

8.3 Sphere on Flat Contact: Variation in Force/Scrub Profile

Two force/scrub contact profiles were studied. In the first, referred to as a constant force/scrub profile, a sphere and flat were brought together with a contact force of 50 mN. After this force was achieved, the sphere and flat were scrubbed relative to each other by a distance of 15 μm. In the second, referred to as a linear force/scrub profile, the membrane of the top coupon is compressed just until contact is made with the bottom coupon. At this point, contact force and scrub are both increased and rates such as the maximum contact force of 50 mN is achieved at the same time as the maximum scrub of 15 μm. The top contact surface was one micron of sputtered aluminum. Sputtered aluminum grows a non conductive oxide almost instantly at room temperature. The sphere side of the contacts were comprised of the same metal layers shown in Figure 8-1 with the top contacting surface being one micron of plated gold. These two contact profiles were each performed using spheres of 21 μm and 42 μm radii. Figure 8-5 has two frames. The first shows contact resistance as a function of force. For the two linear profile samples, they have also been scrubbed. The second frame shows the effect that scrubbing then has on the constant force profile samples. The resistance predicted by Equation 8.3 using the Holm equivalent radius and the Hertz radius for the 21 and 42 μ spheres are also shown.

For the two linear profile contacts, both achieve stable contact resistance at about the same point, about 2.5 mN of force which corresponds to 0.75 μm of scrub. At this point, the Hertz contact radius in the 21μm radius sphere was 0.984 μm and the Hertz contact radius in the 42 μm radius sphere was 1.24 μm. The corresponding contact pressures were 0.82 GPa in the 21μm radius sphere and 0.52 GPa in the 42 μm sphere. The stable contact resistance seen in the 40 μm linear profile case is actually higher than the stable contact resistance seen in the 20 μm linear profile case, the opposite of what was seen in the gold, non scrubbing sphere on flat contacts. This may be because there is greater contact pressure on the 21 μm sphere which facilitates the better penetration of surface oxide on the aluminum. The 20 μm constant force

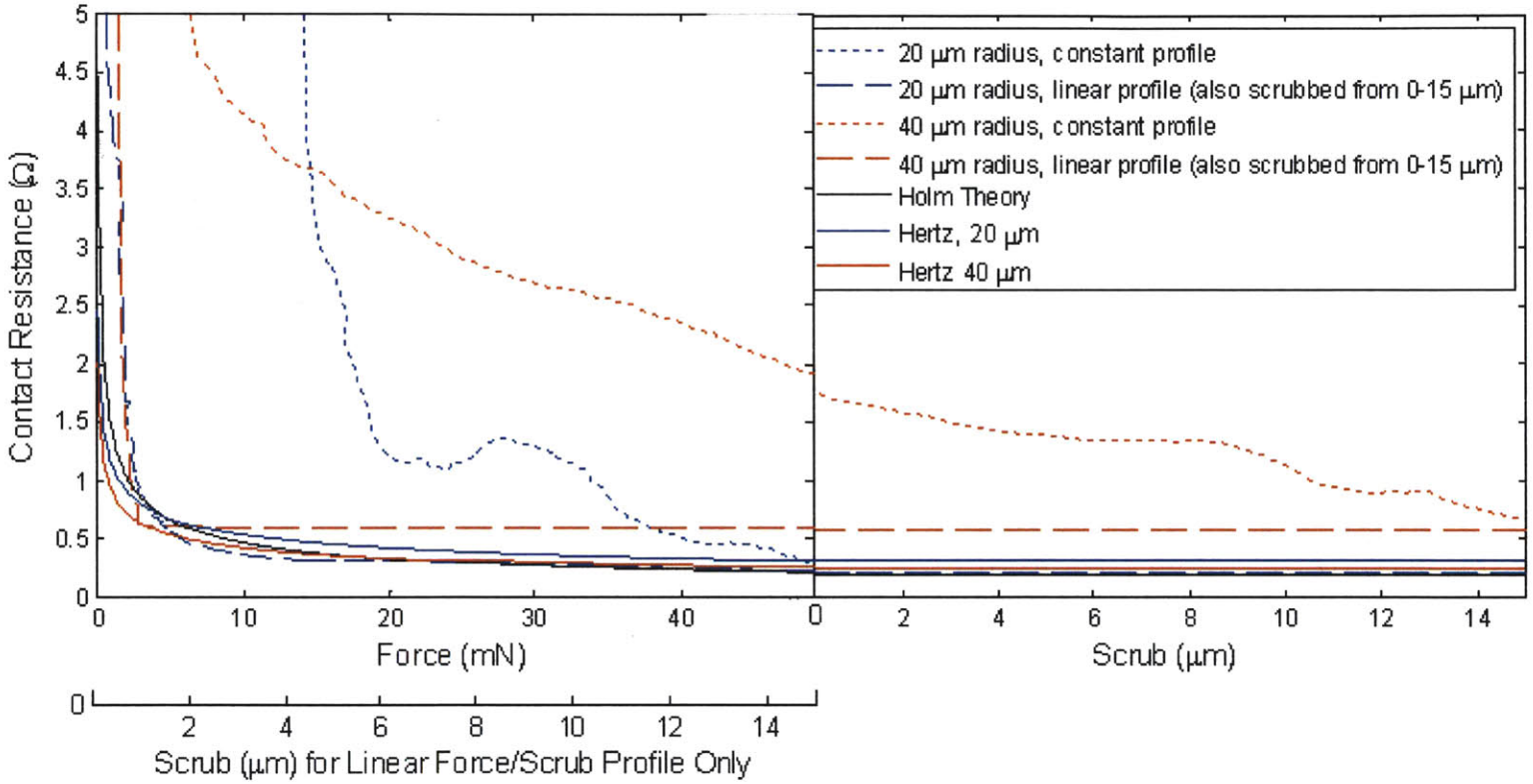

Figure 8-5: The effects of the force/scrub profile on sphere-on-flat contacts of 21 and 42 μ radii. The top contact metal is aluminum and the bottom contact material is gold. Contact resistance predicted by Hertz and Holm is also shown.

profile case sees contact resistance drop to a stable value, around 1 Ω at about 20 mN of force. At this point, the Hertz radius of contact is 1.97 μm which corresponds to a contact pressure of 1.64 GPa. The contact resistance then seems to go up and down a bit as force is further increased. This could be a result of the oxide on the aluminum cracking and shifting. When the contacts are then scrubbed forced, contact resistance is further decreased from 240 mΩ to 190 mΩ. The 42 μm sphere with the constant force/scrub profile does not achieve stable contact resistance during the force portion. At the end of the 50 mN of force increase, the contact resistance is about 1.84 Ω. At this point, the Hertz radius of contact is 3.37 μm which corresponds to a contact pressure of 1.4 GPa, less than the contact pressure at which the 21 μm sphere with the constance force/scrub profile saw stable contact resistance. As scrub was imparted, the contact resistance in the 42 μm sphere with the constant force/scrub decreased from 1.84 Ω to 661 mΩ.

It appears to require much more force to achieve stable contact resistance on oxidized surfaces when scrub is not imparted at the same time as force. With less than 1 μm of scrub, stable contact resistance was seen at 0.53 and 0.82 GPa of contact pressure. However, with no scrub, stable contact resistance was not seen until the contact experienced 1.64 GPa of contact pressure. This higher pressure, and higher contact force, can be difficult to achieve in some MEMS products such as electrostatic actuators or can damage the contact surface. Therefore it seems this small amount of scrub is crucial.

8.3.1 Sphere-on-Flat: Pure Gold vs. Chrome Gold

When testing spheres coated in pure gold, occasionally the contact resistance would be abnormally high. Using an SEM it was observed that the pure gold coating could delaminate from the spheres onto the flat contact surface, resulting in a higher contact resistance. This material transfer is shown in Figure 8-6. If hard gold, with 0.3% chromium is plated instead of pure gold, then the adhesion of the gold to the spheres is greatly improved. A hard gold coated sphere and the resulting smear mark are shown in Figure 8-7.

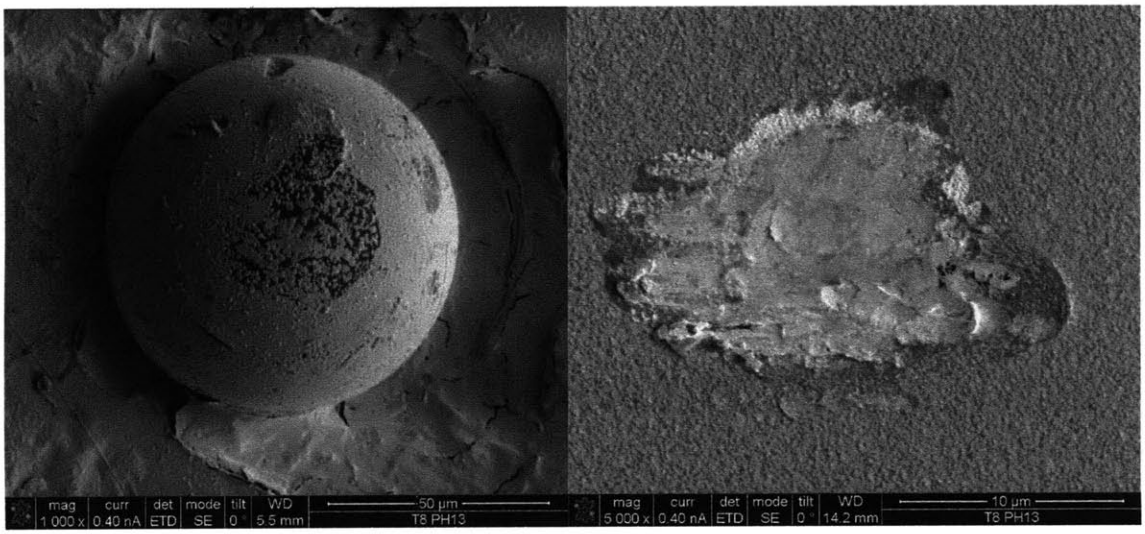

Figure 8-6: Pure gold transferring from the sphere to the aluminum flat contact surface.

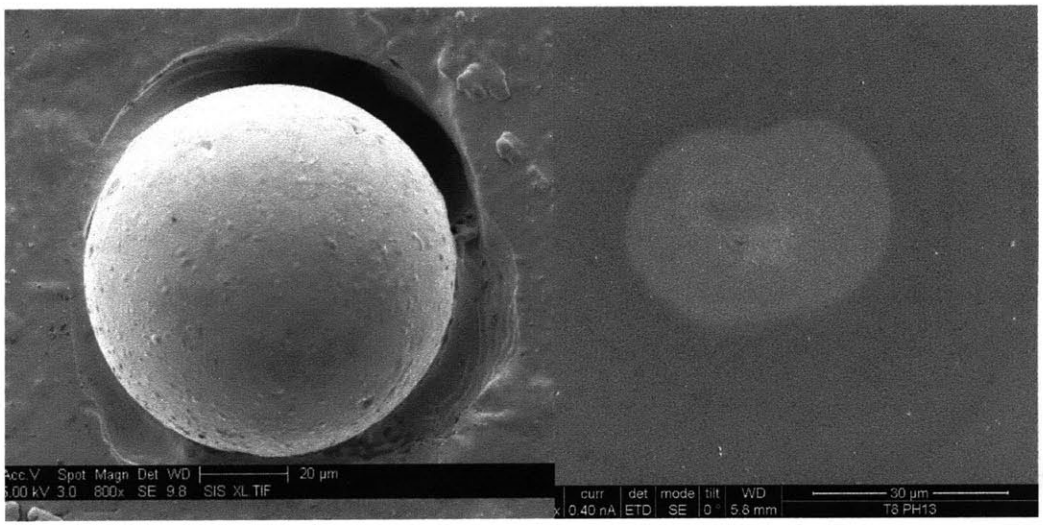

Figure 8-7: A hard gold coated sphere and the mark it leaves on the aluminum flat contact surface.

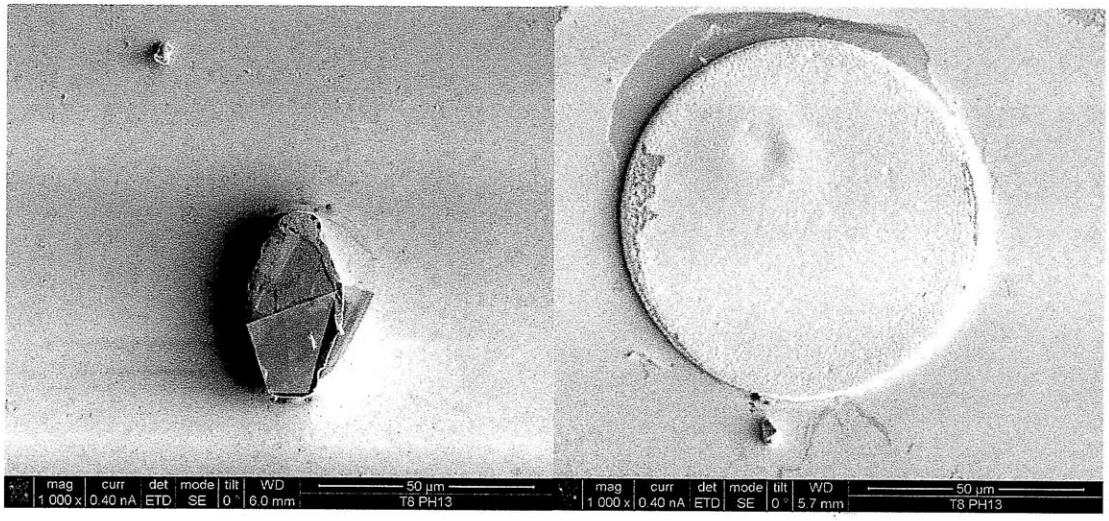

Figure 8-8: A 84 μm circle tip and the 126° diamond-shaped plated tip.

8.4 Plated Tips

Four shapes of plated tips were fabricated and tested. These four shapes were an 84 μm diameter circle, a 42 μm diameter circle, a diamond-shape with 90° angles and 15 μm sides, and a diamond-shape with two 126° angles and two 54° angles and 23.5 μm sides. The 84 μm circle tip and the 126° diamond tip are shown in Figure 8-8.

These are comprised of nickel plated 5 μm tall on top of a 0.1 μm sputtered gold seed layer. They are then coated with 1 μm of gold. The flat side of the contact is 1 μm of sputtered gold or aluminum. Since this is a non-symmetrical contact, the top and bottom contact resistances are calculated separately. The top contact resistance is

$$R_t = \frac{\rho_t}{4a} \tag{8.8}$$

where ρ_t is the resistivity of the top contact material, either gold or aluminum, and a is the Holm radius of equivalent contact. The bottom contact resistance consists of four terms. The first is the contact resistance of the contact material, the second is the transition from the contact material to the nickel plating, the third is the bulk resistance through the nickel, and the fourth is the transition from the nickel to the

sputtered seed layer. This resistance is

$$R_b = \frac{\rho_b}{4a} + (4/\pi)(\rho_b/\rho_n)(L_b/a) + \frac{\rho_n L_n}{A_n} + (4/\pi)(\rho_n/\rho_s)(L_n/a) \tag{8.9}$$

where ρ_b is the resistivity of the bottom contact layer, in this case gold; ρ_n is the resistivity of nickel; L_b is the thickness of the bottom contact layer, in this case 1 μm; L_n is the thickness of the nickel plating, in this case 5 μm, A_n is the area of the nickel plating, and ρ_s is the resistivity of the gold seed layer. The total contact resistance is therefore

$$R_c = \frac{\rho_t}{4a} + \frac{\rho_b}{4a} + (4/\pi)(\rho_b/\rho_n)(L_b/a) + \frac{\rho_n L_n}{A_n} + (4/\pi)(\rho_n/\rho_s)(L_n/a) \tag{8.10}$$

Figure 8-9 shows the results of 42 and 84 μm diameter circle plated tips in contact with gold and 42 and 84 μm diameter circle plated tips in contact with aluminum. The tips follow a linear scrub/force profile reaching a maximum force of 50 mN as scrub reaches a maximum of 15 μm. It also shows the predicted contact resistance from Equation 8.10. Both diameter circular tips making contact with the gold surface obtain a low, stable contact resistance at a force of less than one mN and a contact resistance value close to that predicted by Equation 8.10. The predicted values for both the two circle-shaped tips and the two diamond-shaped tips contacting gold or aluminum were all within 1 mΩ of each other which is why they appear as one line in Figure 8-9. The two circles contacting the aluminum never make stable contact resistance. For the sphere-on-flat contacts, making contact without scrub required a contact pressure of 1.6 GPa. In the case of these tips, the contact pressure is never locally higher than the hardness of the gold, 1 GPa. It is possible that the flat tips, having many distributed asperities making contact, are not as apt as the spherical tips to break through the oxide while scrubbing. The two diamond-shaped tips, as well as one deformed diamond-shaped tip with decreased contact area were also measured while making contact with an aluminum surface using a linear scrub/force profile reaching a maximum force of 50 mN as scrub reaches a maximum of 15 μm. In the deformed tip, the center of the tip was plated to the full height while the outside of the

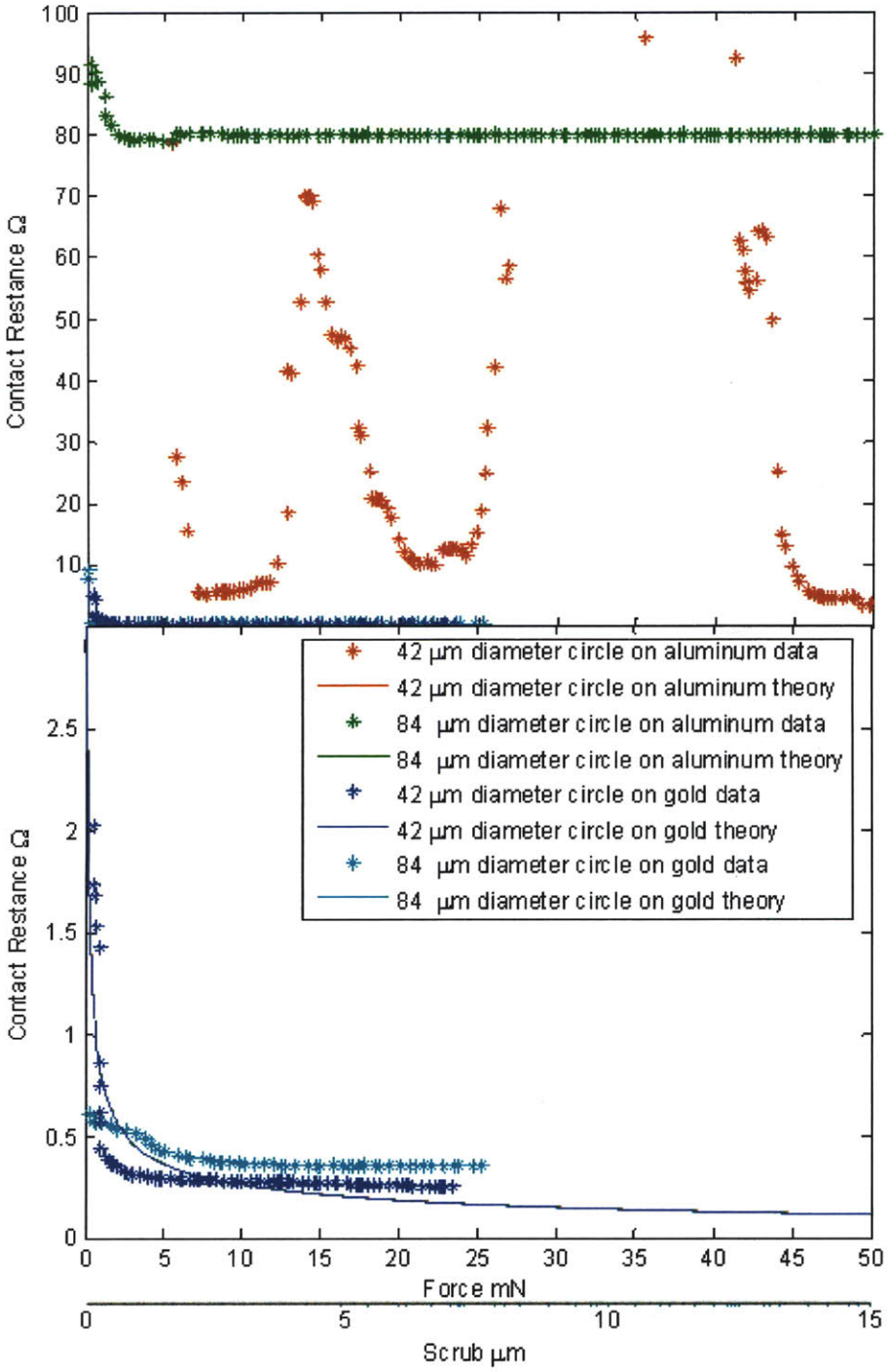

Figure 8-9: Contact resistance of plated circles of 42 and 84 μm in diameter making contact with gold and aluminum surfaces. The theoretical resistances for all four samples are within one mΩ of each other which is why they appear as one line.

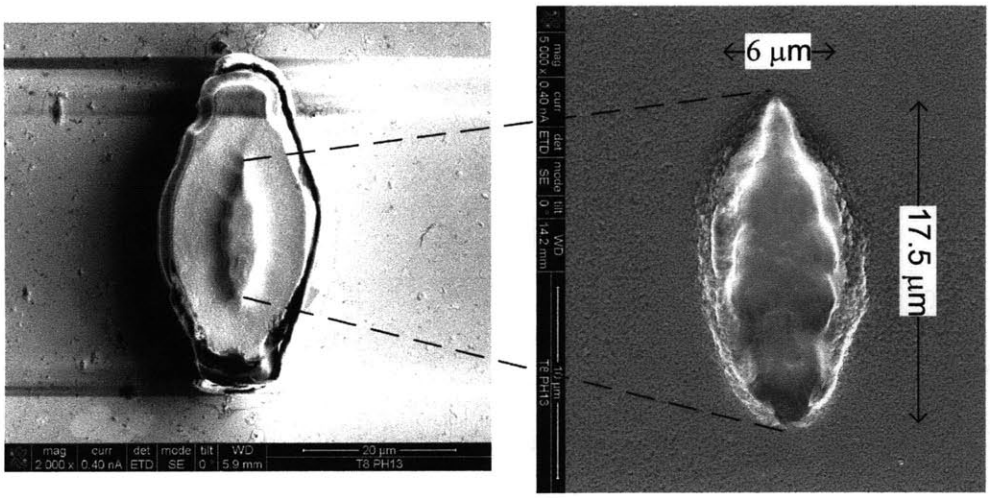

Figure 8-10: A deformed diamond tip and the scrub mark it created in an aluminum contact surface.

tip was not, resulting in a reduced contact area of approximately 52.5 μm^2. An image of this deformed diamond tip and the scrub mark it makes is shown in Figure 8-10. The results of the two circle, two diamond and one deformed diamond tip contacting aluminum are shown in Figure 8-11. The only plated tip which makes low, stable contact is the deformed diamond tip. At the end of the 50 mN of force and 15 μm of travel, the contact resistance is approximately 1 Ω. None of the tips, including the deformed diamond tip, have a contact area small enough such that the contact pressure would exceed the hardness of the material. However, the deformed diamond tip is considerably smaller than the other tips. If the plating were in anyway uneven or the tip slightly crooked, the tip of the diamond could have a very high contact pressure which would be able to break through the non-conductive oxide on the aluminum surface. The other tips do not achieve a high contact pressure and simply skate across the contact surface. The diamond-shaped tip with 90° angles does not obtain finite contact resistance after 50 mN of force and 15 μm of travel. However, this particular tip did achieve significantly lower contact resistance when the voltage across the contact was increased. During this test, force on the contact is held at a constant 50 mN as voltage is increased from 0 to 0.25 V, slightly less than the melting voltage of aluminum. This contact resistance as a function of voltage across

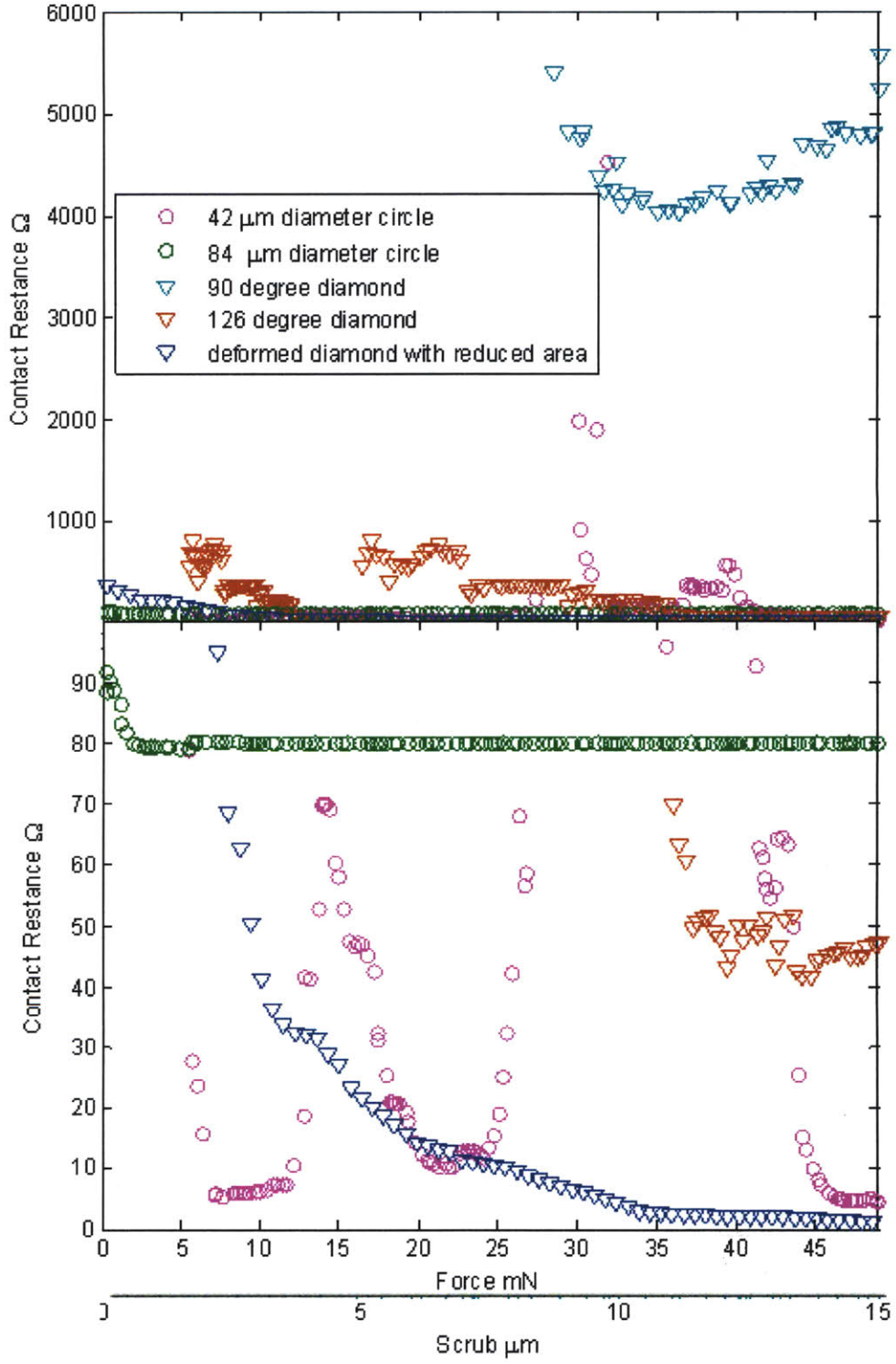

Figure 8-11: A the results of the plated tips contacting an aluminum contact surface.

the contact is shown in Figure 8-12. After the voltage is increased, contact resistance is reduced considerably, to about 35 Ω, however this is still nowhere near as low as the contact resistance obtained from the deformed diamond-shaped tip. Voltage cannot be increased beyond the melting voltage of the contact materials without damaging the contact significantly. To illustrate this, a circular plated tip was contacted with an aluminum surface and voltage was increased to the melting voltage. The results of this are shown in Figure 8-13.

8.5 Chapter Summary

This chapter examined contact between spheres and flats and contact between plated tips and flats. In the case of sphere-on-flat contacts, it was found that the contact area was dominated by the Holm radius of equivalent contact in some cases and the radius defined by Hertz contact theory in other cases. Force and scrub applied together were found to create stable contact resistance at lower forces and lower scrub lengths than if force and scrub are applied in series. Contact pressure was deemed to be critical to penetrating a non-conductive oxide layer on a contact surface. Also determined was that delaminating films can have a detrimental effect on contact resistance and materials should be chosen to avoid this delamination. Contact pressure was also an important issue affecting the contact resistance of the plated tips on flat contact surfaces having a non-conductive oxide. Too little contact pressure and low, stable contact resistance could not be achieved, even with 50 mN of force and 15 μm of scrub applied simultaneously. Increasing the voltage across the contact assists in breaking down the oxide layer, but not to the degree than increasing contact pressure does.

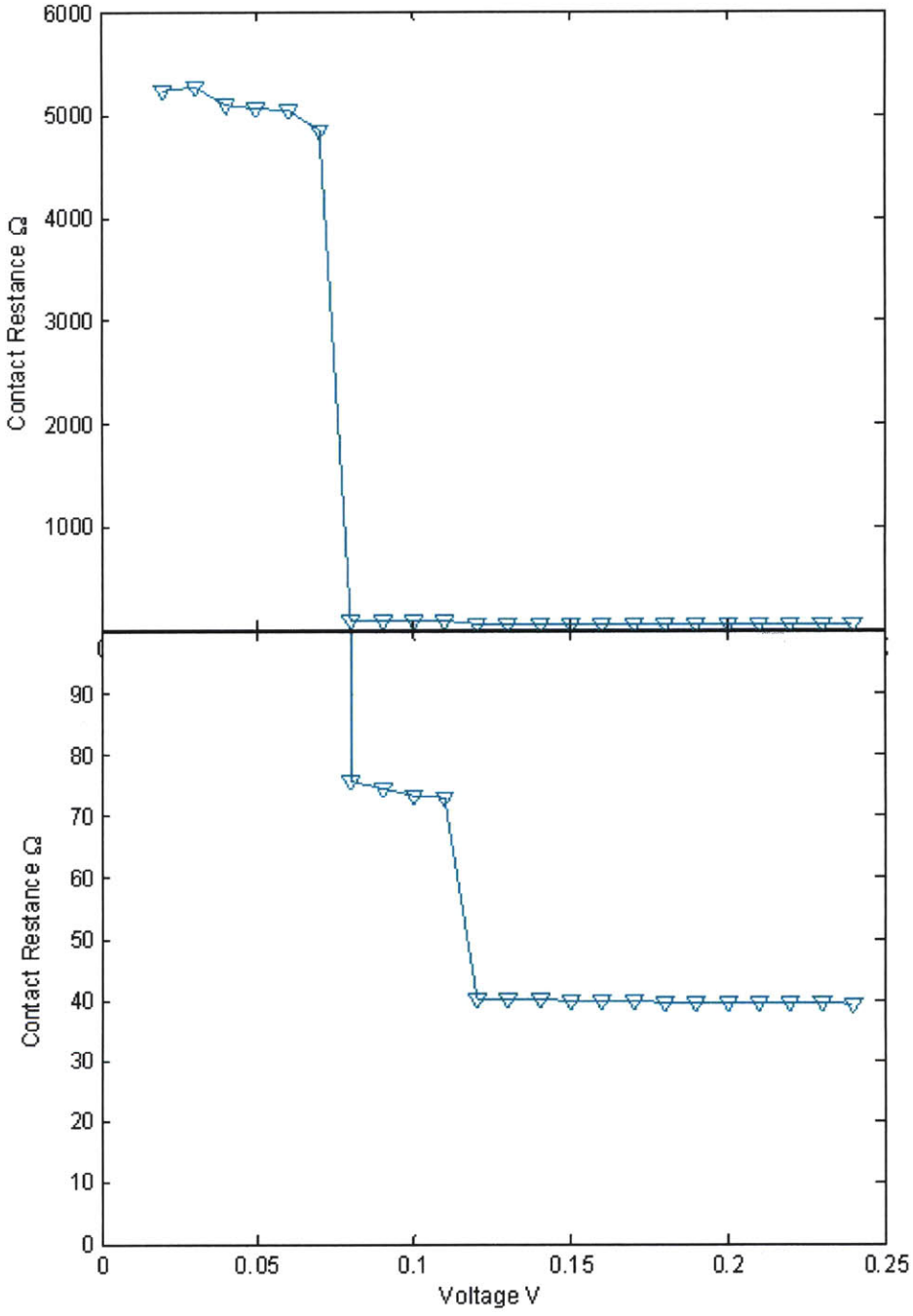

Figure 8-12: Contact resistance as a function of voltage for a 90° diamond-shaped tip contacting aluminum with 50 mN of force.

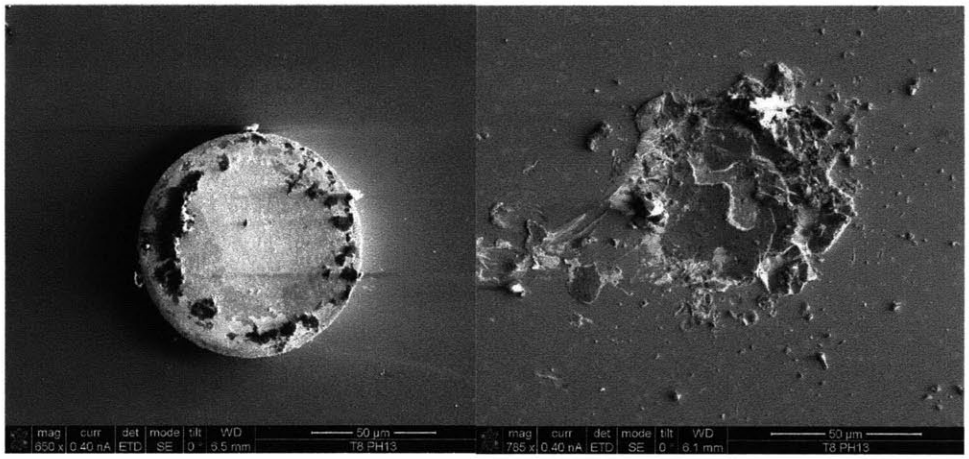

Figure 8-13: A circular plated tip and the aluminum it made contact with after the melting voltage across the contact was increased above the melting voltage of aluminum.

Chapter 9

Summary, Design Considerations, and Future Work

9.1 Summary

A two-coupon system with accompanying instrumentation for the characterization of MEMS fabricated electrical contacts has been designed, built, and verified. Three versions of this two coupon system were designed, built, and tested. The first was capable of measuring only flat-on-flat contacts. The top and bottom contacts were aligned to each other using a kinematic coupling to ensure repeatable alignment. Alignment repeatability was 3.08 μm, which was good, but not quite the 1 μm needed to mimic MEMS relays. Also, whenever the coupons were assembled and disassembled, the balls which were part of the kinematic coupling had to be moved which was very difficult. Additionally, wiring to the top coupon caused the coupons to disassemble without other mechanisms in place to prevent this.

The second design utilized pyramids which mated with pits in an elastic averaging configuration. This achieved far better alignment than the first two-coupon system. It also allowed electrical contact to be made between the two coupons at the metalized pit/pyramid interface eliminating the need for wiring to the top coupon. It was also much easier to use since assembly and disassembly were greatly simplified by eliminating the balls. However, due to the low amount of force at each interface, the

electrical contact between the bottom and top coupons was not always kept.

The final two-coupon system allows for the testing of MEMS contacts with varying materials, deposition methods, and geometries. The system allows the user to impart any combination of force, scrub, and source current and record contact resistance at all times throughout the test. Contact resistance is measured through an integrated Kelvin Structure which eliminates lead resistance. The coupons are aligned relative to each other using a kinematic coupling configuration. This results in the alignment between the coupons being highly repeatable. The translational repeatability is 0.53 μm, the rotational repeatability is 0.082 mrad, the parallelism repeatability is 0.38 mrad, and the gap repeatability is 0.9 μm. This allows the two coupons to be tested, disassembled, the contact surfaces observed with an SEM or other instruments, reassembled, and retested with the same asperities in contact before and after disassembly and reassembly. The final two-coupon system is easy to use as the balls are secured to the bottom coupon. Metalized ball/pit interfaces allow for all wiring to be done to the top coupon.

Much was learned during the design, fabrication, and testing of these three two-coupon systems. The first is that macro-scale alignment mechanisms such as the kinematic coupling configuration and elastic averaging can be utilized very effectively at the micro-scale level. Also learned was how important the user experience is to quality results. If the user has to solder wires or place small balls in pits, there is a greater chance the sample will be contaminated or break. Also, the more difficult it is to obtain data the less data the user will most likely decide to take. Also of note was how small fabrication changes can affect the result. For example, switching from a nitride mask to an oxide mask created KOH-etched pits with a much looser width range.

Custom mechanical test instrumentation was also designed to impart any force and scrub within the range of the machine on the final two-coupon system. This instrumentation could measure contact resistance using a 4-wire resistance measurement and the integrated Kelvin structure of the final two-coupon system. This system shows the overall errors of a system can be reduced by keeping all actuators and sen-

sors in a line and that positioning and adjustment of the samples should be made as simple as possible to ensure on center and on axis force application.

The system was used to perform several experiments. The first involved measuring the contact resistance between flat thin films. Two previous modeling approaches were limited to specific regimes of the force vs. contact resistance curve. These two models were the Timsit numerical model and the Norberg finite element model. They produced seemingly contradictory results. An experiment was designed to measure contact resistance over ranges covered by each of the two models. The results of this experiment showed that the shape of the curve mirrors that in the Timisit model at very low values of force and is very close to the Norberg model at very high values of force. The transition between these models seems to occur when the ratio between contact radius and film thickness is equal to one. When the contact radius is smaller than the film thicknesses, the current lines constrict into the contact; however, when the contact radius is larger than the film thickness, the current lines can actually spread inside the contact. Therefore it makes sense that the relationship between contact resistance and contact force, which is proportional to the square of the contact radius, would have a a transition at that point.

The system was also used to perform several experiments on sphere-on-flat contacts. From these experiments it was determined that the radius of the sphere can affect contact resistance if the radius of contact obtained from Hertz contact theory is less than the Holm equivalent radius. It was also determined that without scrub, additional force is needed to make low, stable contact on materials with a non-conductive oxide. The amount of force needed to make contact through this oxide was dependent on the contact pressure. Multiple contact materials were tested and it was found that materials which did not adhere well to the sphere could rub off during scrubbing which had a detrimental effect on contact resistance.

The last experiments looked at plated tips. It was determined that a minimum pressure threshold was needed for flat, thin tips to make low, stable contact on materials with a non-conductive oxide.

9.2 Design Considerations

Several considerations regarding the design of devices incorporating MEMS fabricated electrical contacts can be taken from this work. The first is that MEMS fabricated electrical contacts do not always behave like macro scale contacts and that this behavior can be difficult to model. Therefore, before designing a device incorporating MEMS fabricated electrical contacts, it is advisable to externally test these contacts using a system like the one presented in this thesis to determine the contact resistance that can be obtained using the contacts, both at the first touchdown and over time.

Second, not all types of contacts are appropriate for all types of applications. Contacts which will not have any scrubbing capability should be made of materials which do not oxidize or have a conductive oxide, such as gold, platinum, or rhodium. If contact must be made to a material with a non conductive oxide, the other side of the contact should provide a large amount of contact pressure and ideally have some scrubbing motion to clear the oxide. If a contact is touching down on a surface which is prone to contamination, scrubbing can also be used to clear the contamination.

9.3 Future Work

This section addresses two main areas of future work. The first is improvements to the two-coupon system and test set up. The second is additional experimental work to be done.

A proposed way to improve the operation of the two-coupon system and the instrumentation would be to shift some of the functionalities of the two-coupon system to the instrumentation. The thin membrane and in-plane flexure in the two-coupon system are both fairly difficult to fabricate. One possible way to accomplish this would be to have two very simple silicon coupons which could mount to two large aluminum plates. The vertical motion and lateral motion previously achieved using the membrane and in-plane flexure, could be achieved fairly easily using a large aluminum mounting plate. This plate would be similar in shape and functionality

to the current top coupon, but be more durable and larger. This plate could have a precision locating device, such as three hemispherical bosses, that mate with the KOH-etched grooves on the backside of the new top coupon. The new top coupon would consist only of a metal trace on the front side and the KOH-etched pits on the backside. Similarly, an aluminum bottom plate could be manufactured having a precision locating device, such as three hemispherical bosses, which mate to three KOH-etched pits on the backside of the bottom coupon. The front side of the bottom coupon would have only a metal trace and a tip if required. The two coupons would be located to their respective aluminum plates and then secured with vacuum. The aluminum plates themselves would then be located to each other using a kinematic coupling which would leave a gap between the two coupons. The kinematic coupling between the aluminum plates would have a mechanism for adjusting the gap between the plates in order to compensate for different tip heights. The instrumentation could then apply force and scrub through the large aluminum plates. This type of system would be advantageous because it would require far less micro fabrication processes to fabricate the samples and many more samples could be fabricated on a single wafer as space would not have to be reserved for the thin membrane of the in-plane structure.

Much experimental work can be done using this test setup. The first area of interest would be examining contact resistance between two flat, thin films at very low forces. In this area, contact resistance as a function of force seems to change from a regime modeled by the Timsit numerical model to a regime modeled by the Norberg finite element model. Additional work could also be done in flat on-sphere contact where the area of contact seems to transition from being governed by the Holm equivalent radius to being governed by Hertz contact theory. Additional contact materials such as solder or carbon nanotubes could be examined. Additional work could be done on achieving low, stable contact resistance on metals which oxidize. Since contact resistance as a function of force varies depending on when and how the oxide cracks and therefore is not entirely deterministic, a large amount of data should be gathered so that statistical analysis could be performed. Finally, this test setup could be used to look at life cycle testing in MEMS switches while using an SEM in

between tests to study the changing morphology of the contact. With regard to all of these experiments, further work needs to be done on the modeling of the results and determining the exact physics behind each of the phenomena.

Bibliography

[1] L. Almeida, R. Ramadoss, R. Jackson, K. Ishikawa, and Q. Yu. Study of the electrical contact resistance of multi-contact MEMS relays fabricated using the MetalMUMPs process. *J. Micromech. Microeng*, 16(7):1189–1194, 2006.

[2] M. Balasubramaniam, E. Golaski, S. Son, K. Sriram, and A. Slocum. An anti-backlash two-part shaft coupling with interlocking elastically averaged teeth. *Precision engineering*, 26(3):314–330, 2002.

[3] Lise Bilhaut, Christophe Poulain, Romain Anciant, and Laurent Duraffourg. Experimental validation of a 2-d constriction resistance model at the microscale. In *Electrical Contacts, 2009. Proceedings of the 55th IEEE Holm Conference on*, pages 290–294, 2009.

[4] IH Brockman, CS Sieber, RS Mroczkowski, AMP Inc, and PA Harrisburg. The effects of the interaction of normal force and wipe distance oncontact resistance in precious metal plated contacts. pages 73–83, 1988.

[5] S.C. Bromley and B.J. Nelson. Performance of microcontacts tested with a novel mems device. *Electrical Contacts, 2001. Proceedings of the Forty-Seventh IEEE Holm Conference on*, pages 122–127, 2001.

[6] D.Y. Chung, B.H. Kim, C.H. Chung, C.B. Park, J.H. Lee, and K. Chun. A Robust MEMS Probe Card for Fine Pitch Test Using a New Cantilever Moving Scheme. *Sensors, 2005 IEEE*, pages 1373–1376, 2005.

[7] R.A. Jr. Coutu, P.E. Kladitis, R. Cortez, R.E. Strawser, and R.L. Crane. Micro-switches with sputtered au, aupd, au-on-aupt, and auptcu alloy electric contacts. *Electrical Contacts, 2004. Proceedings of the 50th IEEE Holm Conference on Electrical Contacts and the 22nd International Conference on Electrical Contacts*, pages 214–221, 20-23 Sept. 2004.

[8] Ronald A. Jr. Coutu, John W. McBride, and LaVern A. Starman. Improved micro-contact resistance model that considers material deformation, electron transport and thin film characteristics. In *Electrical Contacts, 2009. Proceedings of the 55th IEEE Holm Conference on*, pages 295–299, 2009.

[9] J. DeNatale, R. Mihailovich, and J. Waldrop. Techniques for reliability analysis of mems rf switch. *Reliability Physics Symposium Proceedings, 2002. 40th Annual*, pages 116–117, 2002.

[10] DJ Dickrell and MT Dugger. Silicone Oil Contamination and Electrical Contact Resistance Degradation of Low-Force Gold Contacts. *Microelectromechanical Systems, Journal of*, 16(1):24–28, 2007.

[11] D.J. Dickrell and M.T. Dugger. Electrical contact resistance degradation of a hot-switched simulated metal mems contact. *Components and Packaging Technologies, IEEE Transactions on [see also Components, Packaging and Manufacturing Technology, Part A: Packaging Technologies, IEEE Transactions on]*, 30(1):75–80, March 2007.

[12] III Dickrell, D.J. and M.T. Dugger. The effects of surface contamination on resistance degradation of hot-switched low-force mems electrical contacts. *Electrical Contacts, 2005. Proceedings of the Fifty-First IEEE Holm Conference on*, pages 255–258, 26-28 Sept. 2005.

[13] G.D. Gray and P.A. Kohl. Modeling and Performance of a Magnetic MEMS Wiping Actuator. *JOURNAL OF MICROELECTROMECHANICAL SYSTEMS*, 15(4):904, 2006.

[14] JA Greenwood. Constriction resistance and the real area of contact. *British Journal of Applied Physics*, 17:1621–1632, 1966.

[15] JA Greenwood and JBP Williamson. Contact of nominally flat surfaces. *Proceedings of the Royal Society of London. Series A, Mathematical and Physical Sciences*, pages 300–319, 1966.

[16] G. Gregori, R.E. Mihailovich, and D.R. DeNatale, J.F.and Clarke. Development of adhesive contact of mems-switches upon actuation cycling. *Micro Electro Mechanical Systems, 2005. MEMS 2005. 18th IEEE International Conference on*, pages 439–442, 30 Jan.-3 Feb. 2005.

[17] M. Gross, D .Altpeter, T. Stieglitz, M. Schuettler, and J. Meyer. Micromachining of flexible neural implants with low-ohmic wire traces using electroplating. *Sensors and Actuators*, 2002(2-3):105–110, 1996.

[18] R. Holm and E. Holm. *Electric contacts handbook.* Springer, 1958.

[19] R. Holm and E. Holm. *Electric Contacts: Theory and Application.* Springer-Verlag, 1967.

[20] H. Hosaka and K. Kuwano, H.and Yanagiswa. Electromagnetic microrelays: concepts and fundamental characteristics. *Micro Electro Mechanical Systems, 1993, MEMS '93, Proceedings 'An Investigation of Micro Structures, Sensors, Actuators, Machines and Systems'. IEEE.*, pages 12–17, 7-10 Feb 1993.

[21] G. Hotchkiss, G. Ryan, W. Subido, J. Broz, S. Mitchell, R. Rincon, R. Rolda, and L. Guimbaolibot. Effects of probe damage on wire bond integrity. *Electronic Components and Technology Conference, 2001. Proceedings., 51st*, pages 1175–1180, 2001.

[22] D. Hyman and M. Mehregany. Contact physics of gold microcontacts for MEMS switches. *Components and Packaging Technologies, IEEE Transactions on [see also Components, Packaging and Manufacturing Technology, Part A: Packaging Technologies, IEEE Transactions on]*, 22(3):357–364, 1999.

[23] R.L. Jackson and L. Kogut. A Comparison of Flattening and Indentation Approaches for Contact Mechanics Modeling of Single Asperity Contacts. *Journal of Tribology*, 128:209, 2006.

[24] Ben-Hwa Jang, Po-Hsun Tseng, Hsin-Yu Huang, Sheng-T Lee, and Weileun Fang. Characterization of the micro contact resistance using a novel on-chip apparatus. *Solid-State Sensors, Actuators and Microsystems Conference, 2007. TRANSDUCERS 2007. International*, pages 1653–1656, 10-14 June 2007.

[25] D. Jang and D. Kim. Tribological behavior of ultra-thin soft metallic deposits on hard substrates. *Wear*, 196(1-2):171–179, 1996.

[26] K. Kataoka, T. Itoh, K. Inoue, and T. Suga. Multi-layer electroplated microspring array for MEMS probe card. *Micro Electro Mechanical Systems, 2004. 17th IEEE International Conference on.(MEMS)*, pages 733–736, 2004.

[27] L. Kogut and K. Komvopoulos. Analysis of interfacial adhesion based on electrical contact resistance measurements. *Journal of Applied Physics*, 94:6386, 2003.

[28] C. Kruger, W. Mokwa, and U. Schnakenberg. Niw-micro springs for chip connection. *Micro Electro Mechanical Systems, 2004. 17th IEEE International Conference on. (MEMS)*, pages 117–120, 2004.

[29] Qingquan Liu, Daniel T. McCormick, Robert C. Roberts, and Norman C. Tien. Nanoscale al-al and cu-cu contacts. *Solid-State Sensors, Actuators and Microsystems Conference, 2007. TRANSDUCERS 2007. International*, pages 1593–1596, 10-14 June 2007.

[30] Y. Liu, D. Desbiens, T. Luk, and S. Irving. Parameter optimization for wafer probe using simulation. *Thermal, Mechanical and Multi-Physics Simulation and Experiments in Micro-Electronics and Micro-Systems, 2005. EuroSimE 2005. Proceedings of the 6th International Conference on*, pages 156–161, 18-20 April 2005.

[31] S. Majumder, NE McGruer, and GG Adams. Adhesion and contact resistance in an electrostatic MEMS microswitch. *Micro Electro Mechanical Systems, 2005. MEMS 2005. 18th IEEE International Conference on*, pages 215–218.

[32] S. Majumder, NE McGruer, G.G. Adams, PM Zavracky, R.H. Morrison, and J. Krim. Study of contacts in an electrostatically actuated microswitch. *Sensors & Actuators: A. Physical*, 93(1):19–26, 2001.

[33] RD Malucci, M. Inc, and IL Lisle. Effects of wipe on contact resistance of aged surfaces. *IEEE Transactions on Components, Packaging, and Manufacturing Technology, Part A*, 18(3):701–707, 1995.

[34] R.B. Marcus. A new coiled microspring contact technology. *Electronic Components and Technology Conference, 2001. Proceedings., 51st*, pages 1227–1232, 2001.

[35] L. Marot, D. Mathys, G.D. Temmerman, and P. Oelhafen. Characterization of sub-stoichiometric rhodium oxide deposited by magnetron sputtering. *Surface Science*, 602(21):3375–3380, 2008.

[36] I. Minowa, M. Nakamura, and M. Kanno. Conductance of a contact interface depending on the location and distribution of conducting spots. *Proc. Electrical Conference on Contacts, Electromechanical Componentsand Their Applications*, page 19, 1986.

[37] M. Nakamura and I. Minowa. Computer simulation for the conductance of a contact interface. *IEEE transactions on components, Hybrids, and Manufacturing technology*, 9(2):150–155, 1986.

[38] G. Norberg, S. Dejanovic, and H. Hesselbom. Contact resistance of thin metal film contacts. *Components and Packaging Technologies, IEEE Transactions on [see also Components, Packaging and Manufacturing Technology, Part A: Packaging Technologies, IEEE Transactions on]*, 29(2):371–378, June 2006.

[39] Y. Okinaka and M. Hoshino. Some recent topics in gold plating for electronics applications. *Gold Bulletin*, 31:3–13, 1998.

[40] MD Pashley and JB Pethica. The role of surface forces in metal–metal contacts. *Journal of Vacuum Science & Technology A: Vacuum, Surfaces, and Films*, 3:757, 1985.

[41] D. Peroulis and L.P.B. Katehi. A novel device for in situ experimental characterization and reliability analysis of dc-contact rf mems switches. *TRANSDUCERS, Solid-State Sensors, Actuators and Microsystems, 12th International Conference on, 2003*, 1:867–870 vol.1, 8-12 June 2003.

[42] D. Peroulis, K. Sarabandi, and LPB Katehi. Low contact resistance series MEMS switches. *Microwave Symposium Digest, 2002 IEEE MTT-S International*, 1, 2002.

[43] Beth Pruitt. *Piezoresistive Cantilvers for Characterizing Thin-Film Gold Electrical Contacts.* PhD thesis, Standford University, 2002.

[44] B.L. Pruitt and T.W. Kenny. Piezoresistive cantilevers and measurement system for characterizing low force electrical contacts. *Sensors & Actuators: A. Physical*, 104(1):68–77, 2003.

[45] B.L. Pruitt, Woo-Tae Park, and T.W. Kenny. Measurement system for low force and small displacement contacts. *Microelectromechanical Systems, Journal of*, 13(2):220–229, April 2004.

[46] S. Riedel, J. Roeber, and T. Gessner. Electrical properties of copper films produced by mocvd. *Microelectronic Engineering*, 33(1-4):165–172, 1997.

[47] R.J. Roark. *Formulas for stress and strain.* 1965.

[48] R. Saha and W.D. Nix. Effects of the substrate on the determination of thin film mechanical properties by nanoindentation. *Acta Materialia*, 50(1):23–38, 2002.

[49] K. Sato, M. Shikida, T. Yamashiro, K. Asaumi, Y. Iriye, and M. Yamamoto. Anisotropic etching rates of single-crystal silicon for tmah water solution as a function of crystallographic orientation. *Micro Electro Mechanical Systems, 1998. MEMS 98. Proceedings., The Eleventh Annual International Workshop on*, pages 556–561, 25-29 Jan 1998.

[50] J. Schimkat. Contact measurements providing basic design data for microrelay actuators. *Sensors & Actuators: A. Physical*, 73(1-2):138–143, 1999.

[51] J. Schimkat. Contact materials for microrelays. *Micro Electro Mechanical Systems, 1998. MEMS 98. Proceedings., The Eleventh Annual International Workshop on*, pages 190–194, 25-29 Jan 1998.

[52] SP Sharma. Adhesion coefficients of plated contact materials. *Journal of Applied Physics*, 47:3573, 1976.

[53] Y. Shi and S.G. Kim. A lateral, self-cleaning, direct contact MEMS switch. *Micro Electro Mechanical Systems, 2005. MEMS 2005. 18th IEEE International Conference on*, pages 195–198.

[54] P.G. Slade. *Electrical contacts: principles and applications.* Marcel Dekker, 1999.

[55] A.H. Slocum. Design of three-groove kinematic couplings. *Journal of Precision Engineering*, 14(2):67–76, April 1992.

[56] A.H. Slocum. *Precision machine design.* Society of Manufacturing Engineers, 1992.

[57] AH Slocum and AC Weber. Precision passive mechanical alignment of wafers. *Microelectromechanical Systems, Journal of*, 12(6):826–834, 2003.

[58] S. Stalnaker, C. Churchill, V. McBride, K. Burnside, J. Broz, and G. Humphrey. Controlling Contact Resistance with Probe Tip Shape and Cleaning Recipe Optimization. *IEEE Southwest Test Workshop (SWTW)*, 2003.

[59] R. S. Timsit. Electrical conduction through small contact spots. *Components and Packaging Technologies, IEEE Transactions on [see also Components, Packaging and Manufacturing Technology, Part A: Packaging Technologies, IEEE Transactions on]*, 29(4):727–734, Dec. 2006.

[60] RS Timsit. Constriction Resistance of Thin-Film Contacts. In *Electrical Contacts, 2008. Proceedings of the 54th IEEE Holm Conference on*, pages 332–336, 2008.

[61] JW Tringe, TA Uhlman, AC Oliver, and JE Houston. A single asperity study of Au/Au electrical contacts. *Journal of Applied Physics*, 93:4661, 2003.

[62] M Vincent, L Chiesi, P Rousset, C Lapiere, C Poulain, L Carbone, F Houze, and J Delmare. An original apparatus for endurance testing of mems electrical contact materials. In *Electrical Contacts, 2009. Proceedings of the 55th IEEE Holm Conference on*, pages 285–289, 2009.

[63] A.C. Weber. Precision passive alignment of wafers. Master's thesis, Massachusetts Institute of Technology, 2002.

[64] A.C. Weber, J.H. Lang, and A.H. Slocum. 111 si etched planar electrical contacts for power mems-relays. pages 156–159, 16-19 Sept. 2007.

[65] Alexis C. Weber. *MEMS Relays for Make-Break Power Switching Applications: 111 Silicon Etched Planar Electrical Contacts.* PhD thesis, Massachusetts Institue of Technology, 2008.

[66] O. Yagliglu, A.J. Hart, R. Martens, and A.H. Slocum. Method of characterizing electrical contact properties of carbon nanotube coated surfaces. *Review of Scientific Instruments*, 77(095105):1–3, Sep 2006.

[67] Q. Zhang, L. Liu, and Z. Li. A new approach to convex corner compensation for anisotropic etching of (100) Si in KOH. *Sensors & Actuators: A. Physical*, 56(3):251–254, 1996.